中国科学技术大学

博士学位论文

200GeV 金核金核对撞中 粲介子以及粲重子的产生

作者姓名: 谢冠男

学科专业: 粒子物理与原子核物理

导师姓名: 李 澄 教授

董昕 研究员

唐泽波 副教授

完成时间: 二〇一七年四月

University of Science and Technology of China

A dissertation for doctor's degree

Charmed Meson and Baryon Production in Au + Au collisions at $\sqrt{s_{NN}}$ = 200 GeV at RHIC

Author :	Guannan Xie
Specialty :	Particle and Nuclear Physics
Supervisor :	Prof. Cheng Li
	Prof. Xin Dong
	Prof. Zebo Tang
Finished Time :	April, 2017

中国科学技术大学学位论文原创性声明

本人声明所呈交的学位论文，是本人在导师指导下进行研究工作所取得的成果。除已特别加以标注和致谢的地方外，论文中不包含任何他人已经发表或撰写过的研究成果。与我一同工作的同志对本研究所做的贡献均已在论文中作了明确的说明。

作者签名：_____　　签字日期：_____

中国科学技术大学学位论文授权使用声明

作为申请学位的条件之一，学位论文著作权拥有者授权中国科学技术大学拥有学位论文的部分使用权，即：学校有权按有关规定向国家有关部门或机构送交论文的复印件和电子版，允许论文被查阅和借阅，可以将学位论文编入《中国学位论文全文数据库》等有关数据库进行检索，可以采用影印、缩印或扫描等复制手段保存、汇编学位论文。本人提交的电子文档的内容和纸质论文的内容相一致。

保密的学位论文在解密后也遵守此规定。

□公开　□保密（____ 年）

作者签名：_____　　导师签名：_____

签字日期：_____　　签字日期：_____

摘 要

在相对论重离子碰撞中，质心能量高达每核子对 200GeV 的金核金核碰撞后会产生一种高温高密的物质。这种解禁闭的物质被称为夸克胶子等离子体（QGP），研究它的性质是重离子物理实验的主要目标之一。

由于重味夸克的质量比较大，在 RHIC 能区其主要是通过在碰撞早期的硬散射过程而产生。重味夸克经历了整个系统的演化，因此可以提供非常独特的信息以用来研究这种高温高密的 QGP 性质。

重味夸克强子的衰变长度通常都很短，实验上测量重味夸克一般通过两种途径。一种是通过半轻子衰变道测量（semi-leptonic channel），另一种是通过强子衰变道（hadronic channel），两种方法具有各自的优缺点。通过半轻子衰变道衰变而来的电子通常也被称为非光电子（NPE）。这种方法具有相对较大的衰变道分支比，同时电子相对容易被探测器触发。但是，半轻子衰变道这种方法依赖于复杂的理论解释去区分半轻子衰变是来自于粲夸克（c）衰变还是来自于底夸克（b）衰变。与此同时，由于衰变，实验上测量的半轻子动力学区间所对应的重味夸克母粒子通常是来自于非常宽的动力学区间，致使测量具有较大的不确定性。第二种方法是通过强子衰变道方法测量，强子衰变道可以完全重建粲夸克强子的动力学信息同时又不受到半轻子衰变道方法的各种弊端。但是通过这种方法的测量通常都具有十分大的挑战性，因为重离子碰撞中重建过程中来自于随机组合的背景非常大，同时强子衰变道的衰变分支比相对较小。因此想要实现这种强子衰变道的精确测量需要探测器提供非常高的精度，以达到几十微米量级的精度。STAR 合作组 2014 年安装的重味径迹探测器（HFT）就是为了这个目的而专门建造的。

重味夸克的核修正因子（R_{AA}）一直被当做是研究部分子在介质中相互作用从而导致能量损失的重要观测量，这对研究能量损失对于不同味夸克的依赖很重要，最终帮助我们理解介质的性质，例如介质中的输运系数，阻力系数以及扩散系数。

低横动量区间重味夸克的椭圆流（v_2）测量对于研究介质热化程度具有很大的意义。低横动量以及中间横动量区间的重味夸克可以通过夸克重组机制强子化从而形成强子，这将影响重味夸克强子的横动量产额谱以及 v_2。高横动量区间的 D 介子 v_2 可以与 R_{AA} 一起限制部分子在介质中能损对于路径长度的依赖。

实验上粲夸克强子的精确测量不仅对粲夸克产生截面很重要，同时对于粲偶素的产额压制以及重组机制研究（coalescence）意义重大。例如，如果低横动量区间的粲偶素是通过粲夸克和反粲夸克的重组机制产生的，那么粲偶素会携带粲夸克最原始的集体流信息。而如果粲偶素不是通过这个机制产生的，那么粲偶素很可能不会携带粲夸克的原始集体流信息。

RHIC 能区，在重离子碰撞实验中观测到了重子相较于介子的产额增强（enhancements in the baryon-to-meson ratio）。相较于偏心碰撞以及质子质子碰撞，这种产额增强发生在中心核子核子碰撞中，而且是在中间横动量区间（$2 < p_T < 6$ GeV/c），这种产额增强既存在于轻夸克强子中，同时也存在于奇异夸克强子中。这种产额增强可以被强子化机制中的重组机制理论很好的描述。Λ_c 作为质量最轻的粲夸克重子，其质量也最接近 D^0 介子，同时它的寿命非常短，只有 $c\tau \sim 60$ μm。不同的理论模型对于 Λ_c/D^0 的比值预测具有很大的区别，因为这些理论模型对于粲夸克在介质中的热化程度以及重组机制的具体应用都有很大的区别。

对于包含轻味夸克以及奇异夸克的重子相较于介子产额增强在实验上都已观测到，因此对于含有重味夸克的 Λ_c/D^0 的首次测量在实验上就显得意义重大。相较于粲夸克介子，粲夸克重子衰变到轻子的衰变分支比会小一些，因此如果实验上 Λ_c/D^0 的产额有所增强，那么对于非光电子的测量会有一定的压制影响。同时，Λ_c 和 D_s 强子的测量对于中间快度区的粲夸克产生截面也很重要。

因此，本论文主要讨论在 STAR 合作组首次利用重味径迹探测器重建粲夸克强子的具体方法及结果，其中包含 D^0，$D^{\pm}$ 以及 Λ_c 的测量。本论文会报告探测效率修正后的 D^0 和 $D^{\pm}$ 横动量产额谱，其中 D^0 是通过 $D^0(\bar{D^0}) \to K^{\mp}\pi^{\pm}$ 的衰变道测量，而 $D^{\pm}$ 是通过 $D^{\pm} \to K^{\mp}\pi^{\pm}\pi^{\pm}$ 衰变道测量。本论文还会报告在金核金核 200GeV 中心碰撞中 D^0 介子的核修正因子。

本论文还将报告重离子碰撞中 Λ_c 的首次测量。Λ_c 是通过 $\Lambda_c^+ \to p^+K^-\pi^+$ 衰变道测量。在金核金核 200GeV 碰撞中，中心度处于 10-60%，横动量处于 $3 < p_T < 6$ GeV/c 范围内的 Λ_c 产额谱也将会展示。同时本论文还会报告重离子碰撞中的 Λ_c/D^0 产额比值的首次测量，并且会与不同的理论计算作比较并作讨论。

STAR 合作组安装 HFT 后的首次 D^0 产额谱测量以及核修正因子的测量，其测量精度相较于 STAR 已发表的实验结果有很大的提升。新的实验结果显示并确认重离子碰撞中，高横动量区间的 D^0 产额相较于质子质子碰撞中具有很强的压制效应，这意味着粲夸克与介质之间存在着很强的相互作用，并且损失能量。实验结果显示 D^0 介子 R_{AA} 跟轻夸克强子的 R_{AA} 具有很相似的趋势。重建效率修正后的 $D^{\pm}$ 产额谱也将会与 D^0 产额谱作比较，考虑到粲夸克分裂的分支比影响，D^0 与 $D^{\pm}$ 介子的产额谱具有相似（相同）的形状，意味着这两者之间的产生机制是相似的。

重离子碰撞实验中的首次 Λ_c 测量结果将会在本论文中展示，实验结果显示 Λ_c/D^0 产额比值与轻夸克的重子介子产额比值相似，而且实验结果与包含粲夸克热化的夸克重组理论模型预测结果一致。

结合本论文中的所有实验结果以及 STAR 最近发表的 D^0 椭圆流结果，实验结果显示粲夸克与 QGP 之间存在着强烈的耦合作用，而且粲夸克在介质中有着很显著的能量损失。同时粲夸克存在着明显的集体流效应，预示着粲夸克可能在

QGP 物质中已达到热平衡。实验结果显示粲夸克的各种观测量与轻夸克以及奇异夸克之间并没有特别大的区别，这不禁让人产生一个问题，粲夸克作为 QGP 物质的探针是否合适，其重量是否足够大，在未来我们是否需要需要一些新的、更重的探针，例如底夸克?

关键词： 夸克胶子等离子体，重味径迹探测器，Λ_c，D^0，重子介子产额比，核修正因子，夸克重组模型

ABSTRACT

A hot and dense form of matter is believed to be produced in Au+Au collisions at $\sqrt{s_{NN}}$ = 200 GeV at the Relativistic Heavy-Ion Collider (RHIC). To measure the properties of this new deconfined state of matter, the Quark-Gluon Plasma (QGP), is one of the main goals of the heavy-ion collision experiments.

Due to the large quark mass, charm quarks are dominantly produced in the early stage of the collision in hard scattering processes at RHIC. And they experience the whole evolution of the system, offer unique information for the study of hot and dense strongly-coupled QGP matter.

Open heavy flavor hadrons have a very short decay length. Experimentally, heavy flavor hadron reconstruction is carried out through semi-leptonic decays or the hadronic decays both with their respective advantages and disadvantages.

Electrons from semi-leptonic decays, referred to as non-photonic electrons (NPE), have relatively high branching ratios and can be triggered by detectors. The interpretation of the NPE measurements relies on good understanding of leptons from the various charmed and bottom decays contribution. Also, due to decay smearing the p_T of their parent heavy flavor hadrons can come from a wide kinematic region.

The hadronic channels allow to fully reconstruct the charmed hadrons and do not suffer from the complications in the semi-leptonic decays. However the measurement can be challenging due to large combinatorial backgrounds and lower branching ratios. This requires the detectors must be able to resolve differences on the order of tens of microns. The Heavy Flavor Tracker is an excellent dector in charged track projections for this propose.

Heavy quarks nuclear modification factor (R_{AA}) has been proposed as an important measurement to study the flavor dependence of partons energy loss in the medium, and eventually to help in extracting the medium transport, drag and diffusion coefficients.

Measurements of heavy quarks v_2 at low transverse momentum promise to quantify the degree of thermalization of the bulk matter. In particular, low and mid momentum heavy quarks could hadronize via recombination, this could affect the p_T dependence of measured spectra and v_2. At high p_T the D meson v_2 can constrain, together with the R_{AA}, the path dependence of the in medium energy loss.

The precise measurement of charm hadron production could be crucial for the total charm yield, and provide the baseline for charmonium suppression and coalescence. For example, if the charmonium states at low p_T are created by coalescence of flowing charm and anti-charm from the medium, they will carry the original flow of these charm

quarks. On the other hand, if charmonium states are produced promptly, they are less likely to flow.

At RHIC, enhancements in the baryon-to-meson ratio for light hadrons and hadrons containing strange quarks have been observed in central heavy-ion collisions compared to those in p+p and peripheral heavy-ion collisions in the intermediate transverse momentum (p_T) range ($2 < p_T < 6$ GeV/c). This can be explained by the hadronization mechanism involving multi-parton coalescence. Λ_c is the lightest charmed baryon with mass close to that of D^0 meson, and has an extremely short life time ($c\tau \sim 60$ μm). Different models predict different magnitudes of enhancement in the Λ_c/D^0 ratio depending on the degree to which charm quarks are thermalized in the medium and how the coalescence mechanism is implemented.

From the experiment side, it would be nature to measure this baryon-to-meson ratio for heavy quarks. Also, since charm baryon decays produce less electrons than charm meson decays, an enhancement in Λ_c/D^0 ratio will result in a suppression in the non-photonic electron yield in heavy-ion collisions. Measurement of Λ_c and D_s hadrons are important to determine the total charm yield at mid-rapdity.

The baryon-to-meson enhancement can be explained by the coalescence hadronization through recombination of constituent quarks. Theoretical calculations for such an enhancement would be sensitive to how the coalescence mechanism is implemented and the degree to which charm quarks are thermalized in the medium.

Therefore it is important to measure Λ_c and D_s charm hadron yields to better constrain the total charm yield in heavy-ion collisions, and also crucial for distinguishing these models and shed lights on the charm quark hadronization in the hot and dense medium.

So in these dissertation, I report the details of our first measurement of D^0, $D^{\pm}$ and Λ_c production via their topological reconstruction using the Heavy Flavor Tracker (HFT) at STAR.

We report the measurement of efficiency corrected spectrum for D^0 and $D^{\pm}$ through the hadronic channels ($D^0(\bar{D^0}) \to K^{\mp}\pi^{\pm}$ and $D^{\pm} \to K^{\mp}\pi^{\pm}\pi^{\pm}$), the Nuclear Modification Factor (R_{AA}) of D^0 mesons in central Au+Au collisions at $\sqrt{s_{NN}}$ = 200 GeV.

In these dissertation, I also report the first measurement of Λ_c production in heavy-ion collisions through the hadronic channel $\Lambda_c^+ \to p^+K^-\pi^+$. The invariant yield of Λ_c for $3 < p_T < 6$ GeV/c is measured in 10-60% central Au+Au collisions at $\sqrt{s_{NN}}$ = 200 GeV. The Λ_c/D^0 ratio is compared to different model calculations, and the physics implications are discussed.

The first measurement of corrected spectra and R_{AA} for D^0 from HFT were shown, the precision was much better compared to previous published one. The new R_{AA} re-

sults show significant suppression at high p_T which means the strong interaction between charm quark and the medium and loose energy. While the D^0 R_{AA} shows quite similar trend as light hadrons. The efficiency corrected spectra for $D^{\pm}$ was also presented. After taken into the charm fragmentation, the $D^{\pm}$ and D^0 spectra have similar/same shape, which means the production mechanism are similar for them.

The first measurement of Λ_c in heavy-ion collisions was presented in this dissertation. The enhancement of Λ_c/D^0 ratio was compared to light hadrons and several different models predictions. And the coalescence model with thermalized charm quarks are consistent with our data.

From all the observed measurements from this dissertation together with our recently results on D^0 v_2, charm quarks strongly coupled with the QGP and significantly loss energy. Evidence of charm quark flowing and possibly thermalized in the QGP. Which make charm quarks no big difference compare with light and strangeness quarks. Then a native question will be does charm quark heavy enough as a clean probe to determinate the QGP properties? Should we turn to even heavy quark such as bottom in the future?

Keywords: Quark-gluon plasma, Heavy Flavor Tracker, Λ_c, D^0, Baryon to Meson Ratio, Nuclear modification factor, Coalescence

Table of Contents

摘　要 I

ABSTRACT V

Table of Contents IX

List of Tables XIII

List of Figures XV

Chapter 1　Introduction 1

1.1 Standard Model 1

1.2 Quantum Chromodynamics 1

1.2.1 Asymptotic Freedom and Confinement 3

1.2.2 Perturbative QCD (pQCD) 4

1.2.3 Chiral Symmetry 5

1.3 Quark Gluon Plasma and Phase Transition 6

1.4 Relativistic Heavy Ion Collisions 8

1.4.1 QGP evolution 8

1.4.2 Collectivity motion 9

1.4.3 Elliptic flow 12

1.4.4 Energy loss and jet quenching 13

1.4.5 Heavy flavor quarks as probes of sQGP 14

1.5 Open Heavy Flavor Reconstruction 16

1.5.1 Previous measurements 17

Chapter 2　Experimental Setup 21

2.1 Relativistic Heavy Ion Collider 21

2.2 The STAR detector 21

2.3 Time Projection Chamber 22

2.4 Time of Flight detector 23

2.5 Heavy Flavor Tracker 25

2.5.1 HFT performance and status 27

2.5.2 HFT related physics 29

Chapter 3 D^0 Analysis Details 31
3.1 Data Set 31
3.2 Trigger and Event Selection 31
3.3 Centrality Definition 32
3.4 D^0 Reconstruction 36
3.4.1 Daughter Selection 38
3.4.2 Topological Cut Optimization 39
3.4.3 Mixed Event Background 44
3.4.4 Correlated background 'bump' for D^0 meson 46
3.5 D^0 Efficiency and Acceptance Corrections 49
3.5.1 Single Track Efficiency 50
3.5.2 TPC Tracking efficiency 50
3.5.3 TOF Matching Efficiency 51
3.5.4 PID Cut Efficiency 52
3.5.5 Data-driven Fast Simulation for HFT and Topological Cut Efficiency 54
3.6 Validation Data-Driven Fast-Simulation with Full GEANT + Hijing Simulation 62
3.6.1 Hijing Samples Performance 62
3.6.2 Validation Procedures 63
3.6.3 Validation with K_s Spectra 72
3.7 Systematic Uncertainties 72
3.8 Other Systematics for the Fast-Simulation 74
3.8.1 Secondary Track Contribution 74
3.8.2 Vertex Resolution Contribution 76
Chapter 4 Λ_c Analysis Details 77
4.1 Data Set and Event Selections 77
4.2 Λ_c Reconstruction 77
4.2.1 Daughter Selection 78
4.2.2 Topological Cut Optimization 79
4.2.3 Λ_c Signals 81

4.3 Λ_c Efficiency and Acceptance Corrections · · · · · 85
4.3.1 Single Track Efficiency · · · · · 86
4.3.2 TPC Tracking efficiency · · · · · 86
4.3.3 TOF Matching Efficiency · · · · · 86
4.3.4 PID Cut Efficiency · · · · · 88
4.3.5 Data-driven Fast Simulation for HFT and Topological Cut Efficiency · · · · · 88
4.4 Validation Data-Driven Fast-Simulation with Full GEANT + Hijing Simulation · · · · · 90
4.4.1 Validation Procedures · · · · · 91
4.5 Systematic Uncertainties · · · · · 97
4.6 Other Systematics for the Fast-Simulation · · · · · 98
Chapter 5 $D^{\pm}$ Analysis Details · · · · · 101
5.1 Data Set and Event Selections · · · · · 101
5.2 $D^{\pm}$ Reconstruction · · · · · 101
5.2.1 Daughter Selection · · · · · 101
5.2.2 Topological Cut · · · · · 102
5.2.3 $D^{\pm}$ Signals · · · · · 103
5.3 $D^{\pm}$ Efficiency and Acceptance Corrections · · · · · 104
5.3.1 Data-driven Fast Simulation for HFT and Topological Cut Efficiency · · · · · 106
5.4 Validation Data-Driven Fast-Simulation with Full GEANT + Hijing Simulation · · · · · 109
5.4.1 Validation Procedures · · · · · 110
5.5 Systematic Uncertainties · · · · · 115
5.6 Other Systematics for the Fast-Simulation · · · · · 116
Chapter 6 Experimental Results and Discussions · · · · · 117
6.1 The Total D^0 Spectra · · · · · 117
6.2 Blast Wave (BW) Model Fit · · · · · 118
6.3 D^0 Nuclear Modification Factor · · · · · 119
6.4 $D^{\pm}$ Spectra · · · · · 121
6.5 Λ_c/D^0 Ratio and Comparisons to Models · · · · · 121
6.6 Some Other's HFT Results (D^0 v_2) · · · · · 124
Chapter 7 Summary and Outlook · · · · · 127
7.1 Summary · · · · · 127
7.2 Outlook · · · · · 128

References ····· 131
Appendix A Appendix ····· 135
ACKNOWLEDGMENTS ····· 137
Presentations and Publication List ····· 139

List of Tables

3.1 Triggers ID used in this analysis from run14 31
3.2 Event selection in Au+Au collisions at 200 GeV for D^0. 32
3.3 Centrality defintion based on gRefMult 37
3.4 Standard geometrical cuts for different D^0 p_T. 43
3.5 Tight geometrical cuts for different D^0 p_T. 43
3.6 Loose geometrical cuts for different D^0 p_T. 43
3.7 Summary of information saved for the event mixing 44
3.8 Systematic uncertainties from different sources 74

4.1 Event selection in Au+Au collisions at 200 GeV for Λ_c. 77
4.2 Default Geometrical cuts for Λ_c $p_T \geq 3$ GeV/c. 81
4.3 Loose Geometrical cuts for Λ_c $p_T \geq 3$ GeV/c. 82
4.4 Another Loose Geometrical cuts for Λ_c $p_T \geq 3$ GeV/c. 82
4.5 Systematic uncertainties for Λ_c from different sources 98

5.1 Geometrical cuts for different $D^{\pm}$ p_T. 103
5.2 Systematic uncertainties from different sources 116

List of Figures

1.1 The Standard Model of elementary particles (more schematic depiction), with the three generations of matter, gauge bosons in the fourth column, and the Higgs boson in the fifth (CERN). 2

1.2 Experimentally measured α_s as function of the respective energy scale Q. 3

1.3 Quark masses in the QCD vacuum and the Higgs vacuum. A large fraction of the light quark masses is due to the chiral symmetry breaking in the QCD vacuum. The numerical values were taken from PDG. 6

1.4 Lattice calculations for the heavy-mass quark potential in different temperature cases. The band depicts the Cornell potential of $V(r) = -\alpha/r + \sigma r$ with α = 0.25 $\pm$ 0.05 [92] 7

1.5 A conjectured QCD phase diagram with boundaries that define various states of QCD matter. 7

1.6 A cartoon depicting the space-time history of the QGP as generated in a heavy ion collision at LHC energies. The overlay on the right shows the lab-frame evolution. 9

1.7 The m_T spectra for light hadrons (π, K, p), Λ, Ξ and multi-strange hadrons (Φ, Ω) in 200 GeV central Au+Au collisions, and charmed hadron (D^0) in 200 GeV minimum bias Au+Au collisions are shown in symbols. The Blast Wave fit results are shown in curves. The BW fit for D^0 was done by combining D^0 spectrum and the measured charm decay leptons spectra below 2 GeV/c. The BW fits were done for π^-, K^-, $\bar{p}$ simultaneously and for other particles separately. The arrows show the expected increasing freeze-out temperature and decreasing collective velocity from bottom to top. 10

1.8 The χ^2 contours, extracted from BW (thermal + radial flow) fits, for produced hadrons π, K and p and multi-strange hadrons Φ and Ω. For Φ and Ω, only the most central results are presented. Dashed and solid lines are the 1-σ and 2-σ contours, respectively. 11

1.9 Identified particle v_2 as a function of m_T - m in 0-80% Au+Au collisions at $\sqrt{s_{NN}}$=200 GeV. Open circles, open squares, solid triangles and solid circles represent K^0_s , Λ, Ξ and Ω, respectively. (right): Identified particle v_2 scaled by the number of constituent quarks (n_q) versus (m_T - m)/n_q. 13

1.10 (Left) $R_{AB}(p_T)$ for minimum bias and central d + Au and central Au + Au collisions. (Right) Two particle azimuthal distributions in p + p, d + Au and central Au + Au collisions. 14
1.11 (left) Charm quark pair production cross section vs. p_T at mid-rapidity in p + p ($\bar{p}$) collisions at = $\sqrt{s_{NN}}$ = 200 GeV-7 TeV. FONLL pQCD calculations are shown as shaded bands. (right) Charm cross section at mid-rapidity from p+ p to central Au+Au collisions from STAR. 15
1.12 Jet flavor tomography level crossing pattern of nuclear modification factors at middle rapidity of π, D, B, e calculations for central Au + Au 200 GeV collisions. 17
1.13 (upper) D^0, π, $h^{\pm}$ R_{AA} from different measurements. (bottom) v_2 of D and $h^{\pm}$ from ALICE. 17
1.14 v_2 as a function of p_T for D^0 and some other particles in 10–40% centrality Au+Au collisions from STAR. 18
1.15 Baryon-to-meson ratio for p/π (left) and Λ/K_s (right) measured in Au+Au collisions by the STAR experiment 18

2.1 The RHIC accelerator complex. 21
2.2 Perspective view of the STAR detector. 22
2.3 The schematics of the STAR TPC. 23
2.4 TPC dE/dx versus charge$\times$momentum achieved from Run14 Au+Au 200GeV. 24
2.5 Two side views of MRPC. The upper is for long side view and the lower is for short side view. 24
2.6 TOF 1/Beta versus momentum achieved from Run14 Au+Au 200GeV. . 25
2.7 3D model of HFT detector as it sits inside the STAR TPC. 26
2.8 Schematic of the HFT cross section. 26
2.9 DCA_{XY} resolution with the STAR HFT achieved in 2014 for pions. . . 28
2.10 DCA_Z resolution with the STAR HFT achieved in 2014 for pions. . . . 28
2.11 PXL inner sensor status vs. all runs in 2014. 29
2.12 PXL outer sensor status vs. all runs in 2014. 29

3.1 The mean value of gRefmult ($\langle$gRefmult$\rangle$) as a function of run index from QA. 33
3.2 The mean value of p_T for HFT matched track ($\langle$HFT $p_T\rangle$) as a function of index. 33
3.3 The mean value of HFT matching ratio ($\langle$HFT $p_T\rangle$) as a function of run index at the transverse momentum range 0.7 < p_T < 0.8 GeV/c. 33

3.4 The mean value of HFT matching ratio ($\langle$HFT $p_T\rangle$) as a function of run index at the transverse momenaum range p_T > 2.0 GeV/c. 33
3.5 Normalized gRefmult distribution for VpdMB5 trigger along different V_z range 34
3.6 Normalized gRefmult distribution for VpdMB30 trigger along different V_z range 34
3.7 <gRefmult> as function of ZdcX before correction. 34
3.8 <gRefmult> as function of ZdcX after correction. 34
3.9 Fitting gRefmult tail distribution in the range of 1<V_z<2 cm by Eq. 3.3. 35
3.10 High end point as function of V_z after correction. 35
3.11 High end point as function of V_z after correction. 35
3.12 The double ratio of normalized gRefmult distribution from VpdMB5 over VpdMB30, this additional correction factor was try to normalized VpdMB5 to VpdMB30 trigger. 36
3.13 The comparison of corrected gRefMult between Data and Glauber MC. The red line is data and the black line is from Glauber MC. 36
3.14 MC/data gRefmult distribution for Vpd MinBias trigger efficiency correction. The red line fit function is the correction reweight function. . . 36
3.15 The comparison of corrected gRefMult (after all corrections and reweight) between Data and Glauber MC. The red line is data and the black line is from Glauber MC. 37
3.16 The topology of a D^0 decaying to a kaon and a pion. 40
3.17 comparison of simulated position resolution (DCA XY) vs. p for kaon (black), pion (red) and data measurements (blue). 40
3.18 Distributions of the 5 geometry variables for signal (blue) and background (red). 41
3.19 Signal efficiency, lowest background efficiency, significance and so on vs. signal efficiency. 42
3.20 Signal efficiency, lowest background efficiency, significance and so on vs. signal efficiency. 42
3.21 Invariant mass distribution for foreground and two descriptions of combinatorial background in 1 < p_T < 2 GeV/c. 45
3.22 Invariant mass distribution for foreground and two descriptions of combinatorial background in 4 < p_T < 5 GeV/c. 46
3.23 Simulated contribution to the invariant mass spectrum from cocktail without topological cut 47

3.24 Simulated contribution to the invariant mass spectrum from cocktail with topological cut 48
3.25 Comparison of $K\pi$ invariant mass distribution for unlike-sign (US) foreground, like-sign combinatorial background, unlike-sign (US) mixed events combinatorial background, and unlike-sign (US) mixed events combinatorial background + toy montecarlo cocktail for correlated background, for 2 < p_T < 3 GeV/c. 48
3.26 Similar Comparison of $K\pi$ invariant mass distribution as Fig. 3.25, for 3 < p_T < 10 GeV/c. 49
3.27 TPC tracking efficiency in Run14 Au+Au collisions at 200 GeV for Pion. 51
3.28 TPC tracking efficiency in Run14 Au+Au collisions at 200 GeV for Kaon. 51
3.29 TOF match efficiency in Run14 Au+Au collisions at 200 GeV for positive charge particle in 0-10%. 52
3.30 TOF match efficiency in Run14 Au+Au collisions at 200 GeV for negative charge particle in 40-80%. 52
3.31 $n\sigma_K$ distributions for 0.5 < p_T < 0.7 GeV/c. The solid lines are from TPC and dashed lines are from TPC + TOF. 53
3.32 $n\sigma_K$ distributions for 0.2 < p_T < 0.5 GeV/c. The solid lines are from TPC and dashed lines are from TPC + TOF. 53
3.33 $n\sigma_K$ distributions for 1.0 < p_T < 1.5 GeV/c. The solid lines are from TPC and dashed lines are from TPC + TOF. 53
3.34 The $\pi\pi$ pairs invariant mass distributions. The black line is the unlike-sign foreground, and the red line is background using likesign method. 54
3.35 The KK pairs invariant mass distributions. The black line is the unlike-sign foreground, and the red line is background using likesign method. 54
3.36 The mean value of $n\sigma_\pi$ distributions vs momentum. The red line is fitted function with polynomial function. 55
3.37 The sigma value of $n\sigma_\pi$ distributions vs momentum. The red line is fitted function with polynomial function. 55
3.38 $n\sigma_\pi$ cut efficiency along with momentum. Red line is the fitted polynomial function 55
3.39 $1/\beta$ cut efficiency along with momentum for pion. Red line is the fitted function. 56

3.40 $1/\beta$ cut efficiency along with momentum for kaon. Red line is the fitted function. . . . 56
3.41 HFT to TPC track match ratio for pion at certain η,V_Z,ϕ,centrality range. 58
3.42 Dca_{XY} vs. Dca_Z for pion at certain η,V_Z,centrality range. . . . 58
3.43 D^0 efficiency step by step from TPC, HFT Ratio, Topological cut in most central 0-10%. . . . 59
3.44 D^0 efficiency including TPC, HFT and Topological cut in several centralities. . . . 59
3.45 D^0 invariant mass distributions in the $2 < p_T < 3$ GeV/c, 0-10% centrality. Black is unlikesign foreground, blue is likesign background and red is mixed event background. The blue vertical lines are the mass window used for the topological comparison. . . . 60
3.46 D^0 cosTheta distribution in most central 0-10% between Fast-Simulation and Real Data. . . . 60
3.47 D^0 decay length distribution in most central 0-10% between Fast-Simulation and Real Data. . . . 60
3.48 D^0 dcaDaughters distribution in most central 0-10% between Fast-Simulation and Real Data. . . . 61
3.49 D^0 dca to Vertex distribution in most central 0-10% between Fast-Simulation and Real Data. . . . 61
3.50 D^0 pionDca distribution in most central 0-10% between Fast-Simulation and Real Data. . . . 61
3.51 D^0 kaonDca distribution in most central 0-10% between Fast-Simulation and Real Data. . . . 61
3.52 (top)HFT Efficiency Factorization comparison. (bottom) Double Ratio of these factorization. . . . 63
3.53 Comparison of Dca between data (red) and Fast-Simulation (black). From top to bottom, the comparison is for Dca_{XY}, Dca_Z and Dca. From left to right the transverse momentum is from low p_T to high p_T. . . . 64
3.54 HFT Ratio comparison between data and Hijing simulation in Au+Au 200 GeV/c, 0-10%. . . . 64
3.55 $\pi^{\pm}$ Dca_{XY} comparison between data and Hijing simulation in Au+Au 200 GeV/c, 0-10%. . . . 64
3.56 Hjiing validation procedure and workflow . . . 65
3.57 D^0 pure acceptance from different MC decayer, such as PYTHIA, Hijing, evtGen and PhaseSpace class. (right) Double ratio of the acceptance to PYTHIA. . . . 66

3.58 The comparison of D^0 TPC acceptance $\times$ efficiency between Hijing + GEANT (red) and Fast-Simulation with Hijing input (black). (right) Double ratio of these acceptance to Hijing. 66

3.59 The comparison of D^0 TPC + HFT match acceptance $\times$ efficiency between Hijing + GEANT (red) and Fast-Simulation with Hijing input (black). (right) Double ratio of these acceptance to Hijing. 67

3.60 The comparison of D^0 TPC + HFT match + Topological acceptance $\times$ efficiency between Hijing + GEANT (red) and Fast-Simulation with Hijing input (black). (right) Double ratio of these acceptance to Hijing. 68

3.61 The comparison of D^0 TPC + HFT match + Topological acceptance $\times$ efficiency between Hijing + GEANT (red) and Fast-Simulation with Hijing input with wide binning (black). (right) Double ratio of these acceptance to Hijing. 69

3.62 The comparison of D^0 TPC + HFT Real match + Topological acceptance $\times$ efficiency between Hijing + GEANT (red) and Fast-Simulation with Hijing input (black). (right) Double ratio of these acceptance to Hijing. 69

3.63 The comparison of D^0 TPC + HFT Real match + Topological acceptance $\times$ efficiency between Hijing + GEANT (red) and Fast-Simulation with Hijing input with wide binning (black). (right) Double ratio of these acceptance to Hijing. 70

3.64 The comparison of D^0 TPC + HFT (real/mis) match + Topological acceptance $\times$ efficiency for Hijing + GEANT. (right) Double ratio of the components form Hijing. 70

3.65 D^0 cosTheta distribution in most central 0-10% between Hijing and Fast-Simulation. 71

3.66 D^0 decay length distribution in most central 0-10% between Hijing and Fast-Simulation. 71

3.67 D^0 pions Dca distribution in most central 0-10% between Hijing and Fast-Simulation. 71

3.68 D^0 kaons Dca distribution in most central 0-10% between Hijing and Fast-Simulation. 71

3.69 D^0 dcaDaughters distribution in most central 0-10% between Hijing and Fast-Simulation. 72

3.70 K_s corrected spectra in Au+Au collisions at 10-20% centrality. Open symbols are published results and solid symbols are new results from HFT with data-driven Fast-Simulation method. Bottom panel shows the ratios to the fitting function. 73
3.71 The vertex distribution for Pions from secondary decay. Top left is the overall secondary pion tracks, top right is pion decayed from GeantID=8/9 (which is $\pi^{\pm}$), bottom left is pion decayed from GeantID=15/25 (which is anti-proton and anti-neutron), bottom right is decayed from other source 75
3.72 HFT Matching Ratio for Pions, compare between primary track and secondary tracks relay on Hijing. (bottom) The double ratios of inclusive one to primary tracks. 76
3.73 HFT Matching Ratio for Kaons, compare between primary track and secondary tracks relay on Hijing. (bottom) The double ratios of inclusive one to primary tracks. 76

4.1 The topology of a Λ_c decaying to a kaon, pion and a proton. 79
4.2 Distributions of the 6 geometry variables for Λ_c signal (blue) and background (red). 80
4.3 Signal efficiency, lowest background efficiency, significance and so on vs. signal efficiency. 81
4.4 Λ_c invariant mass distribution for foreground (red) and wrong-sign background (grey) in 3 < p_T < 6 GeV/c at 0-80% centrality. 83
4.5 Λ_c invariant mass distribution for foreground (red) and wrong-sign background (grey) in 3 < p_T < 6 GeV/c at 10-80% centrality. 83
4.6 Λ_c invariant mass distribution for foreground (red) and wrong-sign background (grey) in 3 < p_T < 6 GeV/c at 40-80% centrality. 84
4.7 Λ_c invariant mass distribution for foreground (red) and wrong-sign background (grey) in 3 < p_T < 6 GeV/c at 10-60% centrality. 84
4.8 Λ_c invariant mass distribution for foreground (red) and wrong-sign background (grey) in 3 < p_T < 6 GeV/c at 10-40% centrality. 85
4.9 TPC tracking efficiency in Run14 Au+Au collisions at 200 GeV for Proton. 87
4.10 TPC tracking efficiency in Run14 Au+Au collisions at 200 GeV for AntiProton. 87
4.11 TOF match efficiency in Run14 Au+Au collisions at 200 GeV for positive charge particle in 0-10%. 87

4.12 TOF match efficiency in Run14 Au+Au collisions at 200 GeV for negative charge particle in 40-80%. 87
4.13 The πp pairs invariant mass distributions. The black line is the unlikesign foreground, and the red line is background using likesign method. . 88
4.14 $n\sigma_p$ cut efficiency along with momentum. Line is the fitted polynomial function. 89
4.15 $1/\beta$ cut efficiency along with momentum for proton. Line is the fitted function. 89
4.16 Λ_c efficiency step by step from TPC, HFT Ratio, Topological cut in 10-60%. 90
4.17 Λ_c efficiency including TPC, HFT and Topological cut in several centralities. 90
4.18 Hjiing validation procedure and workflow for Λ_c. 91
4.19 Λ_c pure acceptance from different MC decayer, such as PYTHIA, Hijing, evtGen and PhaseSpace class. (right) Double ratio of the acceptance to evtGen PHSP. 92
4.20 The comparison of Λ_c TPC acceptance $\times$ efficiency between Hijing + GEANT (red) and Fast-Simulation with Hijing input (black). (right) Double ratio of these acceptance to Hijing. 93
4.21 The comparison of Λ_c TPC + HFT match acceptance $\times$ efficiency between Hijing + GEANT (red) and Fast-Simulation with Hijing input (black). (right) Double ratio of these acceptance to Hijing. 93
4.22 The comparison of Λ_c TPC + HFT match + Topological acceptance $\times$ efficiency between Hijing + GEANT (red) and Fast-Simulation with Hijing input (black). (right) Double ratio of these acceptance to Hijing. 94
4.23 The comparison of Λ_c TPC + HFT Real match + Topological acceptance $\times$ efficiency between Hijing + GEANT (red) and Fast-Simulation with Hijing input (black). (right) Double ratio of these acceptance to Hijing. 95
4.24 The comparison of Λ_c TPC + HFT (real/mis) match + Topological acceptance $\times$ efficiency for Hijing + GEANT. (right) Double ratio of the components form Hijing. 95
4.25 Λ_c cosTheta distribution in most central 0-10% between Hijing and Fast-Simulation. 96
4.26 Λ_c decay length distribution in most central 0-10% between Hijing and Fast-Simulation. 96
4.27 Λ_c pions Dca distribution in most central 0-10% between Hijing and Fast-Simulation. 96

4.28 Λ_c kaons Dca distribution in most central 0-10% between Hijing and Fast-Simulation. 96
4.29 Λ_c protons Dca distribution in most central 0-10% between Hijing and Fast-Simulation. 97
4.30 Λ_c dcaDaughters distribution in most central 0-10% between Hijing and Fast-Simulation. 97
4.31 The vertex distribution for Protons from secondary decay. Top left is the overall secondary pion tracks, top right is pion decayed from GeantID=8/9 (which is $\pi^{\pm}$), bottom left is pion decayed from GeantID=15/25 (which is anti-proton and anti-neutron), bottom right is decayed from Λ. 99
4.32 HFT Matching Ratio for Protons, compare between primary track and secondary tracks relay on Hijing. (bottom) The double ratios of inclusive one to primary tracks. 99

5.1 The topology of a $D^{\pm}$ decaying to a kaon and two pions. 103
5.2 $D^{\pm}$ invariant mass distribution for foreground (red) and wrong-sign background (grey) in $1 < p_T < 8$ GeV/c at 0-80% centrality. 104
5.3 $D^{\pm}$ invariant mass distribution for foreground (red) and wrong-sign background (grey) in $1 < p_T < 8$ GeV/c at 0-10% centrality. 105
5.4 $D^{\pm}$ invariant mass distribution for foreground (red) and wrong-sign background (grey) in $1 < p_T < 8$ GeV/c at 20-40% centrality. 105
5.5 $D^{\pm}$ invariant mass distribution for foreground (red) and wrong-sign background (grey) in $1 < p_T < 8$ GeV/c at 40-80% centrality. 106
5.6 $D^{\pm}$ efficiency step by step from TPC, HFT Ratio, Topological cut in 0-10%. 107
5.7 $D^{\pm}$ efficiency including TPC, HFT and Topological cut in several centralities. 107
5.8 $D^{\pm}$ cosTheta distribution in most central 0-10% between Fast-Simulation and Real Data. 108
5.9 $D^{\pm}$ decay length distribution in most central 0-10% between Fast-Simulation and Real Data. 108
5.10 $D^{\pm}$ dcaDaughters distribution in most central 0-10% between Fast-Simulation and Real Data. 108
5.11 $D^{\pm}$ dca to Vertex distribution in most central 0-10% between Fast-Simulation and Real Data. 108
5.12 $D^{\pm}$ pionDca distribution in most central 0-10% between Fast-Simulation and Real Data. 109

5.13 $D^{\pm}$ kaonDca distribution in most central 0-10% between Fast-Simulation and Real Data. . . . 109
5.14 $D^{\pm}$ pure acceptance from different MC decayer, such as PYTHIA, Hijing, evtGen and PhaseSpace class. (right) Double ratio of the acceptance to PYTHIA PHSP. . . . 110
5.15 The comparison of $D^{\pm}$ TPC acceptance $\times$ efficiency between Hijing + GEANT (red) and Fast-Simulation with Hijing input (black). (right) Double ratio of these acceptance to Hijing. . . . 111
5.16 The comparison of $D^{\pm}$ TPC + HFT match acceptance $\times$ efficiency between Hijing + GEANT (red) and Fast-Simulation with Hijing input (black). (right) Double ratio of these acceptance to Hijing. . . . 112
5.17 The comparison of $D^{\pm}$ TPC + HFT match + Topological acceptance $\times$ efficiency between Hijing + GEANT (red) and Fast-Simulation with Hijing input (black). (right) Double ratio of these acceptance to Hijing. 112
5.18 The comparison of $D^{\pm}$ TPC + HFT (real/mis) match + Topological acceptance $\times$ efficiency for Hijing + GEANT. (right) Double ratio of the components form Hijing. . . . 113
5.19 The comparison of $D^{\pm}$ TPC + HFT Real match + Topological acceptance $\times$ efficiency between Hijing + GEANT (red) and Fast-Simulation with Hijing input (black). (right) Double ratio of these acceptance to Hijing. . . . 114
5.20 $D^{\pm}$ cosTheta distribution in most central 0-10% between Hijing and Fast-Simulation. . . . 114
5.21 $D^{\pm}$ decay length distribution in most central 0-10% between Hijing and Fast-Simulation. . . . 114
5.22 $D^{\pm}$ pions1 Dca distribution in most central 0-10% between Hijing and Fast-Simulation. . . . 115
5.23 $D^{\pm}$ pions2 Dca distribution in most central 0-10% between Hijing and Fast-Simulation. . . . 115
5.24 $D^{\pm}$ kaons Dca distribution in most central 0-10% between Hijing and Fast-Simulation. . . . 115
5.25 $D^{\pm}$ dcaDaughters distribution in most central 0-10% between Hijing and Fast-Simulation. . . . 115

6.1 D^0 corrected spectra in Au+Au collisions from several centralities. . . . 117
6.2 D^0 corrected spectra in Au+Au collisions fitting with BW model. . . . 118
6.3 D^0 R_{AA} in Au+Au collisions from 0-10% centrality. . . . 119

6.4 D^0 R_{AA} in Au+Au collisions from 0-10% centrality comparison with various models. 120
6.5 $D^{\pm}$ corrected spectra in Au+Au collisions from several centralities. . . 121
6.6 $D^{\pm}$ corrected spectra in Au+Au collisions from several centralities comparing with D^0. $D^{\pm}$ is after the charm fragmentation scale to the same level of D^0 for comparison. 122
6.7 Measured Λ_c/D^0 ratio for $3 < p_T < 6$ GeV/c in 10-60% central Au+Au collisions at $\sqrt{s_{\rm NN}}$ = 200 GeV compared to model predictions from PYTHIA, statistical hadronization model (SHM) and coalescence models from Ko and Greco. 123
6.8 Baryon-to-meson ratio for p/π (left panel), Λ/K_s (middle panel) and Λ_c/D^0 (right panel) measured in Au+Au collisions by the STAR experiment. Several model predictions also shown for Λ_c/D^0. 123
6.9 v_2 as a function of p_T for D^0 in 10−40% centrality Au+Au collisions compared with K^0_S, Λ, and Ξ^-. 124
6.10 v_2/n_q as a function of $(m_T - m_0)/n_q$ for D^0 in 10 − 40% centrality Au+Au collisions compared with K^0_S, Λ, and Ξ^-. 124

7.1 PXL inner sensor status vs. all runs in 2016. 128
7.2 PXL outer sensor status vs. all runs in 2016. 128
7.3 The R_{AA} of J/Ψ (top panel), D^0 (middle panel) and electron (bottom panel) from B (filled circles) and D (open circles) hadron decays as a function of p_T in Au+Au collisions at $\sqrt{s_{NN}}$ = 200 GeV. 130

Chapter 1 Introduction

1.1 Standard Model

There are four known fundamental forces in the universe including the electromagnetic, weak interactions, strong interactions and the gravity. The Standard Model of particle physics is a theory describe the first three of the forces as well as classifying all known elementary particles. It has successfully explained almost all the experimental results and provided varieties of precise experimental predictions [1].

According to the standard model, particles are classified in terms of two groups, the fundamental fermions and the gauge vector bosons. The fermions have spin = 1/2 while the bosons have spin = 1. There are 12 known fermions, known as 6 quarks and 6 leptons, each with a corresponding antiparticle. The quarks are consist of up (u), down (d), charm (c), strange (s), top (t) and bottom (b) while the leptons including electron (e), muon (μ), tauon (τ), and their corresponding neutrinos. Pairs from each classification are grouped together to form a generation as shown in Fig. 1.1.

Quarks carry color charge, they interact via the strong force. They also carry electric charge and weak isospin, hence they interact with other fermions both electromagnetically and via the weak nuclear interaction. The other six fermions do not carry color charge. While e, μ and τ carries electric charge thus interact electromagnetically. The other three neutrinos do not, so their motion is directly influenced only by the weak force.

The forces between these fermions are mediated by the force-carrier particles (gauge vector bosons in the last column of Fig. 1.1). The electromagnetic force between the electrically charged particles is mediated by massless photon and initially described by quantum electrodynamics (QED). The weak force between different flavors particles is mediated by massive $W^{\pm}$ and Z bosons. The gluon mediates the strong force which is described by quantum chromodynamics (QCD).

In the prediction of the standard model of particle physics, there is an elementary particle, Higgs boson, finally discovered by the Large Hadron Collider (LHC) at CERN. And this is one big discovery so far from LHC and the success of standard model [2].

1.2 Quantum Chromodynamics

Quantum Chromodynamics (QCD) is a renormalized non-abelian gauge theory based on the $SU(3)_C$ group to describe strong interactions between color charged particles [3].

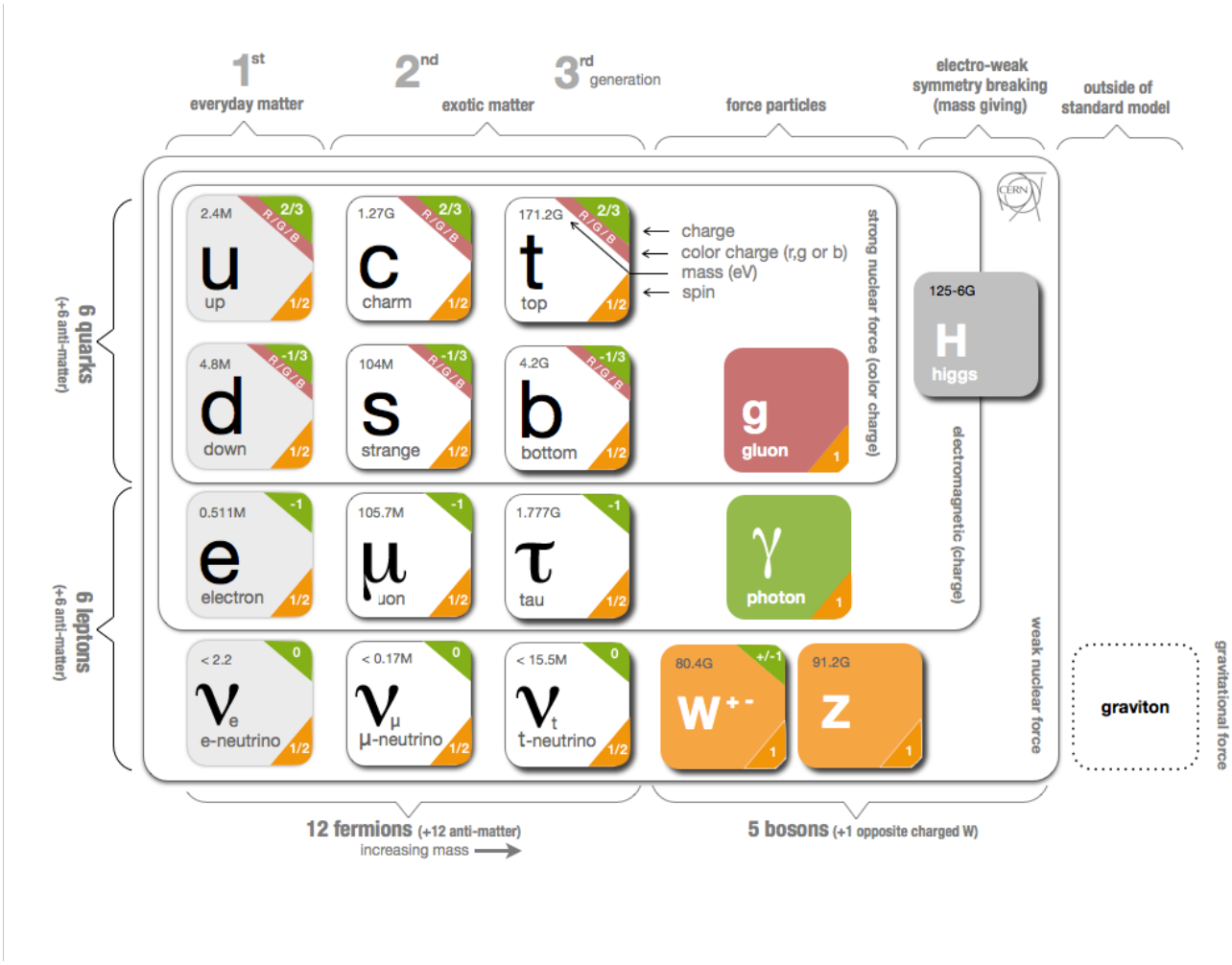

Figure 1.1: The Standard Model of elementary particles (more schematic depiction), with the three generations of matter, gauge bosons in the fourth column, and the Higgs boson in the fifth (CERN).

The gauge invariant Lagrangian that describes the dynamics of quarks and gluons in a color field is:

$$\mathcal{L}_{QCD} = -\frac{1}{4} G^a_{\mu v} G^{\mu v}_a + \bar{\psi}_i (i(\gamma^\mu D_\mu)_{ij} - m\delta_{ij})\psi_j \tag{1.1}$$

Where ψ_i is the quark field, γ^μ is the Dirac matrices and $G^a_{\mu v}$ the gluonic field-strength tensors:

$$G^a_{\mu v} = \partial_\mu A^a_v - \partial_v A^a_\mu + g_s f^{abc} A^b_v A^c_v \tag{1.2}$$

Above, f^{abc} are the structural constant of the $SU(3)$ symmetry group, m and g_s control the quark mass and coupling in the theory, and $D_\mu := -ieA_\mu$ is the covariant derivative responsible for the interaction between the quarks and the gauge potentials A^a_μ. One difference compare to QED is that gluons can interactive with themselves.

QCD has two peculiar properties: 1) Asymptotic freedom; 2) Confinement.

1.2.1 Asymptotic Freedom and Confinement

Experimentally, free quarks are never observed. Only the color-neutral quark bound states - hadrons ($q\bar{q}$, qqq or $\bar{q}\bar{q}\bar{q}$) can be observed. This suggests the interaction between quarks and gluons must be strong on large distance scale. However, in the deep inelastic scattering experiments. It was found that with large momentum transfer, the quarks inside the hadron behaved as if they were almost free. According to the behaviors of short and long distance, the static QCD potential can be described as:

$$V_s = -\frac{4}{3} \times \frac{\alpha_s}{r} + k \times r \tag{1.3}$$

where the first term dominating at small distance is similar to the Coulomb potential between two charges in QED, while the second term is linked to the confinement of quarks and gluons inside hadrons.

The effective coupling constant depends on the renormalization scale, which can be written as:

$$\alpha_s(\mu) = \frac{g_s^2(\mu)}{4\pi} \approx \frac{4\pi}{\beta_0 ln(\mu^2/\Lambda_{QCD}^2)} \tag{1.4}$$

where $\beta_0 = (11 - \frac{2}{3}n_f)$ is a constant, depending on the number of active quark flavors with mass less than μ and Λ_{QCD} is a constant QCD scale parameter determined experimentally ($\Lambda_{QCD} \approx 250$ MeV). The world average α_s at common energy scale $\mu = M_Z$ is $\alpha_s(M_Z) = 0.1185 \pm 0.0006$, Figure 1.2 shows the experimental measurements of α_s as a function of Q (momentum transfer) [4].

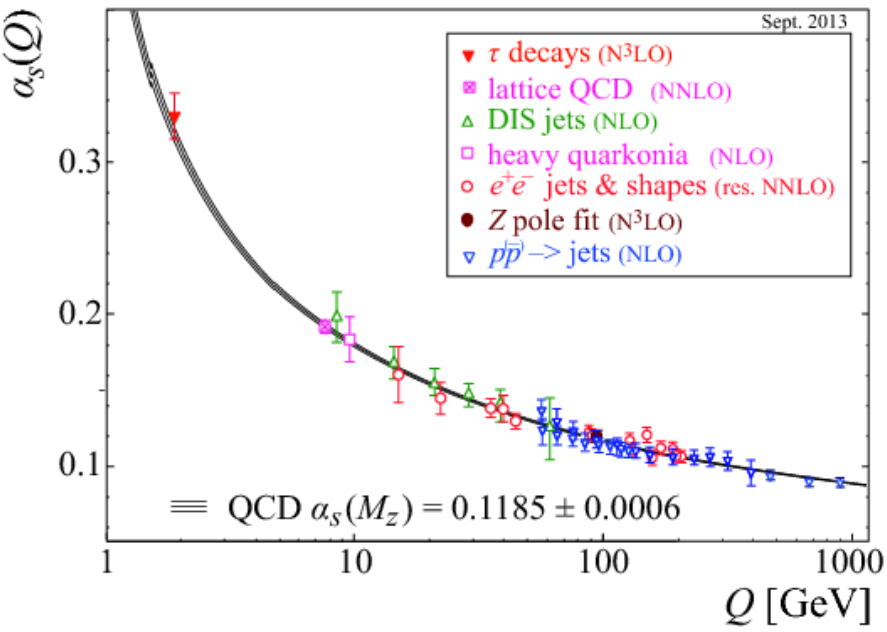

Figure 1.2: Experimentally measured α_s as function of the respective energy scale Q.

Unlike the QED effective coupling which is increase with the energy scale μ, the QCD effective coupling α_s is opposite. With larger Q^2 (probing small length scales),

the α_s becomes smaller. $\alpha_s \to 0$ as $\mu \to \infty$. The small α_s suggests that the quarks and gluons move freely. When $\alpha_s \ll 1$ (high momentum transfer or short distance approach), methods of perturbative QCD (pQCD) are applied to predict the cross sections and distributions of physical processes implying quarks and gluons in the initial, intermediate or final state.

On the contrary, the QCD becomes strongly coupled at $\mu \sim \Lambda_{QCD}$. At low momentum transfer, the QCD coupling constant α_s approach unity quickly as decreasing momentum transfer. In this case, the high order processes will have large contributions and can not be neglected, thus the pQCD is not valid any more. Instead, the Lattice QCD or other Non-Perturbative theory (e.g. AdS/CFT - anti-de-Sitter space/conformal field theory) is used to calculate strong interaction processes.

With smaller Q^2 or larger distance ($\alpha_s \to 1$), the attractive force and gluon binding potential between quarks become larger. When quarks separate, the gluon field form narrow tubes (or strings) of color charge to bring the quarks together. When two quarks have large enough energies and become separated, at some point the gluon field is more energetically favorable to create a new quark and anti-quark pair out of the vacuum than to allow the quarks to separate further. That's why when quarks are produced at high energy, many color-neutral particles clustered together are observed, called jet.

1.2.2 Perturbative QCD (pQCD)

At high momentum transfer, the $\alpha_s \ll 1$ and decrease very slowly, physics quantities, such as the cross sections can be calculated to a truncated series with different α_s dependence (α_s^{n+2}). The terms with lowest power $n(n = 0)$ have the largest contribution and called Leading order (LO). The higher order terms usually have smaller contribution and involves more complicate diagrams which makes the calculation more difficult. Depend on the power n, the corrections are called Next-to-Leading Order (NLO), $n = 1$, Next-to-Next-to-Leading Order ($NNLO$), $n = 2$, etc.

Due to the complexity of hadronic processes, the cross sections calculations are more complicated. For the process on hadron level, the hadron structure which involved nonperturbative nature has to be take into account. The pQCD is only on the parton level. A QCD factorization theorem was develop to calculate the cross section on hadron level, which separate the cross section into 2 parts: the process dependent pQCD calculate short distance parton cross section, and the universal long distance functions. For example, the cross section for a process A + B $\to$ C + ... where A, B and C are hadrons, can be written as:

$$\sigma_{AB\to C} = f_{a/A}(x_a, \mu_F^2) f_{b/B}(x_b, \mu_F^2) \otimes \hat{\sigma}_{ab\to c}(\hat{s}, \mu_F^2, \mu_F^2, \mu_R^2, \alpha_s) \otimes D_{c\to C}(z, \mu_F^2) \quad (1.5)$$

Only the middle term $\hat{\sigma}_{ab\to c}$, the parton cross section, can be calculated in pQCD from Feynman diagrams. The first term $f_{a/A}(x_a, \mu_F^2)$ or $f_{b/B}(x_b, \mu_F^2)$ is the hadron $Parton\ Distribution\ Function$ (PDF) and the last term $D_{c\to C}(z, \mu_F^2)$ is the $Fragmentation\ Function$ (FF) that describes the transition from a parton to a hadron. For leptons, these two terms do to contribute in this formula. Hence, we can measure PDFs through lepton-nucleon DIS interactions and FFs through high energy e^+e^- collisions. μ_R is the renormalization scale, originate from the need to regularize divergent momentum integrals in calculating high order diagram loops. μ_F is the factorization scale, at which the parton density are evaluated. $\hat{s}$ is the partonic center of mass energy squared. As we can see it is complicated to determine the expected hadron production cross section in hadron-hadron collisions [5].

Heavy quark (c, b) production, due to the large masses, is believed to match to pQCD prediction better than light quark production. And because they cannot be produced through the initial light hadron fragmentation, the FF part is irrelevant to the total production cross section of heavy quarks. Hence the measurement of the total heavy quark production cross section offers a powerful test of pQCD.

1.2.3 Chiral Symmetry

The Lagrangian discussed in the previous section has several global symmetries as well as the local $SU(3)$ associated to the color gauge, however there is an additional, approximate symmetry associated to chirality. This can be introduced in the QCD Lagrangian by projecting the Dirac operators into their right and left handed components:

$$\psi_L \equiv \frac{1-\gamma^5}{2}\psi \qquad \psi_R \equiv \frac{1-\gamma^5}{2}\psi \tag{1.6}$$

This symmetry is explicitly broken in the QCD Lagrangian due to the term $m\bar{\psi}\psi$ and as such, massive fermions will not exhibit chiral symmetry. However, for small masses compared to QCD (up, down and to a lesser extent strange quarks), the previous term has near negligible contribution and LQCD becomes invariant under $SU(3)_R \times SU(3)_L$ [6].

There is an important consequence that follows from spontaneous symmetry breaking, proven as part of Goldstone's theorem. In short, the theorem states that the spectrum of physical particles must include at least one particle of zero mass for every symmetry that is spontaneously broken, known as Goldstone bosons. Chiral symmetry is only approximate in QCD, and so the associated psuedo-Goldstone bosons have finite mass, the pions. Thus, the masses of the quarks confined in hadrons have two distinct contributions: a mass generated from the Higgs mechanism as well as a contribution caused by interactions with the pions due to chiral symmetry breaking, known as the QCD

mass [8]. In the case of the lighter quarks (up down and to a lesser extent strange) the QCD mass can account for up to 99% of the observed mass which is in stark contrast with heavy flavor (charm, bottom and top), shown in next Figure [7].

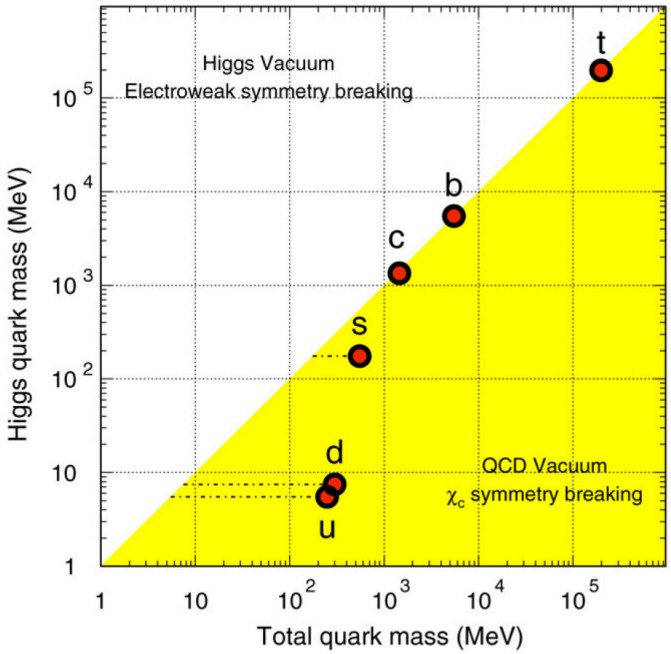

Figure 1.3: Quark masses in the QCD vacuum and the Higgs vacuum. A large fraction of the light quark masses is due to the chiral symmetry breaking in the QCD vacuum. The numerical values were taken from PDG.

Furthermore, as the medium created in a heavy ion collision transits to the QGP state, more and more quark pairs can form and eventually can surpass the binding energy of the R L states and the chiral condensate ceases to exist, known as Chiral Symmetry Restoration. In a QGP where Chiral symmetry has been restored, the light quarks will exhibit, in essence, only their bare masses while the heavy quark masses will remain for the most part unchanged.

1.3 Quark Gluon Plasma and Phase Transition

In normal condition, the QCD matter is mostly observed as quark bound state and can not be isolated. However, at extreme condition like high temperature or high baryon density, quarks and gluons are proposed to be deconfined from a hadron. Then create a new state of deconfined matter so called Quark Gluon Plasma (QGP), with new color $degrees\ of\ freedom$ (DOF). In such an environment, the mesons and baryons lose their identities and dissolve into a fluid of quarks and gluons. The quarks and gluons can move around in a large distance rather than confined in hadrons, which is called $deconfinement$ [9].

Fig. 1.4 depicts the potential between two heavy quarks in different temperature conditions calculated by the 3 flavor Lattice QCD. It shows that at high temperature, the rampart of the potential between two heavy quarks which causes the confinement will bend down due to the Debye color screening, approximately flat at high distance, thus liberate quarks from the trap. In addition, the continuous bending without sudden change indicates a crossover transition at high temperature and vanishing net quark density [92].

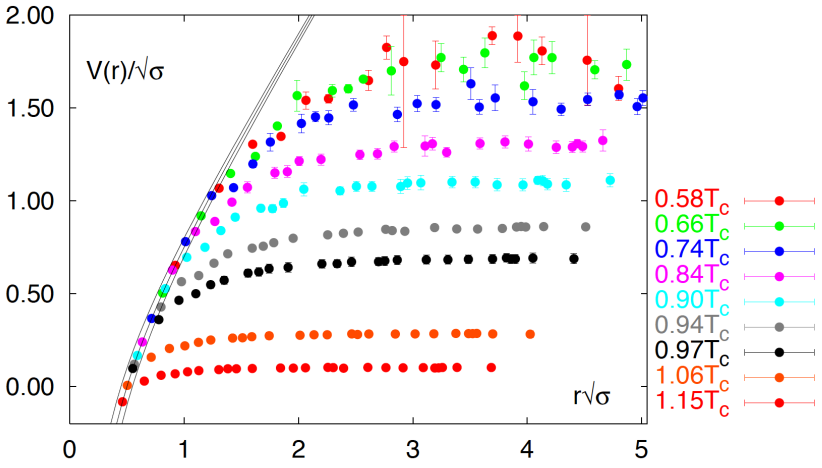

Figure 1.4: Lattice calculations for the heavy-mass quark potential in different temperature cases. The band depicts the Cornell potential of $V(r) = -\alpha/r + \sigma r$ with $\alpha = 0.25 \pm 0.05$ [92]

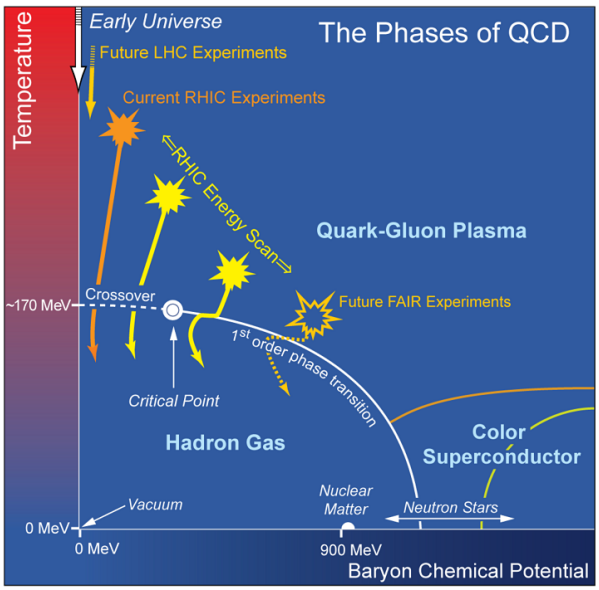

Figure 1.5: A conjectured QCD phase diagram with boundaries that define various states of QCD matter.

Figure 1.5 shows a conjectured phase diagram in $T - \mu_B$ plane, which describes

the phase structure of QCD matter. Lattice QCD calculations predict that the phase transition from hadron gas to the QGP for $T > T_c$ at zero baryon chemical potential ($\mu_B = 0$) is expected to be a smooth crossover (white dashed line) instead of a sudden change of energy density. Lattice QCD calculations also predict that there is a first-order phase transition (white solid line) at large μ_B, and it is expected to be end in a critical point at finite μ_B. The estimation of the location of the critical point (white dot) is depicted in Fig. 1.5 [10].

1.4 Relativistic Heavy Ion Collisions

According the phase diagram, the QGP is possible to be created experimentally in two different directions: 1) high temperature and low baryonic chemical potential (μb); 2) low temperature but large baryonic chemical potential. The relativistic heavy ion colliders are designed to search for the deconfined QGP matter in the first way, including SIS at GSI, AGS at BNL, SPS at CERN, RHIC at BNL and the LHC at CERN.

For the past decades the Relativistic Heavy Ion Collider (RHIC) at Brookhaven National Lab (BNL) has conducted very successful runs. For the data part, RHIC has successfully performed a wide energy ranges for various collision systems including Au+Au collisions at 7.7, 11.5, 14.5, 19.6, 27, 39, 62.4, 130, 200 GeV, Cu+Cu collisions at 62 and 200 GeV, p(d/He^3)+Au(Al) at 200 GeV, p+p collisions at 62, 200, 500 GeV and U+U at 193 GeV [11].

In the following sections, we will force on the evolution of the heavy ion collision (HIC), some expected signatures of the QGP and heavy quark production.

1.4.1 QGP evolution

The heavy-ion collisions can be approximated as the interpenetrating collisions of the constituent nucleons with partonic interactions at high energy. The number of participating nucleons and the produced particle multiplicities in the final hadron state can be calculated by the Glauber model which relates these quantities to the size of the impact parameter, b, which is defined as the distance between the perpendicular bisectors along the colliding direction of the two ions. The impact parameter is large for peripheral collisions, consisting of a small number of participants and small multiplicities. A central collision occurs when the impact parameter is small with large multiplicities.

Fig.1.6 shows the different stages in the space-time evolution of a heavy ion collision. In the relativistic heavy ion collisions, two nuclei can be represented as two thin disks approaching each other at high speed because of the Lorentz contraction effect in the moving direction. Once the nuclei collide, the partons interact through hard processes from which both heavy flavor and high p_T jets form [12].

As the nucleus passing through with each other the energy density increases as more quark and anti-quark pairs are formed. As the temperature approaches the critical value the quarks and gluons become de-cofined and the QGP is formed, QGP continues expanding due to the pressure in the system until cooling enough for confinement again, known as hadronization. As the system continues to expand, the hadrons continue to interact with each other through both elastic and inelastic collisions. Eventually, the system has cooled and expanded enough that the hadrons can only interact through elastic collisions consequently fixing the particle ratios, this stage is known as chemical freeze-out. Finally, the hadrons will reach kinematic freeze-out once the hadrons have drifted far enough from each other and can no longer interact, fixing the particle momenta which are later observed in the detectors.

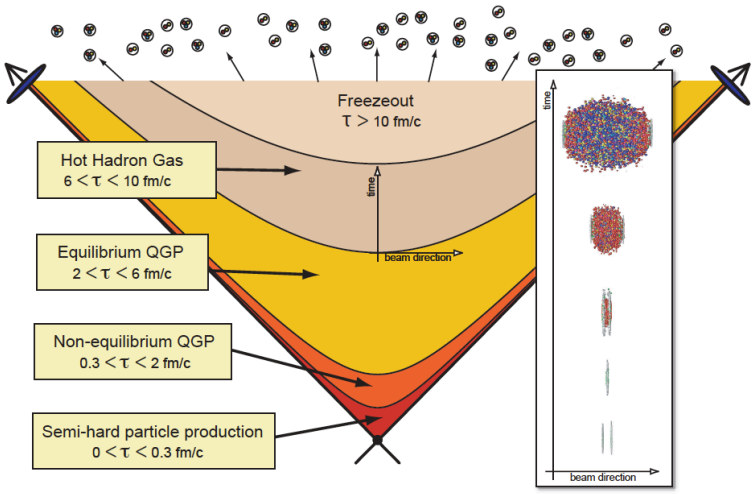

Figure 1.6: A cartoon depicting the space-time history of the QGP as generated in a heavy ion collision at LHC energies. The overlay on the right shows the lab-frame evolution.

Lattice calculations seem to suggest that the onset of QGP should occur at temperatures T_c = 155 MeV or a Bjorken energy density $\varepsilon_c \sim 1$ GeV/fm^3 [13], while the value at RHIC for $\sqrt{s_{NN}}$ = 200 GeV was measured to be 5.4 GeV/fm^3 in the most central collisions [14], well above the requirement for de-confinement. The times indicated in Fig. 1.6 are only estimates, but it is clear that the QGP is extremely short lived and as such, not easy to probe externally. The following two sections will focus on several observables and probes that may carry signatures of the QGP that can be disentangled from the effects of later stages in the collision.

1.4.2 Collectivity motion

The measured hadron spectra are useful tools to study the properties of the bulk system produced in heavy-ion collisions. Specified particles can be used to probe different stages, such as in the soft sector at transverse momenta $p_T < 1.5$ GeV/c reflect

the bulk properties after elastic interactions have stopped among the hadrons at kinetic freeze-out. At this stage the system is already relatively dilute and "cold", however, from the final state hadron spectra at kinetic freeze-out, one can obtain the information about the earlier hotter and denser stage. Since different hadrons have different production (hadronization) mechanisms, by analyzing the transverse momentum distributions for various hadron species we can explore the characteristics of the different stages of the collision system.

Fig. 1.7 shows the measured m_T ($\equiv \sqrt{p_T^2 + m_0^2}$) spectra for light hadrons (π, K, p), Λ, Ξ and multi-strange hadrons (Φ, Ω) in 200 GeV central Au+Au collisions, and charmed hadron (D^0) in 200 GeV minimum bias Au+Au collisions from the previous results [15–19].

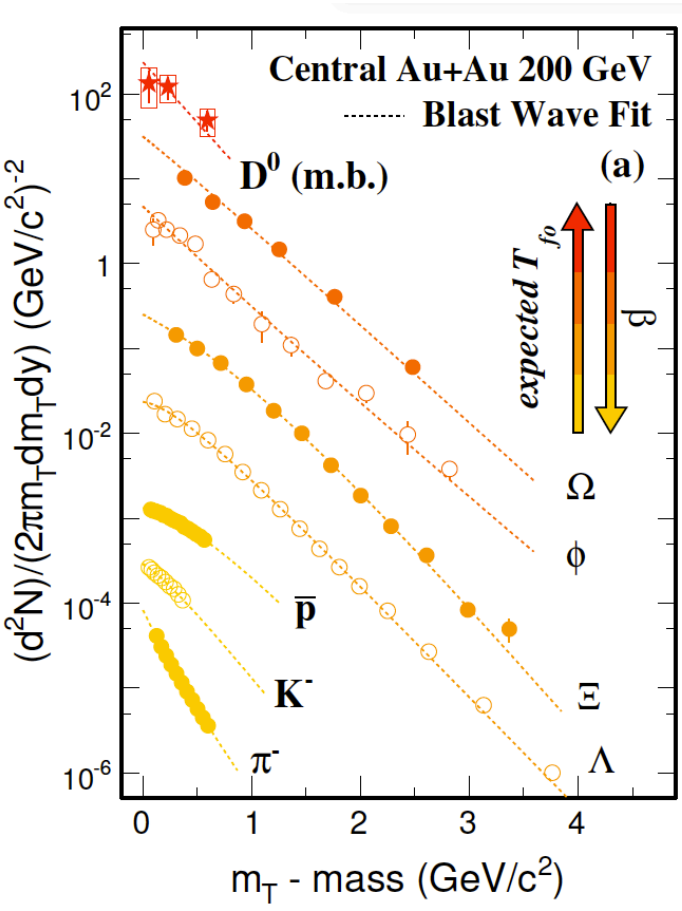

Figure 1.7: The m_T spectra for light hadrons (π, K, p), Λ, Ξ and multi-strange hadrons (Φ, Ω) in 200 GeV central Au+Au collisions, and charmed hadron (D^0) in 200 GeV minimum bias Au+Au collisions are shown in symbols. The Blast Wave fit results are shown in curves. The BW fit for D^0 was done by combining D^0 spectrum and the measured charm decay leptons spectra below 2 GeV/c. The BW fits were done for π^-, K^-, $\bar{p}$ simultaneously and for other particles separately. The arrows show the expected increasing freeze-out temperature and decreasing collective velocity from bottom to top.

The plot shows the slopes of particle spectra changes for different particles (masses),

indicating the strong collectivity of final state particles. The dashed lines depict the fit results from the Blast Wave (BW) thermal model [20]. In thermal models, local thermal equilibrium is assumed and hence particles spectra only depend on the mass of particles and the temperature of system. After the collision, the bulk system expands and becomes more dilute and cold, while the particle collective velocity develops large. Under the assumption of simple cylindrical source and boost invariance in rapidity, BW can extract the parameters characterize kinetic freeze-out temperature T_{f0} and collective, radial flow velocity $\langle \beta \rangle$, aspects.

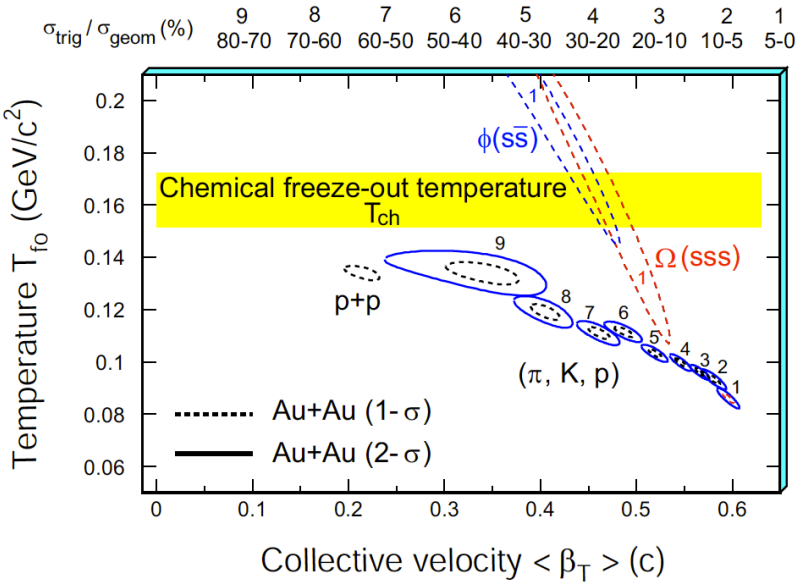

Figure 1.8: The χ^2 contours, extracted from BW (thermal + radial flow) fits, for produced hadrons π, K and p and multi-strange hadrons Φ and Ω. For Φ and Ω, only the most central results are presented. Dashed and solid lines are the 1-σ and 2-σ contours, respectively.

Fig. 1.8 shows the fit results for different particles. For the simultaneous fit to π^-, K^-, p, stronger collectivity is observed from peripheral to central collisions. But the fit to Ω and Φ in central Au + Au collisions shows higher freeze-out temperature and lower transverse velocity, indicating those particles leave the system at the earlier stage than stable hadrons. This can be explained by multi-strange hadrons are expected to have smaller hadronic scattering cross sections and their transverse momentum distributions will not change significantly after chemical freeze-out, the kinetic freeze-out temperature from the fit to those particles is consistent with the chemical freeze-out temperature T_{ch}, albeit with still large uncertainties. The chemical freeze-out temperature T_{ch} is close to the critical temperature T_c, indicating the temperature of the system created in the collisions is greater than T_c and hence the phase transition may take place and QGP may form at RHIC energy of $\sqrt{s_{NN}}$ = 200 GeV [21–27].

Due to relatively heavy quark mass and smaller hadronic scattering cross section,

heavy flavor hadrons are expected to freeze-out early and difficultly participate in collective motion. Thus the larger freeze-out temperature and smaller flow velocity are expected for heavy flavor hadrons. But currently the experimental statistics is not good enough to distinguish the freeze-out properties between D-meson and multi-strange hadrons, this will be discussed in the outlook section.

1.4.3 Elliptic flow

In non-central heavy ion collisions, the initial spatial anisotropy will produce pressure gradients in the expanding medium, boosting particles in the direction of the pressure gradients and transforming into anisotropies the particle momenta. These anisotropies, caused by the collective motion of the particles in the fireball, are generally referred to as flow and can be studied by decomposing the azimuthal distribution of the particles, relative to the reaction plane Ψ_r, shown as:

$$E\frac{d^3N}{dp^3} = \frac{d^2N}{2\pi p_T dp_T dy}(1 + \sum_{n=1}^{\infty} 2v_n \cos[n(\phi - \Phi_{rp})]), \tag{1.7}$$

$$v_n = \langle \cos[n(\phi - \Phi_{rp})] \rangle \tag{1.8}$$

where Φ_{rp} denotes the direction of the reaction plane. The Fourier expansion coefficient v_n stands for the n-th harmonic of the event azimuthal anisotropies. v_1 is so-called directed flow and v_2 is the elliptic flow. Due to the approximate elliptic shape of the overlapping region, the elliptic flow v_2 is the largest harmonic observed in mid-rapidity. Because of the quenching of coordinate-space-anisotropy, elliptic flow can reveal early information about the system and because it depends on rescattering, elliptic flow is sensitive to the degree of thermalization of the system in the early stage.

The identified particle elliptic flow v_2 shows strong transverse momentum dependence in Fig. 1.9. In the low p_T region, v_2 has larger values for lower mass particles, which are described by hydrodynamical models and negligible relaxation time compared to the time scale of the equilibrated system. The agreement implies early thermalization, i.e. strongly interacting matter with a very short mean free path dominates the early stages of the collisions [28, 29].

The right panel of Fig. 1.9 shows v_2 scaled by number of constituent quarks (NCQ) as a function of the NCQ scaled (m_T - m) . All of the particles at (m_T - m)/n_q < 1.0 GeV/c^2 fall onto one universal curve. This meson/baryon grouping phenomenon was also observed in the nuclear modification factor at moderate p_T. Coalescence models which assume hadrons are formed through coalescing of constituent quarks provide

a viable explanation for these observations. This indicates the flow developed during a sub-hadronic (partonic) epoch, and offers a strong evidence of deconfinement at RHIC [30, 31].

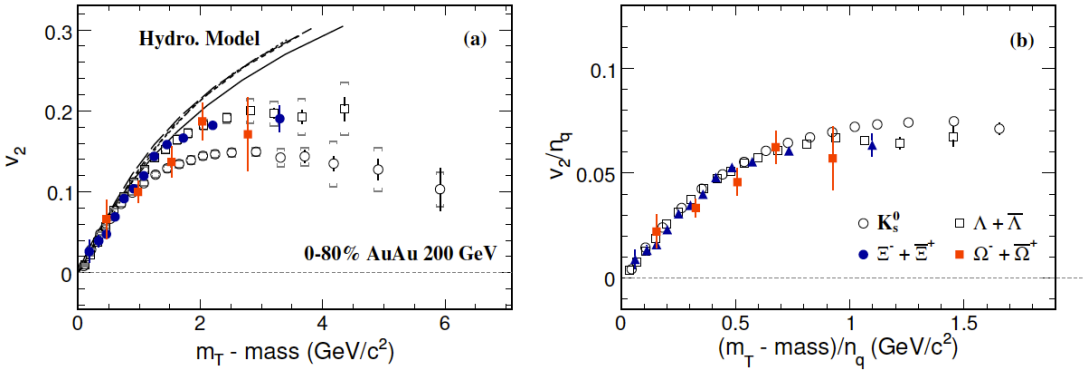

Figure 1.9: Identified particle v_2 as a function of m_T - m in 0-80% Au+Au collisions at $\sqrt{s_{NN}}$=200 GeV. Open circles, open squares, solid triangles and solid circles represent K^0_s , Λ, Ξ and Ω, respectively. (right): Identified particle v_2 scaled by the number of constituent quarks (n_q) versus (m_T - m)/n_q.

1.4.4 Energy loss and jet quenching

In relativistic heavy ion collisions, the high p_T ($p_T > 5$ GeV/c) particles mostly are produced mainly from the initial QCD scattering processes following by parton fragmentation. They can be used as unique probes by studying the interaction of partons with the hot dense medium. A widely used observable is the nuclear modification factor R_{AB} which is the ratio of the spectra in heavy-ion (A + B) collision and those in p + p collisions, scaled by the number of binary nucleon-nucleon collisions [32]:

$$R_{AB}(p_T) = \frac{d^2N_{AB}/dp_Tdy}{T_{AB}d^2\sigma^{pp}/dp_Tdy} \tag{1.9}$$

where $T_{AB} = \langle N_{bin}\rangle/\sigma^{inel}_{pp}$ in the nuclear overlap geometry factor, calculated from the Glauber model. If the nucleus-nucleus interaction is an superposition of incoherent multiple p+p collisions, the R_{AB} should be consistent with unity [33].

The left panel of Fig. 1.10 shows the R_{AB} in minimum bias and central d + Au and central Au + Au collisions at $\sqrt{s_{NN}}$ = 200 GeV. At high p_T, the R_{AuAu} is a constant (0.2) and significantly lower than 1, in contrast with that in d + Au collisions, in which the initial state condition is similar as in Au + Au collisions but final state is different [34–36]. These results suggest that the strong suppression in Au + Au collisions is due to the final state interactions rather than initial state effect and thus a very dense matter must be created in central Au + Au collisions at RHIC. The consistent picture of away-side

jet quenching has also been observed in di-hadron azimuthal angle correlations shown on the right panel. Near side correlation peak was observed in p + p, d + Au and Au + Au collisions due to the single jet, while the back-to-back jet correlations was dramatic suppressed in Au + Au collisions compared those in p + p and d + Au collisions [34, 37].

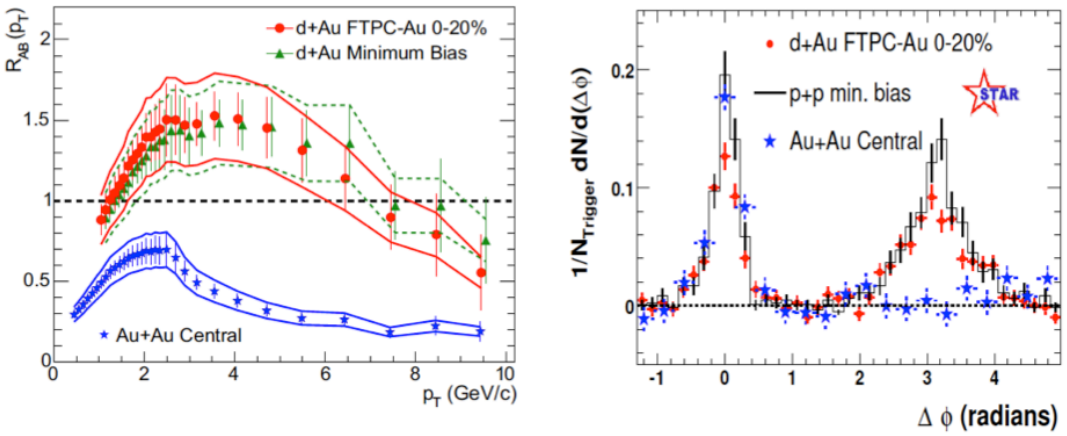

Figure 1.10: (Left) $R_{AB}(p_T)$ for minimum bias and central d + Au and central Au + Au collisions. (Right) Two particle azimuthal distributions in p + p, d + Au and central Au + Au collisions.

All these high p_T suppression or away-side jet quenching observations indicate that light quarks strongly lose energy in the interacting dense medium. However, due to their large quark mass and small gluon radiative angle, heavy quarks are predicted to lose less energy compared to light quarks since pQCD energy-loss calculation assumes only gluon radiation [38–40]. The finite mass generalization of the small x (soft radiation x $\ll$ 1) invariant DGLAP radiation spectrum is given by

$$w\frac{dN_g^{(0)}}{d^3\vec{k}} \approx \frac{C_R\alpha_s}{\pi^2}\frac{k^2}{(k^2+m_g^2+x^2M^2)^2} \tag{1.10}$$

where $w(k)$ is the energy carried by radiated gluons in the medium with momentum k, and α_s is the strong coupling constant. The color charge factor $C_R = \frac{N_c^2-1}{2N_c} = \frac{4}{3}$withthe number of color flavor $N_c = 3$in this case. The gluon radiation angle is defined as $\theta_c \equiv \sqrt{m_g^2+x^2M^2}/(xE)$. Due to large quark mass M, the gluon radiation is suppressed at smaller angles $\theta < \theta_c$. This effect is known as the "dead cone" phenomenon [39].

1.4.5 Heavy flavor quarks as probes of sQGP

The lifetime of the hot and dense matter produced in heavy ion collisions at RHIC is expected to last on the order of a few fm/c and it has an initial transverse radius of roughly 6 fm [42]. Because of this short-lived nature, studying the QGP must rely on probes that are produced in the collision itself. Heavy quarks are used as probes from

within the medium and utilized as 'controlled' probes of the bulk matter in HIC. In this section we will discuss what makes heavy quarks such ideal probes to study sQGP.

Due to their large mass, $m_c \approx 1.3$ GeV/c^2 and $m_b \approx 4.2$ GeV/c^2 heavy quark production through thermal processes is considerably suppressed relative to lighter flavors and as such they are predominantly produced in early stages in hard scatterings and the total cross section amenable to pQCD calculations at sufficiently high p_T. Fig. 1.11 left panel shows the charm differential cross-section at midrapidity versus transverse momentum in p + p collisions at$\sqrt{s_{NN}}$ = 200 GeV - 7 TeV from various experiments. Experimental data are compared with Fixed-Order Next-to-Leading-Log (FONLL) pQCD calculations shown as grey bands. Within uncertainties, FONLL pQCD calculations describe the data over a broad range of collision energies. Not only the mid-rapidity, the LHCb measurements at forward rapidity can be also described by FONLL [43–47].

The hard-scattering production of heavy quarks occurs at the very early stages of the heavy-ion collisions, and also the thermal production rate in the QGP is small (T $<< m_c$) thus, the number of heavy quarks is approximately conserved during the sQGP evolution, and the total cross-section in nucleus-nucleus collisions scales with the number of binary collisions (N_{bin}). Fig.1.11 right panel shows the charm total cross section follows the N_{bin} scaling from STAR [48, 49]. Possibility of production of charm during the QGP phase has been theoretically investigated and turned out to be insignificant at RHIC energies. One merit of heavy quarks which is important to make this binary scaling possible is that the heavy quark masses are dominated by the Higgs mass originated via EM symmetry break, which implies that their masses are, to a good approximation, not modified by their presence in the medium created at RHIC and the LHC [50].

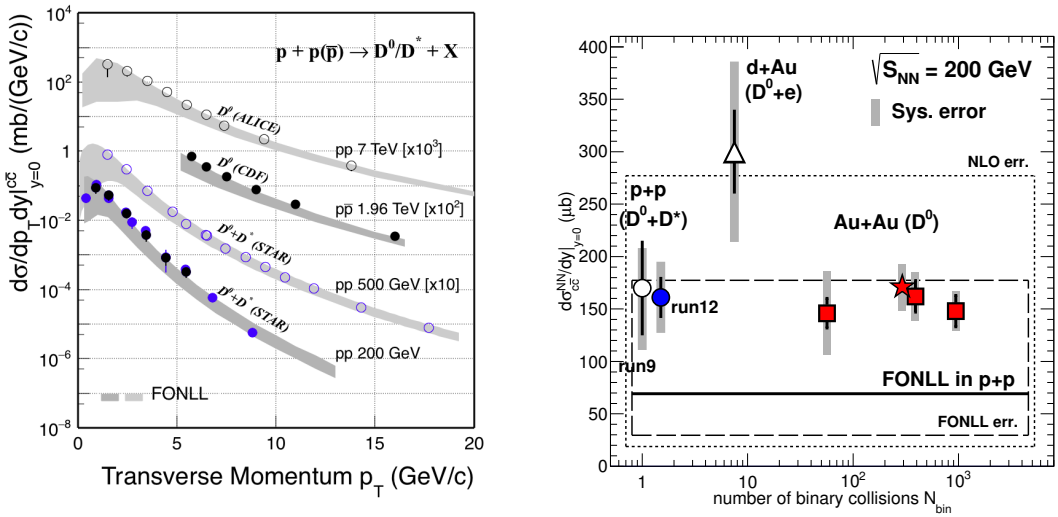

Figure 1.11: (left) Charm quark pair production cross section vs. p_T at mid-rapidity in p + p ($\bar{p}$) collisions at = $\sqrt{s_{NN}}$ = 200 GeV-7 TeV. FONLL pQCD calculations are shown as shaded bands. (right) Charm cross section at mid-rapidity from p+ p to central Au+Au collisions from STAR.

For these merits of heavy quarks they are regarded as clean probes to study the otherwise "thermal" bulk matter even though the degree of thermalization of charm quarks is still under experimental and theoretical study.

1.5 Open Heavy Flavor Reconstruction

Open heavy flavor hadrons have a very short decay length, experimentally, heavy quark reconstruction is carried out through measured leptons from semi-leptonic decays or from the hadronic decays both with their respective advantages and disadvantages.

Electrons from semi-leptonic decays, referred to as non-photonic electrons (NPE), have relatively high branching ratios and can be triggered by detectors, the measurement relies on careful interpretation to disentangle the contribution from the various charmed and bottom decays. Also, due to decay smearing the p_T of their parent heavy flavor hadrons can come from a wide kinematic region.

The hadronic channels allow to fully reconstruct the charmed hadrons and do not suffer from the complications in the semi-leptonic decays, however the measurement can be challenging due to large combinatorial backgrounds and lower branching ratios. This requires the detectors must be able to resolve differences on the order of tens of microns.

Heavy quarks nuclear modification factor (R_{AA}) has been proposed as an important measurement to study the flavor dependence of partons energy loss in the medium, and eventually to help in extracting the medium transport, drag and diffusion coefficients.

There are lots of theoretical calculations for the energy losses for different flavor particles. Fig. 1.12 shows the jet flavor tomography level crossing pattern of nuclear modification factors at middle rapidity of π, D, B, e from CUJT calculations for central Au + Au 200 GeV collisions. As clearly see the mass hierarchy of the different flavor energy loss [41].

Measurements of heavy quarks v_2 at low transverse momentum promise to quantify the degree of thermalization of the bulk matter. In particular, low and mid momentum heavy quarks could hadronize via recombination, this could affect the p_T dependence of measured spectra and v_2. At high p_T the D meson v_2 can constrain, together with the R_{AA}, the path dependence of the in medium energy loss.

The precise measurement of charm hadron production could be crucial for the total charm yield, and provide the baseline for charmonium suppression and coalescence. For example, if the charmonium states at low p_T are created by coalescence of flowing charm and anti-charm from the medium, they will carry the original flow of these charm quarks. On the other hand, if charmonium states are produced promptly, they are less likely to flow.

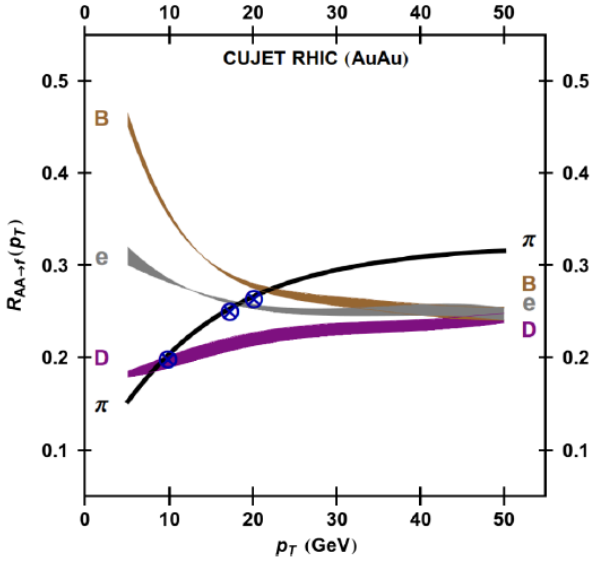

Figure 1.12: Jet flavor tomography level crossing pattern of nuclear modification factors at middle rapidity of π, D, B, e calculations for central Au + Au 200 GeV collisions.

1.5.1 Previous measurements

Fig. 1.13 upper panel shows the R_{AA} of D^0, π, $h^{\pm}$ from various measurements. A significant suppression is clearly seen at the high p_T range for both light hadrons and charmed hadrons both in RHIC energy and LHC energy. The enhancement observed in the intermediate p_T range from STAR can be described by the models including coalescence of charm and light quarks, even though the uncertainties are still large in the low transverse momentum range [48, 51].

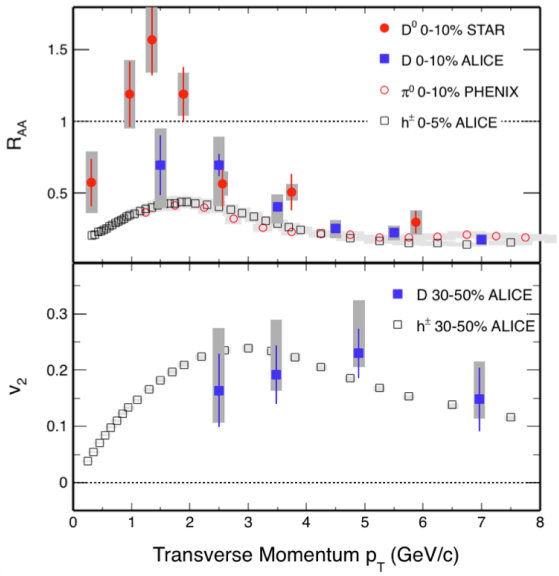

Figure 1.13: (upper) D^0, π, $h^{\pm}$ R_{AA} from different measurements. (bottom) v_2 of D and $h^{\pm}$ from ALICE.

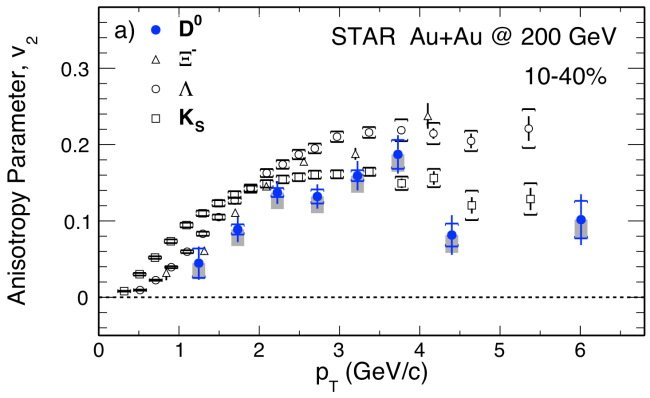

Figure 1.14: v_2 as a function of p_T for D^0 and some other particles in 10−40% centrality Au+Au collisions from STAR.

Fig. 1.13 bottom panel shows the v_2 measurements of D and $h^{\pm}$ from ALICE [51, 52]. With large uncertainties, but still there are clearly non zero v_2 was observed in the middle central collisions. Fig. 1.14 shows the v_2 measurements of D^0 and some other light hadrons from STAR [53, 54].

Fig. 1.15 shows the baryon-to-meson ratio for light hadrons and hadrons containing strange quarks observed in the central and peripheral Au + Au collisions, there is a clear enhancement in the intermediate transverse momentum range from $2 < p_T < 6$ GeV/c [55–57].

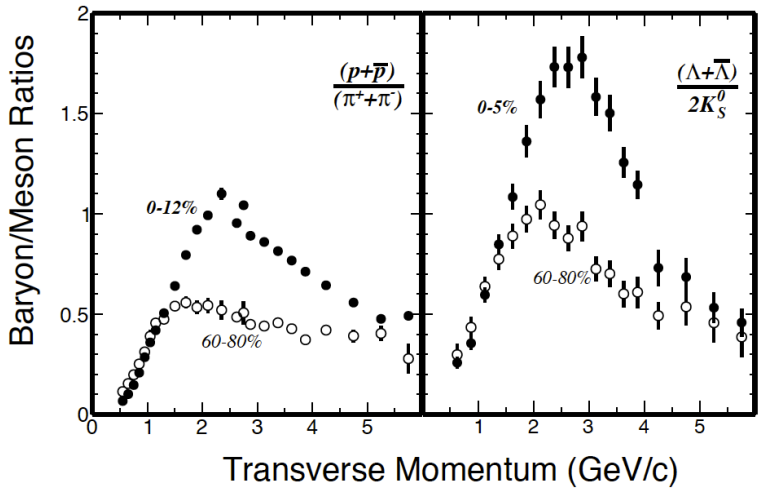

Figure 1.15: Baryon-to-meson ratio for p/π (left) and Λ/K_s (right) measured in Au+Au collisions by the STAR experiment

From the experiment side, it would be nature to measure this baryon-to-meson ratio for heavy quarks. Also, since charm baryon decays produce less electrons than charm meson decays, an enhancement in Λ_c/D^0 ratio will result in a suppression in the non-photonic electron yield in heavy-ion collisions [58]. Measurement of Λ_c and D_s hadrons are important to determine the total charm yield at mid-rapdity. The total charm yield

is also a critical input to calculate charmonium yields in the coalescence/recombination scenario.

The baryon-to-meson enhancement can be explained by the coalescence hadronization through recombination of constituent quarks [59, 60]. Theoretical calculations for such an enhancement would be sensitive to how the coalescence mechanism is implemented and the degree to which charm quarks are thermalized in the medium [62, 64, 65].

Therefore it is important to measure Λ_c and D_s charm hadron yields to better constrain the total charm yield in heavy-ion collisions, and also crucial for distinguishing these models and shed lights on the charm quark hadronization in the hot and dense medium [61, 63].

In the following sections, we will forces on the charm hadron productions using the newly installed Heavy Flavor Tracker at STAR, including the D^0, $D^{\pm}$ and Λ_c.

Chapter 2 Experimental Setup

2.1 Relativistic Heavy Ion Collider

The Relativistic Heavy Ion Collider (RHIC) at Brookhaven National Laboratory (BNL), is a multi-ion species high energy collider as shown in Fig. 2.1. The collider consists of two independent rings with radii 3.8 km used to accelerate and store heavy ions and protons [66]. There are six interaction regions where the two rings intersect out which four originally housed experiments: PHOBOS, BRAHMS, PHENIX and STAR (and only STAR continue to operate today).

Since year 2000, RHIC has successfully collided $p + p$, p + Al, p + Au, d + Au, ^{3}He + Au, Cu + Cu, Cu + Au, Au + Au, and U + U at different energies. The top energy for the gold ions is 100 GeV/u and that for protons is 250 GeV. A major scientific goal of RHIC is to study the properties of hot, dense and strongly interacting quantum chromodynamics (QCD) matter created in the laboratory.

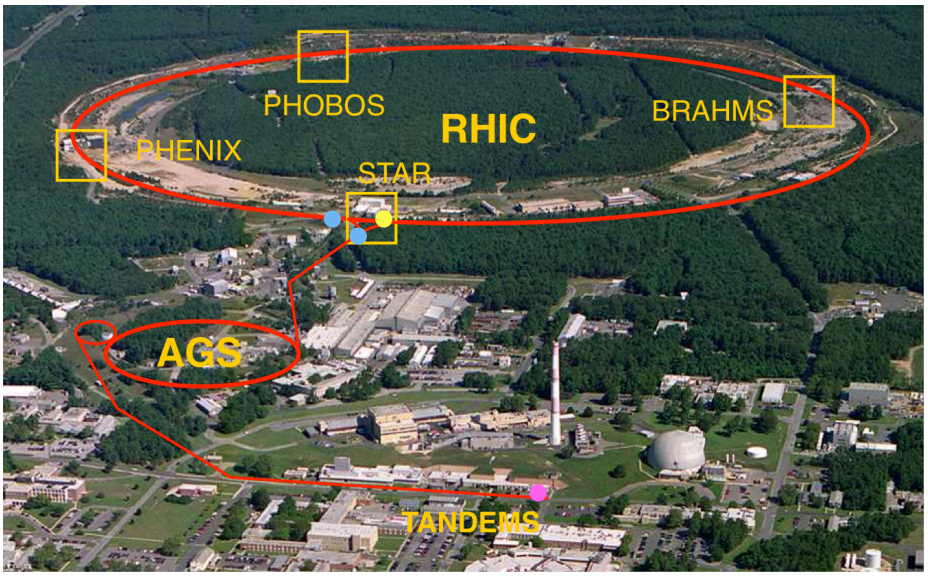

Figure 2.1: The RHIC accelerator complex.

2.2 The STAR detector

The Solenoidal Tracker At RHIC (STAR) is a multi-purpose particle detector located at 6 o'clock of RHIC ring [67]. Fig. 2.2 shows a 3D cartoon of STAR detector and its different subsystems. The large and uniform acceptance ($0 < \phi < 2$, $|\eta| < 1$) of the STAR detector, makes it well suited for event-by-event characterization of high charged particle multiplicity heavy-ion collisions. The heavy-ion events can have more

than 1000 particles per unit of psuedo-rapidity, and within the acceptance, STAR provide excellent particles identification.

Along the beam axis, there are three fast trigger detectors: Beam Beam Counter (BBC) [68], Vertex Position Detector (VPD) [69] and Zero Degree Calorimeter (ZDC) [70]. For this analysis, we mainly use the VPD triggered data.

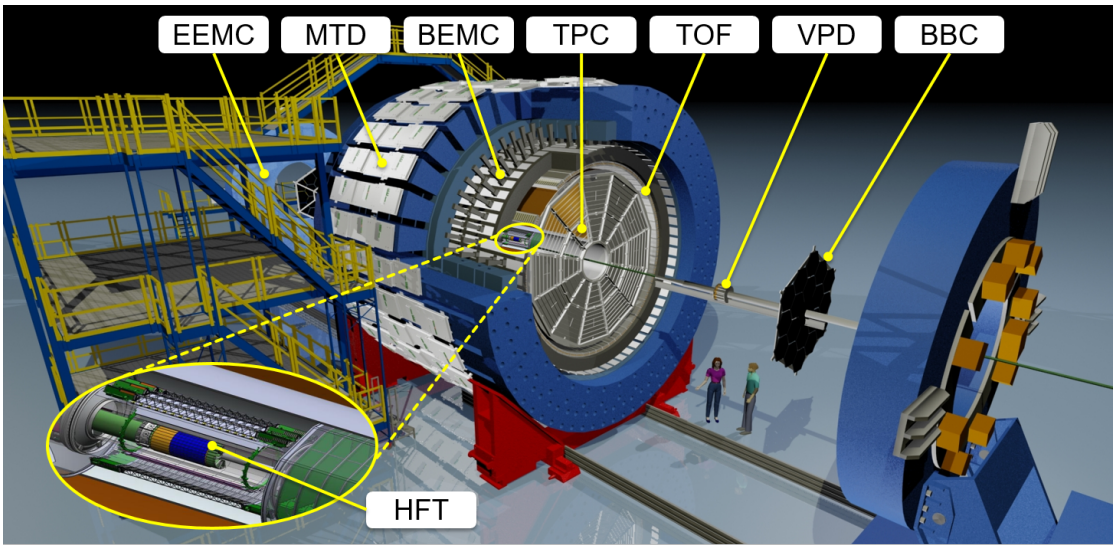

Figure 2.2: Perspective view of the STAR detector.

The two assemblies of the VPD are symmetrically located at a distance of 5.7 m with respect to the interaction region and the VPD covers a pseudo-rapidity of $4.24 < |\eta| < 5.1$. The VPD for the trigger system can provides the primary input to the minimum-bias trigger in nucleus-nucleus collisons. The precise timing information from the VPD detector channels is used both in online (150 ps in $\sqrt{s_{NN}}$ = 200 GeV Au + Au) and offline (30 ps in $\sqrt{s_{NN}}$ = 200 GeV Au + Au) to measure the z position of primary vertex and provide "start time" for the TOF.

Next sections will briefly discuss the main detectors used in the analysis, including Time Projection Chamber, Time of Flight Detector and Heavy Flavor Tracker Detector.

2.3 Time Projection Chamber

The Time Projection Chamber (TPC) is the heart of STAR [71]. Fig. 2.3 shows a schematics cartoon of the TPC. The TPC barrel is 4 m in diameter and 4.2 m long with the volume filled with P10 (90% Argon, 10% Methane) gas. Charged tracks traversing the volume ionize the gas along their paths, released secondary electrons drift in a 135 V/cm electric field to the TPC endcaps to be collected by readout pads. The charge signal measured in the pads together with timing information are used to reconstruct the tracks of the particles.

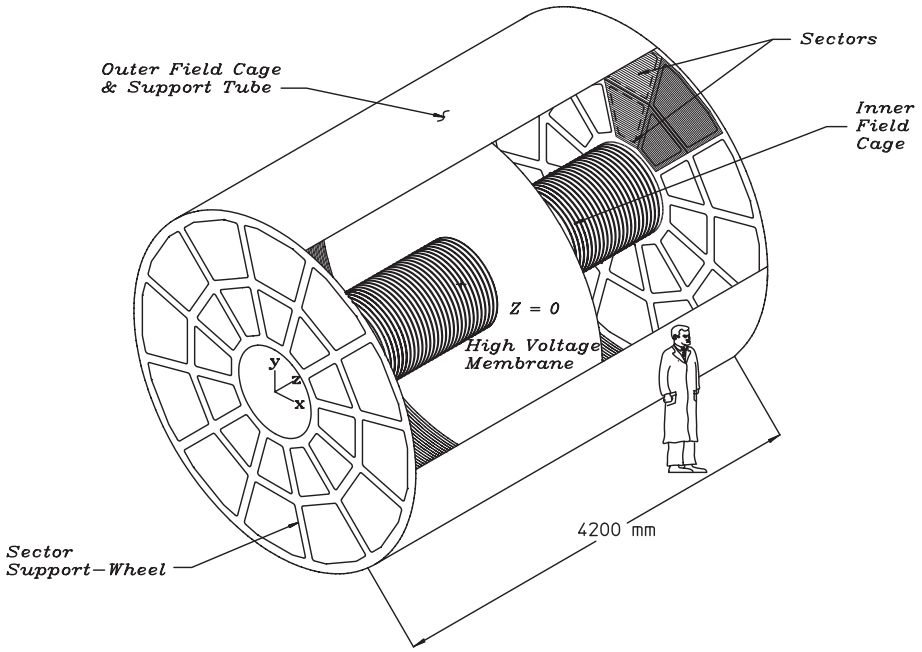

Figure 2.3: The schematics of the STAR TPC.

The TPC Outter Field Cage (OFC) covers two units of psuedo-rapidity in the center-of-mass frame and the full azimuth and it is immersed in a 0.5 Tesla uniform magnetic field along the beam axis. The curvature of the tracks in the magnetic field is used to measure tracks momenta ranging from 150 MeV/c to 30 GeV/c. In addition to tracking and momenta measurements the TPC is used to identify particle species using their ionization energy loss dE/dx allowing to separate pions and protons up to momentum p $\sim$ 1.1 GeV/c, and kaons and pions up to p $\sim$ 0.6 GeV/c [72–74].

Fig. 2.4 shows the TPC energy loss dE/dx information versus momentum achieved from Run14 Au+Au 200GeV, there are several clear bands for different particle species such as π, K, p and e.

2.4 Time of Flight detector

The Time-of-Flight detector is made of 120 trays utilizing Multi-gap Resistive Plate Chambers (MRPCs) technology [75–77], with 60 on east side and 60 on west side. Each tray consists of 32 single-end readout MRPC modules, whose structure is shown in Fig. 2.5. Each tray covers a pseudo rapidity interval of 0.9 and 1/60th of the azimuth and each tray has 32 MRPC's arranged nearly projectively for collisions at the center of STAR.

TOF has a total timing resolution of 100 ps. The time of flight information together

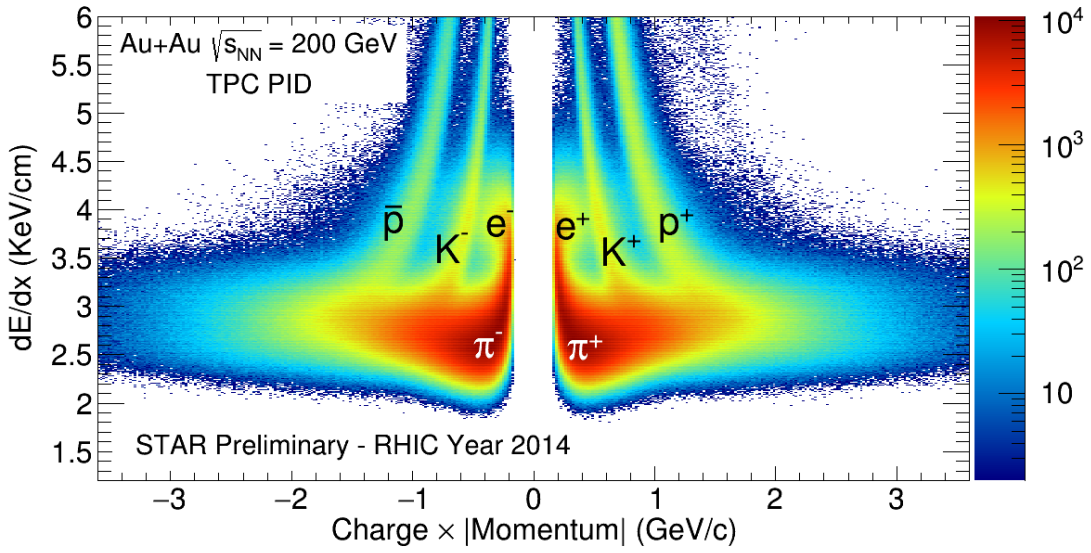

Figure 2.4: TPC dE/dx versus charge×momentum achieved from Run14 Au+Au 200GeV.

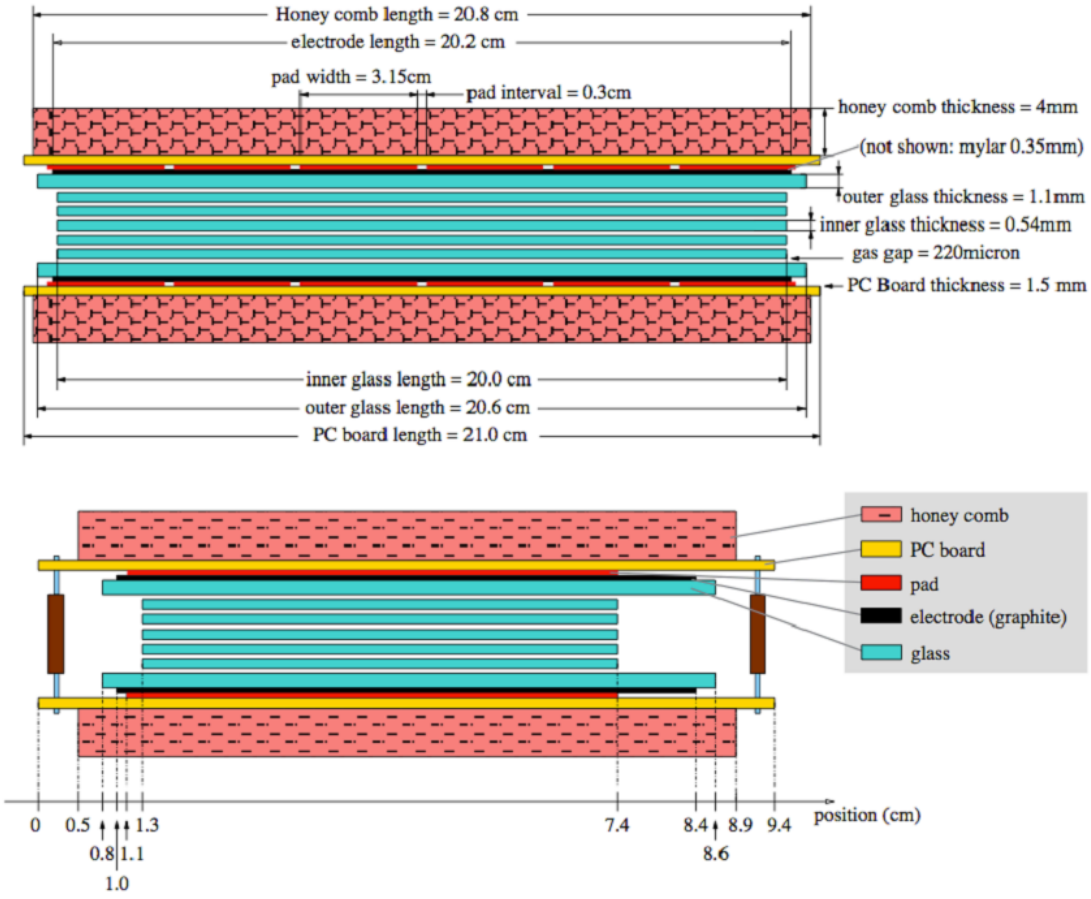

Figure 2.5: Two side views of MRPC. The upper is for long side view and the lower is for short side view.

with the particles momentum from TPC tracking significantly improves STAR particle identification capabilities (PID) allowing π:K:p direct PID up to p $\sim$ 1.7 - 1.9GeV/c and (π+K):p up to p $\sim$ 2.9 - 3.1GeV/c.

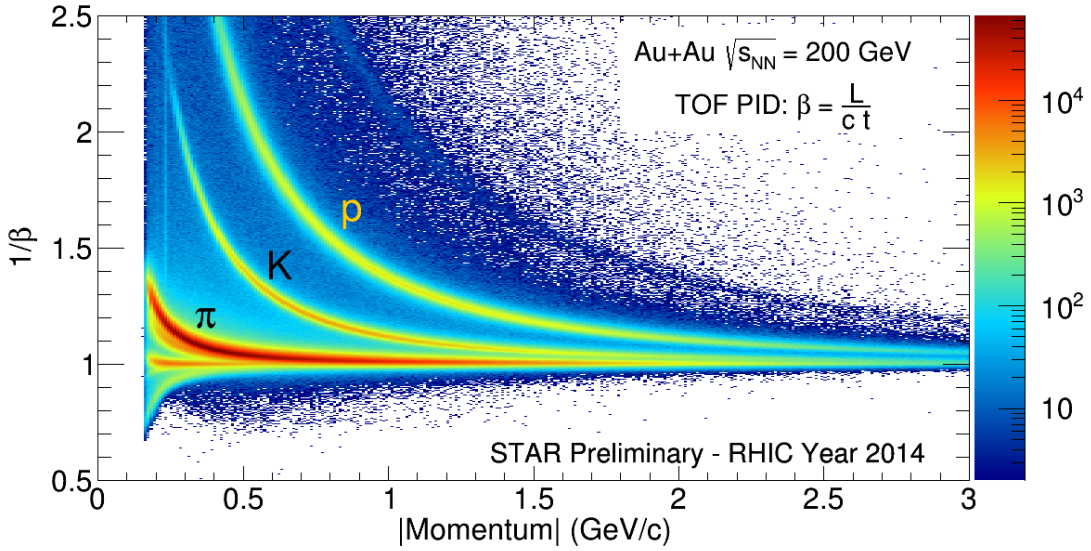

Figure 2.6: TOF 1/Beta versus momentum achieved from Run14 Au+Au 200GeV.

Fig. 2.6 shows the TOF 1/β information versus momentum achieved from Run14 Au+Au 200GeV, clearly see there are several bands represent for different particle species such as π, K, p.

2.5 Heavy Flavor Tracker

The Heavy Flavor Tracker (HFT) is a state-of-the-art micro-vertex detector utilizing active pixel sensors and silicon strip technology [78–80]. The HFT will significantly extend the physics reach of the STAR experiment for precision measurements of the yields and spectra of particles containing heavy quarks. This will be accomplished through topological identification of mesons and baryons containing charm quarks, such as D^0 and Λ_c, by the reconstruction of their displaced decay vertices with a precision of approximately 30 μm. For instance, the channel D^0(cu) $\rightarrow$ Kπ has decay length $c\tau$ $\sim$120 μm and tracking with HFT must be able to distinguish between particles coming from the collision's primary vertex and those coming from these displaced vertices.

The HFT, shown in Fig. 2.7 and 2.8, consists of 4 layers of silicon detectors grouped into two sub-systems with different technologies, guaranteeing increasing resolution when tracking from the TPC and the Silicon Strip Detector (SSD) towards the vertex of the collision. The Intermediate Silicon Tracker (IST), consisting of two layers of single-sided strips, is located inside the SSD. Two layers of Silicon Pixel Detector

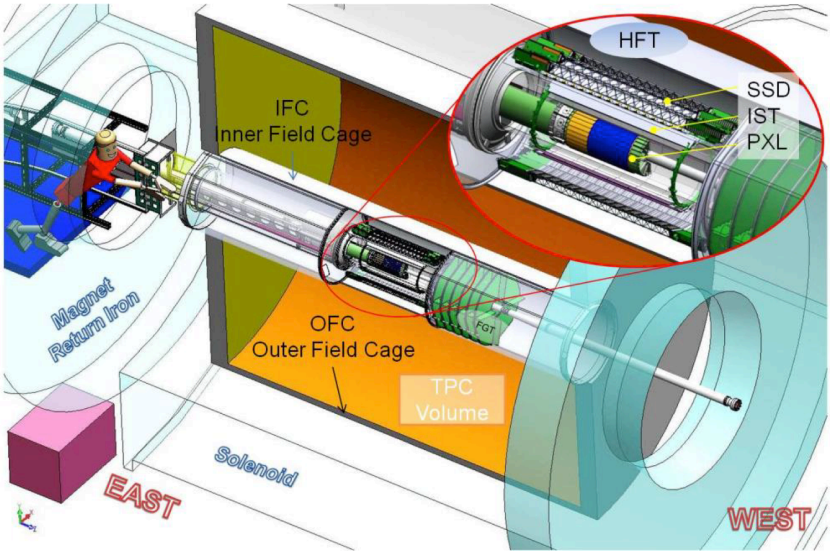

Figure 2.7: 3D model of HFT detector as it sits inside the STAR TPC.

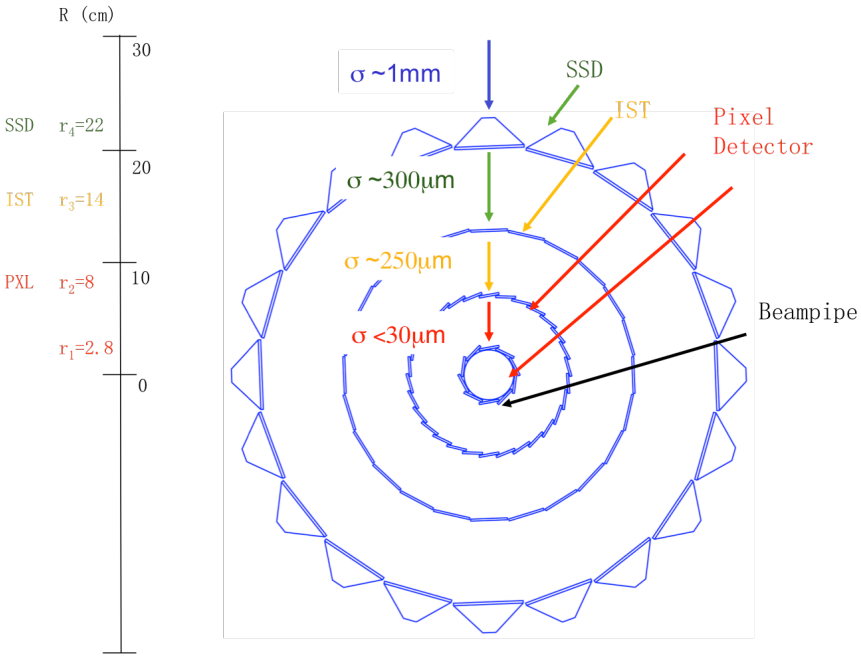

Figure 2.8: Schematic of the HFT cross section.

(PIXEL) are inside the IST. The PIXEL detectors have the resolution necessary for a precision measurement of the displaced vertex [81, 82].

- The SSD is a high-resolution, double-sided silicon strip detector that is mounted at a radius of 22 cm with a length of $\sim$106 cm. Its radial location puts it midway between the event vertex and the first active row of the TPC. Thus, it is ideally suited for the purpose of improving the TPC's pointing and momentum resolution. The SSD was designed to work with the TPC and the STAR Silicon Vertex Tracker (SVT). The existing silicon strips were refurbished with faster readout electronics and repurposed as the outermost layer of the HFT.

  The SSD has full azimuthal coverage in $|\eta| < 1.2$ and has a thickness of roughly 1% radiation length, the pitch size is roughly 95 μm.

- The IST consists of a barrel of approximately $0.4m^2$ of silicon pad sensors at a radius of 14 cm with a length of $\sim$ 50 cm. They use single sided double-metal silicon pad with 600 μm $\times$ 6 mm pitch.

  The IST also has full coverage in the azimuth in $|\eta| < 1.2$ and an overall thickness of roughly 1.5% radiation length

- The PXL detector is a low mass detector that located very close to the beam pipe. It consists of two layers of silicon pixel detectors, one layer at 2.8 cm average radius and the other at 8.0 cm average radius. The PXL length is roughly 20 cm. The PXL has a total of 40 ladders, 10 in the inner layer and 30 in the outer layer. Each ladder contains a row of 10 monolithic CMOS detector chips and each ladder has an active area of $\sim$19.2 cm $\times$ $\sim$1.92 cm. The CMOS chips contain a $\sim$1000 $\times$ $\sim$1000 array of 20.7 μm square pixels and will be thinned down to a thickness of 50 μm to minimize multiple coulomb scattering (MCS) in the detector.

  The PXL has full azimuth coverage in $|\eta| < 1$, and the effective thickness of each ladder is 0.37% of a radiation length.

2.5.1 HFT performance and status

For the HFT, there is a so call the Distance of Closest Approach (DCA) resolution to determine the performance. Fig. 2.9, shows the DCA resolution in the transverse plane achieved in 2014 data for pions, kaons and protons, which exceeds the design goal of 55 μm resolution for kaons at p_T = 750 MeV/c. Fig. 2.10, shows the same plots of the DCA resolution in the beam direction achieved in 2014 [53, 86].

In the year of 2014, there are 80% channels operational for SSD, there is one ladder off. And nearly $\sim$95% channels operational stably for IST. Fig. 2.11 shows the inner

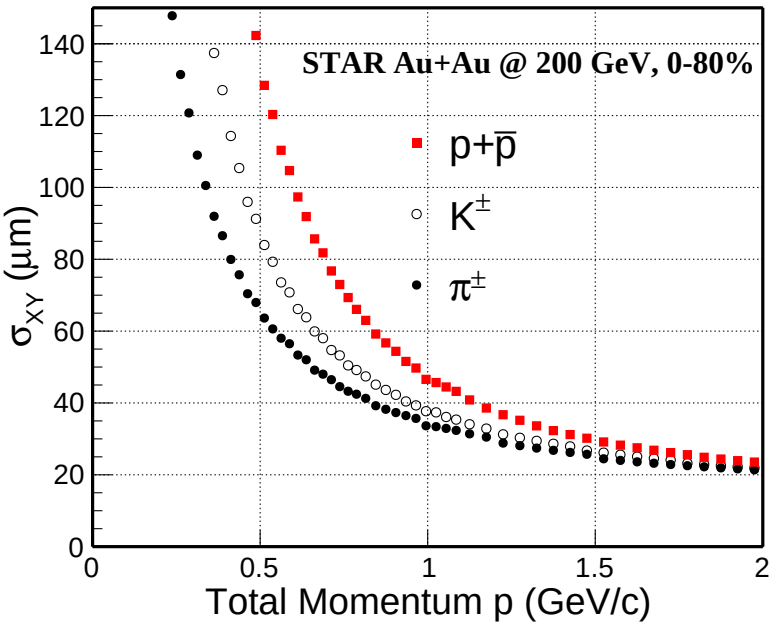

Figure 2.9: DCA_{XY} resolution with the STAR HFT achieved in 2014 for pions.

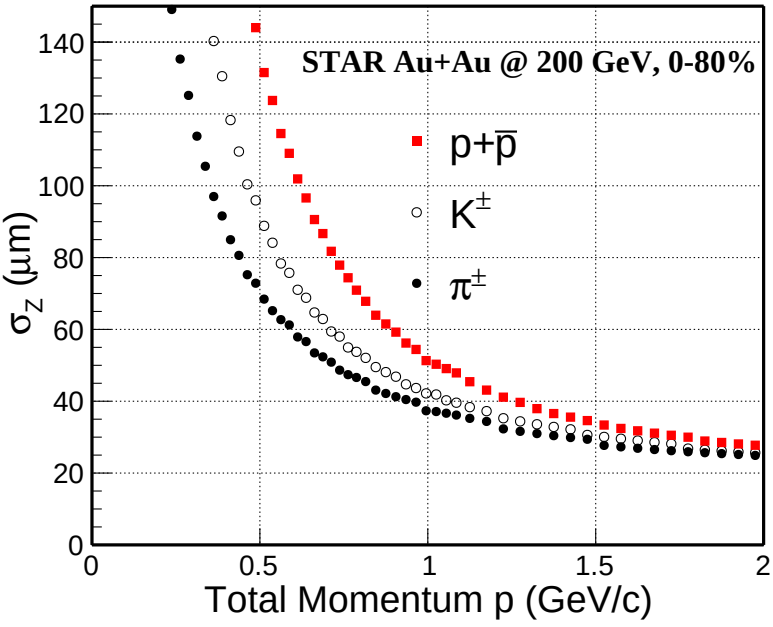

Figure 2.10: DCA_Z resolution with the STAR HFT achieved in 2014 for pions.

PXL status in 2014, and Fig. 2.12 shows the outer PXL status in 2014. In average, there are 82% active sensors for inner PXL and 95% active outer sensors for outer PXL [83].

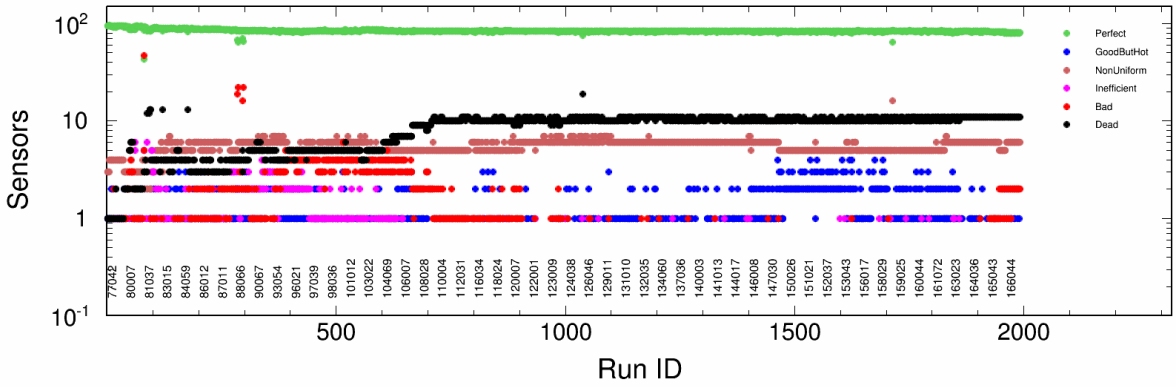

Figure 2.11: PXL inner sensor status vs. all runs in 2014.

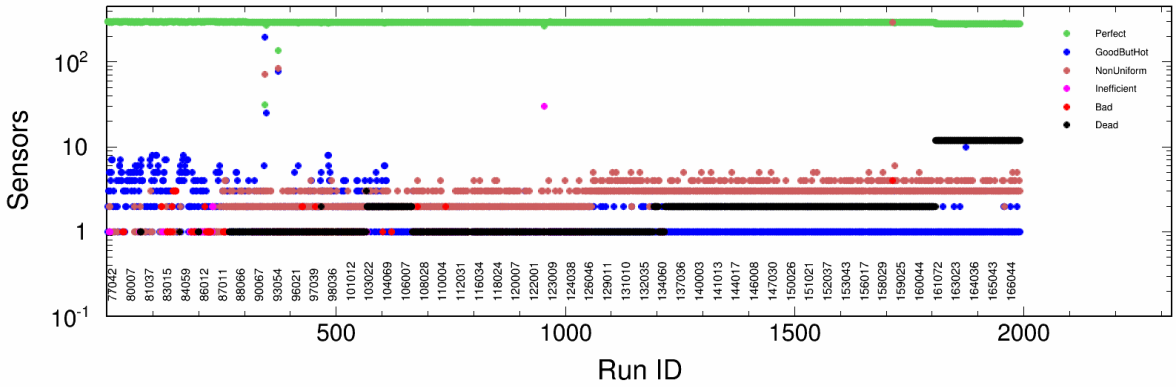

Figure 2.12: PXL outer sensor status vs. all runs in 2014.

2.5.2 HFT related physics

As discussed before, the HFT will significantly extend the physics reach of the STAR experiment for precision measurements of the yields and spectra of particles containing heavy quarks. In particular there are several topics would be interesting:

- **Total charm yield**

  by measuring the D^0, $D^{\pm}$ spectra to determine the total charm yield, provide a base line for charmonium suppression and coalescence

- **R_{cp}, R_{AA} of charm and bottom**

  crucial for the understanding of the energy loss in QGP

- Charm (D^0) flow

  good approach for the understanding of charm thermalization or not

- c$\bar{c}$ angular correlation

  interaction with the medium

- Λ_c /**D^0 ratio**

  test coalescence model

This analysis work will mainly force on the items 1, 2 and 5 in the next sections.

Chapter 3 D^0 Analysis Details

3.1 Data Set

The data set used in this analysis is from Au+Au collisions at $\sqrt{s_{NN}}$ = 200 GeV from RHIC run year 2014 (Run14). This is the first year of physics running the new STAR Heavy Flavor Tracker (HFT) Detector. The data set is processed with SL16d library. The analysis uses picoDst which is produced from MuDst. Details of picoDst can be found at [87]

3.2 Trigger and Event Selection

The Minimum-Bias (MinBias) trigger is defined as a coincidence between the two VPDs, and an online collision vertex cut. Moreover, a pile-up protection at the trigger level was applied for the data taking. In this analysis, the MinBias trigger, denoted as "vpdmb-5-p-nobsmd" and "vpdmb-5-p-nobsmd-hlt", is used. The triggers used in this analysis are listed in Table 3.1.

Table 3.1: Triggers ID used in this analysis from run14

Trigger ID	description
450050	vpdmb-5-p-nobsmd-hlt
450060	vpdmb-5-p-nobsmd-hlt
450005	vpdmb-5-p-nobsmd
450015	vpdmb-5-p-nobsmd
450025	vpdmb-5-p-nobsmd

Events used in this analysis are required to have a valid collision vertex V_z (primary vertex) within 6 cm of the TPC center along z direction (the beam direction) to ensure a uniform TPC acceptance and make sure the most tracks are within the PiXeL (PXL) detector coverage. The PXL detector is about 20 cm along the z direction, and the radius of the inner layer is about 2.8cm and outer layer is about 8 cm. Furthermore, the distance between the V_z constructed by TPC and the vertex constructed by VPD (V_z^{VPD}, fast detector) is within 3 cm to reject the bad events. A radial length less than 2 cm for the vertex is required to reject the events from the beam hitting the beam pipe. After event selection, $\sim$875 million MinBias events are used for this analysis. Table 3.2 lists the event selection criterion.

Table 3.2: Event selection in Au+Au collisions at 200 GeV for D^0.

Event Selection Criteria
$!(\|V_x\| == 0 \;\&\&\; \|V_y\| == 0 \;\&\&\; \|V_z\| == 0)$
$\|V_z\| < 6$ cm
$\|V_r\| < 2$ cm
$\|V_z - V_z^{VPD}\| < 3$ cm

3.3 Centrality Definition

The centrality for Run14 200GeV Au+Au collisions MinBias sample is based on gRefMult [88]. The gRefMult is defined as the number of global tracks with $|\eta| < 0.5$, no less than 10 TPC hits, and Distance of Closest Approach (DCA) to primary vertex less than 3 cm with some correction according to V_z and luminosity. The centrality definition according to the corrected gRefMult is listed in Table 3.3. This is decided by comparing the measured gRefMult distribution with the Glauber model simulation.

The basic procedure for centrality definition have three steps. First, need the quality assurance (QA) for the data set and remove those outlier runs. The second step would be correct the V_z and luminosity dependence for the reference multiplicity (gRefmult). The last step would be compare our data with Glauber MC simulation and determine the centrality classification.

For the QA, several variables are used for the outlier selection, such as Refmult (primary track multiplicity), gRefmult (global track multiplicity), TofRefmult (tof track multiplicity) and etc. In the Fig. 3.1 shows the $\langle$gRefmult$\rangle$ as a function of run index for the QA, and there are several outliers are identified. Those dashed lines are the 4$\times$RMS range, beyond those range, the runs are identified as bad run. And several iterations are did until all the runs are within these 4$\times$RMS range.

In the Fig. 3.2 shows the $\langle$HFT $p_T\rangle$, which is the mean p_T of HFT tracks, as a function of run index for the QA, and we can clearly see there is a deep before the run index $\sim$520 which corresponding to the run number 15107008. And also we saw the same structure in the Fig. 3.3, which shows the average of HFT matching Ratio in the p_T range between 0.7 to 0.8 GeV/c and Fig. 3.4 shows this HFT matching ratio in the high p_T range. So, basically those runs before day 107 were taken out for this analysis, since it will complicate our efficiency calculation.

This deep was identified later on with a lot of effort, it was due to the firmware

issue. And more details can be found in the STAR documents below [89].

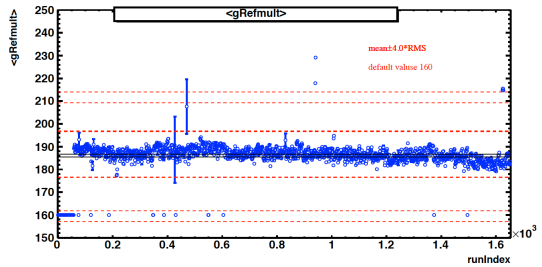

Figure 3.1: The mean value of gRefmult ($\langle$gRefmult$\rangle$) as a function of run index from QA.

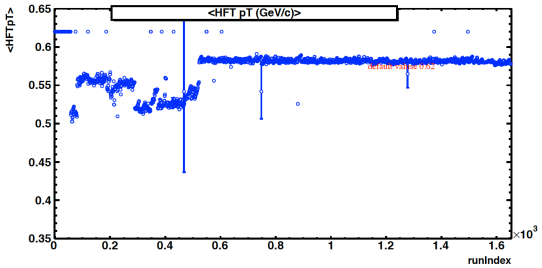

Figure 3.2: The mean value of p_T for HFT matched track ($\langle$HFT $p_T\rangle$) as a function of index.

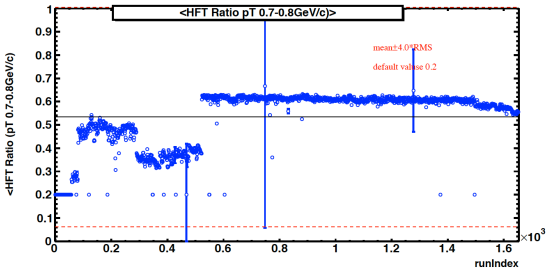

Figure 3.3: The mean value of HFT matching ratio ($\langle$HFT $p_T\rangle$) as a function of run index at the transverse momentum range 0.7 < p_T < 0.8 GeV/c.

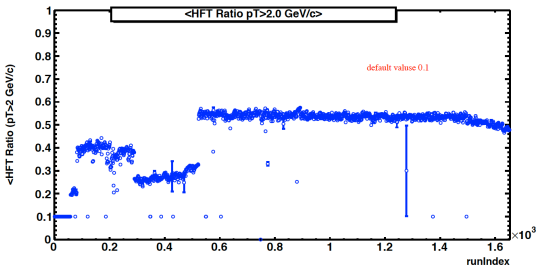

Figure 3.4: The mean value of HFT matching ratio ($\langle$HFT $p_T\rangle$) as a function of run index at the transverse momenaum range p_T > 2.0 GeV/c.

Fig. 3.5 and Fig. 3.6 show the normalized gRefmult distribution for several different V_z range from -6 cm to 6 cm. The shape are quite different for VpdMB5 trigger in Fig. 3.5 while the Fig. 3.6 shows the same plots for VpdMB30 trigger (V_z within range from -30 cm to 30 cm). This difference was explained by that the online Vpd vertex cut have a negative offset and the Vpd resolution has centrality dependence. As for the most central collisions, the resolution will be better than the most peripheral collisions. That is the reason we saw more events in the negative V_z range and more central events for VpdMB5 trigger compared to VpdMB30 trigger.

As the gRefmult have the luminosity dependence (related to the TPC tracking efficiency have luminosity dependence), we need to take out this effect by doing ZdcX (Zdc coincidence rate) correction. Fig. 3.7 shows the mean value of gRefmult (<gRefmult>) distribution as a function of ZdcX. There was a clear slope for this distribution as shown by the fitting parameters. Here the fitting function is Eq. 3.1,

$$f_{ZdcX} = p0 + p1 * ZdcX \tag{3.1}$$

The goal of this correction is try to flatten this ZdcX dependence to take out of the luminosity effect. So here the correction factor was shown by Eq. 3.2.

$$f_{ZdcX} = \frac{1}{1 + p1/p0 * ZdcX} \tag{3.2}$$

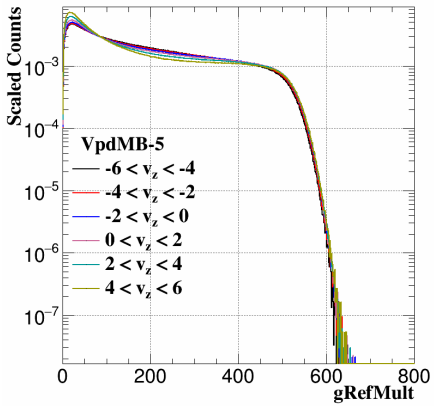

Figure 3.5: Normalized gRefmult distribution for VpdMB5 trigger along different V_z range

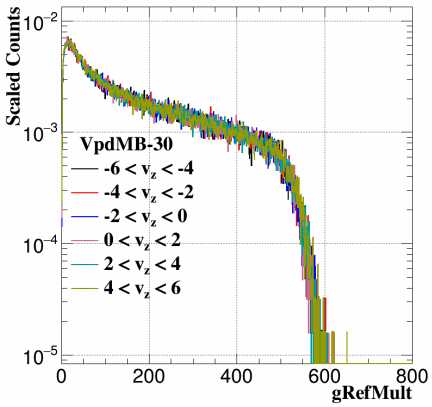

Figure 3.6: Normalized gRefmult distribution for VpdMB30 trigger along different V_z range

After the ZdcX correction, this <gRefmult> is flat as shown by Fig. 3.8.

For the V_z dependence correction, we extract the high end point (h) from the fitting of gRefmult tail by the function of Eq. 3.3.

$$f_x = A * TMath :: Erf(-\sigma * (x - h)) + A \tag{3.3}$$

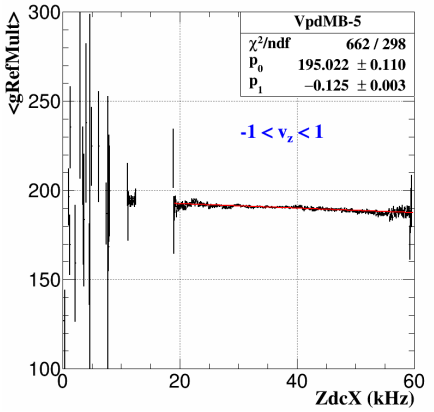

Figure 3.7: <gRefmult> as function of ZdcX before correction.

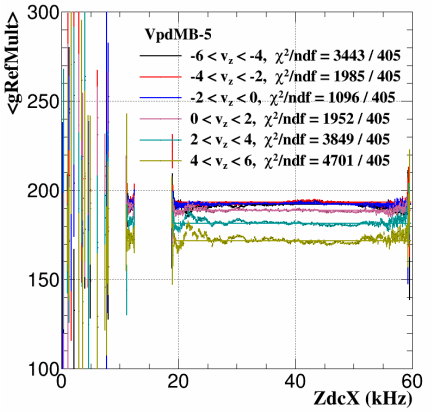

Figure 3.8: <gRefmult> as function of ZdcX after correction.

Fig. 3.9 shows an example of the fitting of gRefmult tail in the V_z range from 1 cm to 2 cm. The fitting parameters were shown on the plot.

With all the high end point value extracted along V_z direction, this V_z dependence was shown on Fig. 3.10. The similar method as ZdcX correction, we need to flatten this V_z dependence, then the data point was fitted by 5th order polynomial function Eq. 3.4, and then the correction factor was shown by Eq. 3.5 After the V_z correction, this high end point is flat as shown by Fig. 3.11.

$$f_{V_z} = p0 + p1 * x + p2 * x^2 + p3 * x^3 + p4 * x^4 + p5 * x^5 \tag{3.4}$$

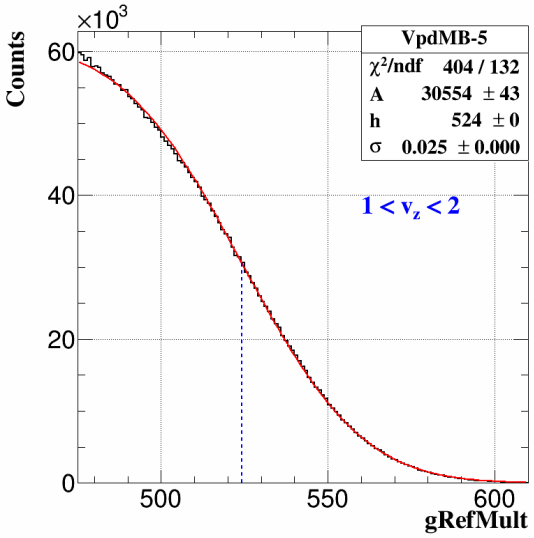

Figure 3.9: Fitting gRefmult tail distribution in the range of 1<V_z<2 cm by Eq. 3.3.

$$f_{V_z} = \frac{p0}{p0 + p1 * x + p2 * x^2 + p3 * x^3 + p4 * x^4 + p5 * x^5} \tag{3.5}$$

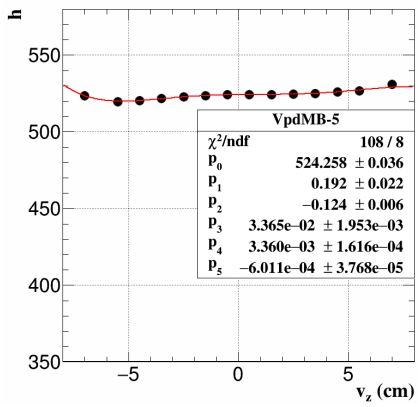

Figure 3.10: High end point as function of V_z after correction.

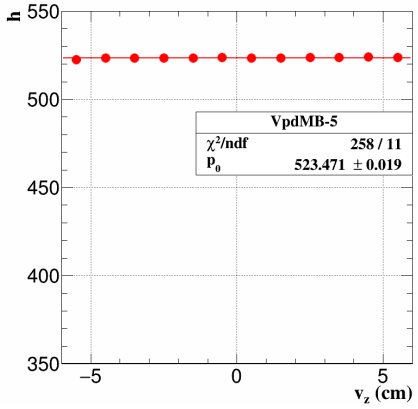

Figure 3.11: High end point as function of V_z after correction.

As shown from Fig. 3.5 and Fig. 3.6, the clear V_z dependence need to avoid for VpdMB5 trigger. So, the centrality definition for VpdMB5 trigger was normalized to VpdMB30. After the ZdcX correction and V_z correction, we directly take it as an additional correction factor for VpdMB5. These correction factor was show in Fig. 3.12. After this additional correction, the distributions from VpdMB5 and VpdMB30 are same.

The Vpd MinBias trigger has a trigger efficiency that are lower for periheral events. Fig. 3.13 shows the gRefmult after V_z and ZdcX correction from data comparison with Glauber MC simulation. In the high end part the agreement was well, but in the low end part, due to this trigger ineffciency, there is clearly discrepancy between data and simulation. To do the measurement without centrality bias, a weight proportional to

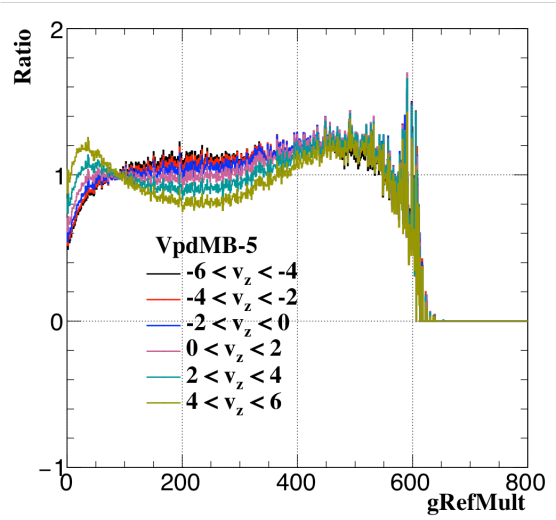

Figure 3.12: The double ratio of normalized gRefmult distribution from VpdMB5 over VpdMB30, this additional correction factor was try to normalized VpdMB5 to VpdMB30 trigger.

inverse trigger efficiency is applied. The weight as a function of corrected gRefMult is shown in Fig. 3.14.

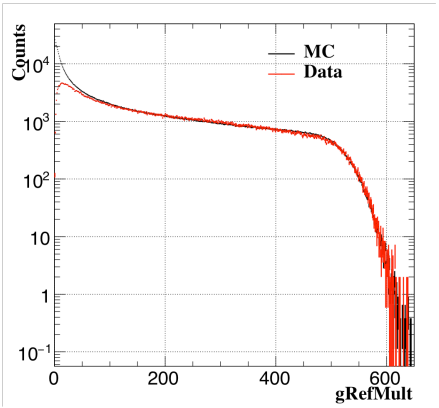

Figure 3.13: The comparison of corrected gRefMult between Data and Glauber MC. The red line is data and the black line is from Glauber MC.

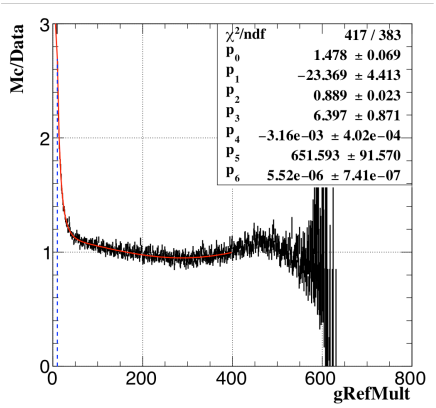

Figure 3.14: MC/data gRefmult distribution for Vpd MinBias trigger efficiency correction. The red line fit function is the correction reweight function.

After all these corrections including V_z, ZdcX, Vpd trigger inefficiency, and Vpd resolution for different centralities as discussed before. Final step, the data was compared to Glauber MC simulation as shown in Fig. 3.15. And then the determined centrality classification can be found at Table 3.3.

3.4 D^0 Reconstruction

D^0 and $\bar{D^0}$ are reconstructed through the typically hadronic channel $K^{\mp}\pi^{\pm}$ using the topological method [8]. In the following we will describe the daughter selection, the geometry cuts and how they are obtained through the TMVA tuning [90]. We will

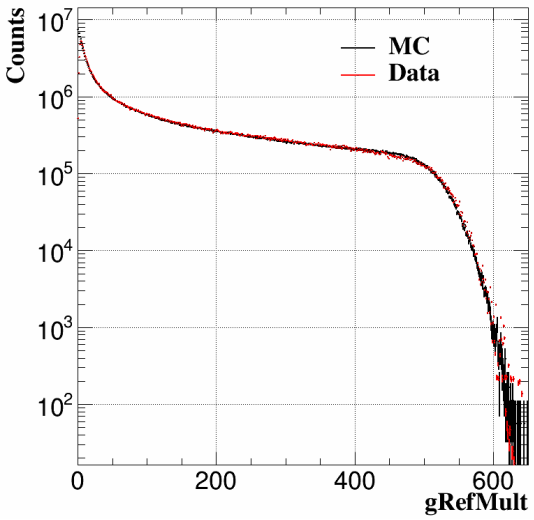

Figure 3.15: The comparison of corrected gRefMult (after all corrections and reweight) between Data and Glauber MC. The red line is data and the black line is from Glauber MC.

centrality	gRefMult	$\langle N_{coll} \rangle$	$\langle N_{part} \rangle$
75-80%	10-15	10.48	11.82
70-75%	15-21	16.11	16.68
65-70%	21-30	24.59	23.25
60-65%	30-41	36.13	31.15
55-60%	41-56	52.77	41.27
50-55%	56-73	75.36	53.46
45-50%	73-94	105.25	67.93
40-45%	94-119	143.54	84.71
35-40%	119-148	191.83	103.99
30-35%	148-182	253.13	126.52
25-30%	182-221	328.99	152.31
20-25%	221-266	422.49	181.93
15-20%	266-317	537.52	215.98
10-15%	317-376	677.99	254.90
5-10 %	376-443	852.75	299.95
0-5 %	>443	1066.50	348.74

Table 3.3: Centrality defintion based on gRefMult

show the D^0 signals for different p_T bins. We will also discuss some related topics: the primary vertex reconstructed by the Kalman Filter algorithm compare with the STAR default one Minuit Vertex algorithm, the mixed event to reconstruct the combinatorial background, and the correlated background source shown as a 'bump' at invariant mass lower than the D^0.

3.4.1 Daughter Selection

D^0 have a lifetime of $c\tau \sim 123\mu$m. Thus the global tracks for daughter tracks are used in this analysis. The transverse momentum are required to $\geq$ 0.3 GeV/c to ensure that the track can pass through the TPC and have less HFT miss matching, the number of hit points (nHits) along the track is $\geq$ 20 (of a maximum of 45) to ensure good momentum resolution.

The pion and kaon tracks are identified by combining Time Projection Chamber (TPC) and Time Of Flight detector (TOF). The TPC provides particle identification utilizing the energy loss information dE/dx, different particle species with the same momentum may have different dE/dx. In additional, different particle species with the same momentum have different velocities, thus the TOF can be used to identify different particle species in the dE/dx crossover regions by precise velocity information ($1/\beta = ct/l$). The normalized dE/dx, $n\sigma_x$ (x = π, K, p, e etc.), defined in Eq. 3.6, instead of dE/dx is used in this analysis. Where $\langle dE/dx\rangle_{measured}$ and $\langle dE/dx\rangle_x$ represent measured and theoretical dE/dx, and R is the STAR TPC dE/dx resolution (typically ~8%). The $n\sigma_x$ should be close to a standard Gaussian distribution for each corresponding particle species (mean = 0, σ = 1).

$$n\sigma_x = \frac{1}{R} log \frac{\langle dE/dx\rangle_{measured}}{\langle dE/dx\rangle_x} \tag{3.6}$$

In summary, next list all the related track selections for D^0 daughters including track quality cut and particle identification cut.

- global tracks
- p_T > 0.3 GeV/c
- $|\eta| < 1$
- $nHitsFit \geq 20$, in TPC
- at least one hit in every layer of PXL and IST

pion PID:

- $|n\sigma_\pi| < 3.0$, based on TPC dE/dx
- If TOF is avaliable (hybrid PID): $|\frac{1}{\beta} - \frac{1}{\beta_{exp}}| < 0.03$

kaon PID:

- $|n\sigma_K| < 2.0$, based on TPC dE/dx
- If TOF is avaliable (hybrid PID): $|\frac{1}{\beta} - \frac{1}{\beta_{exp}}| < 0.03$

3.4.2 Topological Cut Optimization

The secondary vertex is reconstructed with selected kaon and pion global tracks. In this analysis, the middle point on the Distance of the Closest Approach (DCA) between two daughter tracks is considered as the secondary decay vertex of the candidate D^0. As shown in Fig. 3.16, 5 geometrical variables are chosen to select D^0 and reject combinatorial background, which is dominated by a pair of tracks directly from the primary vertex: decay length (the distance between the decay vertex and Primary Vertex PV), DCA between the 2 daughters, DCA between the reconstructed D^0 flying path and PV, DCA between the π track and PV, and DCA between the K track and PV. The cuts on these variables are optimized by the Toolkit for Multivariate Data Analysis (TMVA) package. They change according to the D^0 candidate p_T in order to have the best significance in all the covered p_T range. Additionally there is a $cos(\theta) > 0$ cut to make sure the decay vertex with respect to the primary vertex is roughly in the same direction as the momentum.

The TMVA need signal and background sample input for training. The signal sample is obtained from a toy fast-simulation and the background sample is from real data like sign pairs in D^0 mass window and unlike sign pairs in side bands range.

The daughters' acceptance and reconstruction efficiency is considered, together with the momentum smearing as shown in Eq. 3.7

$$\sigma = p_T(0.6 + 0.38p_T)/100 \tag{3.7}$$

For geometry cuts simulation, the p_T resolution is not very important. It only makes the D^0 peak width more realistic.

The position smearing need to be precise to reproduce the behavior of the real data, so that the effects of geometry cuts are reproduced realistically. In the toy simulation the position resolution has 2 parts: a) due to hit error, including pixel size, vibration, and alignment, which is a constant contribution; and b) due to multiple Coulomb scattering, whose angular dispersion is described by Eq. 3.8

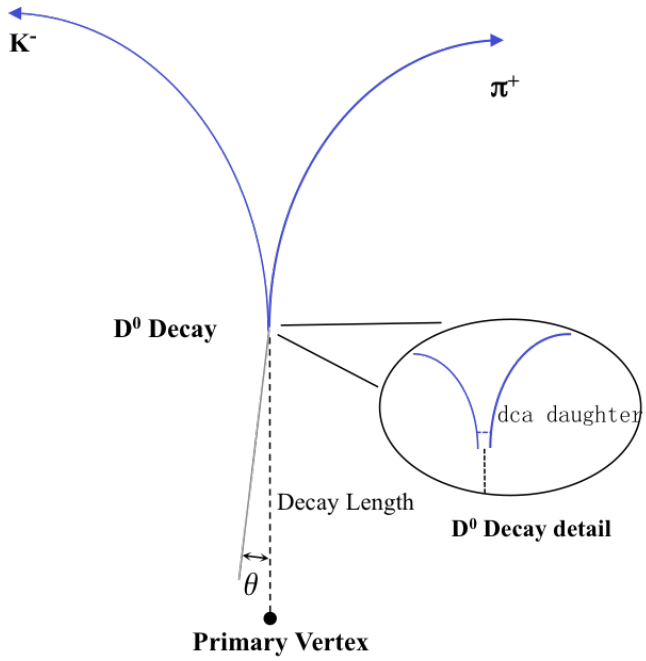

Figure 3.16: The topology of a D^0 decaying to a kaon and a pion.

$$\theta_0 = 13.6MeV/(\beta cp)z\sqrt{x/X_0}(1 + 0.038ln(x/X_0)) \tag{3.8}$$

where z is the charge of the particle (=1 for most particles produced in STAR), x is the thickness of the material and X_0 is the radiation length to the material. The parameters for position smearing in the toy fast-simulation (constant for hit error effect = 15.2 μm and x/X_0 = 0.00486) are calibrated using DCA position resolution vs. p from real data, as shown in Fig. 3.17. For data the PID is done with TPC dE/dx and TOF. The agreement is very good after calibration for $p > 0.6$ GeV/c used for this analysis. The discrepancy at very low p could be a bin width effect, and / or mis-identification of π and K.

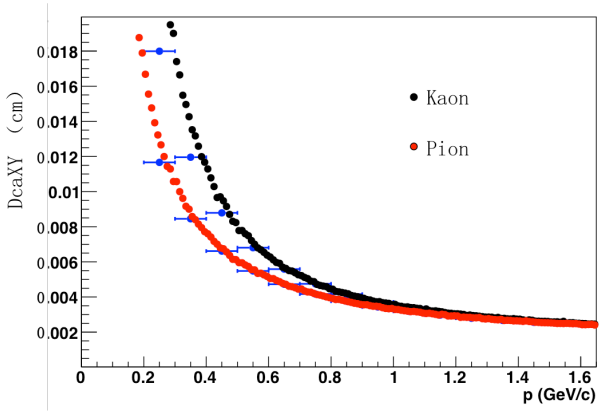

Figure 3.17: comparison of simulated position resolution (DCA XY) vs. p for kaon (black), pion (red) and data measurements (blue).

The D^0 daughter efficiency includes TPC efficiency which is from embedding in p+p collisions from previous measurement [91].

The toy simulation use flat p_T input from 0 to 10 GeV/c. When used for TMVA training, the input shape after detector acceptance and efficiency are weighted by a function fit to the measured D^0 p_T spectrum, and the yield is scaled to what is expected for the whole data set of 1.3 B events.

The background from real data naturally has the real p_T distribution. However, in order to have enough statistics from low to high p_T, while keep the tree file size and the CPU time for training acceptable, the low p_T part is randomly sampled to form a flat distribution below 3 GeV/c. When used for TMVA training, the sample is weighted back to original distribution. Only part of the Run 14 data is sampled for background in TMVA training, so the background yield is scaled to the whole data set of 1.3 B events.

Fig. 3.18 shows distributions of the 5 geometry variables for signal (blue) and background (red) plotted by the TMVA, for p_T between 2 and 3 GeV/c.

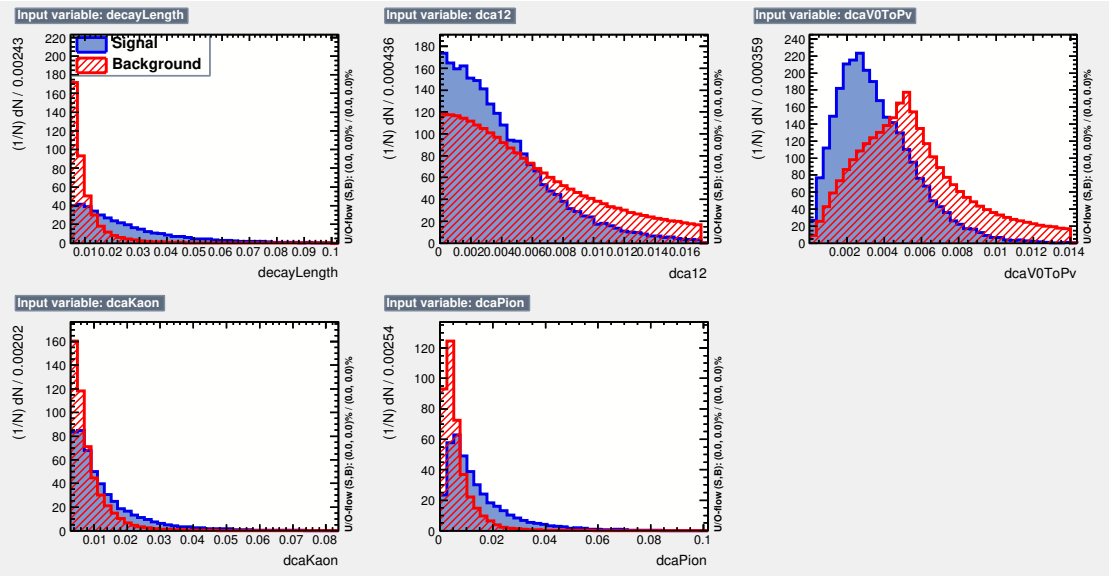

Figure 3.18: Distributions of the 5 geometry variables for signal (blue) and background (red).

The 'cuts' option of TMVA is used to tune D^0 cuts. This option randomly sample different cut sets in the variable space, calculate signal and background efficiency for each cut set. Then one cut set with lowest background efficiency at certain signal efficiency. We can then pick the cut set with the best significance according to the signal and background yield corresponding to the whole data set of 1.3 B events. Fig. 3.19 shows the lowest background efficiency, significance and so on vs. signal efficiency for p_T between 2 and 3 GeV/c. We can see that as cuts get tighter, signal and background efficiency both decrease, but background efficiency decreases much faster. The best significance for 1.3 B events is around signal efficiency of 10%. However, because the

background efficiency is too low, there are a lot of fluctuations for the significance.

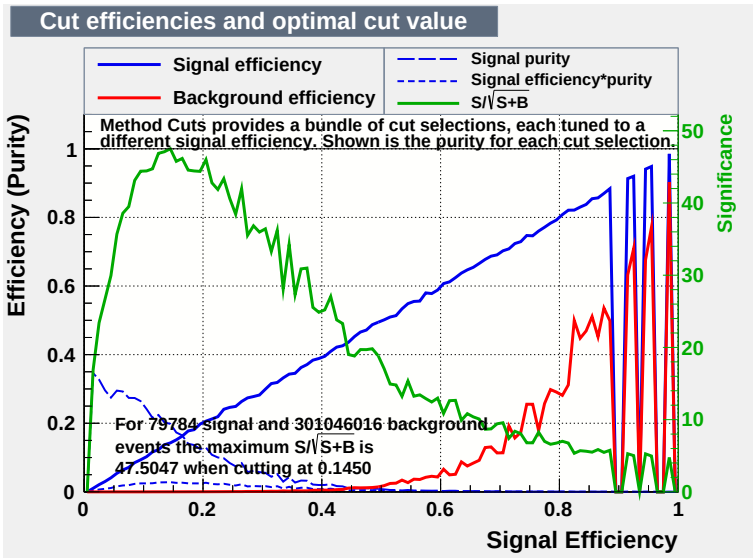

Figure 3.19: Signal efficiency, lowest background efficiency, significance and so on vs. signal efficiency.

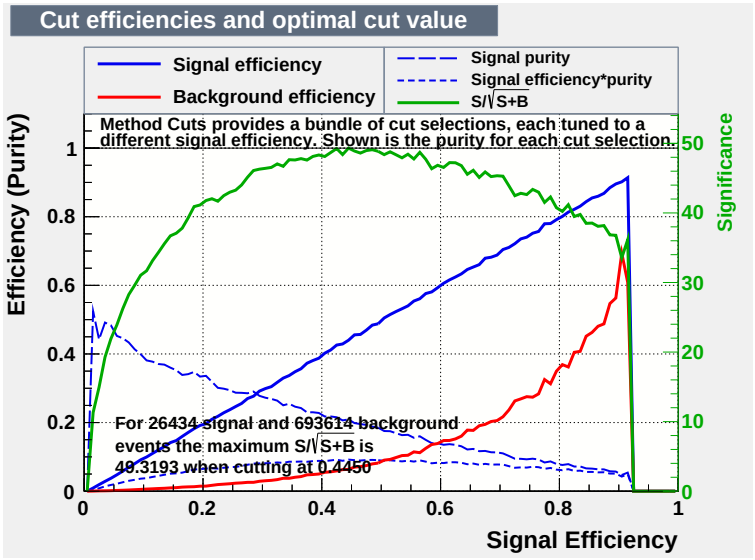

Figure 3.20: Signal efficiency, lowest background efficiency, significance and so on vs. signal efficiency.

We can solve the problem by having loose cuts on the 5 variables before putting into TMVA training. So a majority of background is rejected by the loose cuts, and the left sample is more sensitive. In this way with the same sample size the cut tuning is more precise. The loose cuts can be obtained also with TMVA training, requiring higher signal efficiency than the best significance, for example, 60% signal efficiency in Fig. 3.19, so that all 5 variable cuts are looser than the potential best cuts. And this procedure can be repeated to tighten the cuts step by step, until the statistics around

the best significance region is good. Depending on the p_T bin, 3 or 2 steps are needed. Fig. 3.20 shows the same lowest background efficiency, significance and so on vs. signal efficiency plot, in the last step of tuning. The cuts with the best siginificance is the result of the TMVA tuning.

Table 3.4: Standard geometrical cuts for different D^0 p_T.

D^0 p_T (GeV/c)	0-1	1-2	2-3	3-5	5-10
decay length (μm) $>$	145	181	212	247	259
DCA between 2 daughters (μm) $<$	84	66	57	50	60
DCA between D^0 and PV (μm) $<$	61	49	38	38	40
DCA between π and PV (μm) $>$	110	111	86	81	62
DCA between K and PV (μm) $>$	103	91	95	79	58

Table 3.5: Tight geometrical cuts for different D^0 p_T.

D^0 p_T (GeV/c)	0-1	1-2	2-3	3-5	5-10
decay length (μm) $>$	144	204	242	245	300
DCA between 2 daughters (μm) $<$	69	48	44	49	47
DCA between D^0 and PV (μm) $<$	44	36	31	26	32
DCA between π and PV (μm) $>$	120	102	118	109	96
DCA between K and PV (μm) $>$	119	110	109	106	80

Table 3.6: Loose geometrical cuts for different D^0 p_T.

D^0 p_T (GeV/c)	0-1	1-2	2-3	3-5	5-10
decay length (μm) $>$	110	168	187	199	180
DCA between 2 daughters (μm) $<$	77	78	74	68	66
DCA between D^0 and PV (μm) $<$	72	53	47	42	62
DCA between π and PV (μm) $>$	92	78	86	65	47
DCA between K and PV (μm) $>$	105	68	80	66	41

The result of the geometry cuts tuned for best significance are shown in Table 3.4. These are the standard cuts used in the D^0 reconstruction to calculate the spectra central value.

For D^0 estimation, another 2 sets of geometry cuts are tuned with TMVA, with 50% and 150% signal efficiency relative to the standard cuts. They do not give the overall best D^0 significance, but for the certain signal efficiency, they are still the cuts

with the lowest background efficiency and best D^0 significance. As shown in Fig. 3.20, with 50% and 150% signal efficiency relative to the standard cuts, their significance is still about 80% of the standard cuts with the overall best significance. These 2 cuts sets are listed in Table 3.5 and 3.6.

3.4.3 Mixed Event Background

Several procedures are established to statistically describe the uncorrelated background to the foreground when studying particle reconstruction. In particular, all correlations between particles can be broken by mixing tracks from different events with the benefit of improved statistical precision as a single event can be mixed with many others [93, 94].

To construct the mixed event background it is important to combine events with some degree of similarity, such as events are classified according to the position of the primary vertex (PV) along the beam-line, the centrality class and the orientation of the event plane. Ten bins of equal width were used for both the event plane ($\Psi \in [-\pi, \pi]$) and the position of the primary vertex($V_z \in [-6, 6]$), as well as nine centrality classes between 0-80%, for a total of 900 event 'categories'.

Table 3.7 summarizes the important information saved for the event mixing:

Table 3.7: Summary of information saved for the event mixing

StMixerTrack	StMixerEvent
Origin	PV Origin
Momentum	Magnetic Field
Q-Vector	Event Plane
Track information	Array of mixer tracks
	Array of indices to identified pions
	Array of indices to identified kaons

In the current implementation studying $D^0 \to K\pi$ reconstruction, only pions and kaons were identified and the position of their associated tracks in the array of mixer tracks is saved for quick access. To illustrate the advantage lets assume a simple scenario in which two events, both with identical number of kaons N_K and pions N_π, are to be mixed. If we were to simply loop over all tracks in each event in search of pair candidates the total number of loops is:

$$N^2 = N_K^2 + N_\pi^2 + 2N_K N_\pi \tag{3.9}$$

On the other hand, assuming that pions and kaons have already been identified, then the number of loops is reduced to:

$$N_K N_\pi + N_\pi N_k = 2N_K N_\pi < N^2 \tag{3.10}$$

For the first order of an estimate on the performance, we can assume an average distribution of produced particles, such that: $N_\pi = 0.8N$ and $N_K = 0.2N$. In this case the difference between both procedures is more that a factor of three $2N_K N_\pi \simeq 0.32N^2$.

Once the buffer has been filled the pions from the first event are combined with kaons from the rest of the events in the buffer, considering both like-sign and unlike-sign combinations. In the first iteration the pions and kaons from the same event are combined to produce the foreground (unlike-sign) as well the same event like-sign background. In order to apply the topological cuts to the background, the second event is moved during the mixing such that the position of the primary vertex in both coincides.

Once the mixing has been completed, the first event is removed from the buffer leaving space for another event to be added at the end. Fig. 3.21 and Fig. 3.22 show the invariant mass distribution for the foreground and two different uncorrelated backgrounds: same event like-sign and mixed event unlike-sign in two p_T bins include 1-2 GeV/c and 4-5 GeV/c. The mixed event backgrounds have been scaled to the foreground using the integration range $m_{K\pi} \in [1.6, 2.1]$ GeV/c^2.

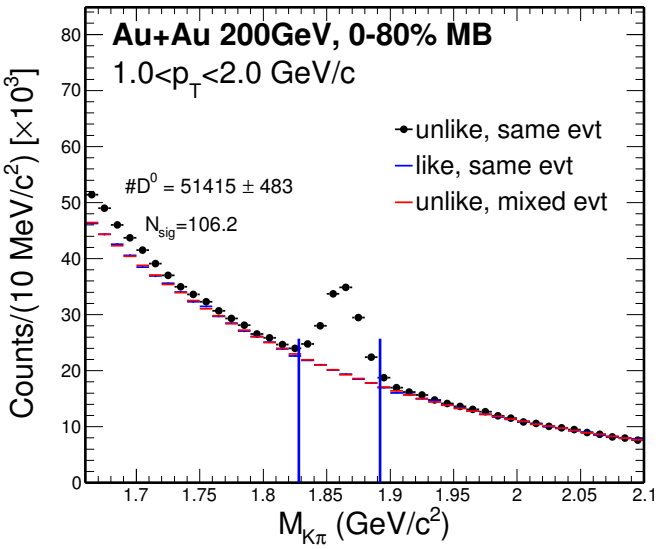

Figure 3.21: Invariant mass distribution for foreground and two descriptions of combinatorial background in $1 < p_T < 2$ GeV/c.

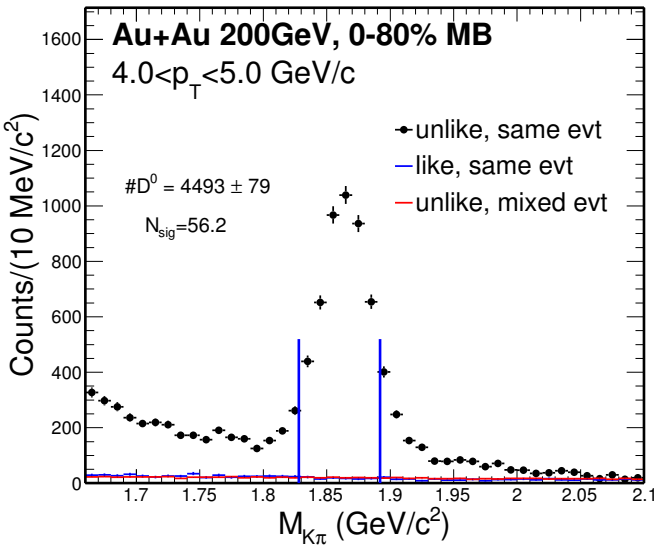

Figure 3.22: Invariant mass distribution for foreground and two descriptions of combinatorial background in $4 < p_T < 5$ GeV/c.

There is good agreement between the two descriptions of the combinatorial background and they appear to provide an adequate description in the vicinity of the D^0 signal and the mixed event backgrounds have improved statistical precision.

It is interesting to observe the presence of an 'excess' in the foreground, relative to all of the background curves, below roughly 1.75 GeV/c^2. This so called bump was investigated using the Data Driven Fast Simulator, and will be covered briefly in the following section.

3.4.4 Correlated background 'bump' for D^0 meson

In order to study the possible contributions to the observed D^0 background, a cocktail of particle decays were generated with realistic p_T distributions (from published D^0 data) and flat η and ϕ distributions, which were then decayed using a simple MonteCarlo simulation and sampling distributions obtained from data and embedding.

Once the particles are decayed, the daughter momentum and the distance of closest approach to the primary vertex are smeared using our Fast-Simulation package according to distributions obtained from data.

Pion-kaon pairs are formed from the decays using the topological cuts as we discussed before to study the contributions that fall within the invariant mass spectrum studied. The finite probability of double mis-PID, where a pion is confused with a kaon and vice a versa, was also included in this study by sampling TPC dE/dx distributions from data.

The contributions to the invariant mass spectrum from the following D^0 and $D^{\pm}$ decays were included in a qualitative study of the correlated background [8]:

- $D^0 \to K^-\pi^+$ (B.R. 0.039)
- $D^0 \to K^-\pi^+\pi^0$ (B.R. 0.011)
- $D^0 \to K^-\rho^+ \to K^-\pi^+\pi^0$ (B.R. 0.108)
- $D^0 \to K^{*-}\pi^+ \to K^-\pi^+\pi^0$ (B.R. 0.007)
- $D^+ \to K^-\pi^+\pi^+$ (B.R. 0.073 $\times$ 0.415)

The charm fragmentation ratio used is the following from ZEUS Collaboration (arXiv:hep-ex/0508019 - Table 4):

- f($c \to D^+$) = 0.217
- f($c \to D^0$) = 0.523
- f($c \to D_s^+$) = 0.095
- f($c \to {}^+_c$) = 0.144
- f($c \to D^{*+}$) = 0.200

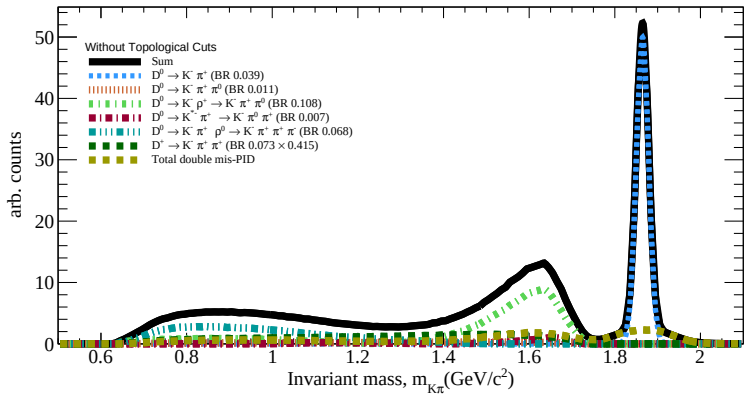

Figure 3.23: Simulated contribution to the invariant mass spectrum from cocktail without topological cut

Fig. 3.23 and Fig. 3.24 show the invariant mass spectrum obtained from the cocktail after scaling by the branching ratio for different decays as well as the fragmentation ratio for the different charmed meson species.

The spectrum is shown before and after the $D^0 \to K\pi$ topological cuts have been applied. It is clear that the contributions from correlated background can, at least in part, account for the enhancement observed below roughly 1.7 GeV/c^2.

The cocktail simulation was then scaled by fitting the amplitude of the D^0 peak obtained from fast simulator to the signal observed in data, and the cocktail was then

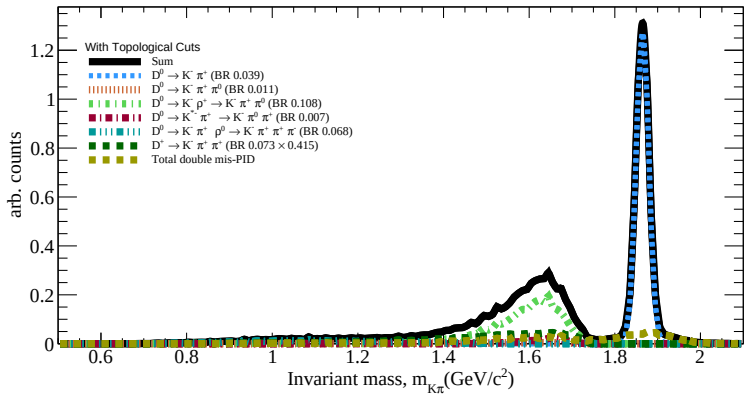

Figure 3.24: Simulated contribution to the invariant mass spectrum from cocktail with topological cut

added to the mixed event background. Fig. 3.25 and Fig. 3.26 shows a comparison between the invariant mass distribution obtained from data and the spectrum obtained by combining the mixed event background and the results from the data-driven Fast-Simulator.

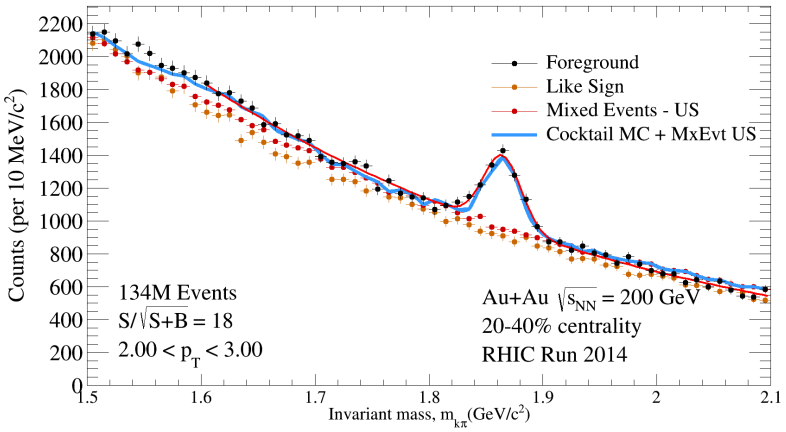

Figure 3.25: Comparison of $K\pi$ invariant mass distribution for unlike-sign (US) foreground, like-sign combinatorial background, unlike-sign (US) mixed events combinatorial background, and unlike-sign (US) mixed events combinatorial background + toy montecarlo cocktail for correlated background, for $2 < p_T < 3$ GeV/c.

The inclusion of correlated background sources can qualitatively describe the foreground observed, reproducing the location of the bump structure albeit underestimating the degree of enhancement itself. Furthermore, there is likely a finite contribution to the observed bump originating from jet correlations which should be included to improve on the description of the background.

It should also be noted that the studies presented here were done with an early version of the fast simulator which only included the p_T and centrality dependence of

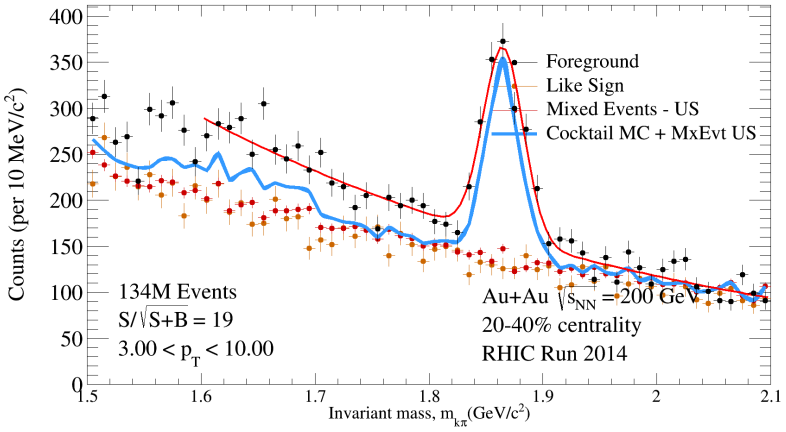

Figure 3.26: Similar Comparison of $K\pi$ invariant mass distribution as Fig. 3.25, for $3 < p_T < 10$ GeV/c.

sampled distributions, revisiting the studies with more differential distributions should improve on these results.

Nonetheless, the results provide confidence in a qualitative understanding on the sources of the correlated background and, what is more, suggest that the contribution from these source in the D^0 signal range is dominated by double mis-PID, and is nearly negligible as shown in the following sub-section.

3.5 D^0 Efficiency and Acceptance Corrections

To obtain the real invariant mass spectrum of D^0 within STAR acceptance ($|\eta_\pi| \leq 1, |\eta_K| \leq 1, |Y_{K\pi}| \leq 1$), the raw spectrum should correct for the efficiency. The $K\pi$ pair efficiency within STAR acceptance is evaluated by folding the TPC related efficiency to the HFT related efficiency as shown on Eq. 3.11. For the TPC related tracking efficiency shows on the first term, we use STAR standard Full GEANT simulation. For the HFT related efficiency include the second and third terms which reflect to HFT acceptance and topological cuts, we developed the 'Data-Driven Fast simulation' which will discuss later [84].

$$\text{Efficiency} \times \text{Acceptance} = \text{TPC Tracking Eff} \otimes \text{HFT Tracking Eff} \otimes \text{Topollogy Cuts} \tag{3.11}$$

This formula can be written in another way when we consider the particles identification (PID) Eq. 3.12. Here the PID part are able to factorized as Eq. 3.13, Eq. 3.14.

$$\frac{\text{HFT}}{\text{MC}} = \frac{\text{TPC}_{\text{withPID}}}{\text{MC}} \otimes \frac{\text{HFT}_{\text{withPID}}}{\text{TPC}_{\text{withPID}}} \otimes \text{PID} \tag{3.12}$$

$$\varepsilon(HFT\&PID_{TPC}\&PID_{TOF}) = \varepsilon(HFT|_{PID_{TPC}\&PID_{TOF}}) \times \varepsilon_{PID}(TPC\&TOF) \tag{3.13}$$

$$\varepsilon_{PID}(TPC\&TOF) = \varepsilon_{PID}(TOF|TPC) \times \varepsilon_{TPC} \tag{3.14}$$

3.5.1 Single Track Efficiency

The single track efficiency losses have two contributions, the detector inefficiency and particle identification cuts. The detector efficiency includes the TPC tracking efficiency (ε_{TPC}) and the TOF matching efficiency (ε_{TOF}). The particle identification cut efficiency (ε_{PID}) includes the efficiencies of TOF velocity ($1/\beta$) and the dE/dx selection cuts. So the single track efficiency can be derived by the Eq. 3.15

$$\varepsilon = \varepsilon_{TPC} \times \varepsilon_{TOF} \times \varepsilon_{PID} \tag{3.15}$$

3.5.2 TPC Tracking efficiency

The TPC tracking efficiency (ε_{TPC}) is evaluated via the standard STAR embedding technique [95]. TPC efficiency including two parts, TPC response and acceptance efficiency. The Monte Carlo (MC) tracks are embedded into the raw data to have a realistic detector occupancy environment. The raw data is randomly sampled over the entire Au+Au minimum-bias data set, while the number of embedded MC tracks is constrained to 5% of the measured multiplicity of the real events to avoid a sizable impact on the realistic TPC tracking efficiency. The MC tracks, with flat p_T, η, and ϕ, are generated and passed through the full GEANT simulation of the STAR detector geometry, and then mixed with the real data . The mixed signals are processed using the same procedures as real data. The quality assurance is made to ensure the MC simulation reproduces the real data before studying the TPC tracking efficiency (Embedding QA). The TPC tracking efficiency is derived by taking the ratio of the number of reconstructed MC tracks (N_{rec}), satisfying the track quality cuts used in the data analysis, over the number of embedded MC tracks (N_{emb}), as shown in Eq. 3.16

$$\varepsilon_{TPC} = \frac{N_{rec}\ (nHitsFit \geq 20\ \&\ dca \leq 1\ \&\ |\eta| \leq 1\ \&\ nCommonHits > 10)}{N_{emb}\ (|\eta| \leq 1)} \tag{3.16}$$

The TPC tracking efficiency in Run14 Au+Au collisions at 200 GeV is shown below. Fig 3.27 shows the TPC tracking efficiency for pion plus from four different classifications, from up to down, the centrality is from the most peripheral to most

central collision. As we see, in the most central top 0-5% collisions, due to the large occupancy the TPC tracking efficiency is much lower than the central one. Fig. 3.28 shows the same plot for kaon minus. The Kaon can be decay inside TPC, that's the reason the TPC tracking efficiency is lower than pion.

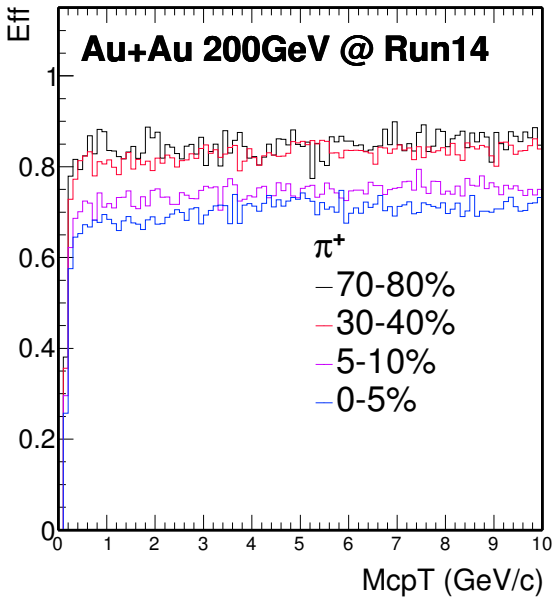

Figure 3.27: TPC tracking efficiency in Run14 Au+Au collisions at 200 GeV for Pion.

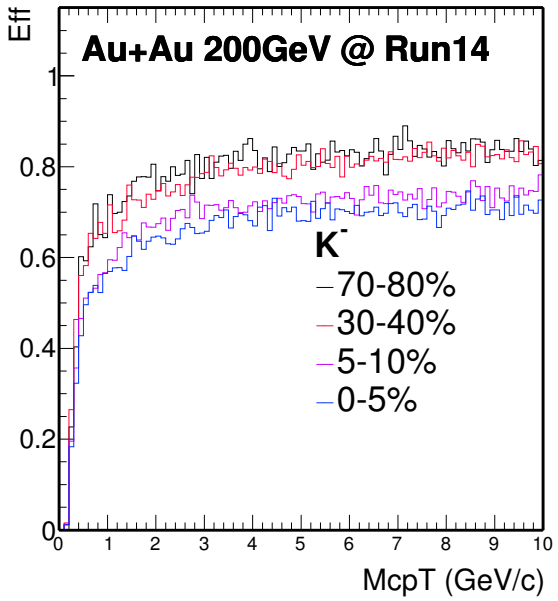

Figure 3.28: TPC tracking efficiency in Run14 Au+Au collisions at 200 GeV for Kaon.

3.5.3 TOF Matching Efficiency

For the D^0 analysis, we use the hybrid PID for TOF. Which means when TOF is available we use TOF and TPC, when it's not available we just use TPC. The TOF matching efficiency (ε_{TOF}), including the TOF response and the acceptance difference between the TPC and TOF, is evaluated by the real data. It can be calculated by comparing the number of qualified tracks matched with the TOF (with $\beta > 0$, $N_{matched}$) over the number of qualified tracks (N_{TPC}).

Fig. 3.29 shows the TOF match efficiency in Run14 Au+Au collisions at 200 GeV for positive charge particles such as π^+,K^+ in the centrality 0-10%. Fig. 3.30 shows the same plots for negative charge particles in the centrality from 40-80%. For the pion TOF match efficiency, the tread is much smooth compare to kaon. As we see, there are some deep for the TOF match efficiency at some certain p_T range from kaon, such as kaon in the p_T around 0.6 GeV/c. This effect was studied using Hijing simulation, it's found that this is due to the hadron contaminations.

Fig. 3.31 shows the $n\sigma_K$ distributions from Hijing in the p_T range from 0.5 - 0.7 GeV/c. The solid lines are for particles from TPC , and the dashed lines are for particles also include TOF match information. The total yield was scaled to have the same

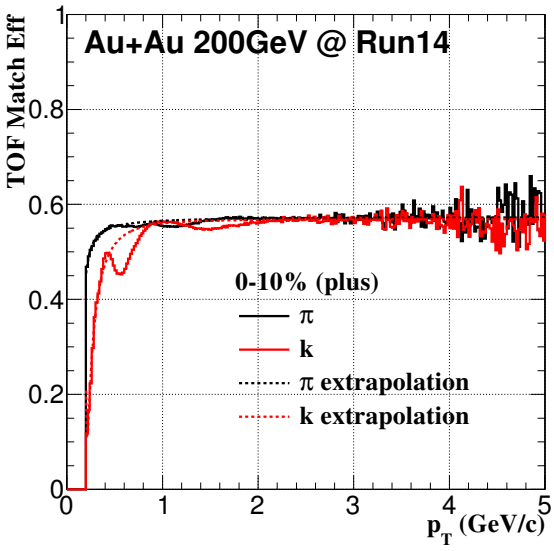

Figure 3.29: TOF match efficiency in Run14 Au+Au collisions at 200 GeV for positive charge particle in 0-10%.

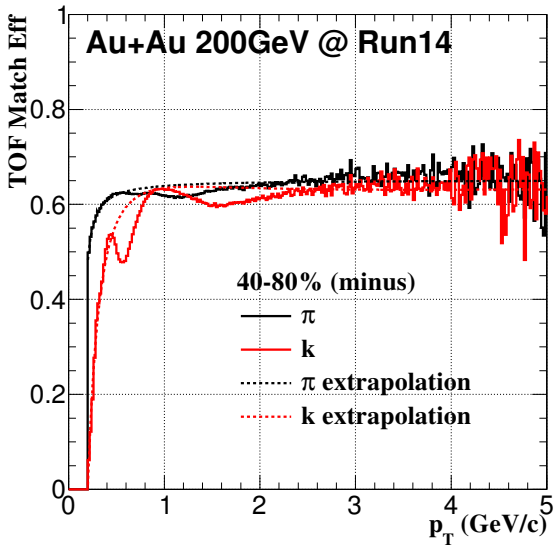

Figure 3.30: TOF match efficiency in Run14 Au+Au collisions at 200 GeV for negative charge particle in 40-80%.

number of pions for this comparison, since the TOF matching have ∼30-40% efficiency lost. In a simple case, if we select kaons with the cut $|n\sigma_K| < 1$, after the requiring of TOF match,the width of this $n\sigma_{K/\pi}$ distribution changed, and the contaminations from pions are reduced. As what we see the dashed black line have less contributions to the kaons peak within $|n\sigma_K| < 1$ compare to the solid black line. We also checked this effect in the other p_T range such as 0.2 - 0.5 GeV/c and 1.0 - 1.5 GeV/c as shown in Fig. 3.32 and Fig. 3.33. This effect is neglectable in the low p_T range 0.2 - 0.5 GeV/c since the TPC can well separate pions and kaon. In the high p_T range, the dE/dex are overlap with each other for kaon and pion, it's not able to distinguish them only use TPC.

3.5.4 PID Cut Efficiency

The particle identification cut efficiency (ε_{PID}) includes two components: the TOF velocity ($1/\beta$) cut efficiency and dE/dx cut ($n\sigma_{K/\pi}$) efficiency. Pure pions and kaons sample are used to evaluate the TOF velocity cut efficiency and TPC $n\sigma_{K/\pi}$ cut efficiency. Fig. 3.34 shows the $\pi\pi$ pairs invariant mass distributions. The black line is the unlikesign foreground, and the red line is background using likesign method. With this K^0_s candidates, we can statistical extract the pure pion sample for the PID efficiency study. Fig. 3.35 shows the KK pairs invariant mass distributions. Still with the unlikesign and likesign method, the Φ meson candidates are reconstructed, and we can statistical extract the pure kaon sample for the PID efficiency study.

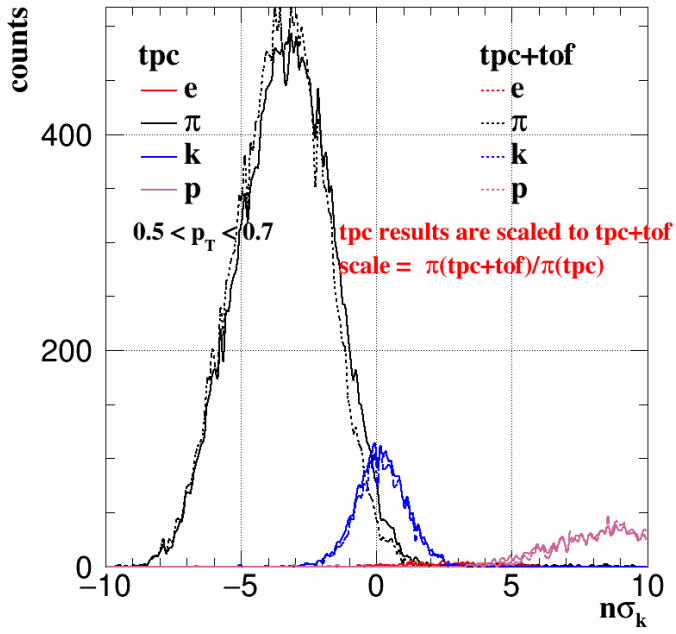

Figure 3.31: $n\sigma_K$ distributions for $0.5 < p_T < 0.7$ GeV/c. The solid lines are from TPC and dashed lines are from TPC + TOF.

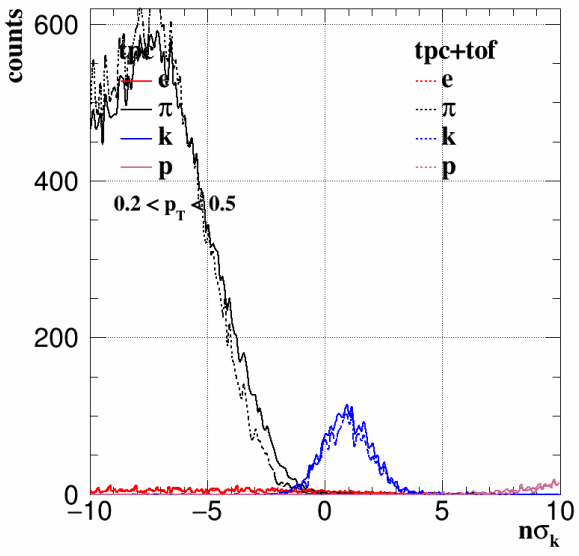

Figure 3.32: $n\sigma_K$ distributions for $0.2 < p_T < 0.5$ GeV/c. The solid lines are from TPC and dashed lines are from TPC + TOF.

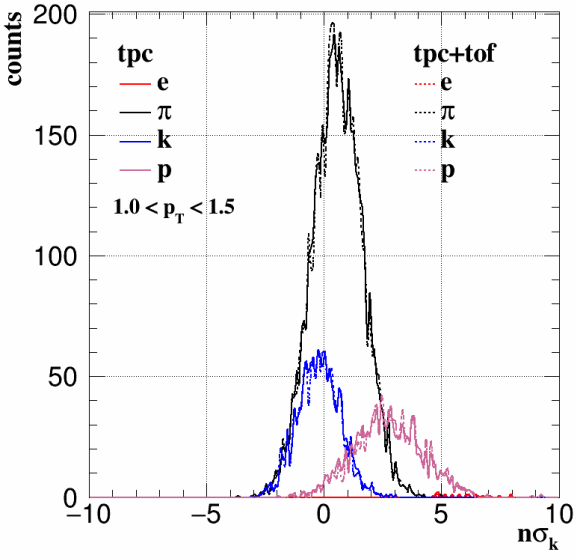

Figure 3.33: $n\sigma_K$ distributions for $1.0 < p_T < 1.5$ GeV/c. The solid lines are from TPC and dashed lines are from TPC + TOF.

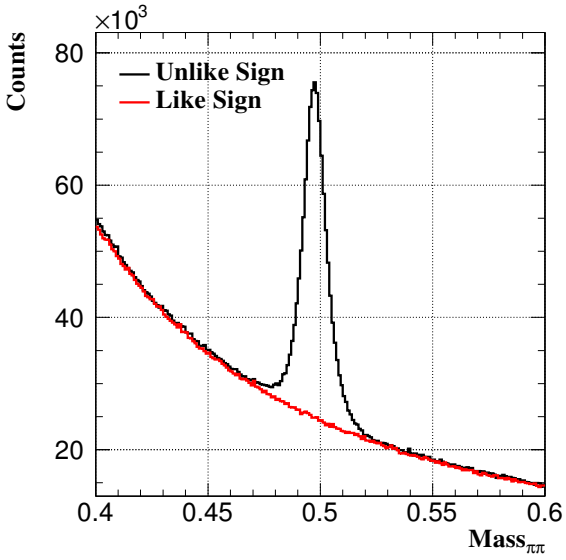

Figure 3.34: The $\pi\pi$ pairs invariant mass distributions. The black line is the unlikesign foreground, and the red line is background using likesign method.

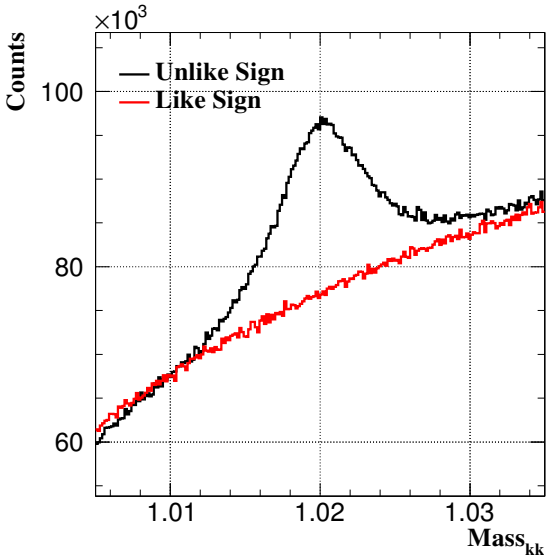

Figure 3.35: The KK pairs invariant mass distributions. The black line is the unlikesign foreground, and the red line is background using likesign method.

3.5.4.1 $n\sigma_{K/\pi}$ Cut Efficiency

The $n\sigma_{K/\pi}$ cut efficiency is derived from the Gaussian fit using those pure samples. The $n\sigma_{K/\pi}$ distributions are fitted with Gaussian function, the mean value and sigma value are plotted as Fig. 3.36 and Fig. 3.37. With these mean and sigma distributions, assuming they follow the Gaussian function, for example, Fig. 3.38 depicts the $n\sigma_{\pi}$ cut efficiency in Run14 Au + Au collisions at 200 GeV for pions. For kaons, we use the same method extracting this $n\sigma_{K}$ cut efficiency.

3.5.4.2 $1/\beta$ Cut Efficiency

The $1/\beta$ cut efficiency is also derived from the Gaussian fit using those pure samples. The efficiency is very high since the $1/\beta$ cut is very loose, it's almost $\sim$100% for this analysis as shown on Fig. 3.39 and Fig. 3.40.

3.5.5 Data-driven Fast Simulation for HFT and Topological Cut Efficiency

As discussed in the beginning of this section 3.5, the HFT related efficiency shown on Eq. 3.11 including two items: HFT acceptance and topological cuts. Since the HFT embedding is not ready yet at that time, we developed the 'Data-Driven Fast simulation' for the HFT related efficiency correction. And this method was validated with full GEANT simulation and will be discuss later.

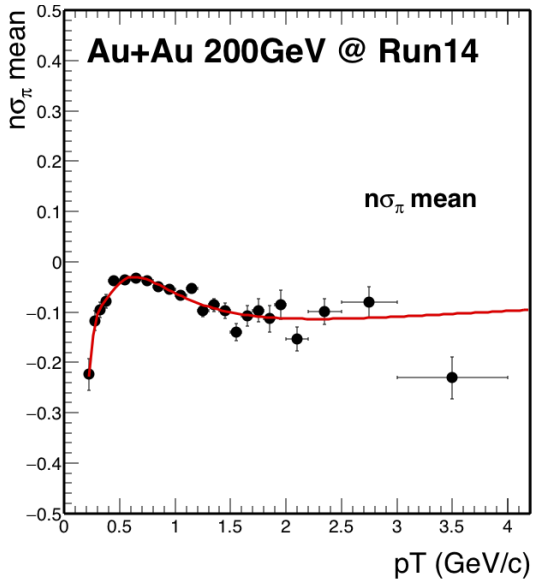

Figure 3.36: The mean value of $n\sigma_\pi$ distributions vs momentum. The red line is fitted function with polynomial function.

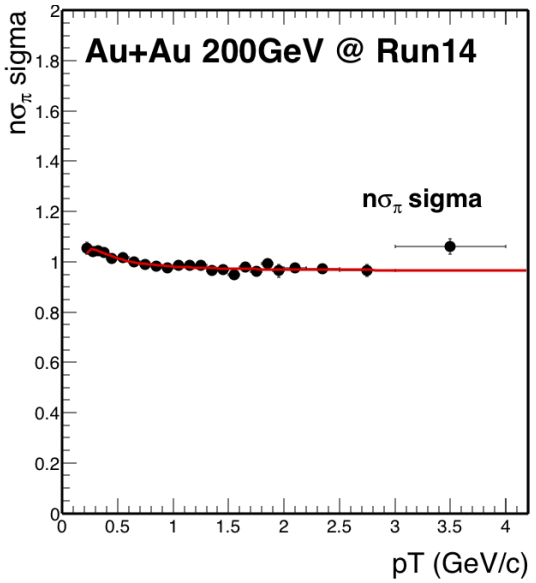

Figure 3.37: The sigma value of $n\sigma_\pi$ distributions vs momentum. The red line is fitted function with polynomial function.

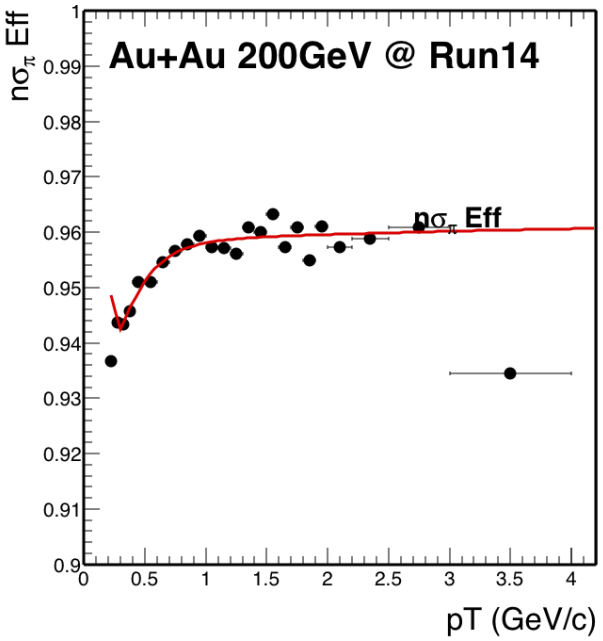

Figure 3.38: $n\sigma_\pi$ cut efficiency along with momentum. Red line is the fitted polynomial function

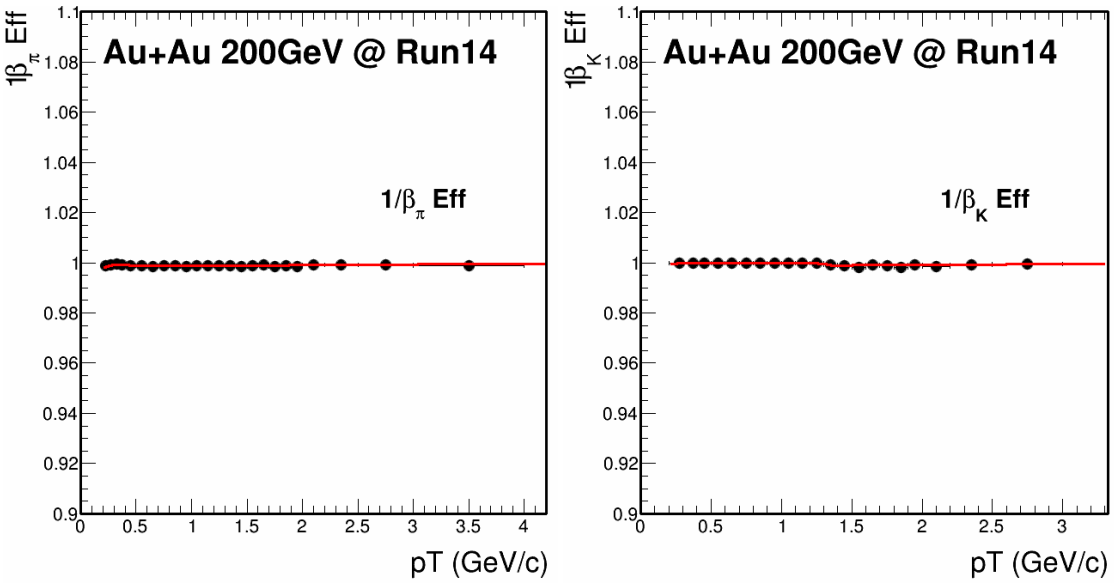

Figure 3.39: $1/\beta$ cut efficiency along with momentum for pion. Red line is the fitted function.

Figure 3.40: $1/\beta$ cut efficiency along with momentum for kaon. Red line is the fitted function.

3.5.5.1 Assumptions

Before we discuss the details procedure of the method, it's better to make it clear, this data-driven simulation is based on several assumptions. And the validating will be tested step by step in the later section.

- Factorization of tracking efficiency:

$$\frac{\text{HFT}}{\text{MC}} = \frac{\text{HFT}}{\text{TPC}} \times \frac{\text{TPC}}{\text{MC}} \tag{3.17}$$

- Spatial resolution of HFT is encoded in two variables: DCA_{XY} and DCA_{Z} (two dimensions correlated).
- Vertex resolution, which is possibly folded in the DCA resolution of single tracks and correlated for kaons and pions, is a negligible, at least for semi-central to central events.
- The contribution of feed-down particles from secondary decays to DCA distributions is negligible.
- Mis-matched daughter tracks are removed by topological cuts.

3.5.5.2 Ingredients

There are several input ingredients for this fast-simulation package which is extracted from data.

- Extract V_z distributions from data (centrality dependent).
- Extract ratio of HFT matched tracks to TPC tracks from data (This ratio includes all mismatched tracks) (particle species, centrality, p_T, η, ϕ, V_z dependence).
- Extract DCA_{XY} - DCA_Z distributions from data. Assuming that data DCA distributions is dominated by primary particles (particle species, centrality, p_T, η, V_z dependence).
- Extract TPC efficiency and momentum resolution from embedding (particles, centrality and p_T dependence).

Fig. 3.41 shows an example of the input HFT match ratio in the certain η, V_Z, ϕ and centrality range. The HFT match ratio increase in the low pt range due to the high mismatch occupancy and keep flat in the high p_T range. This ratio have a strong dependence on these differential such as η and V_Z since this is effected by HFT acceptance. Fig. 3.42 shows an example of the Dca_{XY} vs Dca_Z distribution in the certain p_T, η, V_Z and centrality range. The axis binning is dynamic binning (non-uniform) since the most central (around 0) part is the dominate part. Limited by the computing memory, the most central part use fine binning and others use the unrefined binning as shown on the plots.

In total, there are 11 (ϕ) $\times$ 10 (η) $\times$ 6 (V_z) $\times$ 9 (centrality) $\times$ 2 (particles) 1D histograms (36 p_T binning) for HFT match efficiency. There are 5 (η) $\times$ 4 (V_z) $\times$ 9 (centrality) $\times$ 2 (particles) histograms $\times$ 19 (p_T) 2D histograms (144 $\times$ 144 Dca binning) for Dca resolution smearing.

Effectively, these 1D and 2D histograms encode HFT efficiency, acceptance and spatial resolution performance in Run14 data.

3.5.5.3 Recipe

After all the input ingredients ready for the fast-simulation, a simple toy MC simulation (PYTHIA/EvtGen) is applied for the efficiency study. The basic recipe is following:

- Sample V_z distribution according to data distribution.
- Generate D^0 flat in p_T and rapidity and decay it.
- Smear momentum according the embedding.
- Smear DCA_{XY} and DCA_Z of Kaons and Pions independently according to distributions from data.

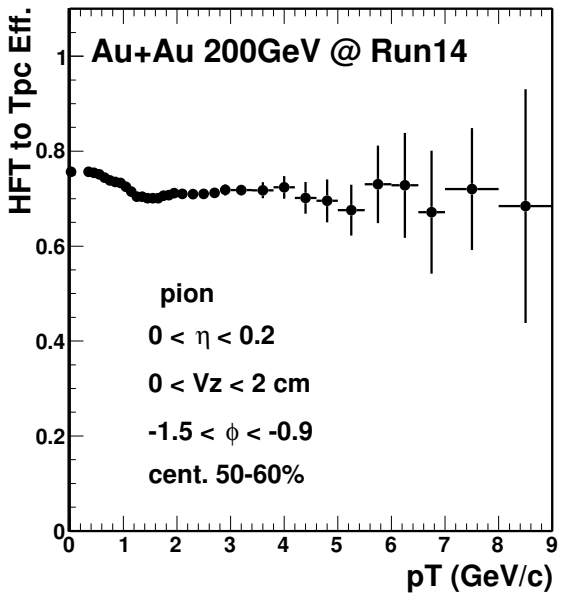

Figure 3.41: HFT to TPC track match ratio for pion at certain η,V_Z,ϕ,centrality range.

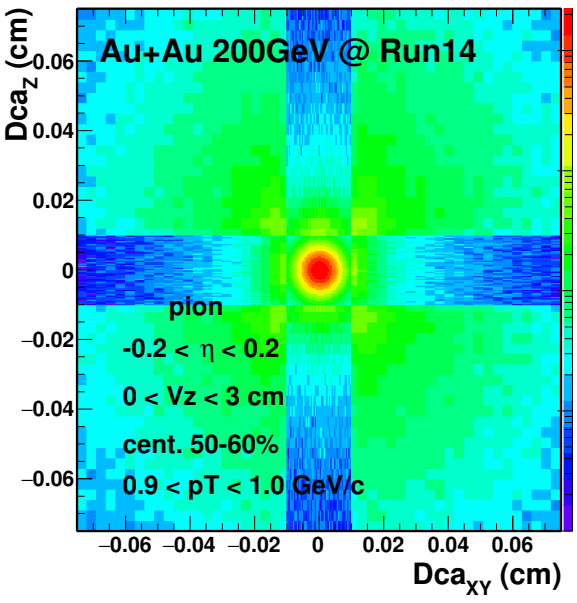

Figure 3.42: Dca_{XY} vs. Dca_Z for pion at certain η,V_Z,centrality range.

- Apply HFT matching efficiency from HFT ratio.
- Apply TPC reconstruction efficiency.
- Reconstruct D^0

3.5.5.4 D^0 Efficiency and Topological Distribution

As discussed in the recipe, we obtain the efficiency step by step as shown on Fig. 3.43. First we have the TPC efficiency shown by red maker which is after the p_T, η acceptance cut and TPC tracking efficiency from embedding. Then after folding in the HFT matching efficiency, the second item is obtained on black circle. Last step is after the topological cut, as shown by the cyan marker. As see in the low p_T part, the topological cut efficiency is really small due to the tight cut as the combinatorial background is huge.

We study all the efficiencies with small centrality bin width, in total we have 9 centrality bins from our StRefmultCorr class. Since the D^0 production is scaled by the number of binary collisions (N_{bin}), the D^0 is favor produced in more central collisions. So the final efficiencies for the wider centrality bins 0-10%, 10-40%, 40-80% and 0-80% are calculated using N_{bin} as weights, for example, the efficiency in 0-80% is calculated as the following Eq. 3.18. Fig 3.44 shows the D^0 efficiency for 4 wide centralities after TPC, HFT match and Topological efficiency included [96].

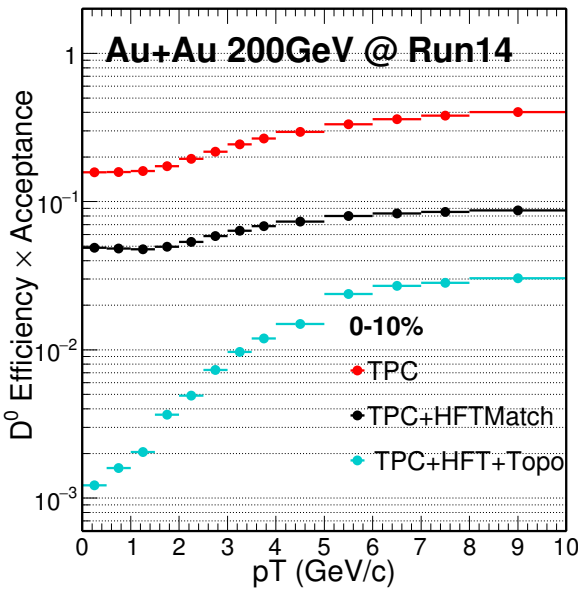

Figure 3.43: D^0 efficiency step by step from TPC, HFT HFT Ratio, Topological cut in most central 0-10%.

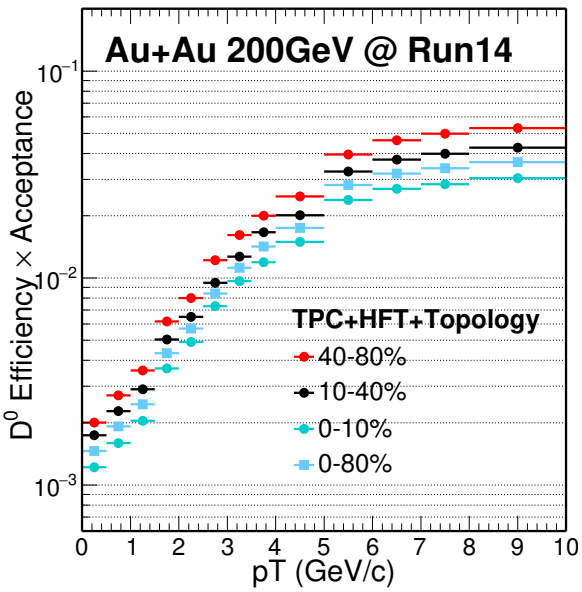

Figure 3.44: D^0 efficiency including TPC, HFT and Topological cut in several centralities.

$$\text{Efficiency}_{0-80\%} = \sum_{i=1}^{9}(\text{Efficiency}_i \times N^i_{bin})/ < \text{N}_{\text{bin}} > \tag{3.18}$$

The Data-Driven Fast-Simulation also provide the topological information, can be used for the comparison with real data. For the real data part, within the D^0 mass window we can statistical subtract the background and extract the pure D^0 topological distributions. The invariant mass plots shown as Fig. 3.45. D^0 is in the $2 < p_T < 3$ GeV/c, 0-80% centrality. Black is unlikesign foreground, blue is likesign background and red is mixed event background. The blue vertical lines are the mass window used for the topological comparison. For each topological variable, that corresponding topological cut was removed when reconstruct the D^0 candidate, so that we can compare that variable in a wide range.

From Fig. 3.46 to Fig. 3.51, these are the topological variables (cos(θ), decayLength, dcaDaughters, D0DcaToVtx, PionDca and KaonDca) used for the D^0 reconstruction. The distributions from the real data part are using mixed event method to statistical subtract the background. The Data-Driven Fast-Simulation part was the package we relayed on for our efficiency study as shown before.

Comparison these topological variables between real data and Fast-Simulation, the agreement is reasonable good, which means our Data-Driven Fast-Simulation method can well reproduce the topological variables in real data. In another word, the efficiency estimation from Data-Driven Fast-Simulation is reliable. Note, there are some small discrepancy such as single track Dca distributions in the low end, that's because in the

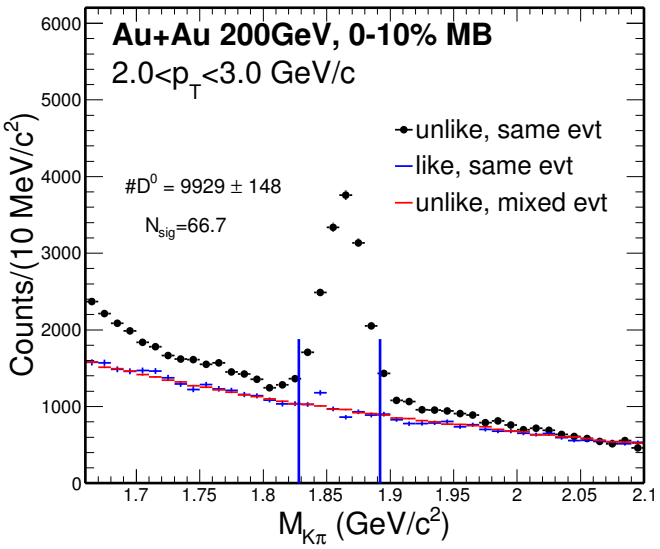

Figure 3.45: D^0 invariant mass distributions in the $2 < p_T < 3$ GeV/c, 0-10% centrality. Black is unlikesign foreground, blue is likesign background and red is mixed event background. The blue vertical lines are the mass window used for the topological comparison.

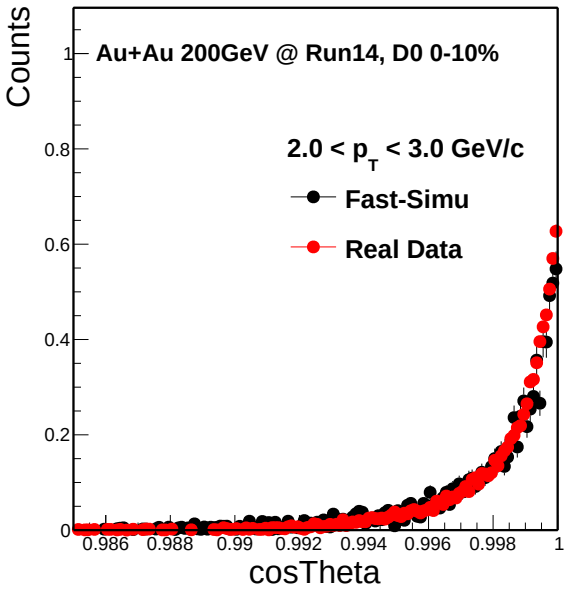

Figure 3.46: D^0 cosTheta distribution in most central 0-10% between Fast-Simulation and Real Data.

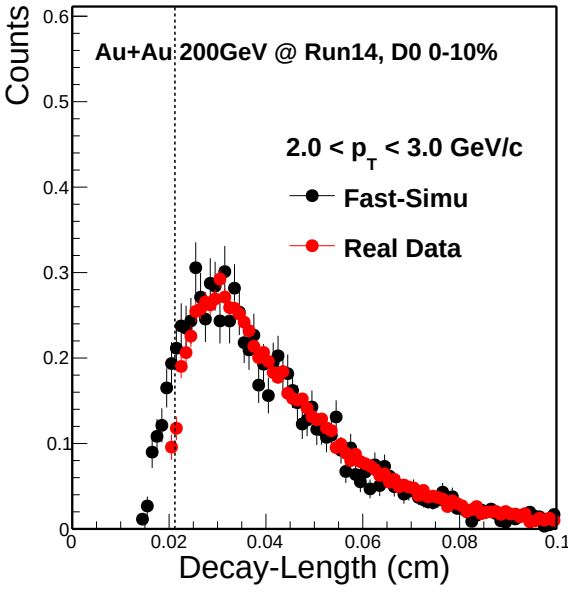

Figure 3.47: D^0 decay length distribution in most central 0-10% between Fast-Simulation and Real Data.

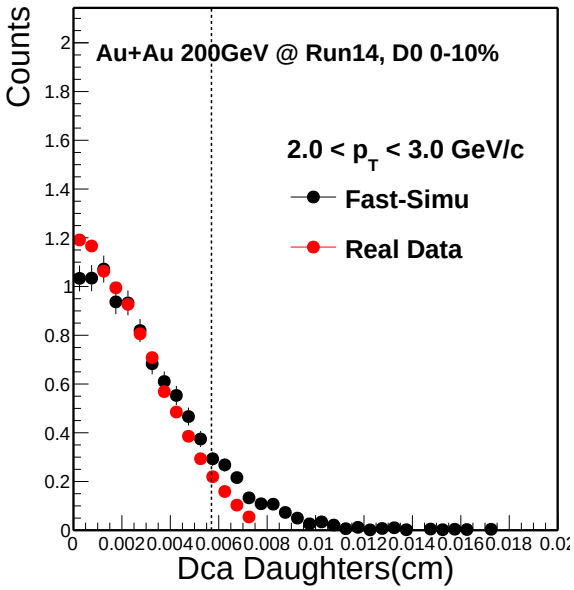

Figure 3.48: D^0 dcaDaughters distribution in most central 0-10% between Fast-Simulation and Real Data.

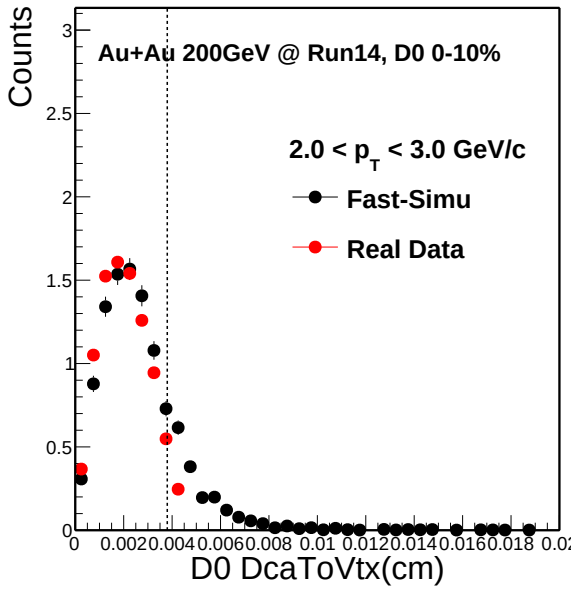

Figure 3.49: D^0 dca to Vertex distribution in most central 0-10% between Fast-Simulation and Real Data.

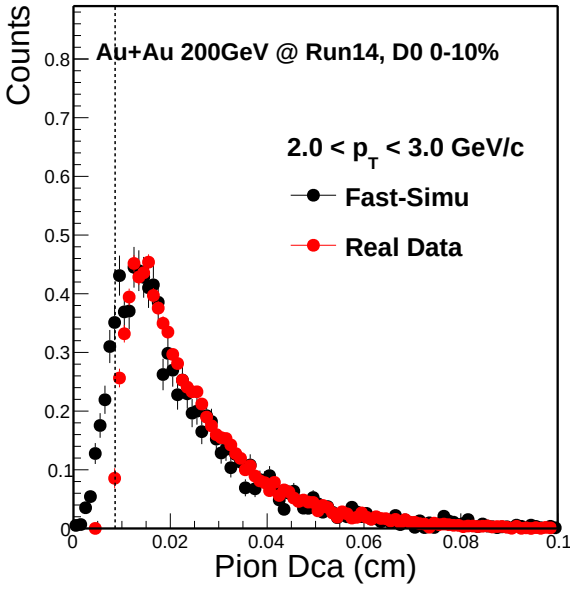

Figure 3.50: D^0 pionDca distribution in most central 0-10% between Fast-Simulation and Real Data.

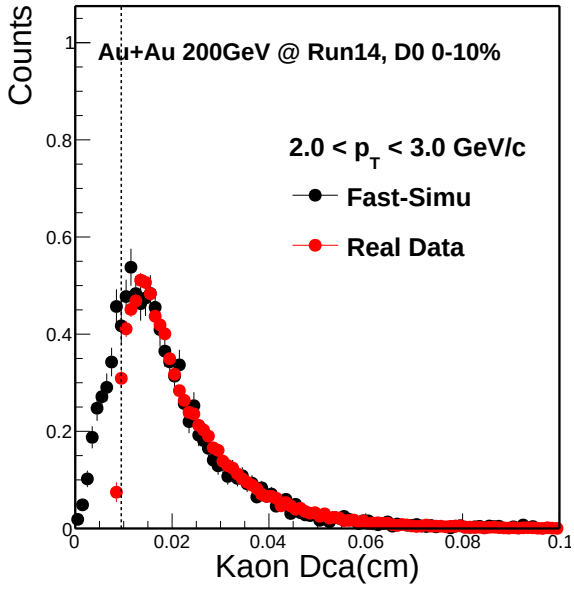

Figure 3.51: D^0 kaonDca distribution in most central 0-10% between Fast-Simulation and Real Data.

data analysis part, we already require some minimum cut in order to save the computing resource. There is another method we are going to discuss in the following section, also can be used to validating our Fast-Simulation method.

3.6 Validation Data-Driven Fast-Simulation with Full GEANT + Hijing Simulation

Before discuss the details of this Hijing validation, it's better to conclude those assumptions we made before. The first assumption is the factorization shown in Eq. 3.17. Relaying on the Hijing simulation, we have two samples. One is only include TPC tracking, another one include both HFT and TPC in tracking. From the first sample, we can extract the TPC factorized tracking efficiency, and the second sample can be used to extract the overall total efficiency and HFT over TPC factorized efficiency separately. Fig. 3.52 shows the comparison between the overall efficiency and the multiplied factorization efficiency. The red one is from overall efficiency from the second sample, and the blue one is multiplied efficiency from two components. The bottom panel shows the double ratio of these two efficiency, and they are perfectly factorized as the ratio is flat as unity.

The second assumption is for the spatial resolution, it is encoded in those $\mathrm{Dca_{XY}}$ and $\mathrm{Dca_Z}$ variables, and they are correlated in the two dimensions. Fig. 3.53 shows the comparison between the input Dca from real data and output Dca from Fast-Simulation in three dimensions. The first row is Dca in XY plane, the second row is in Z plane and the last row is in the 3-D dimension. From the left to right is the comparison from low p_T to high p_T. As shown the red line is from data and black line is from fast simulation, the agreement is pretty good. For the others assumption, they will be discussed separately in the following section.

3.6.1 Hijing Samples Performance

The Hijing sample was run through the Full Hijing + GEANT simulation with realistic pileup hits (UPC+MB) in PXL and sensor masking tables. They can provide reasonable performance for the HFT matching ratio and Dca resolution [97]. In total we have $\sim$45K 0-10% centrality Hijing events, and for each event is embedded with 20 D^0's. So in total, we have $\sim$900K D^0 for this Hijing sample. The embedded D^0 has small effect on the tracking since the multiplicity is much higher compared to 20 $\times$ 2 D^0' decayed daughters.

As shown in Fig. 3.54 is the HFT matching ratio comparison between data (red) and Hijing samples (black) in Au+Au 200 GeV/c from 0-10% centrality, the bottom

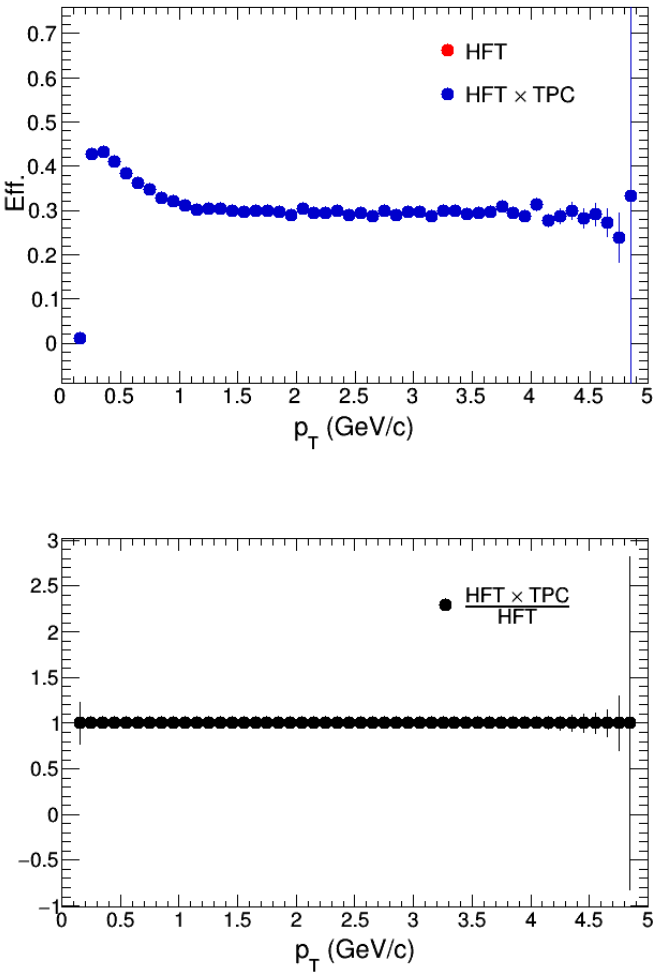

Figure 3.52: (top)HFT Efficiency Factorization comparison. (bottom) Double Ratio of these factorization.

panel is the double ratio of these two HFT matching ratio. The value is around unity, which means the Hijng simulation can well reproduce these matching performance.

Fig. 3.55 shows the pions $\mathrm{Dca_{XY}}$ comparison between data (red) and Hijing samples (black) in Au+Au 200 GeV/c from 0-10% centrality at $1.0 < p_T < 1.2$GeV/c, the bottom panel is the double ratio of these two Dca distributions. The value is also around unity, which means the Hijng simulation well describes the real data.

3.6.2 Validation Procedures

The idea is simple for this Hijing validation, we have the enriched D^0 Hijing sample. After run through the detector and full GEANT simulation, the D^0 efficiency and topological variables distributions can be extracted. Another procedure is extract the necessary ingredients from Hijng sample for the Fast-Simulation input (Fast-Simulation with Hijing input), such as the TPC Tracking efficiency, the HFT matching ratio and the

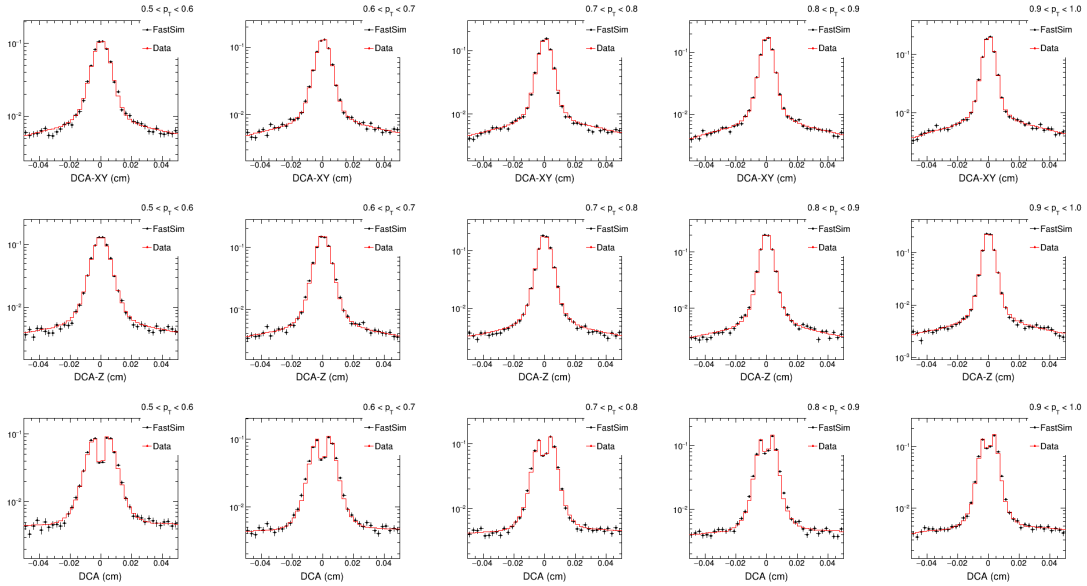

Figure 3.53: Comparison of Dca between data (red) and Fast-Simulation (black). From top to bottom, the comparison is for $\mathrm{Dca_{XY}}$, $\mathrm{Dca_Z}$ and Dca. From left to right the transverse momentum is from low p_T to high p_T.

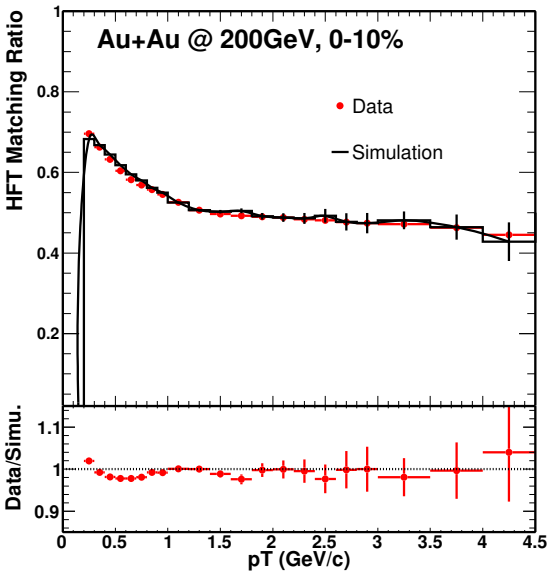

Figure 3.54: HFT Ratio comparison between data and Hijing simulation in Au+Au 200 GeV/c, 0-10%.

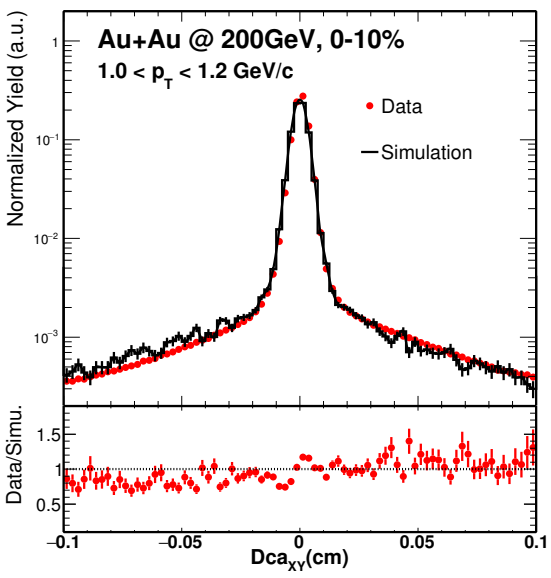

Figure 3.55: $\pi^{\pm}$ $\mathrm{Dca_{XY}}$ comparison between data and Hijing simulation in Au+Au 200 GeV/c, 0-10%.

2D Dca_{XY}-Dca_Z distributions similar as we used in real data analysis and discussed in the previous section 3.5.5. Then run through the Fast Simulation, as discussed before, the D^0 efficiency and topological variables are also available in this way and can be compared to the first Hijing + GEANT procedure. The workflow is shown in Fig. 3.56.

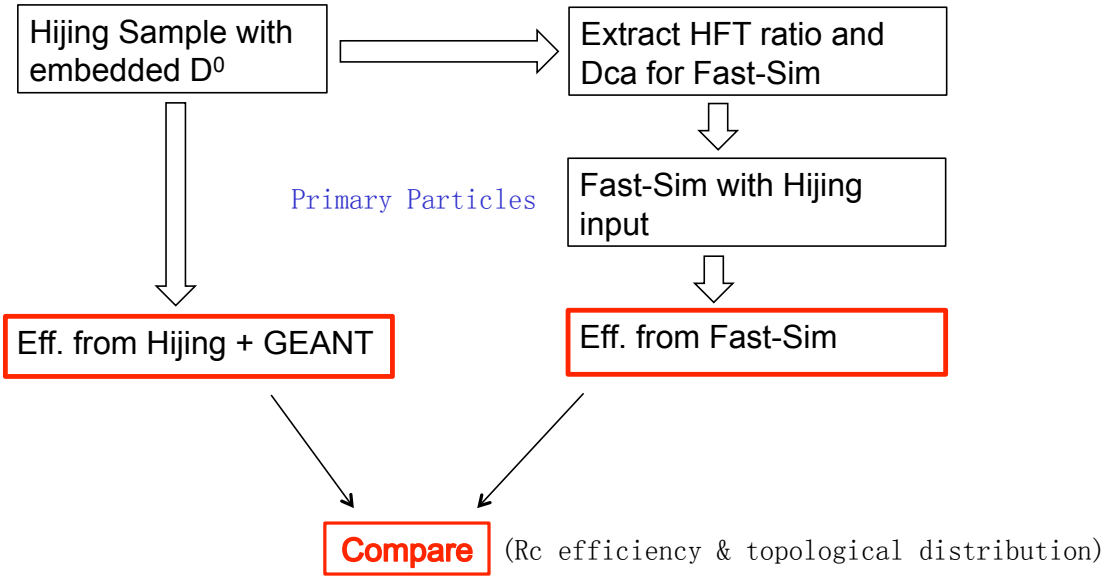

Figure 3.56: Hjiing validation procedure and workflow

3.6.2.1 Validation Efficiency

The first step is to check the kinematic form different MC decayer such as PYTHIA, Hijing, evtGen and PhaseSpace class from ROOT. Need to make sure the decayer used for Fast-Simulation has the same kinematic as the Hijng. After the basic acceptance cut, such as D^0 |y| < 1, daughter $p_T > 0.2$ GeV/c and $|\eta|$ <1 cut. D^0 is the simple phase space decay, all these decayer give the same acceptance efficiency as shown in Fig. 3.57 left panel, the right panel shows the double ratio to PYTHIA. As all the decayer follow the same trend they have the same decay kinematic, so, for our Fast-Simulation decayer we choose PYTHIA for this validation and also for our real data analysis.

The second step is to check the kinematic with the reconstructed TPC tracking information. Compare to the first step, this one fold in the momentum resolution and the TPC acceptance effect. Fig. 3.58 left panel shows this efficiency $\times$ Acceptance comparison between Hijing + GEANT (red) and Fast-Simulation with Hijing input (black), the right panel shows the double ratio to Hijing. As the red line is the fit function and the fit results around $\sim$1 shows very good agreement, which means this step is also doing right work.

The next step is to trying to fold in the HFT matching efficiency and this is to consider the HFT acceptance effect. Fig. 3.59 left panel shows this efficiency $\times$ Ac-

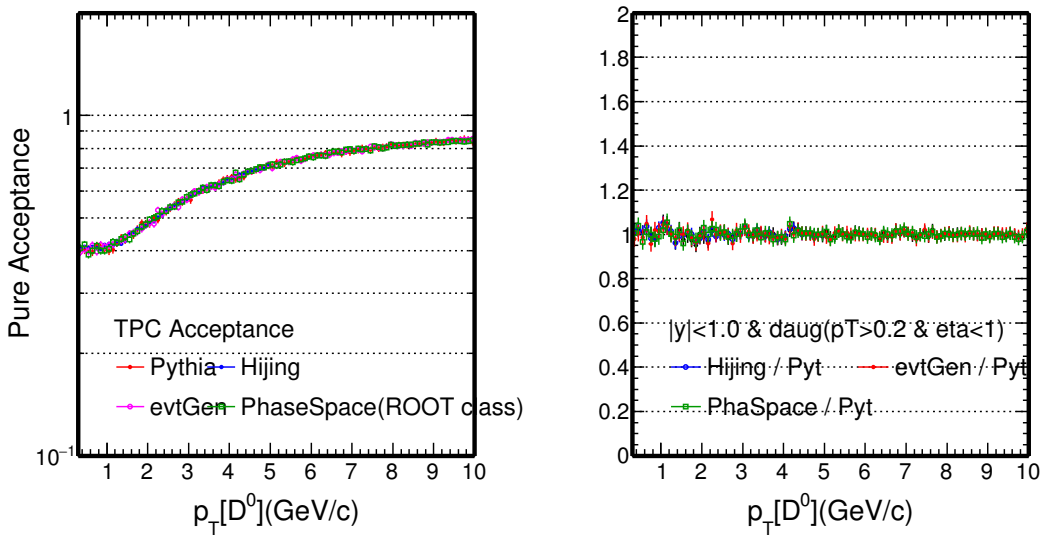

Figure 3.57: D^0 pure acceptance from different MC decayer, such as PYTHIA, Hijing, evtGen and PhaseSpace class. (right) Double ratio of the acceptance to PYTHIA.

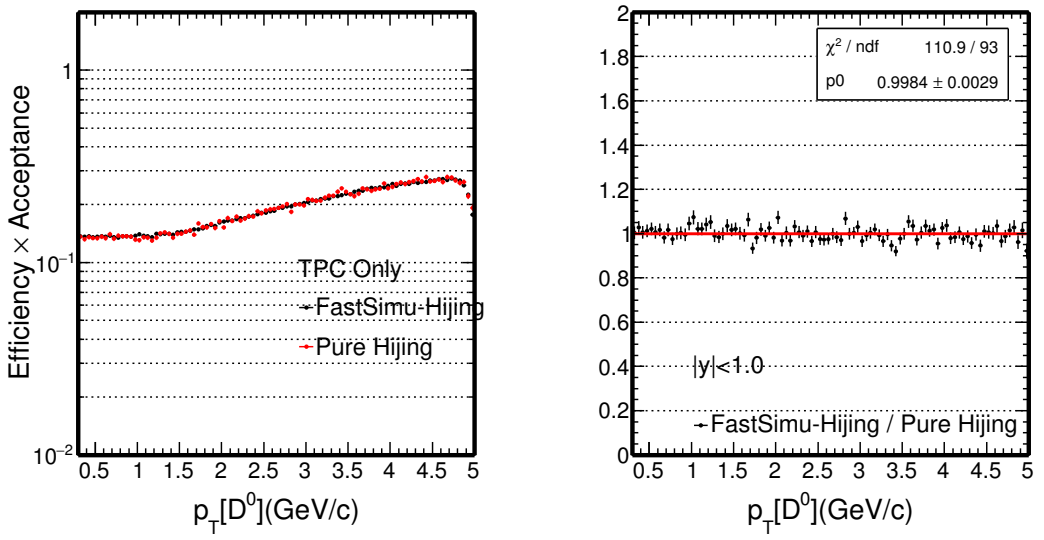

Figure 3.58: The comparison of D^0 TPC acceptance $\times$ efficiency between Hijing + GEANT (red) and Fast-Simulation with Hijing input (black). (right) Double ratio of these acceptance to Hijing.

ceptance comparison after TPC and HFT matching between Hijing + GEANT (red) and Fast-Simulation (black), the right panel shows the double ratio to Hijing. As the red line is the fit function and the fit results around ∼1 shows good agreement, which means this HFT matching step is also correctly implemented in the package. For the small discrepancy at the high p_T range, this is purely due to the limited statistics. Since the Hijing sample is time consumption, we do not have enough statistics for the HFT match ratio input. But this problem is not exist for our real data analysis since we have ∼900M events which is totally enough and we checked the HFT match ratio, they can extend to a reasonable high p_T range in real data. We did another small check, use one quart of these Hijing statistics for this validation, and the discrepancy shown here is bigger than the current results, which is another approve of the limited Hijing statistics.

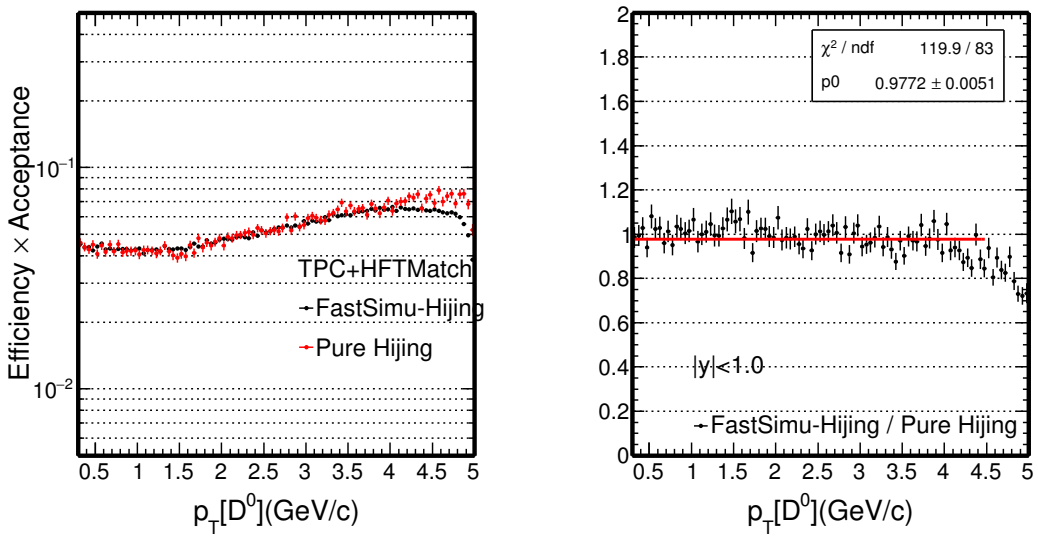

Figure 3.59: The comparison of D^0 TPC + HFT match acceptance × efficiency between Hijing + GEANT (red) and Fast-Simulation with Hijing input (black). (right) Double ratio of these acceptance to Hijing.

The last step is folding in the topological cuts and then compare between the Hijing and Fast-Simulation. Fig. 3.60 left panel shows this efficiency × Acceptance comparison after TPC, HFT matching and topological cuts between Hijing + GEANT (red) and Fast-Simulation (black), the right panel shows the double ratio to Hijing. Still the red line is the fit function and the fit results around ∼0.93 shows good agreement, which means this topological variables are well described in the package. For the left panel, there are some twist for this efficiency × acceptance at p_T ∼1 GeV/c and 2 GeV/c, this is due to the topological cuts are different in separate p_T ranges. As the red points show the efficiency from Hijing + GEANT, the statistics error is larger compared to the Fast-Simulation which shows by black. This is also the reason we use data-driven

Fast-Simulation for our efficiency study, it can be easily enlarge the statistics by a factor of 100 or even 1000 compare to the traditional Full GEANT simulation especially for this kind of low efficiency studies. Fig. 3.61 shows the same plots of the comparison as Fig. 3.60 with different binning, we merged some binning for statistics concern. After merged the binning, the agreement is even better from the fitting shown on the right panel, the fitting results is ∼0.96.

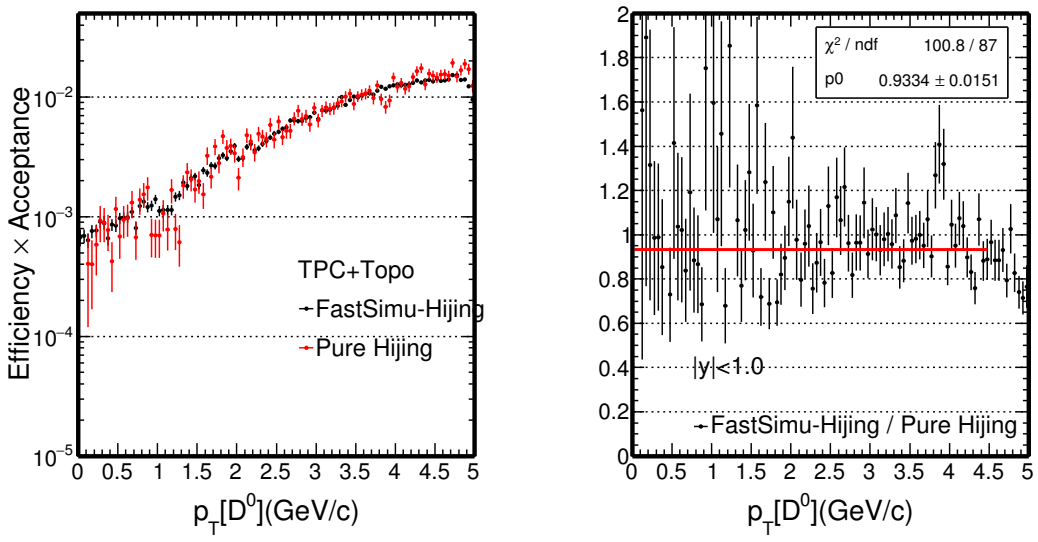

Figure 3.60: The comparison of D^0 TPC + HFT match + Topological acceptance × efficiency between Hijing + GEANT (red) and Fast-Simulation with Hijing input (black). (right) Double ratio of these acceptance to Hijing.

From Hijing + GEANT simulation, we know exactly whether the HFT matched track is real match or mismatch, so we can determine the HFT real matched efficiency × acceptance for D^0 reconstruction from Hijing sample. Fig. 3.62 shows these real matched efficiency × acceptance comparison between Hijng + GEANT and our previously Fast-Simulation. The right panel shows the double ratio of these efficiency and fitted with a line, the parameters shows ∼0.98 which means the (previous) Fast-Simulation can well reproduce the real HFT matched reconstruction efficiency. Fig. 3.63 shows the same plots of the comparison with different binning.

If we compare with the previous Hijing HFT matched efficiency (not necessary to be real matched), it also indicate that most of the Mis-matched daughter tracks are removed by topological cuts as we said in the assumptions. Fig. 3.64 shows the different components contributions directly from Hijing, the black one is HFT matched, red one requires all the daughter tracks are real matched and the blue one shows at least one of the daughter tracks are mis-matched. Right panel shows the relative fraction of the real match and mis-mismatch contribution. As see, most of the mis-matched tracks are

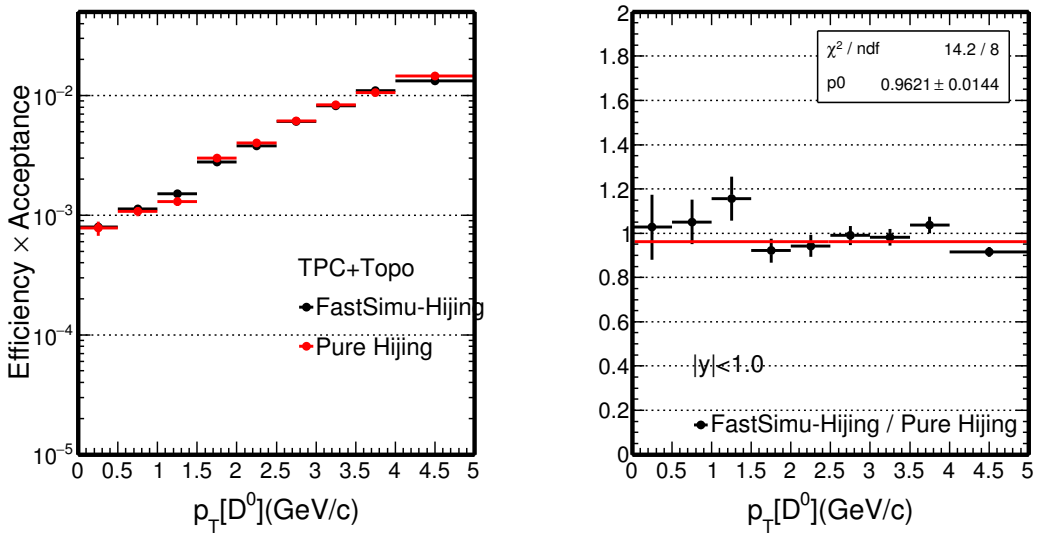

Figure 3.61: The comparison of D^0 TPC + HFT match + Topological acceptance × efficiency between Hijing + GEANT (red) and Fast-Simulation with Hijing input with wide binning (black). (right) Double ratio of these acceptance to Hijing.

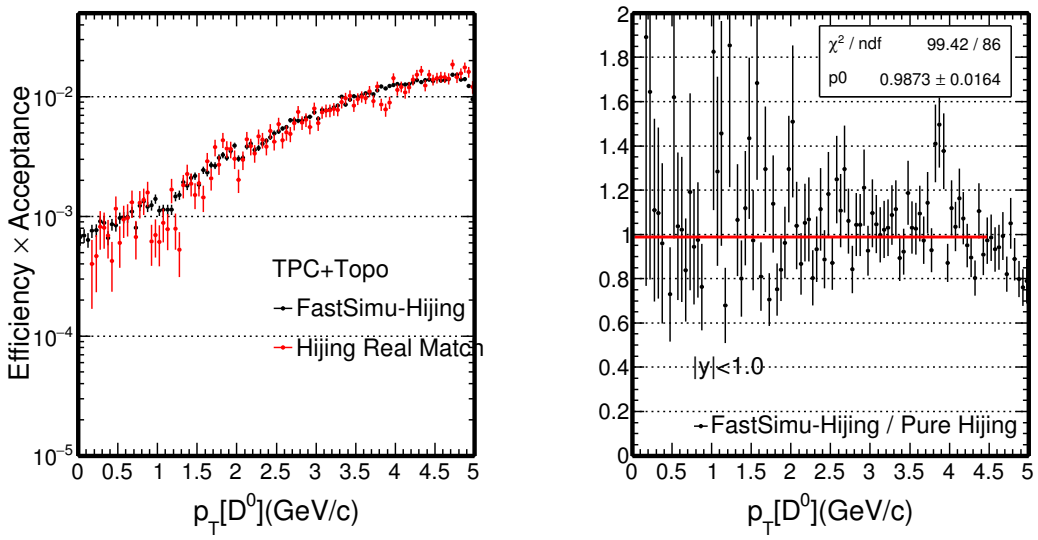

Figure 3.62: The comparison of D^0 TPC + HFT Real match + Topological acceptance × efficiency between Hijing + GEANT (red) and Fast-Simulation with Hijing input (black). (right) Double ratio of these acceptance to Hijing.

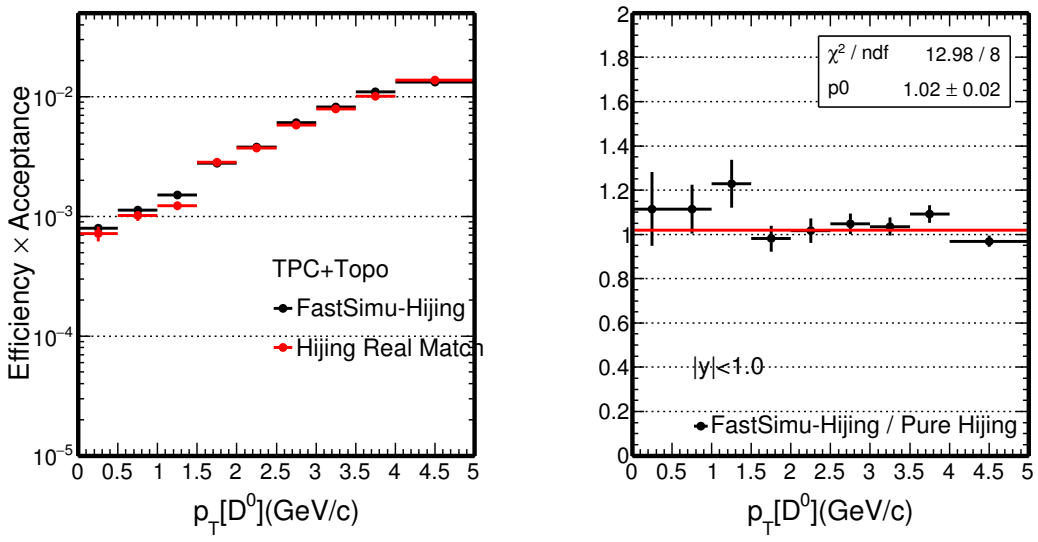

Figure 3.63: The comparison of D^0 TPC + HFT Real match + Topological acceptance × efficiency between Hijing + GEANT (red) and Fast-Simulation with Hijing input with wide binning (black). (right) Double ratio of these acceptance to Hijing.

removed, but still there are ∼5% contribution from this study.

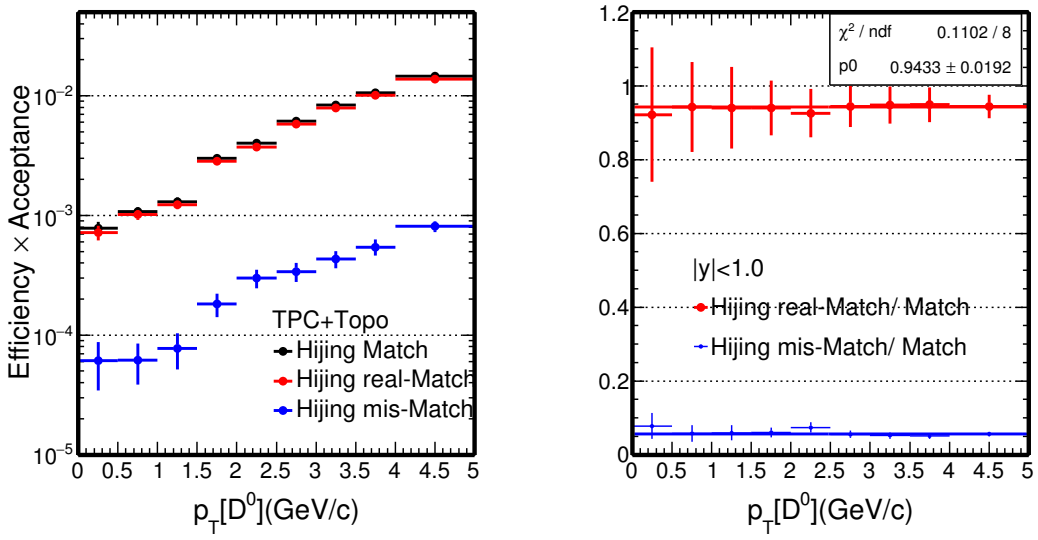

Figure 3.64: The comparison of D^0 TPC + HFT (real/mis) match + Topological acceptance × efficiency for Hijing + GEANT. (right) Double ratio of the components form Hijing.

Above all the discussions in this section 3.6.2.1, we are confident that the Fast-Simulation method can well reproduce the acceptance and efficiency for this HFT related analysis. The precision as shown on Fig. 3.61 is good enough for our efficiency study. For the missed-match check, there are ∼5% contributions in the signals. And there is another approvement that will describe in the following section.

3.6.2.2 Validation Topological Distributions

As discussed before, we can extract the topological variables from both Hijing + GEANT and Fast-Simulation relay on those Hijing input. Similar as we did in Sec. 3.5.5.4, we can compare the topological distributions from these two procedures. This will be another evidence that our Fast-Simulation can well reproduce the topological variables which is crucial for these kind of secondary vertex reconstruction analysis.

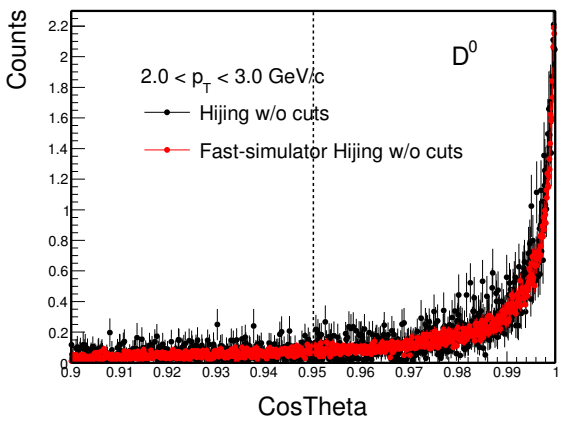

Figure 3.65: D^0 cosTheta distribution in most central 0-10% between Hijing and Fast-Simulation.

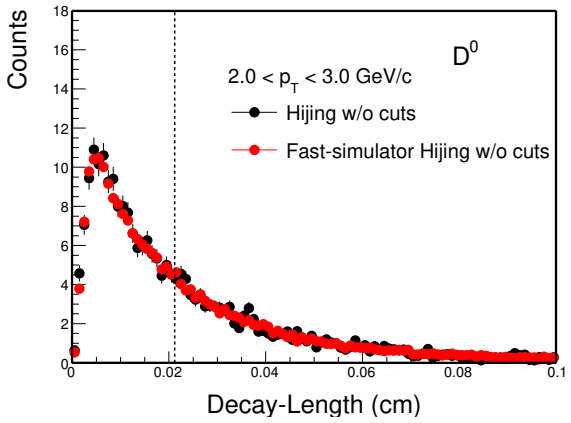

Figure 3.66: D^0 decay length distribution in most central 0-10% between Hijing and Fast-Simulation.

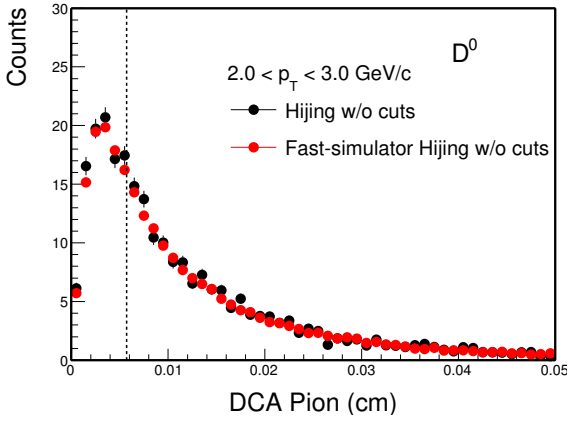

Figure 3.67: D^0 pions Dca distribution in most central 0-10% between Hijing and Fast-Simulation.

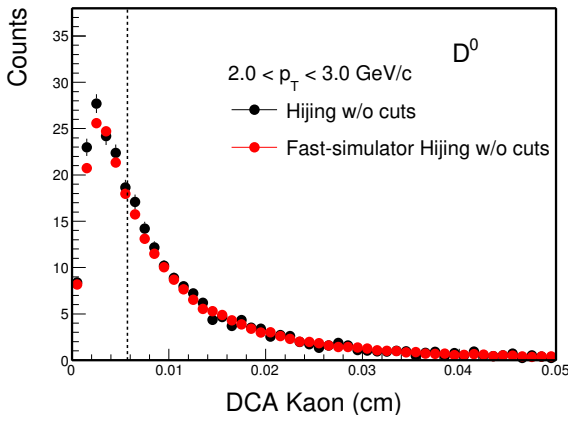

Figure 3.68: D^0 kaons Dca distribution in most central 0-10% between Hijing and Fast-Simulation.

From Fig. 3.65 to Fig. 3.69, these are the topological variables used for the D^0 reconstruction. The topological distributions can be extracted both directly from Hijng + GEANT and from Fast-Simulation relay on Hijing input. The Fast-Simulation part was the same package as we used for the efficiency study before.

As seen, the comparison of topological variables from Hijing have a very good agreement, which means again our Fast-Simulation method can well reproduce the topo-

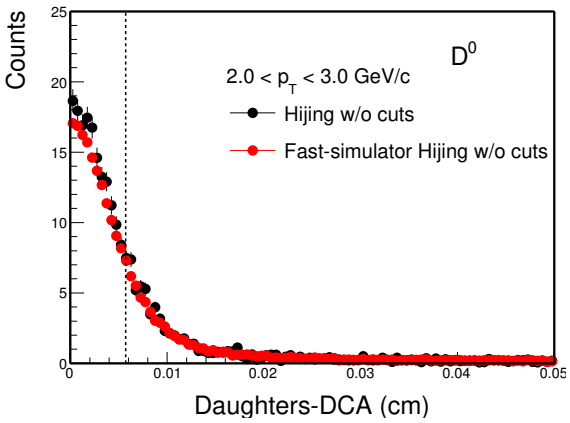

Figure 3.69: D^0 dcaDaughters distribution in most central 0-10% between Hijing and Fast-Simulation.

logical variables in Hijing sample just as in the real data case. In another word, the efficiency estimation from this Hijing-Data-Driven Fast-Simulation is reliable. This is the other confident as we discussed in the last part of previous section 3.6.2.1.

3.6.3 Validation with K_s Spectra

In order to validate our data-driven Fast-Simulation package, another related analysis was studied. The K_s spectra with HFT using Fast-Simulation method was compared with published one since the published TPC K_s results have much better precision compare to published D^0 [98].

The event and track quality cuts are same as those in D^0 analysis. The topological cuts are also similar as D^0 cuts. Fig. 3.70 the K_s corrected spectra in Au+Au collisions at 10-20% centrality. Open symbols are published results and solid symbols are new results from HFT with data-driven Fast-Simulation method for efficiency correction. The red line are the fitted function. Bottom panel shows the ratios to the fitted function. As we see, the ratios are around $\sim$1 which means the published results and the new HFT results are consistent within $\sim$10%.

3.7 Systematic Uncertainties

The approach for the D^0 spectrum systematic uncertainties are well studied. Several sources can be contributed to the uncertainties. The first one is coming from the raw yield extraction. We varied the signals fitting range, the fitting exclusion mass range and the signals counting windows to estimate the uncertainties for yield extraction. The second one is from the TPC embedding uncertainties, this one is well studied before in STAR collaboration and we quota 3% for single track. The next one is from the fast-simulation part, as discussed in the previous section, there are $\sim$5% difference between

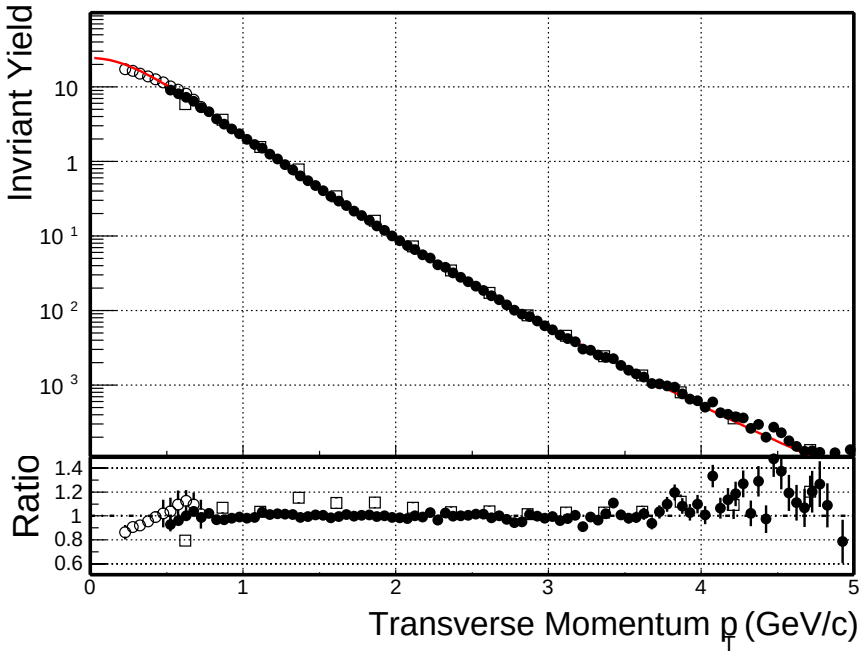

Figure 3.70: K_s corrected spectra in Au+Au collisions at 10-20% centrality. Open symbols are published results and solid symbols are new results from HFT with data-driven Fast-Simulation method. Bottom panel shows the ratios to the fitting function.

the pure Hijing and fast-simulation relay on Hijing when we validating the packages. We quote this 5% contribution as one of the systematic sources. Another source would be the vertex resolution contribution as we discussed before, since the most central collisions does not suffer the vertex contribution while the impact on the most peripheral collisions could be visible. We quote a separate systematic errors for difference centralities, 10% for the most peripheral (40-80%) collision, 5% for the mid-central collisions (10-40%) and 0 for the most central (0-10%) collisions. The next one source coming from the bin shift correction, there are several functions can be used for the bin correction such as the levy function and fonll function, the difference between these two methods are quoted as one of the systematic source. The last source is by varying the topological cuts and daughter p_t cuts. The standard TMVA cuts, the 50% efficiency and 150% efficiency cuts are calculated, and also the daughter p_T cuts are scanned from 300 MeV, 400 MeV and 500 MeV. The difference between the corrected yield are quoted as the systematic source.

Table 3.8 shows the D^0 spectrum different sources contribution in the most central 0-10% centrality. As we see, the systematic uncertainties is quite small in the most of the p_T range except the first two and last two p_T ranges due to the limited statistics and large contribution from yield extraction.

For the R_{AA} results shown in Figure 6.3, they share the most of the systematic uncertainties with the spectrum, but for the TPC part, the TPC contribution from Au+Au

and p+p collisions can be canceled out. The black bracket only represented the uncertainties from Au+Au.

Table 3.8: Systematic uncertainties from different sources

p_T range	Yield extra	Embedding	fast-simu	Topo Scan	bin shift	daughter p_T	total
0.0 - 0.5	0.28575	0.06	0.05	0.150186	0.206038	0.0961785	0.402506
0.5 - 1.0	0.276043	0.06	0.05	0.124592	0.0641394	0.104796	0.336034
1.0 - 1.5	0.0332581	0.06	0.05	0.08445	0.0416632	0.0354619	0.131648
1.5 - 2.0	0.0284874	0.06	0.05	0.0430791	0.0179911	0.013235	0.096261
2.0 - 2.5	0.0152306	0.06	0.05	0.0597399	0.00416767	0.00651388	0.0998029
2.5 - 3.0	0.0173818	0.06	0.05	0.0762663	0.00261387	0.00930911	0.11096
3.0 - 3.5	0.0164046	0.06	0.05	0.0368647	0.00551249	0.0177607	0.0898551
3.5 - 4.0	0.0301197	0.06	0.05	0.0712203	0.00646695	0.0237711	0.112634
4.0 - 5.0	0.0736611	0.06	0.05	0.0615253	0.0312138	0.0214862	0.129411
5.0 - 6.0	0.0751424	0.06	0.05	0.11637	0.0261331	0.0226671	0.162742
6.0 - 7.0	0.0944053	0.06	0.05	0.0465479	0.0210969	0.00687676	0.132934
7.0 - 8.0	0.0730125	0.06	0.05	0.409901	0.0169993	0.00289802	0.423966
8.0 - 10.0	0.0984801	0.06	0.05	0.696775	0.048144	0.061042	0.712276

3.8 Other Systematics for the Fast-Simulation

In the Fast-Simulation section 3.5.5.1, we have two more assumptions which were not answered yet. Here we are trying to discuss a little bit in the following part.

3.8.1 Secondary Track Contribution

The Fast-Simulation is validated with primary track in the procedure Fig. 3.56. All the tracks for HFT matching ratio and Dca inputted to Fast-Simulation is primary track. Based on the Hijing sample we can study the secondary track contribution since in the real data part we can't distinguish primary track and secondary track. In Hijing simulation, we use the start vertex of that track to determine whether it's primary track or secondary track.

Fig. 3.71 shows the pions vertex distributions from the secondary decay. The first one is the overall secondary pion vertex distributions and we can clearly saw some HFT structure. Top right panel is pions decayed from GeantID==8/9 (which is $\pi^{\pm}$), this part is the knocked out particles with HFT. The bottom left is pion decayed from GeantID==15/25 (which is anti-proton and anti-neutron), this is the normal annihilation particles. The last one bottom right shows the pions decayed from other source.

The secondary track have kind of different performance compare to the primary track such as the HFT match ratio shown on Fig. 3.72. The solid circle is the inclusive

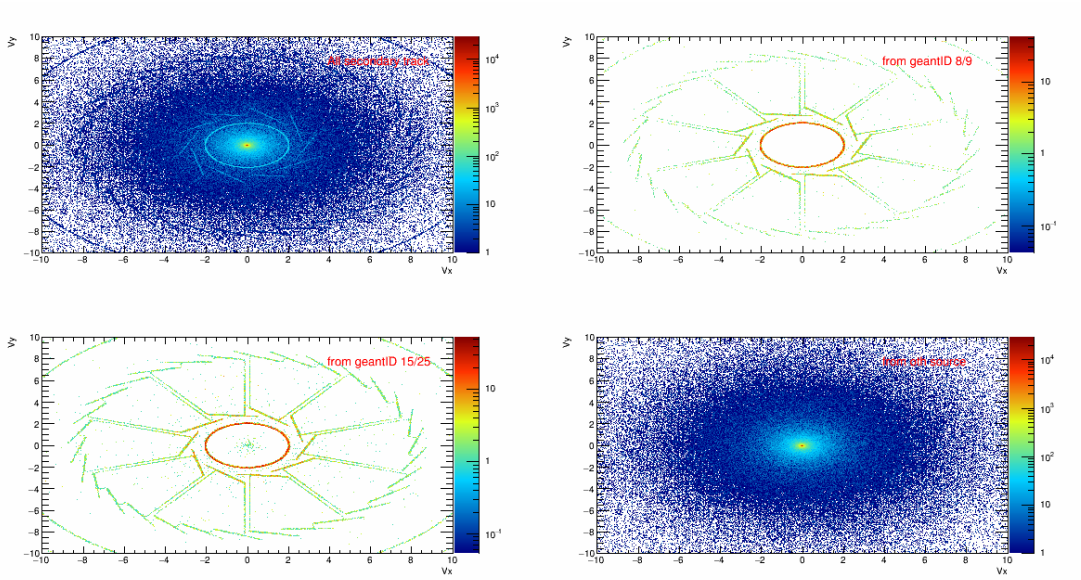

Figure 3.71: The vertex distribution for Pions from secondary decay. Top left is the overall secondary pion tracks, top right is pion decayed from GeantID=8/9 (which is $\pi^{\pm}$), bottom left is pion decayed from GeantID=15/25 (which is anti-proton and anti-neutron), bottom right is decayed from other source

one for HFT matching ratio, the empty circle is for the primary pions and the solid square is for the secondary pions. All these HFT match ratios are after applying exactly the same cut as real data analysis. The low match ratio for secondary track is reasonable since they are decayed far away from the vertex and most of them do not have three HFT hits. The more contribution from the secondary track, the more difference we observed between inclusive one and primary one. The bottom panel shows the HFT matching double ratio of inclusive one over primary one. For the pions, since the secondary pion have some contributions, we do saw the different between primary one ans inclusive one at some certain p_T range for this HFT match ratio. For the kaons, the relative secondary contribution is small, that's why there is no big difference between primary and inclusive ones as see on Fig. 3.73.

This secondary track contribution for our efficiency correction need to be take care, especially for Pions. There are a few percent contributions from our Hjing simulation study. In our real data efficiency correction, we took this double ratio from Hijing as an additional correction factor for the HFT matching ratio, since the data part can only obtained the inclusive one. After this additional correction, we still be able to obtain the precision like Fig. 3.61.

For the secondary track Dca contributions, we tested with the inclusive track Dca or primary track Dca. In principle, with the inclusive tracks, they should have slightly broader distributions. But in our test, it seems that these contributions to the final D^0

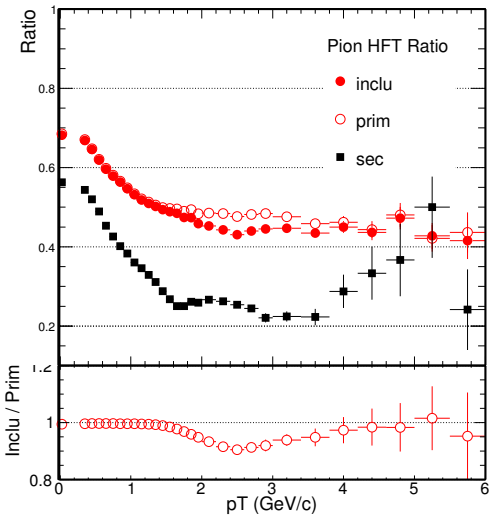

Figure 3.72: HFT Matching Ratio for Pions, compare between primary track and secondary tracks relay on Hijing. (bottom) The double ratios of inclusive one to primary tracks.

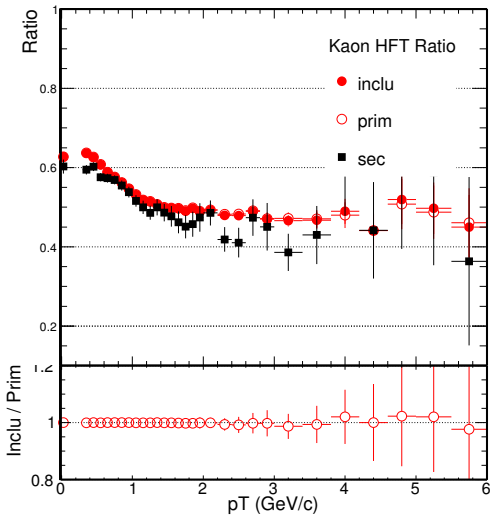

Figure 3.73: HFT Matching Ratio for Kaons, compare between primary track and secondary tracks relay on Hijing. (bottom) The double ratios of inclusive one to primary tracks.

efficiency is really small. This maybe due to the limited Hijing statistics or the slightly Dca difference does not contribute much. But in our real data case, we do not take this secondary Dca contributions as additional correction factor yet.

3.8.2 Vertex Resolution Contribution

As seen in the previous section **??**. The vertex resolution in peripheral events still have some contributions. If those peripheral events vertices are out of hundreds or dozens of μ m vertex resolution, they are not likely to contribute to the D mesons foreground (maybe not even the background). To correctly count the number of peripheral events we need to understand the vertex resolution. The 2D Dca_{XY} Dca_{Z} distributions are the only input to the Fast-Simulation for this effect. They contain both the vertices and tracks contribution.

To solve this problem, we need to unfold the vertex resolution from 2D Dca distributions, and this is not straightforward since the vertex resolution contribution could be in the same order of the Dca resolution and this is not reliable (subtracting two numbers that are close to each other have very large uncertainties). There is another way we can relay on to obtain this correction factor, which is the Minimum Bias Hjing simulation sample. From Hijing sample we know the true efficiency for any centrality species, and from the Fast-Simulation we can obtain the efficiency including those vertex effect. The difference can be took as the additional correction factor for real data analysis if this effect is not too big. The Hijing sample is still ongoing production, this need a huge data sample for the study and it's time consumption at this moment.

Chapter 4 Λ_c Analysis Details

4.1 Data Set and Event Selections

The data set used in this Λ_c analysis is also from Au+Au collisions at $\sqrt{s_{NN}}$ = 200 GeV from RHIC run year 2014 (Run14), the same data set as the D^0 analysis.

The event selection criterion for Λ_c analysis can be found from Table 4.1, they are the same as D^0. After event selection, ~875 million Minimum Bias events are used for this analysis. The centrality definition is the same as in D^0 since they are the same data set (See section 3.3).

Table 4.1: Event selection in Au+Au collisions at 200 GeV for Λ_c.

Event Selection Criteria
$!(\|V_x\| == 0$ && $\|V_y\| == 0$ && $\|V_z\| == 0)$
$\|V_z\| < 6$ cm
$\|V_r\| < 2$ cm
$\|V_z - V_z^{VPD}\| < 3$ cm

4.2 Λ_c Reconstruction

Λ_c^+ and $\overline{\Lambda}_c^-$ are reconstructed through the typically hadronic channel $p(\bar{p})K^{\mp}\pi^{\pm}$. From the latest PDG, Λ_c have four different decay channels, including one non-resonance channel and three resonance channels shown below [8]:

In total, $\Lambda_c^+ \to p^+K^-\pi^+$ ($\sim 6.35\%$) :

- $\Lambda_c^+ \to p^+K^* \to p^+K^-\pi^+$ (1.98%*66.7%=1.32%)
- $\Lambda_c^+ \to \Delta^{++}K^- \to p^+K^-\pi^+$ (1.09%*100%=1.09%)
- $\Lambda_c^+ \to \Lambda(1520)\pi^+ \to p^+K^-\pi^+$ (2.2%*22.5%=0.495%)
- Non-resonance 3.5%

In the following, we will describe the daughter selection, the geometry cuts and how they are obtained through the TMVA tuning. We will also show the Λ_c signals for different p_T and centrality bins.

4.2.1 Daughter Selection

Our interested Λ_c have a proper decay length of $c\tau \sim 60\mu$m. This is a much shorter distance compare to D^0 $c\tau \sim 123\mu$m and D^+ $c\tau \sim 312\mu$m [8]. The global tracks including the global momentum for daughter tracks are used in this analysis. The daughters transverse momentum are required to ≥ 0.5 GeV/c to ensure that the track can pass through the TPC and have less HFT miss matching and also less combinatorial backgrounds in our interested Λ_c transverse momentum range, the number of hit points (nHitsFit) along the track is ≥ 20 (of a maximum of 45) to ensure good momentum resolution.

The pion, kaon and proton tracks are identified by combining TPC and TOF. The TPC provides particle identification utilizing the energy loss information dE/dx, and TOF provides velocities information for PID. For kaon and proton PID, we always require TPC and TOF. But for pion, only require TOF when TOF is available.

In summary, next list all the related track selections for Λ_c daughters including track quality cut and particle identification cut.

- global tracks
- $p_T > 0.5$ GeV/c
- $|\eta| < 1$
- $nHitsFit \geq 20$, in TPC
- at least one hit in every layer of PXL and IST

pion PID:

- $|n\sigma_\pi| < 3.0$, based on TPC dE/dx
- If TOF is available (hybrid PID): $|\frac{1}{\beta} - \frac{1}{\beta_{exp}}| < 0.03$

kaon PID:

- $|n\sigma_K| < 2.0$, based on TPC dE/dx
- $|\frac{1}{\beta} - \frac{1}{\beta_{exp}}| < 0.03$

proton PID:

- $|n\sigma_p| < 2.0$, based on TPC dE/dx
- $|\frac{1}{\beta} - \frac{1}{\beta_{exp}}| < 0.03$

4.2.2 Topological Cut Optimization

The secondary vertex is reconstructed with selected kaon, pion and proton global tracks. In this analysis, we have three of the middle point on the Distance of the Closest Approach (DCA) between two daughter tracks since we have 3 daughters in total. The average of these three middle points of Dca is considered as the secondary decay vertex of the candidate Λ_c. As shown in Fig. 4.1, 6 geometrical variables are chosen to select Λ_c and reject combinatorial background, which is dominated by a triple of tracks directly from the primary vertex: decay length (the distance between the decay vertex and Primary Vertex PV), the maximum DCA between the 3 daughters, the back pointing angle cos(θ) which is the angular of Λ_c momentum and the decay vertex relative to the primary vertex, DCA between the π track and PV, DCA between the K track and PV and DCA between the p track and PV. The cuts on these variables are optimized by the Toolkit for Multivariate Data Analysis (TMVA) package [90]. They are optimized in order to have the best significance in the covered p_T range. Additionally there is a Λ_c Dca to primary vertex cut to make sure the Λ_c candidate is from prompt decay.

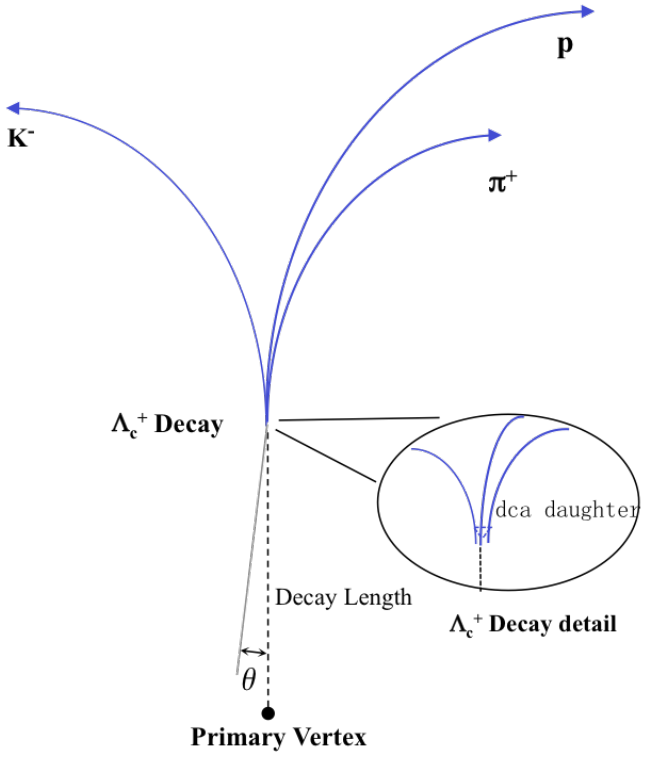

Figure 4.1: The topology of a Λ_c decaying to a kaon, pion and a proton.

The TMVA for Λ_c need signal and background samples input for training. The signal sample is obtained from data-driven Fast-Simulation method similar as D^0 and the background sample is from real data wrong-sign pairs in the Λ_c mass window.

In the Fast-Simulation for Λ_c signals, the MC Λ_c decays, and then the daughters' momentum and position are smeared according to detector response. All those Λ_c daughters efficiency includes TPC efficiency, HFT matching efficiency and Topological cuts efficiency are considered. Similar as D^0, for some other selection methods rather than cuts, the TMVA could be trained to identify Λ_c according to kinetic information like invariant mass rather than geometry information due to the decay. This will create a fake signal, which is not what we want. To avoid this, a mass that has the same distribution with the background sample for TMVA training is assigned to Λ_c in the data-driven fast-simulation. The simulation use flat p_T input. When used for TMVA training, the entries after detector acceptance and efficiency are weighted by a function fit to the measured D^0 p_T spectrum (assume Λ_c and D^0 have similar shape), and the yield is scaled to an expected value for the whole data set.

Fig. 4.2 shows distributions of the 6 geometry variables for signal (blue) and background (red) plotted by the TMVA, for candidates $p_T \geq 3$ GeV/c.

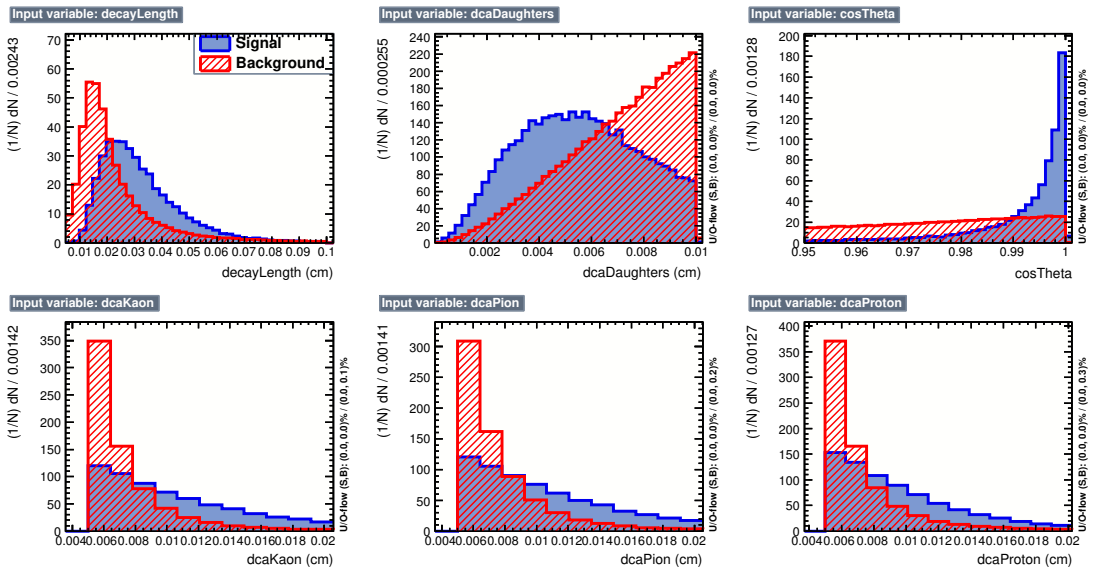

Figure 4.2: Distributions of the 6 geometry variables for Λ_c signal (blue) and background (red).

The 'cuts' option of TMVA is used to tune Λ_c cuts. This option randomly sample different cut sets in the variable space, calculate signal and background efficiency for each cut set. Then chooses one cut set with lowest background efficiency for a certain 1% signal efficiency bin. We can then pick the cut set with the best significance according to the signal and background yield corresponding to the whole data set. Fig. 4.3 shows the lowest background efficiency, significance and so on vs. signal efficiency for $p_T \geq 3$ GeV/c. As cuts get tighter, signal and background efficiency both decrease, but background efficiency decrease much faster. After several iterations as discussed before, the best significance is around signal efficiency of $\sim$38%.

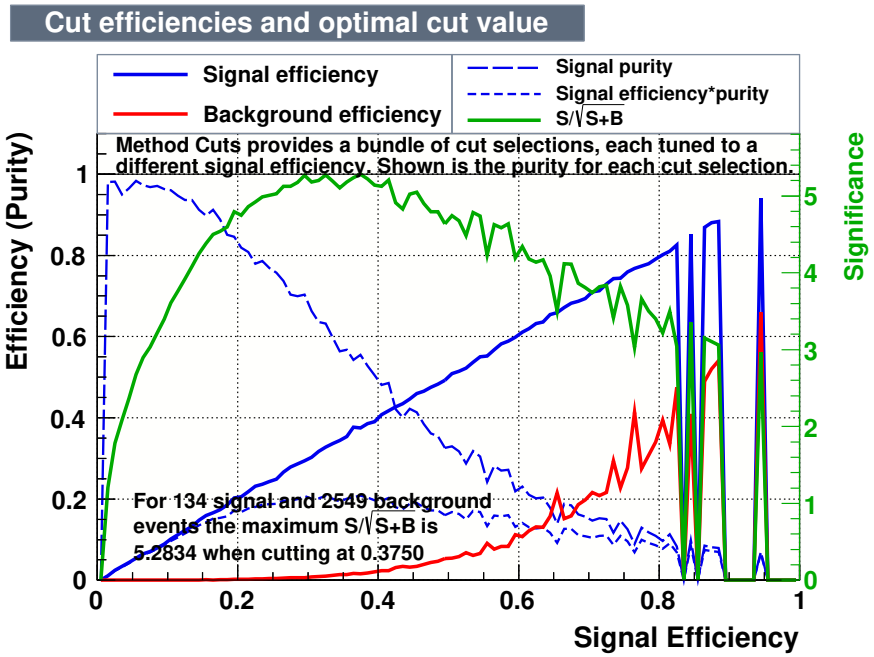

Figure 4.3: Signal efficiency, lowest background efficiency, significance and so on vs. signal efficiency.

Table 4.2: Default Geometrical cuts for Λ_c $p_T \geq 3$ GeV/c.

Λ_c p_T (GeV/c)	$\geq$3
daughter p_T (GeV/c) $>$	0.5
decay length (μm) $>$	250
max DCA between 2 daughters (μm) $<$	50
DCA between Λ_c and PV (μm) $<$	100
DCA between π and PV (μm) $>$	80
DCA between K and PV (μm) $>$	75
DCA between p and PV (μm) $>$	65

The result of the geometry cuts tuned for best significance are shown in Table 4.2. These are the default cuts used in the Λ_c reconstruction to calculate the spectra central value. For the Λ_c systematics estimation, another 2 sets of geometry cuts are tuned with TMVA, with slight different signal efficiency relative to the default cuts. These 2 cuts sets are listed in Table 4.3 and 4.4. The cuts are not changed too much since the total significance is only $\sim 5\sigma$, we need to make sure obtain a relative good signals for all these topology cuts. There is not too much room to play with the topological cuts.

4.2.3 Λ_c Signals

For the Λ_c reconstruction, we have three daughter particles, which means in total have 8 charge combinations. Two of them have the right charge sign for signals

Table 4.3: Loose Geometrical cuts for Λ_c $p_T \geq 3$ GeV/c.

Λ_c p_T (GeV/c)	$\geq$3
daughter p_T (GeV/c) $>$	0.55
decay length (μm) $>$	234
max DCA between 2 daughters (μm) $<$	50
DCA between Λ_c and PV (μm) $<$	100
DCA between π and PV (μm) $>$	65
DCA between K and PV (μm) $>$	96
DCA between p and PV (μm) $>$	75

Table 4.4: Another Loose Geometrical cuts for Λ_c $p_T \geq 3$ GeV/c.

Λ_c p_T (GeV/c)	$\geq$3
daughter p_T (GeV/c) $>$	0.6
decay length (μm) $>$	150
max DCA between 2 daughters (μm) $<$	50
DCA between Λ_c and PV (μm) $<$	100
DCA between π and PV (μm) $>$	65
DCA between K and PV (μm) $>$	96
DCA between p and PV (μm) $>$	75

and the other 6 have wrong signs for background. The wrong-sign (like-sign) methods here can statistically describe the background to the foreground when studying particle reconstruction with three times statistics precision.

Fig. 4.4 shows the invariant mass distribution for the foreground and wrong-sign backgrounds: same event wrong-sign method in the p_T range 3-6 GeV/c from 0-80% centrality. The red points are foreground and the grey points are wrong-sign backgrounds, the wrong-sign backgrounds are directly scaled down by a factor of 1/3, and it shows very good agreement to the foreground. As we can clearly observe the Λ_c signals with the significance $\sim$4.7.

Fig. 4.5 shows the Λ_c signals in the p_T range 3-6 GeV/c from 10-80% centrality. Red points are foreground and grey points are wrong-sign backgrounds after scale. The Λ_c signals with the significance $\sim$5.4, larger than Fig. 4.4. As we know in the most central collisions, the multiplicity is large, even though the most central collisions contribute some Λ_c signals but at the same time the combinatorial backgrounds contribution is also huge. That's the reason after removing the most central 0-10% centrality, the Λ_c significance is even better compare Fig. 4.5 to Fig. 4.4.

Fig. 4.6 shows the Λ_c signals in the p_T range 3-6 GeV/c from the peripheral 40-80%

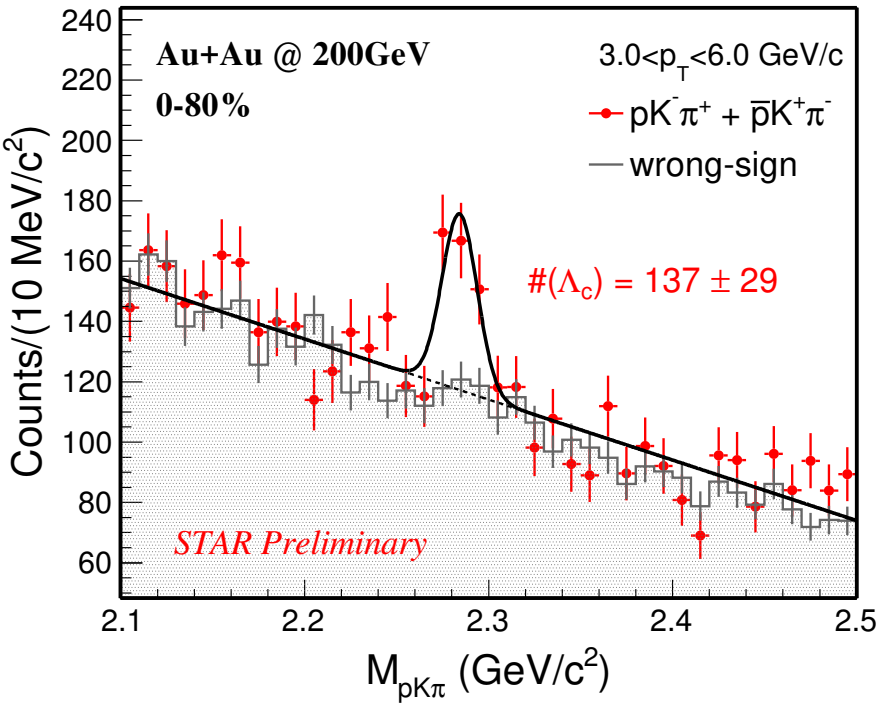

Figure 4.4: Λ_c invariant mass distribution for foreground (red) and wrong-sign background (grey) in $3 < p_T < 6$ GeV/c at 0-80% centrality.

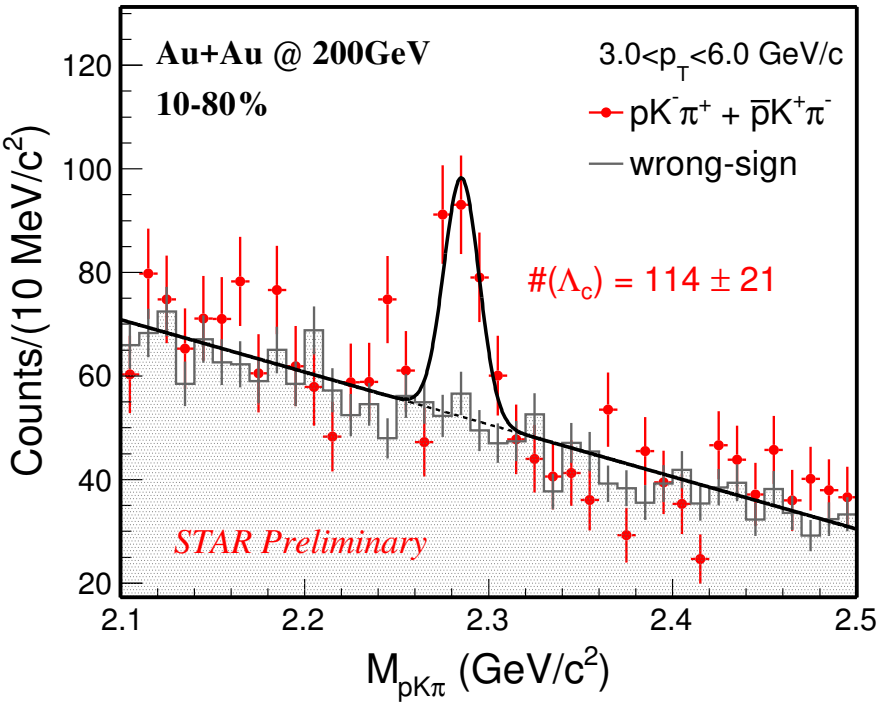

Figure 4.5: Λ_c invariant mass distribution for foreground (red) and wrong-sign background (grey) in $3 < p_T < 6$ GeV/c at 10-80% centrality.

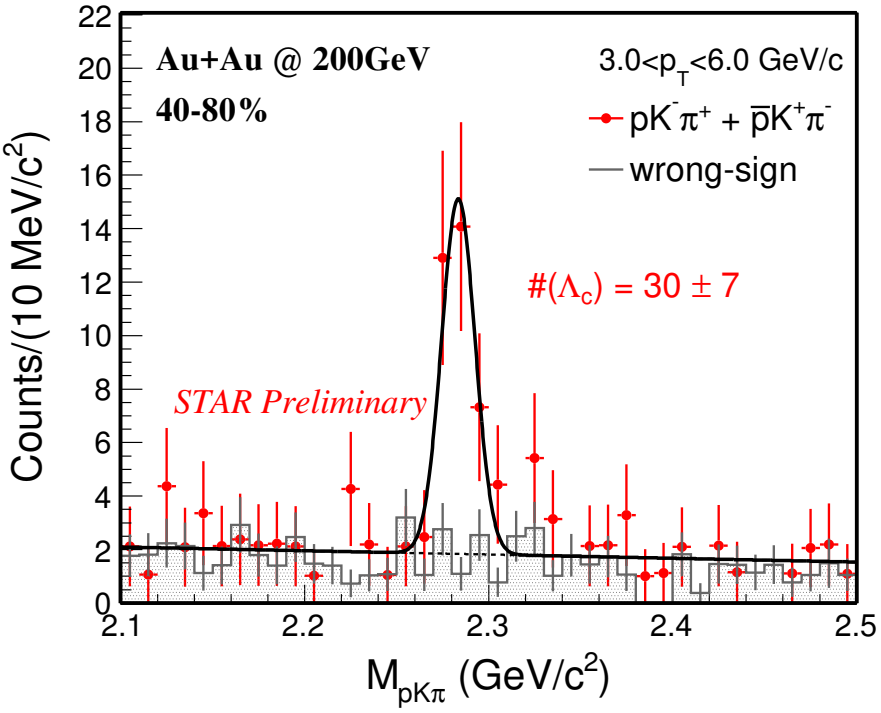

Figure 4.6: Λ_c invariant mass distribution for foreground (red) and wrong-sign background (grey) in $3 < p_T < 6$ GeV/c at 40-80% centrality.

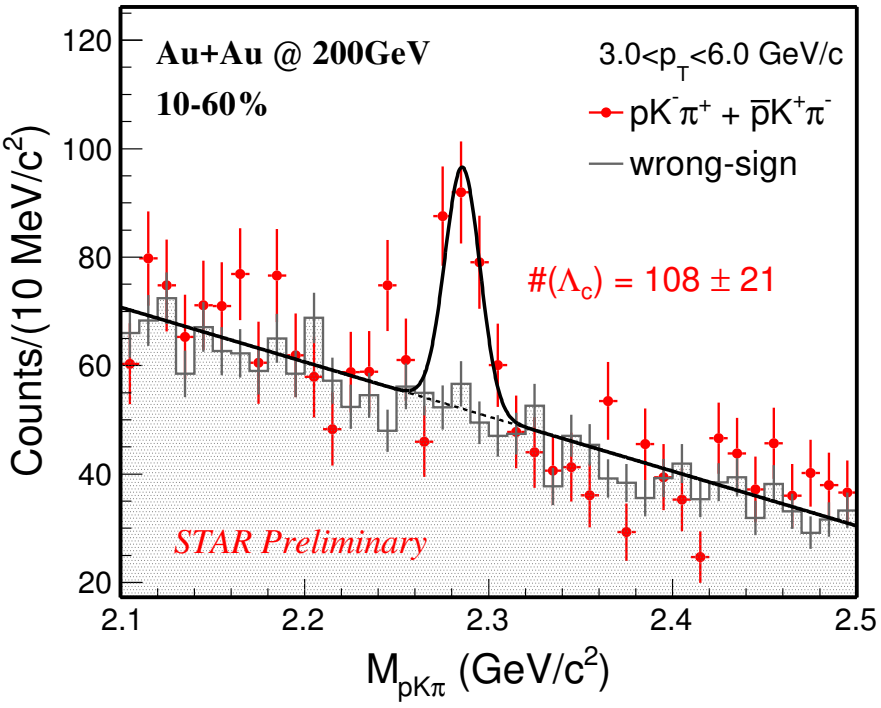

Figure 4.7: Λ_c invariant mass distribution for foreground (red) and wrong-sign background (grey) in $3 < p_T < 6$ GeV/c at 10-60% centrality.

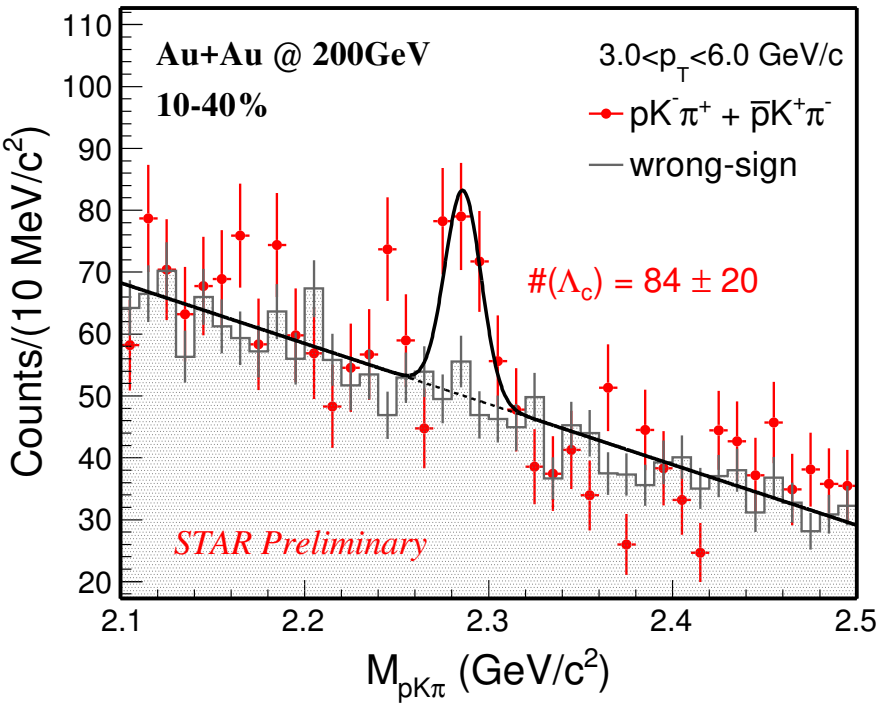

Figure 4.8: Λ_c invariant mass distribution for foreground (red) and wrong-sign background (grey) in $3 < p_T < 6$ GeV/c at 10-40% centrality.

centralities. Still the wrong-sign method after scaling can well describe the background. The Λ_c signals with the significance $\sim$4.2. As we know in the most peripheral collisions, the vertex resolution would play a role for the data-driven Fast-Simulation efficiency correction. That's the reason our corrected spectra was relay on the p_T range 3-6 GeV/c from the mid-central and mid-peripheral 10-60% centralities as shown on Fig. 4.7. The significance was around $\sim$5.2. For the 10-40% centrality, the Λ_c signals was shown on Fig. 4.8, and the significance is less 5σ.

4.3 Λ_c Efficiency and Acceptance Corrections

To obtain the real invariant mass spectrum of Λ_c within STAR acceptance, the raw spectrum should correct for the efficiency. The p$K\pi$ pair efficiency within STAR acceptance is evaluated by folding the TPC related efficiency to the HFT related efficiency similar as we did for D^0 shown on Eq. 3.11. For the TPC related tracking efficiency use STAR standard Full GEANT simulation. For the HFT related efficiency which reflect to HFT acceptance and topological cuts, we still use the 'Data-Driven Fast simulation' as developed for Λ_c.

4.3.1 Single Track Efficiency

Comparing with D^0, Λ_c have one more track which is proton (or anti-proton). The single track efficiency losses for proton have two contributions, the detector inefficiency and particle identification cuts. The detector efficiency includes the TPC tracking efficiency (ε_{TPC}) and the TOF matching efficiency (ε_{TOF}). The particle identification cut efficiency (ε_{PID}) includes the efficiencies of TOF velocity ($1/\beta$) and the dE/dx selection cuts. So the single track efficiency for proton still can be derived by the Eq. 3.15

4.3.2 TPC Tracking efficiency

The TPC tracking efficiency for proton (ε_{TPC}) is evaluated via the standard STAR embedding technique. TPC efficiency including two parts, TPC response and acceptance efficiency. Similar as we did for pion and kaon, the TPC tracking efficiency for proton is derived by taking the ratio of the number of reconstructed MC tracks (N_{rec}), satisfying the track quality cuts used in the data analysis, over the number of embedded MC tracks (N_{emb}), as shown in Eq. 3.16

The TPC tracking efficiency for proton and anti-proton in Run14 Au+Au collisions at 200 GeV is shown below. Fig 4.9 and 4.10 shows the TPC tracking efficiency for proton and anti-proton from four different classifications, from up to down, the centrality is change from the most peripheral to most central collision. As we see, in the most central top 0-5% collisions, due to the large occupancy the TPC tracking efficiency is much lower for the central events. Fig. 4.10 shows the same plot for anti-proton. The anti-proton can be annihilate with the materials, that's the reason the TPC tracking efficiency is slightly lower for anti-proton.

4.3.3 TOF Matching Efficiency

For the Λ_c analysis, as we discussed in the daughter selection section 4.2.1. For kaon and proton PID, TOF is always required. For pion we use the hybrid TOF PID.

Fig. 4.11 shows the TOF match efficiency in Run14 Au+Au collisions at 200 GeV for positive charge particles including p^+ in the centrality 0-10%. Fig. 4.12 shows the same plots for negative charge particles in the centrality from 40-80%. For the proton TOF match efficiency, we also observed some deep for the TOF match efficiency at the certain p_T range. Similar as we observed for kaon in the p_T around 0.6 GeV/c, the protonp_T range was around 1.5 GeV/c. This effect was found due to the hadron contaminations as we discussed before in section 3.5.3.

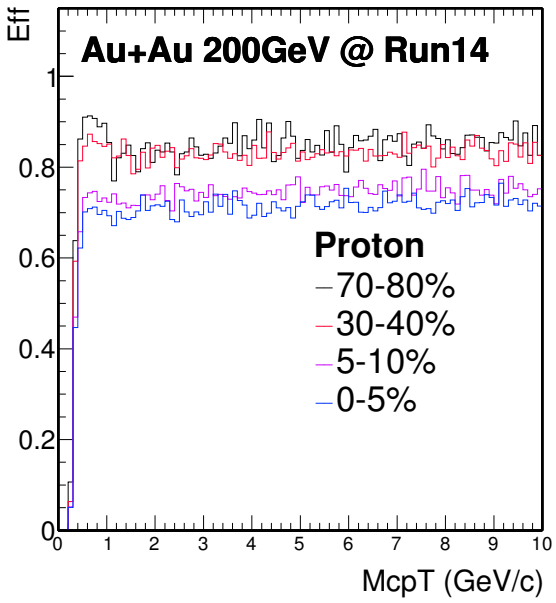

Figure 4.9: TPC tracking efficiency in Run14 Au+Au collisions at 200 GeV for Proton.

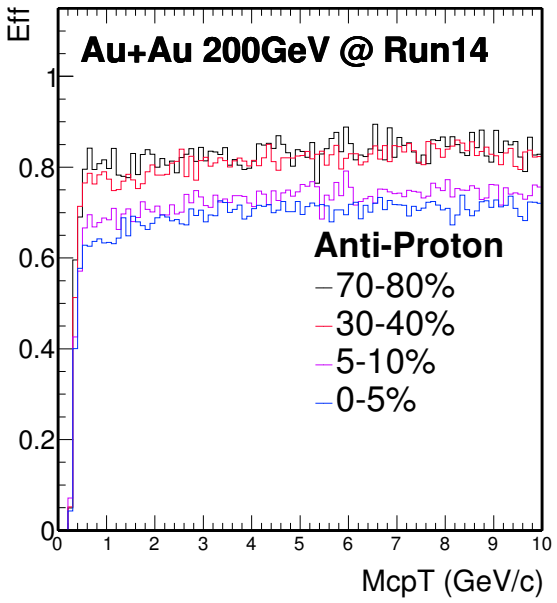

Figure 4.10: TPC tracking efficiency in Run14 Au+Au collisions at 200 GeV for AntiProton.

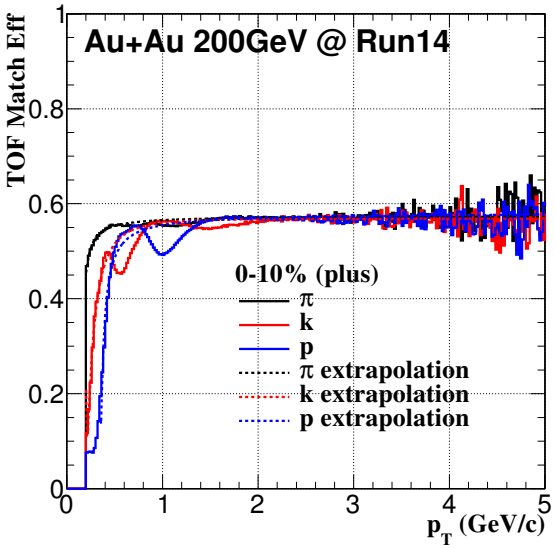

Figure 4.11: TOF match efficiency in Run14 Au+Au collisions at 200 GeV for positive charge particle in 0-10%.

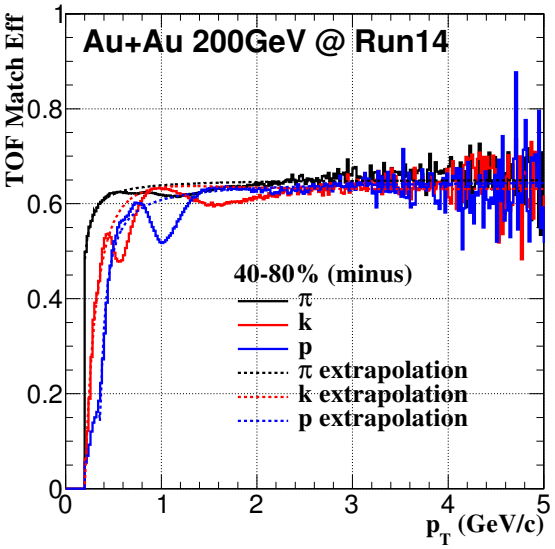

Figure 4.12: TOF match efficiency in Run14 Au+Au collisions at 200 GeV for negative charge particle in 40-80%.

4.3.4 PID Cut Efficiency

The particle identification cut efficiency (ε_{PID}) includes two components: the TOF velocity ($1/\beta$) cut efficiency and dE/dx cut ($n\sigma_{K/\pi/p}$) efficiency. Pure protons sample are used to evaluate the TOF velocity cut efficiency and TPC $n\sigma_p$ cut efficiency. Fig. 4.13 shows the πp pairs invariant mass distributions. The black line is the unlikesign foreground, and the red line is background using likesign method. With this Λ candidates, we can statistical extract the pure proton sample for the PID efficiency study.

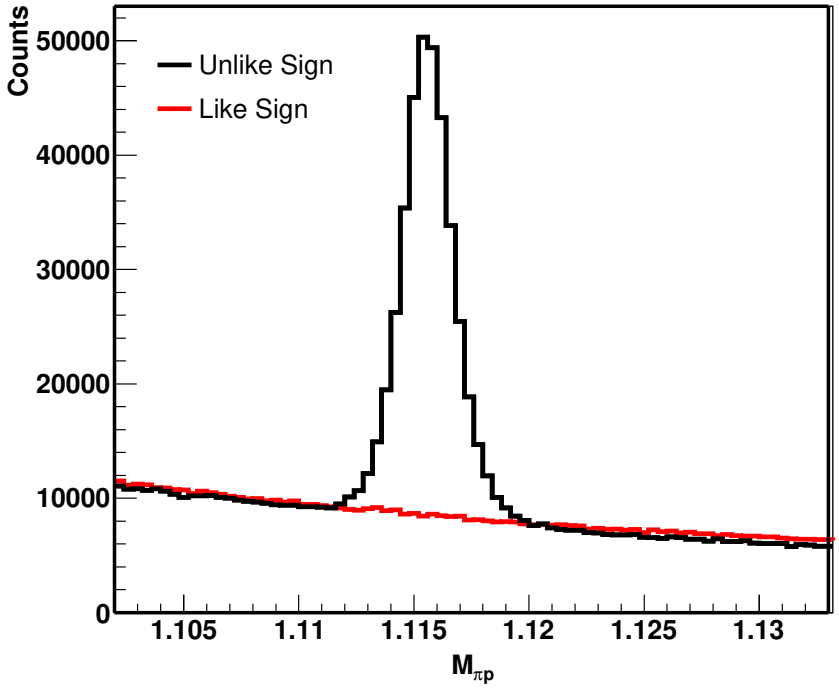

Figure 4.13: The πp pairs invariant mass distributions. The black line is the unlikesign foreground, and the red line is background using likesign method.

The $n\sigma_p$ cut efficiency is derived from the Gaussian fit using those pure proton samples. Similar as pion and kaon, the $n\sigma_p$ distributions are fitted with Gaussian function, the mean and sigma value are extracted. With assuming they follow the Gaussian function, then the $n\sigma_p$ cut efficiency in Run14 Au+Au collisions at 200 GeV for protons are obtained as shown on Fig. 4.14.

The $1/\beta$ cut efficiency is also derived from the Gaussian fit using those pure proton samples. Similar as pion and kaon, the efficiency for proton is shown on Fig. 4.15 .

4.3.5 Data-driven Fast Simulation for HFT and Topological Cut Efficiency

As discussed in the section 4.3, the HFT related efficiency shown on Eq. 3.11 including two items: HFT acceptance and topological cuts. We also used the 'Data-

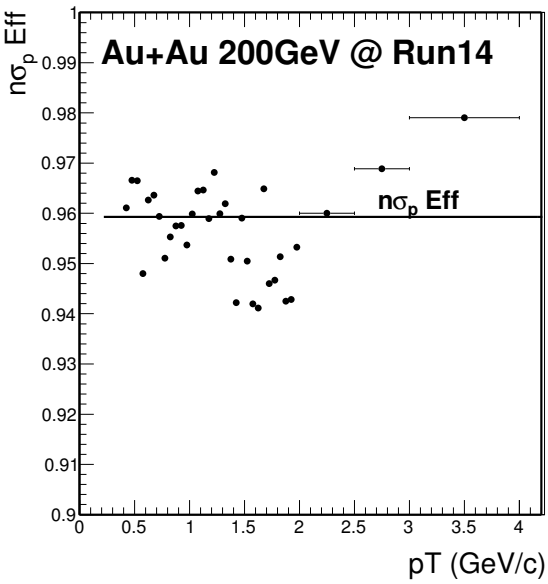

Figure 4.14: $n\sigma_p$ cut efficiency along with momentum. Line is the fitted polynomial function.

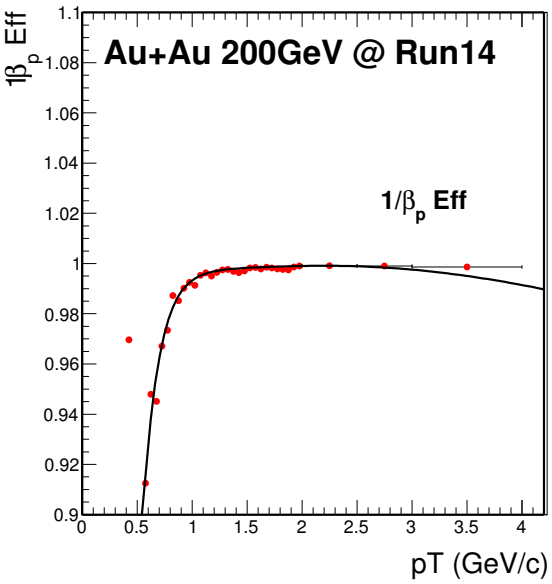

Figure 4.15: $1/\beta$ cut efficiency along with momentum for proton. Line is the fitted function.

Driven Fast simulation' for the Λ_c efficiency correction. And later on we will also validate this method for Λ_c with full GEANT simulation.

4.3.5.1 Ingredients

The only difference for Λ_c ingredients compare to D^0 is proton tracks. Just similar as D^0, we extract the TPC tracking efficiency, HFT match ratio and 2D $\mathrm{DCA_{XY}}$ - $\mathrm{DCA_Z}$ distributions for pion, kaon and proton.

All these distributions will be used as input for the Λ_c efficiency correction with data-driven Fast-Simulation method.

4.3.5.2 Λ_c Efficiency and Topological Distribution

Similar recipe as we discussed for D^0 in section 3.5.5.3, we obtain the efficiency step by step as shown on Fig. 4.16. First we have the TPC efficiency shown by red maker which is after the p_T, η acceptance cut and TPC tracking efficiency from embedding. Then, after folding in the HFT matching efficiency, the second item is obtained on black circle. Next step is fold in the PID efficiency. Last step is after the topological cut, as shown by the cyan marker. As see, the topological cut efficiency is really small due to the tight cut since the combinatorial background is huge, we do need this kind of tight cuts.

We study all the efficiencies with small centrality bin width, in total we have 9 centrality bins from our StRefmultCorr class. Similar as we did for D^0, the final efficiencies for the wider centrality bins 0-40%, 40-80% and 10-60% are calculated using

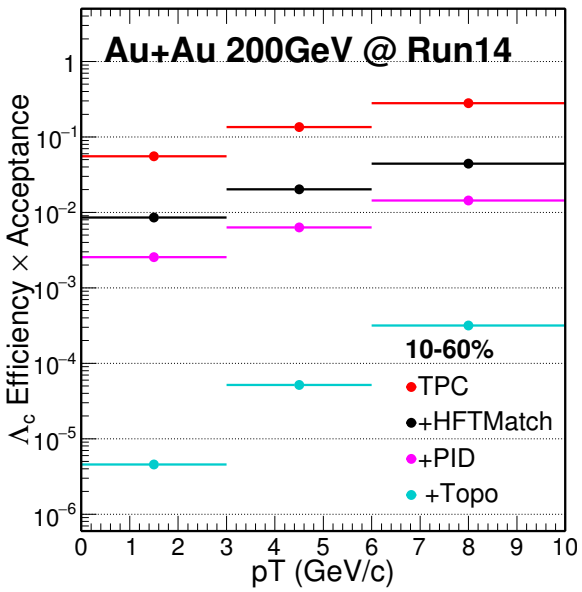

Figure 4.16: Λ_c efficiency step by step from TPC, HFT Ratio, Topological cut in 10-60%.

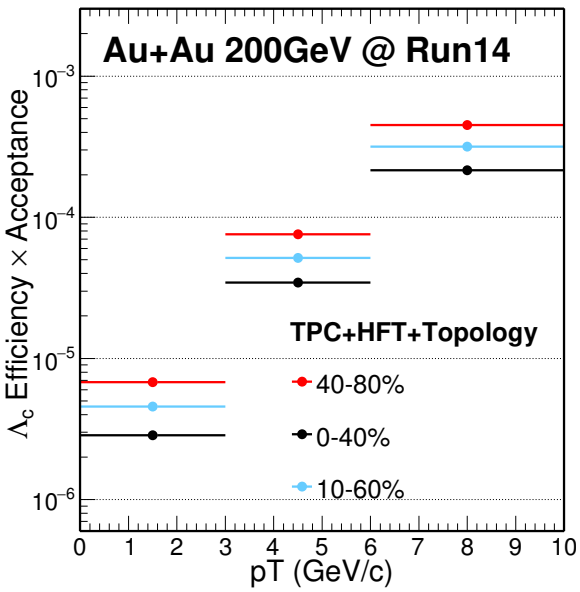

Figure 4.17: Λ_c efficiency including TPC, HFT and Topological cut in several centralities.

N_{bin} as weights. Fig 4.17 shows the Λ_c efficiency for 3 wide centralities after TPC, HFT match and Topological efficiency included.

The Data-Driven Fast-Simulation also provide the topological information, can be used for the comparison with real data. But for the real data part, within the limited Λ_c signals, it's impossible to do this kind of comparison as we did for D^0.

Even though the comparison of topological variables between real data and Fast-Simulation is impossible. We still need to validate and make sure the data-driven Fast-Simulation package works fine for Λ_c. Then the Hijing method we used before will be crucial for Λ_c and will be discussed in the following section.

4.4 Validation Data-Driven Fast-Simulation with Full GEANT + Hijing Simulation

The Hijing sample was run through the Full Hijing + GEANT simulation with realistic pileup hits (UPC+MB) in PXL and sensor masking tables. They can provide reasonable performance for the HFT matching ratio and Dca resolution.

In total, we have ∼145K 0-10% most central Hijing events, and for each event is embedded with 20 Λ_c's. So in total, we have ∼2.88M Λ_c for this Hijing sample. The embedded Λ_c has small effect on the tracking since the multiplicity is much higher compared to 20 × 3 Λ_c' decayed daughters.

The performance of these Λ_c Hijing sample is quite similar as D^0 Hijing samples since all the set up is the same except the embedded Λ_c. And as we discussed before, the embedded Λ_c have very small impact on the Hijing performance. The HFT matching

ratio and Dca comparisons between data and Hijing samples in Au+Au 200 GeV/c from 0-10% centrality, can be found in the previous sections Fig. 3.54 and Fig. 3.55

4.4.1 Validation Procedures

The idea for this Hijing validation is the same as we did before for D^0 in section 3.6.2, we produced the enriched Λ_c Hijing samples. After run through the detector and full GEANT simulation, the Λ_c efficiency and topological variables distributions can be extracted. Another procedure is extract the necessary ingredients from Hijng sample for the Fast-Simulation input (Fast-Simulation with Hijing input). Then run through the Fast Simulation for Λ_c, as discussed before, the Λ_c efficiency and topological variables are also available in this way and can be compared to the first Hijing + GEANT procedure. The workflow is shown in Fig. 4.18.

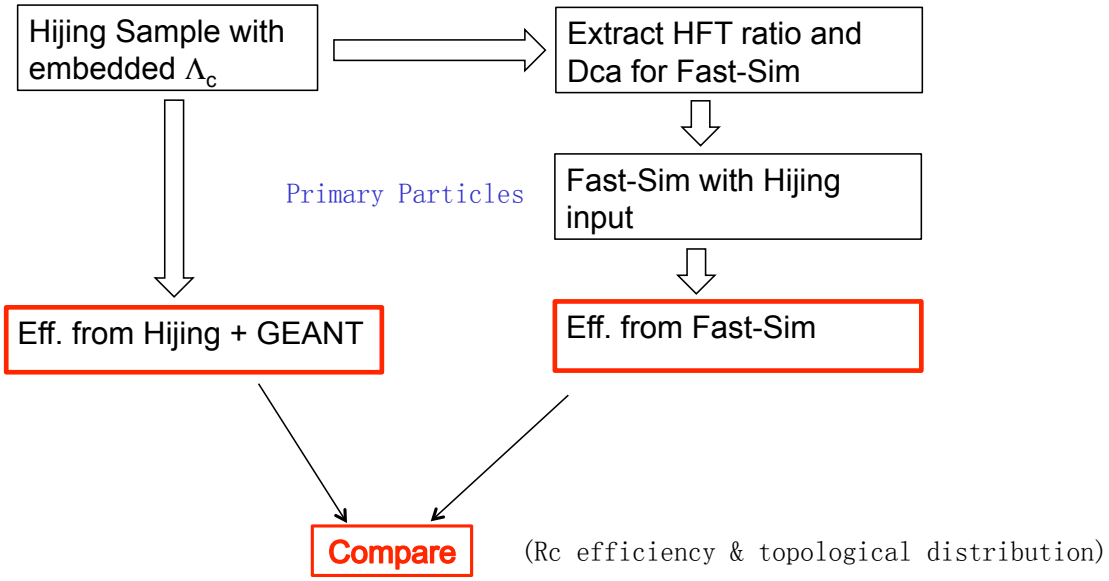

Figure 4.18: Hjiing validation procedure and workflow for Λ_c.

4.4.1.1 Validation Efficiency

The first step is to check the kinematic form different MC decayer such as PYTHIA, Hijing, evtGen and PhaseSpace class from ROOT. Before the validation we need to make sure the decayer used for Fast-Simulation has the same kinematic as the Hijng since Λ_c have 4 different decay channels. After the basic acceptance cut, such as Λ_c |y| < 1, daughter p_T > 0.5 GeV/c and $|\eta|$ <1 cut. Λ_c has different kinematic decay performance from different channels as shown in Fig. 4.19 left panel, the right panel shows the double ratio to evtGen PHSP (non-resonance, phase space). As seen the Hijng decayer follow the same trend as evtGen PHSP, but not the others such as Δ^{++}, K^* and $\Lambda(1520)$ channels. From the PYTHIA decayer, they only provide the Δ^{++} and K^* channels, the

other two channels are not included yet. So, for our Fast-Simulation decayer we choose evtGen PHSP channel for this Hijing validation. But for our real data analysis, we use evtGen but included all these 4 decay channels which depicts as 'evtGen combine' in the plots.

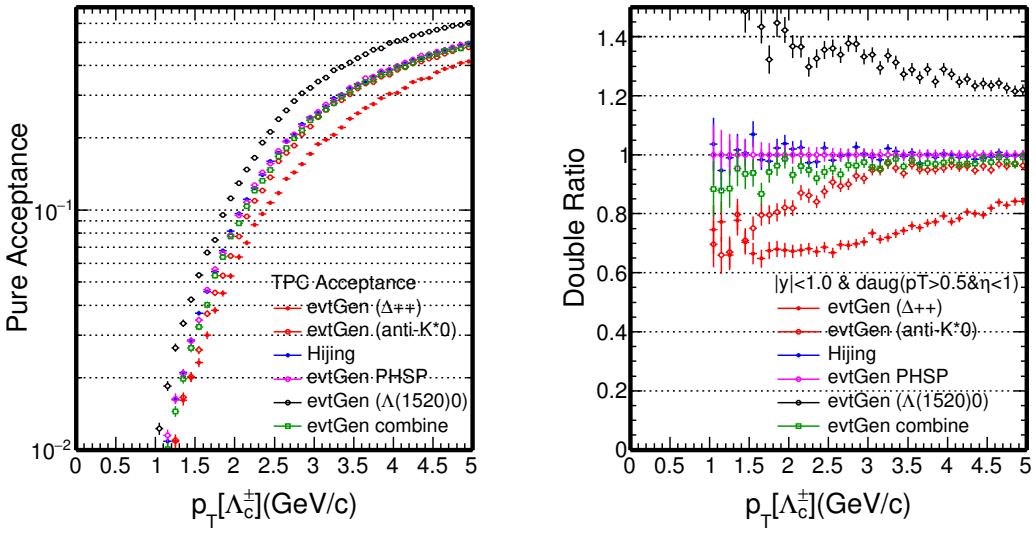

Figure 4.19: Λ_c pure acceptance from different MC decayer, such as PYTHIA, Hijing, evtGen and PhaseSpace class. (right) Double ratio of the acceptance to evtGen PHSP.

The second step is to check the kinematic with the reconstructed TPC tracking information. Compare to the first step, this one fold in the momentum resolution and the TPC acceptance effect. Fig. 4.20 left panel shows this efficiency $\times$ Acceptance comparison between Hijing + GEANT (red) and Fast-Simulation with Hijing input (black), the right panel shows the double ratio to Hijing. As the red line is the fit function and the fit results around $\sim$1 shows very good agreement.

Similar as D^0, the next step is fold in the HFT matching efficiency and consider the HFT acceptance effect. Fig. 4.21 left panel shows this efficiency $\times$ Acceptance comparison after TPC and HFT matching between Hijing + GEANT (red) and Fast-Simulation (black), the right panel shows the double ratio to Hijing. As the red line is the fit function and the fit results around $\sim$1 also shows very good agreement.

The last step is folding in the topological cuts and then compare between the Hijing and Fast-Simulation. Fig. 4.22 left panel shows this efficiency $\times$ Acceptance comparison after TPC, HFT matching and topological cuts between Hijing + GEANT (red) and Fast-Simulation (black), the right panel shows the double ratio to Hijing. Still the red line is the fit function and the fit results around $\sim$0.95 shows good agreement, which means this topological variables are well described in the fast-simulation package. Left panel the red points show the efficiency from Hijing + GEANT, the statistics error is still

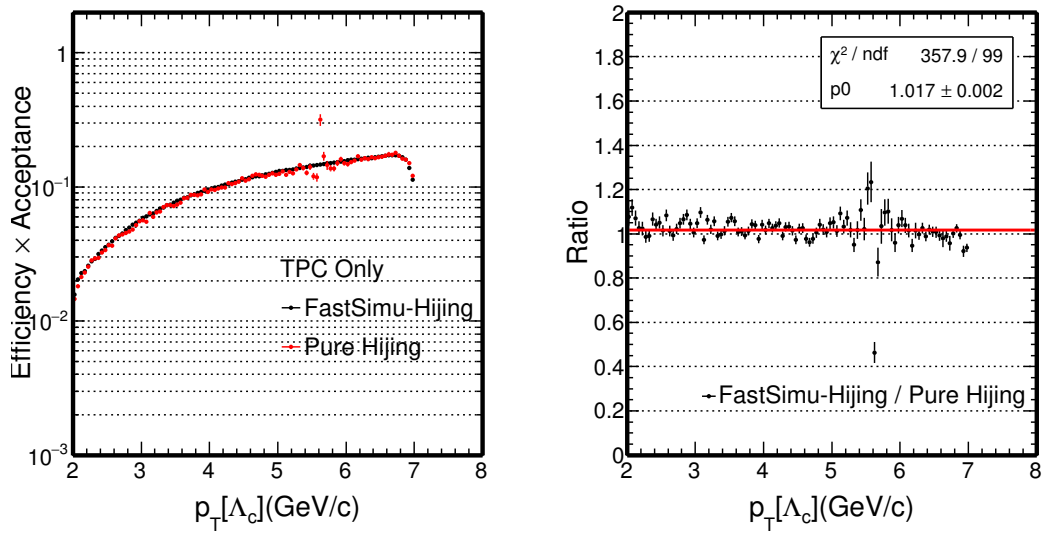

Figure 4.20: The comparison of Λ_c TPC acceptance $\times$ efficiency between Hijing + GEANT (red) and Fast-Simulation with Hijing input (black). (right) Double ratio of these acceptance to Hijing.

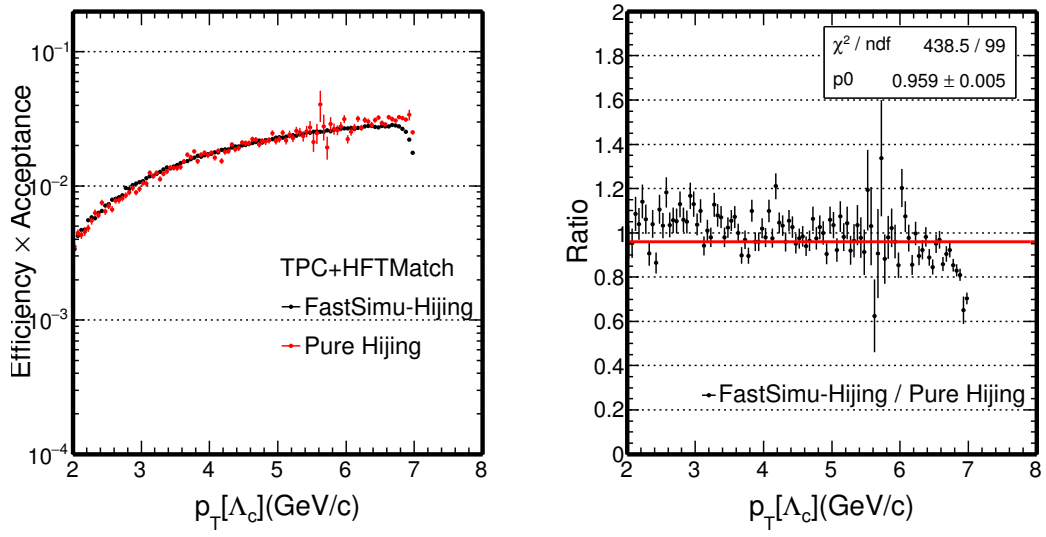

Figure 4.21: The comparison of Λ_c TPC + HFT match acceptance $\times$ efficiency between Hijing + GEANT (red) and Fast-Simulation with Hijing input (black). (right) Double ratio of these acceptance to Hijing.

large. Again this is one of the reasons we use data-driven Fast-Simulation for our efficiency study especially for this low efficiency case, it can be easily enlarge the statistics by a factor of 100 or even 1000 compare to the traditional Full GEANT simulation.

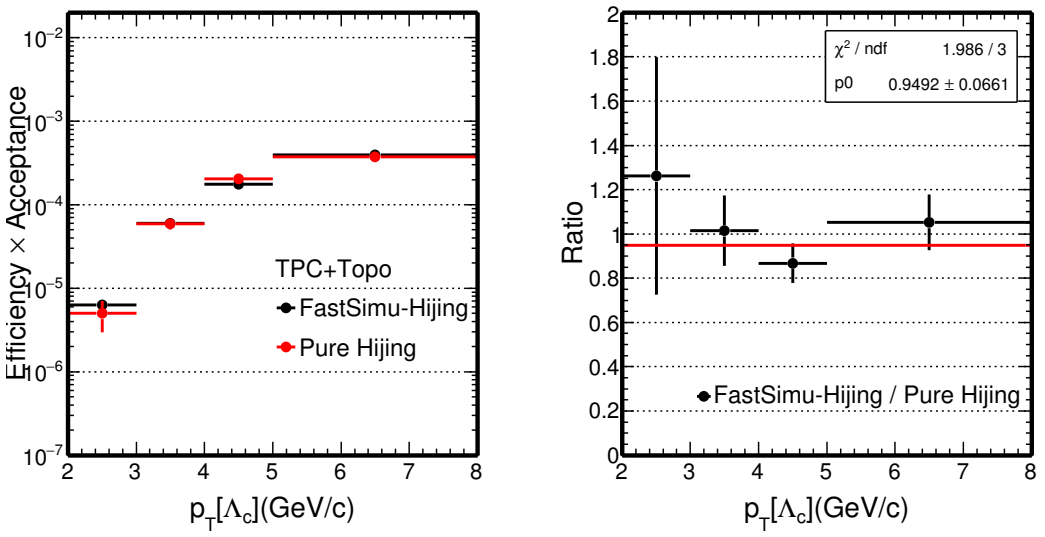

Figure 4.22: The comparison of Λ_c TPC + HFT match + Topological acceptance $\times$ efficiency between Hijing + GEANT (red) and Fast-Simulation with Hijing input (black). (right) Double ratio of these acceptance to Hijing.

From Hijing + GEANT simulation, we know exactly whether the HFT matched track is real match or mismatch, so we can determine the HFT real matched efficiency $\times$ acceptance for Λ_c reconstruction from Hijing sample. As shown on Fig. 4.23 is the real HFT matched efficiency $\times$ acceptance comparison between Hijng + GEANT and our previously Fast-Simulation. The right panel shows the double ratio of these efficiency and fitted with a line, the parameters shows $\sim$1.07 which means the (same) Fast-Simulation can reproduce the real HFT matched reconstruction efficiency with reasonable precision.

If we compare with the previous Hijing HFT matched efficiency (not necessary to be real matched), it also indicate that most of the Mis-matched daughter tracks are removed by topological cuts as we said in the assumptions. Fig. 4.24 shows the different components contributions directly from Hijing, the black one is HFT matched, red one requires all the daughter tracks are real matched and the blue one shows at least one of the daughter tracks are mis-matched. Right panel shows the relative fraction of the real match and mis-mismatch contribution.

As see, most of the mis-matched tracks are removed, but still there are $\sim$10% contribution from this study. Compare to D^0 this relative contributions from mis-matched tracks are slightly big, this is reasonable since we have 3 daughter tracks here. Note

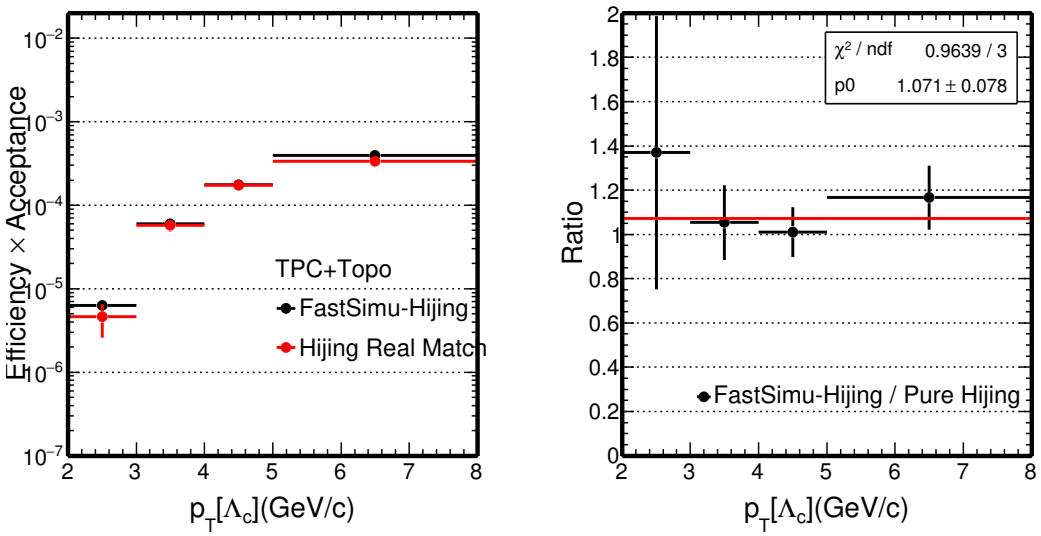

Figure 4.23: The comparison of Λ_c TPC + HFT Real match + Topological acceptance $\times$ efficiency between Hijing + GEANT (red) and Fast-Simulation with Hijing input (black). (right) Double ratio of these acceptance to Hijing.

here limited by the Λ_c Hijing samples, the statistics error from Hijing is still large.

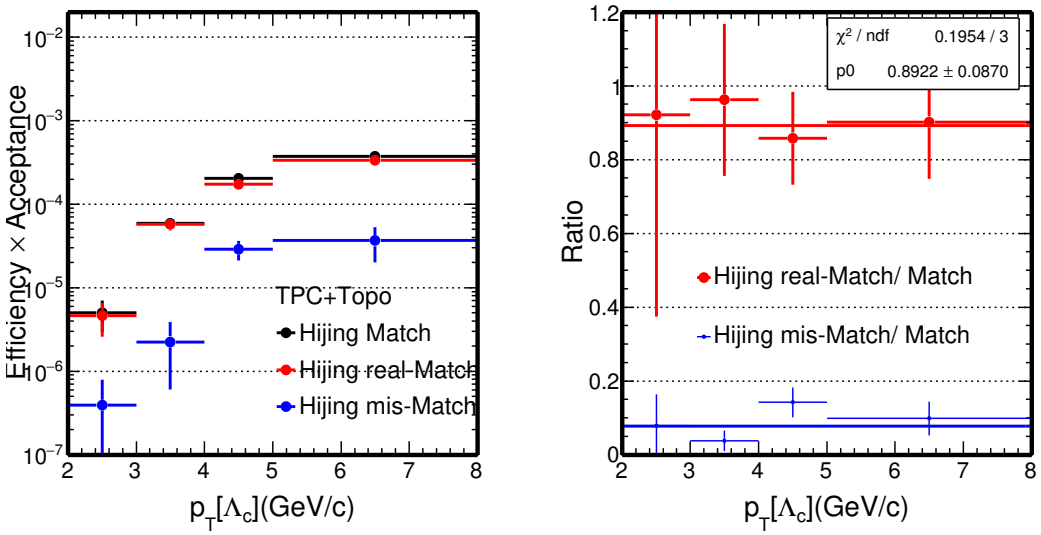

Figure 4.24: The comparison of Λ_c TPC + HFT (real/mis) match + Topological acceptance $\times$ efficiency for Hijing + GEANT. (right) Double ratio of the components form Hijing.

Above all the discussions in the section 4.4.1.1, we are confident that the Fast-Simulation method can also well reproduce the acceptance and efficiency for this Λ_c study. The current Λ_c statistics from real data part is still small, as see the Λ_c signals only have $\sim 5\sigma$ significance, so the current precision form efficiency correction part as shown on Fig. 4.22 is good enough. Similar comparison of topological variables for Λ_c

will be described in the following section.

4.4.1.2 Validation Topological Distributions

We can extract the topological variables from both Hijing + GEANT and Fast-Simulation relay on those Hijing input. Similar as we did for D^0 in Sec. 3.6.2.2, we can compare the topological distributions from these two procedures for Λ_c. This will be another evidence that the Fast-Simulation can well reproduce the crucial topological variables for Λ_c.

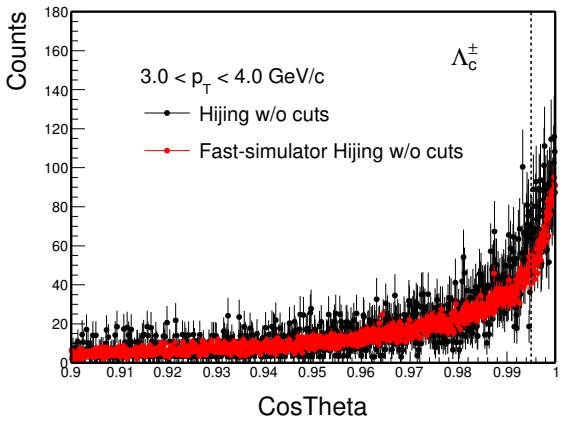

Figure 4.25: Λ_c cosTheta distribution in most central 0-10% between Hijing and Fast-Simulation.

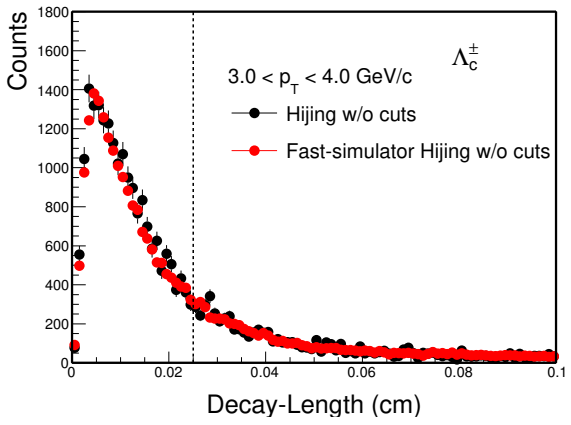

Figure 4.26: Λ_c decay length distribution in most central 0-10% between Hijing and Fast-Simulation.

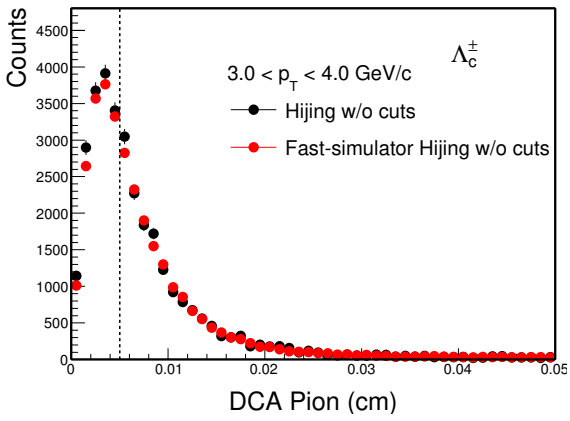

Figure 4.27: Λ_c pions Dca distribution in most central 0-10% between Hijing and Fast-Simulation.

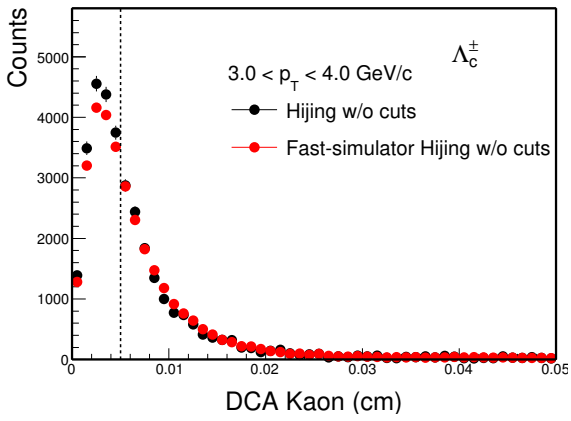

Figure 4.28: Λ_c kaons Dca distribution in most central 0-10% between Hijing and Fast-Simulation.

From Fig. 4.25 to Fig. 4.30, these are the 6 topological variables used for the Λ_c reconstruction. The topological distributions can be extracted both directly from Hijng + GEANT and from Fast-Simulation relay on Hijing input. The Fast-Simulation part was the modified version similar as we used for the D^0 efficiency study.

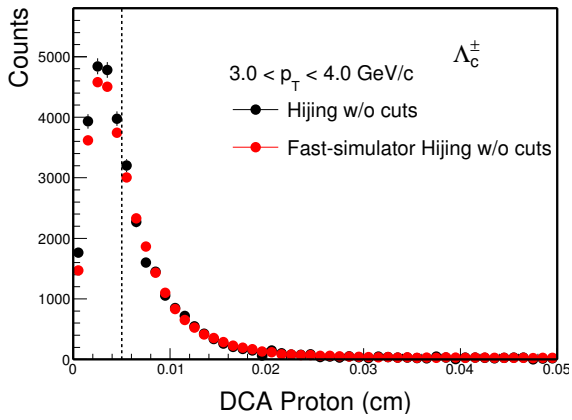

Figure 4.29: Λ_c protons Dca distribution in most central 0-10% between Hijing and Fast-Simulation.

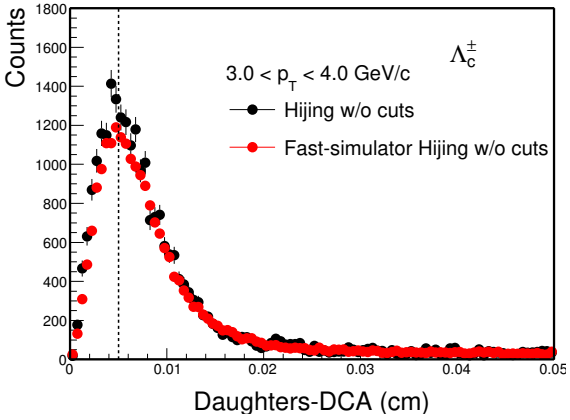

Figure 4.30: Λ_c dcaDaughters distribution in most central 0-10% between Hijing and Fast-Simulation.

As seen, all the comparison of topological variables from Hijing have a very good agreement for Λ_c, which means again Fast-Simulation method can well reproduce the topological variables in Hijing sample. In another word, the topological efficiency estimation for Λ_c from this Hijing-Data-Driven Fast-Simulation is reliable.

4.5 Systematic Uncertainties

The approach for the Λ_c systematic uncertainties are similar as D^0. Several sources are contributed to the uncertainties. The first one is still coming from the raw yield extraction. We varied the signals fitting range and also we use the wrong-sign or fitting for the background description to estimate the uncertainties for yield extraction. The second one is from the TPC embedding uncertainties, this one is quota 5% for single track at that time. The next one is from the fast-simulation part, similar as D^0 when we validating the packages we quote 5% contribution as one of the systematic sources. Another source would be the vertex resolution contribution as we discussed before, since the Λ_c has shorter decay length, we are still not clear about this contribution until we have enough Hijing samples. We quote a conservative 20% contribution for our measured Λ_c and 10% for the D^0 here. There is another source which is from the secondary proton contribution, we quota in total 10% contribution for this, in the real data analysis, this systematic source is quoted as symmetrical 5%. The next one source coming from the bin shift correction, same as we did for D^0, since we do not have the measured Λ_c spectrum in heavy-ion collisions, we use D^0 spectrum instead for the bin correction and quota another 10% as systematic source after varying the p_T shape. Another source is by varying the topological cuts. The default TMVA cuts and another set of cuts are corrected for the spectrum. The difference between the corrected yield are quoted as the systematic source. There are uncertainties on the branch ratio and life time of Λ_c

decay to the hadronic channels, it also contribute to the uncertainties.

Table 4.5 shows the Λ_c different sources contribution in the centrality 10-60%. For the Λ_c/D^0 ratio, they share the same systematic uncertainties for the TPC part and vertex contribution, so the TPC contribution and vertex contribution from Au+Au for Λ_c and D^0 can be largely canceled out.

Table 4.5: Systematic uncertainties for Λ_c from different sources

p_T range	3.0-6.0
Yield extra	0.0458454
TPC Tracking	0.15
Secondary Proton	0.05
fast-simu	0.05
Topo Scan	0.114591
Vertex Reso	0.2
bin Shift	0.263145
BR & cτ	0.0860233
In total for Λ_c/D^0	0.319881

4.6 Other Systematics for the Fast-Simulation

In the previous Fast-Simulation section 3.8, we have two potential concerns for D^0. Here the same as Λ_c.

Fig. 4.31 shows the protons vertex distributions from the secondary decays. The first one is the overall secondary proton vertex distributions and we can clearly saw the HFT structure. Top right panel is protons decayed from GeantID==8/9 (which is $\pi^{\pm}$), this part is the knocked out particles with HFT. The bottom left panel is proton decayed from GeantID==15/25 (which is anti-proton and anti-neutron), this is the normal annihilation particles. The last one bottom right panel shows the protons decayed from the Λ.

The secondary track for protons have different performance compare to the primary track such as the HFT match ratio shown on Fig. 4.32. The solid circle is the inclusive one for HFT matching ratio, the empty circle is for the primary protons and the solid square is for the secondary protons. All these HFT match ratios are after applying exactly the same cut as real data analysis. The HFT match ratio for secondary track is lower since they are decayed far away from the vertex and most of them do not have three HFT hits. For the protons, there are also some contributions from those hyperons such as Λ. The more contribution of the secondary track, the more difference we observed between inclusive one and primary one. The bottom panel shows the HFT

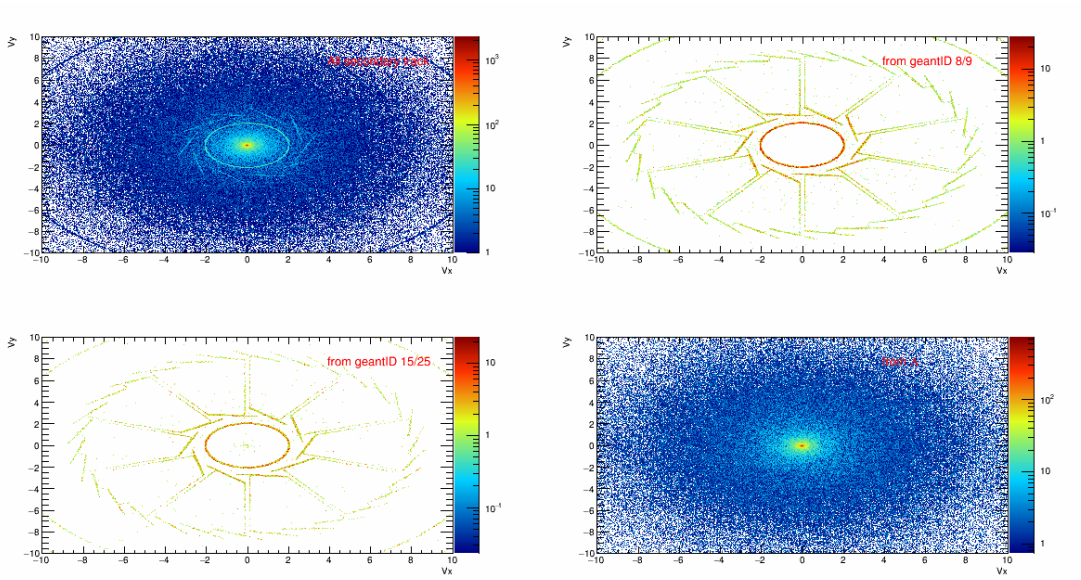

Figure 4.31: The vertex distribution for Protons from secondary decay. Top left is the overall secondary pion tracks, top right is pion decayed from GeantID=8/9 (which is $\pi^{\pm}$), bottom left is pion decayed from GeantID=15/25 (which is anti-proton and anti-neutron), bottom right is decayed from Λ.

matching double ratio of inclusive one over primary one. For the protons, the relative secondary contribution is not small, that's why we saw $\leq$10% difference between primary and inclusive ones.

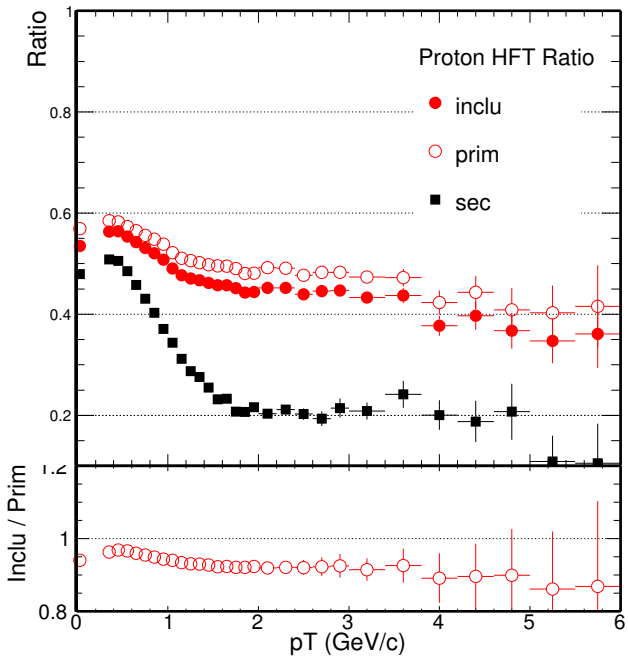

Figure 4.32: HFT Matching Ratio for Protons, compare between primary track and secondary tracks relay on Hijing. (bottom) The double ratios of inclusive one to primary tracks.

This secondary proton contribution for our efficiency correction need to be consider. In our real data efficiency correction, we also (compare to D^0's pion) took this double ratio from Hijing as an additional correction factor for the proton HFT matching ratio, since the data part can only obtained the inclusive one.

The vertex resolution could also contribute to the Λ_c analysis. We also need to relay on the Minimum Bias Hijing simulation sample to obtain the correction factor. From Hijing sample we know the true efficiency for any centrality species, and from the Fast-Simulation we can obtain the efficiency including those vertex effect. The difference was took as the additional correction factor for real data analysis if this effect is not too big. Also the Λ_c Hijing minimum bias sample production is still ongoing, this need a huge data sample for the study.

Chapter 5 $D^{\pm}$ Analysis Details

5.1 Data Set and Event Selections

The data set used in this $D^{\pm}$ analysis is also from Au+Au collisions at $\sqrt{s_{NN}}$ = 200 GeV from RHIC run year 2014 (Run14), the same data set as the D^0 and Λ_c analysis.

The event selection criterion for $D^{\pm}$ analysis can be found from Table 4.1, they are the same as D^0. After event selection, ∼875 million Minimum Bias events are used for this analysis. The centrality definition is the same as in D^0 since they are the same data set (See section 3.3).

5.2 $D^{\pm}$ Reconstruction

$D^{\pm}$ are reconstructed through the typically hadronic channel $K^{\mp}\pi^{\pm}\pi^{\pm}$. From the latest PDG, $D^{\pm}$ have several main decay channels, including non-resonance channel and resonance channels shown below [8]:

In total, $D^+ \to K^-\pi^+\pi^+$ ($\sim 9.46\%$) :

- $D^+ \to (K^- + \pi^+)_{S-wave}\pi^+$ (7.58%)
- $D^+ \to \bar{K}^*(892)^0 + \pi^+$ (1.05%)
- $D^+ \to K^- + (2\pi^+)_{I=2}$ (1.47%)

In the following, we will describe the daughter selection and the geometry cuts. We will also show the $D^{\pm}$ signals for different p_T and centrality bins.

5.2.1 Daughter Selection

Our interested $D^{\pm}$ have a lifetime of $c\tau \sim 312\mu$m. This is a much longer distance compare to D^0 $c\tau \sim 123\mu$m and Λ_c $c\tau \sim 60\mu$m [8]. The global tracks including the global momentum for daughter tracks are used in this analysis. The daughters transverse momentum are required to $\geq$ 0.5 GeV/c.

The pion and kaon tracks are identified by combining TPC and TOF. The TPC provides particle identification utilizing the energy loss information dE/dx, and TOF provides velocities information for PID. In order to get more statistics, for kaon and pion PID, we always use hybrid TOF PID, which means only require TOF when it is available.

In summary, next list all the related track selections for $D^{\pm}$ daughters including track quality cut and particle identification cut.

- global tracks
- p_T > 0.5 GeV/c
- $|\eta| < 1$
- $nHitsFit \geq 20$, in TPC
- at least one hit in every layer of PXL and IST

pion PID:

- $|n\sigma_{\pi}| < 3.0$, based on TPC dE/dx
- If TOF is available (hybrid PID): $|\frac{1}{\beta} - \frac{1}{\beta_{exp}}| < 0.03$

kaon PID:

- $|n\sigma_{K}| < 2.0$, based on TPC dE/dx
- If TOF is available (hybrid PID): $|\frac{1}{\beta} - \frac{1}{\beta_{exp}}| < 0.03$

5.2.2 Topological Cut

The secondary vertex is reconstructed with selected kaon and pion global tracks. Similar as Λ_c, in this analysis, we have three of the middle point on the Distance of the Closest Approach (DCA) between two daughter tracks since we have 3 daughters in total. The average of these three middle points of Dca is considered as the secondary decay vertex of the candidate $D^{\pm}$. As shown in Fig. 5.1, 6 geometrical variables are chosen to select $D^{\pm}$ and reject combinatorial background, which is dominated by a triple of tracks directly from the primary vertex: decay length (the distance between the decay vertex and Primary Vertex PV), the maximum DCA between the 3 daughters, the back pointing angle cos(θ) which is the angular of $D^{\pm}$ momentum and the decay vertex relative to the primary vertex, DCA between the two π tracks and PV and DCA between the K track and PV. The cuts we used on these variables are quite similar as D^0 for a quick study. Additionally there is a $D^{\pm}$ Dca to primary vertex cut to make sure the $D^{\pm}$ candidate is from prompt decay.

The geometry cuts for these $D^{\pm}$ analyses are shown in Table 5.1. These are the default cuts used in the $D^{\pm}$ reconstruction to calculate the spectra central value.

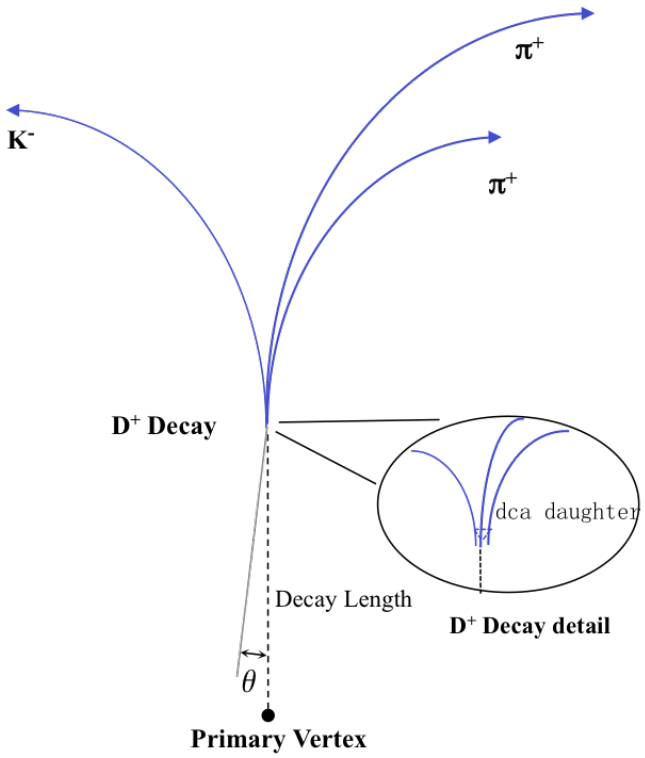

Figure 5.1: The topology of a $D^{\pm}$ decaying to a kaon and two pions.

Table 5.1: Geometrical cuts for different $D^{\pm}$ p_T.

$D^{\pm}$ p_T (GeV/c)	0-1	1-2	2-3	3-5	5-10
decay length (μm) >	300	300	300	247	259
DCA between 2 daughters (μm) <	84	66	57	50	60
DCA between D^0 and PV (μm) <	61	49	38	38	40
DCA between $\pi 1$ and PV (μm) >	110	111	86	81	62
DCA between $\pi 2$ and PV (μm) >	110	111	86	81	62
DCA between K and PV (μm) >	103	91	95	79	58

5.2.3 $D^{\pm}$ Signals

For the $D^{\pm}$ reconstruction, we have three daughter particles, in total have 8 charge combinations. Two of them have the right charge sign for signals and the other 6 have wrong signs for background. The wrong-sign (like-sign) methods here can statistically describe the background to the foreground with three times statistics precision.

Fig. 5.2 shows the invariant mass distribution for the foreground and wrong-sign backgrounds: same event wrong-sign method in the p_T range 1-8 GeV/c from 0-80% centrality. The red points are foreground and the grey points are wrong-sign backgrounds, the wrong-sign backgrounds are directly scaled down by a factor of 1/3, and it shows very good agreement to the foreground. As we can clearly observe the $D^{\pm}$

signals with the significance ∼48.

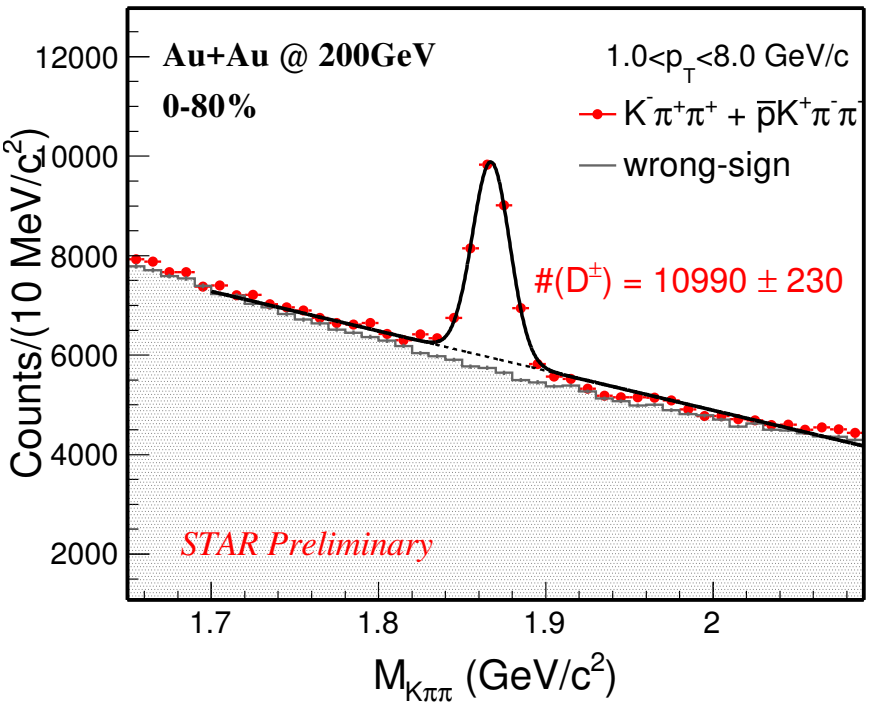

Figure 5.2: $D^{\pm}$ invariant mass distribution for foreground (red) and wrong-sign background (grey) in $1 < p_T < 8$ GeV/c at 0-80% centrality.

Fig. 5.3 shows the $D^{\pm}$ signals in the p_T range 1-8 GeV/c from most central 0-10% centrality. Red points are foreground and grey points are wrong-sign backgrounds after scale. The $D^{\pm}$ signals with the significance ∼14. As we know in the most central collisions, the multiplicity is large, the combinatorial backgrounds contribution is huge.

Fig. 5.4 shows the $D^{\pm}$ signals from the mid-central 20-40% centralities.The $D^{\pm}$ signals with the significance ∼41. For the most peripheral 40-80% centralities, the signals was shown on Fig. 5.5 with significance around ∼38. Still all the wrong-sign method after scaling can well describe the background. From the most central to most peripheral collisions, the signals to background ratio is keep increase.

5.3 $D^{\pm}$ Efficiency and Acceptance Corrections

To obtain the real invariant mass spectrum of $D^{\pm}$ within STAR acceptance, the raw spectrum should correct for the efficiency. The $K\pi\pi$ pair efficiency within STAR acceptance is evaluated by folding the TPC related efficiency to the HFT related efficiency similar as we did for Λ_c shown on Eq. 3.11. We still use the 'Data-Driven Fast simulation' as developed for $D^{\pm}$.

The TPC tracking efficiency for daughter tracks (π, K) (ε_{TPC}) is evaluated via the standard STAR embedding technique and shown in Fig. 3.27 and Fig 3.28.

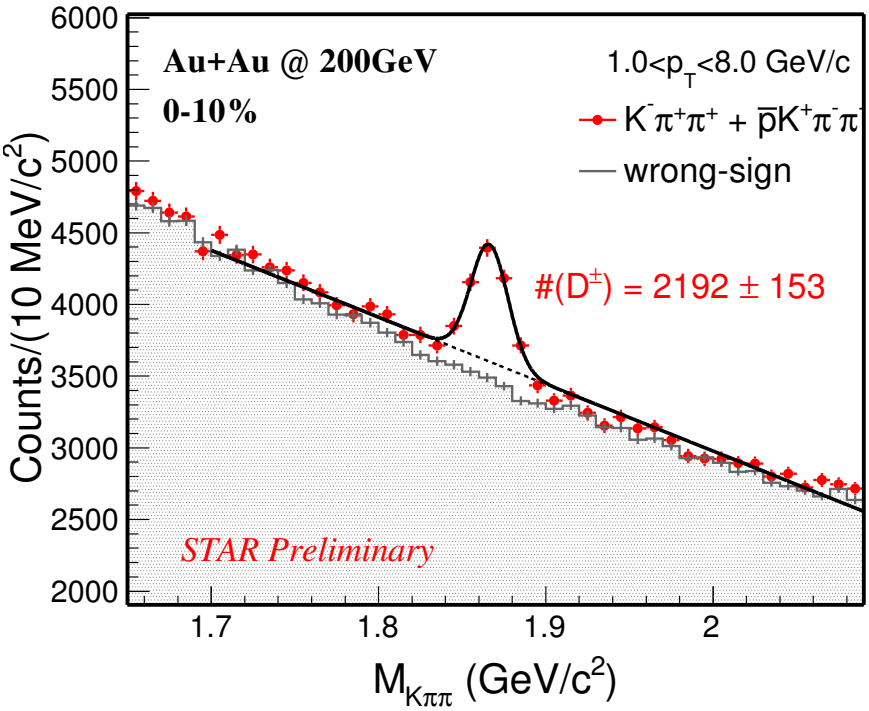

Figure 5.3: $D^{\pm}$ invariant mass distribution for foreground (red) and wrong-sign background (grey) in $1 < p_T < 8$ GeV/c at 0-10% centrality.

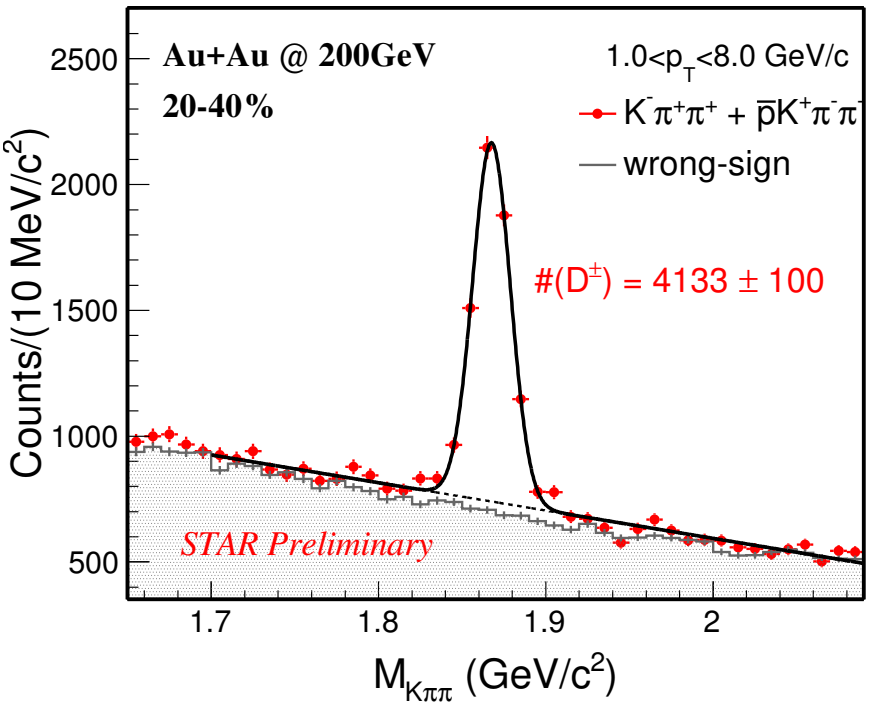

Figure 5.4: $D^{\pm}$ invariant mass distribution for foreground (red) and wrong-sign background (grey) in $1 < p_T < 8$ GeV/c at 20-40% centrality.

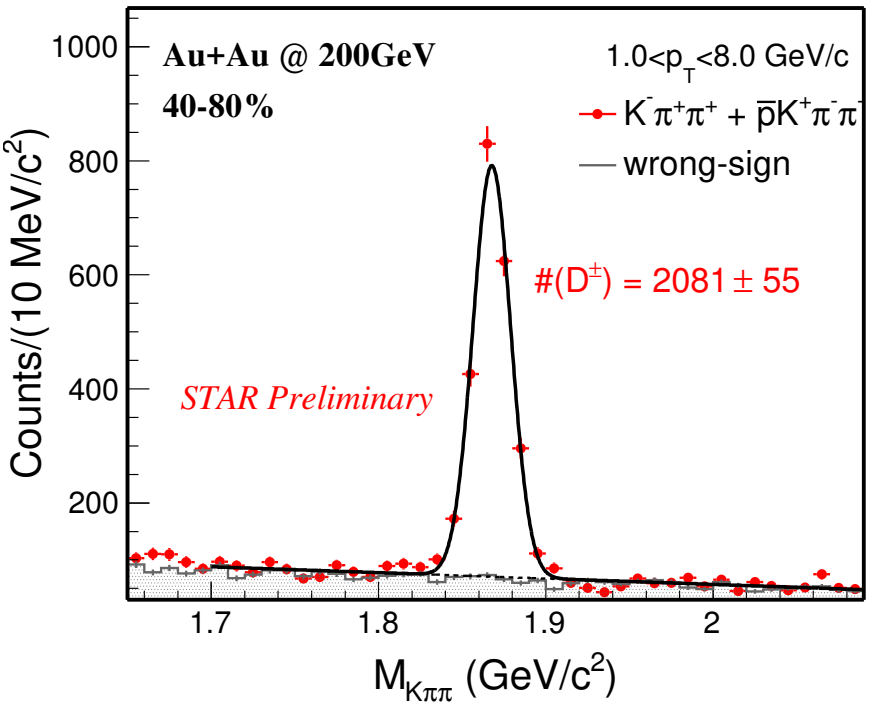

Figure 5.5: $D^{\pm}$ invariant mass distribution for foreground (red) and wrong-sign background (grey) in $1 < p_T < 8$ GeV/c at 40-80% centrality.

The TOF match efficiency in Run14 Au+Au collisions at 200 GeV was shown in Fig. 4.11 for positive charge particles in the centrality 0-10% and Fig. 4.12 shows the same plots for negative charge particles in the centrality from 40-80%.

The particle identification cut efficiency (ε_{PID}) includes two components: the TOF velocity ($1/\beta$) cut efficiency and dE/dx cut ($n\sigma_{K/\pi}$) efficiency. They are also discussed before in the section 4.3.4 and 3.5.4.

5.3.1 Data-driven Fast Simulation for HFT and Topological Cut Efficiency

As discussed, the HFT related efficiency shown on Eq. 3.11 including two items: HFT acceptance and topological cuts. We also used the 'Data-Driven Fast simulation' for the $D^{\pm}$ efficiency correction. And later on we will also validate this method for $D^{\pm}$ with full GEANT simulation.

5.3.1.1 $D^{\pm}$ Efficiency and Topological Distribution

Similar recipe as we discussed for D^0 in section 3.5.5.3, we obtain the efficiency step by step as shown on Fig. 5.6. First we have the TPC efficiency shown by red maker which is after the p_T, η acceptance cut and TPC tracking efficiency from embedding. Then, after folding in the HFT matching efficiency, the second item is obtained on black circle. Next step is fold in the PID efficiency. Last step is after the topological cut, as

shown by the cyan marker. As see, the final cut efficiency is really small due to the tight cut.

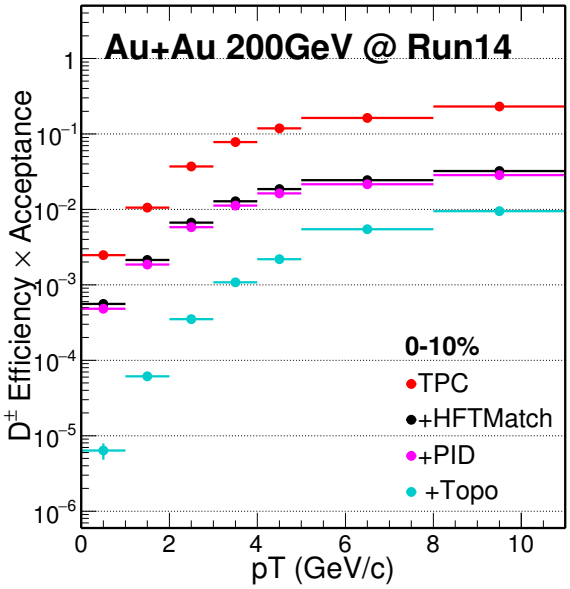

Figure 5.6: $D^{\pm}$ efficiency step by step from TPC, HFT Ratio, Topological cut in 0-10%.

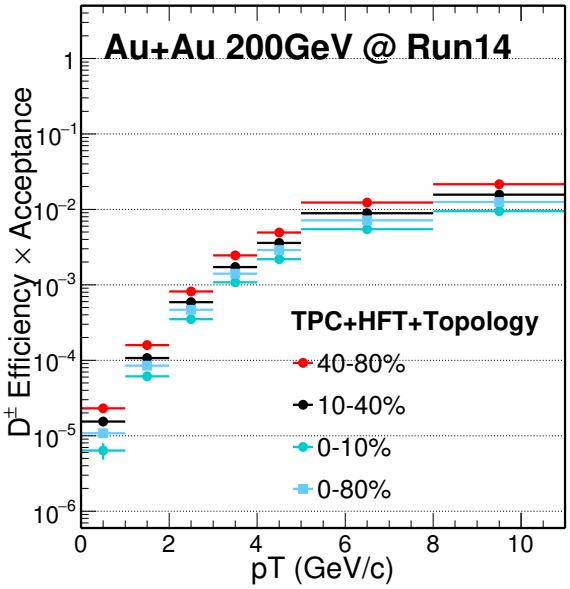

Figure 5.7: $D^{\pm}$ efficiency including TPC, HFT and Topological cut in several centralities.

We study all the efficiencies with small centrality bin width, in total we have 9 centrality bins from our StRefmultCorr class. Similar as we did for D^0 and Λ_c, the final efficiencies for the wider centrality bins 0-10%, 10-40% and 40-80% are calculated using N_{bin} as weights. Fig 5.7 shows the $D^{\pm}$ efficiency for 4 wide centralities after TPC, HFT match and Topological efficiency included.

The Data-Driven Fast-Simulation also provide the topological information, can be used for the comparison with real data. For the $D^{\pm}$ signals, since the statistics is enough for this kind of comparison as we did for D^0.

For the real data part, within the $D^{\pm}$ mass window we can statistical subtract the background and extract the pure $D^{\pm}$ topological distributions. Here the mass window was from 1.843 to 1.898 GeV/c.

From Fig. 5.8 to Fig. 5.13, these are the topological variables (cos(θ), decayLength, dcaDaughters, DpmDcaToVtx, PionDca and KaonDca) used for the $D^{\pm}$ reconstruction. The distributions from the real data part are using wrong-sign method to statistical subtract the background. The Data-Driven Fast-Simulation part was the package we relayed on for our efficiency study as shown before.

Comparison these topological variables between real data and Fast-Simulation, the agreement is good, which means our Data-Driven Fast-Simulation method can well reproduce the topological variables in real data. In another word, the efficiency estimation

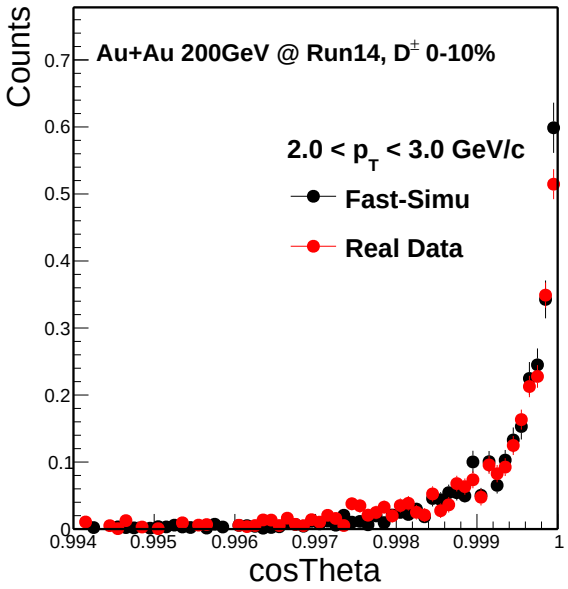

Figure 5.8: $D^{\pm}$ cosTheta distribution in most central 0-10% between Fast-Simulation and Real Data.

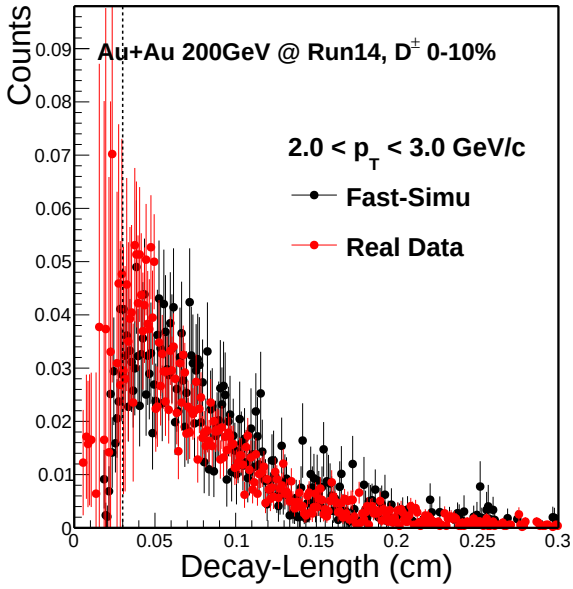

Figure 5.9: $D^{\pm}$ decay length distribution in most central 0-10% between Fast-Simulation and Real Data.

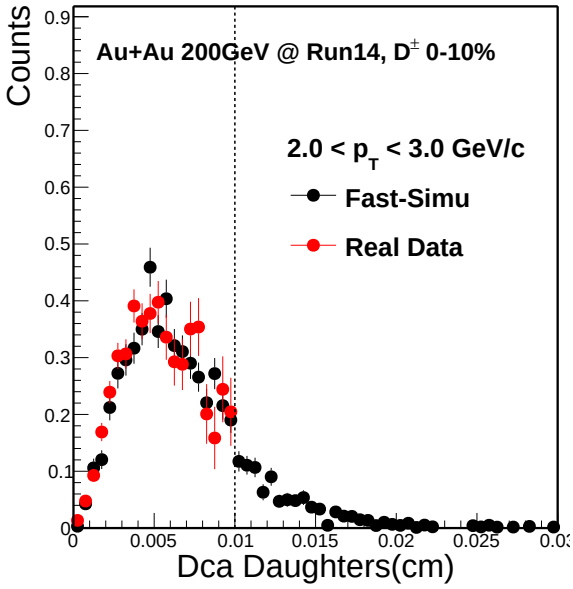

Figure 5.10: $D^{\pm}$ dcaDaughters distribution in most central 0-10% between Fast-Simulation and Real Data.

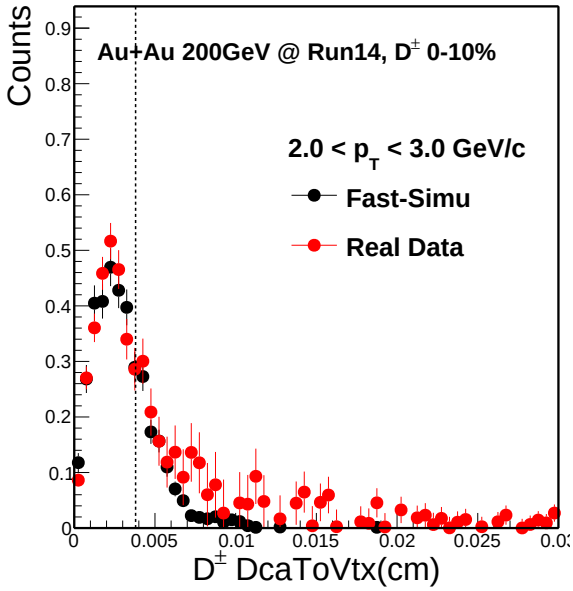

Figure 5.11: $D^{\pm}$ dca to Vertex distribution in most central 0-10% between Fast-Simulation and Real Data.

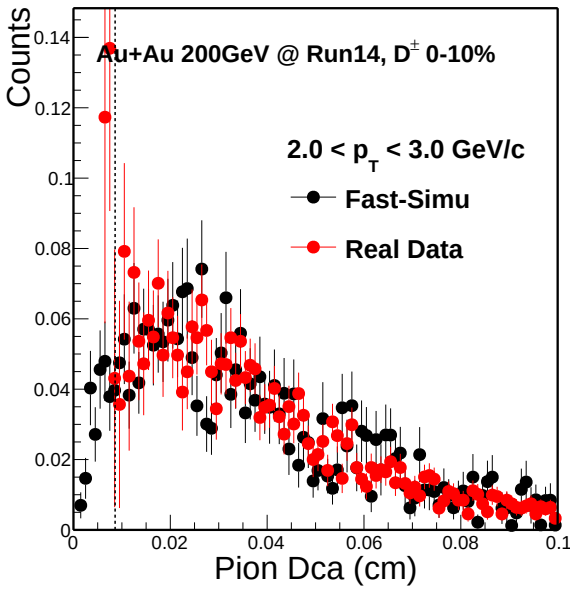

Figure 5.12: $D^{\pm}$ pionDca distribution in most central 0-10% between Fast-Simulation and Real Data.

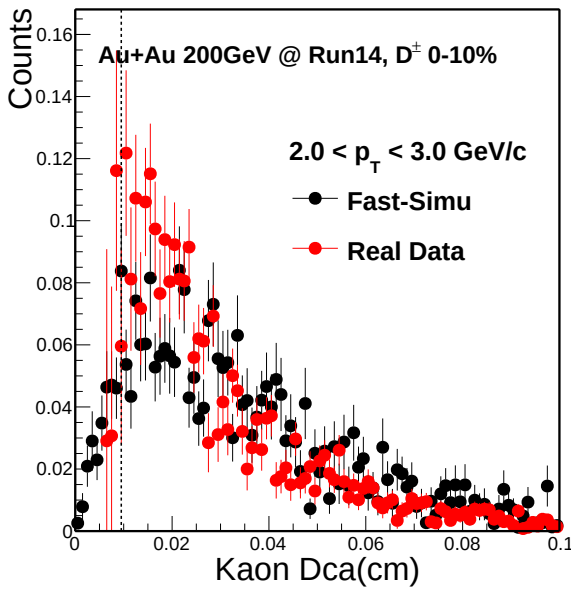

Figure 5.13: $D^{\pm}$ kaonDca distribution in most central 0-10% between Fast-Simulation and Real Data.

from Data-Driven Fast-Simulation is reliable. Similar as D^0, there is another method we are going to discuss in the following section is based on Hijing simulation.

5.4 Validation Data-Driven Fast-Simulation with Full GEANT + Hijing Simulation

Similar as we did for D^0 and Λ_c Hijing, the $D^{\pm}$ Hijing sample was run through the Full Hijing + GEANT simulation with realistic pileup hits (UPC+MB) in PXL and sensor masking tables. They can provide reasonable performance for the HFT matching ratio and Dca resolution.

In total, we have ∼155K 0-10% most central Hijing events, and for each event is embedded with 20 $D^{\pm}$'s. So in total, we have ∼3.05M $D^{\pm}$ for this Hijing sample. The embedded $D^{\pm}$ has small effect on the tracking since the multiplicity is much higher compared to 20 × 3 $D^{\pm}$' decayed daughters.

The performance of these $D^{\pm}$ Hijing sample is also similar as D^0 Hijing samples since all the set up is the same except we embedded $D^{\pm}$ instead of D^0. And as we discussed before, the embedded $D^{\pm}$ have very small impact on the Hijing performance. The HFT matching ratio and Dca comparisons between data and Hijing samples in Au+Au 200 GeV/c from 0-10% centrality, can be found in the previous sections Fig. 3.54 and Fig. 3.55

5.4.1 Validation Procedures

The idea for this Hijing validation is the same as we did before for D^0 and Λ_c in section 3.6.2. With the enriched $D^{\pm}$ Hijing samples, the $D^{\pm}$ efficiency and topological variables distributions can be extracted. Another procedure is extract the necessary ingredients from Hijng sample for the Fast-Simulation input (Fast-Simulation with Hijing input). Then run through the Fast Simulation for $D^{\pm}$, as discussed before, the $D^{\pm}$ efficiency and topological variables are also available in this way and can be compared to the first Hijing + GEANT procedure. The workflow is same as D^0 and Λ_c in Fig. 4.18.

5.4.1.1 Validation Efficiency

Similar as before, the first step is to check the kinematic form different MC decayer such as PYTHIA, Hijing, evtGen and PhaseSpace class from ROOT. Before the validation we need to make sure the decayer used for Fast-Simulation has the same kinematic as the Hijng since $D^{\pm}$ have different decay channels. After the basic acceptance cut, such as $D^{\pm}$ |y| < 1, daughter p_T > 0.5 GeV/c and $|\eta|$ <1 cut. $D^{\pm}$ has different kinematic decay performance from different channels as shown in Fig. 5.14 left panel, the right panel shows the double ratio to PYTHIA non-resonance channel. As seen the Hijng and evtGen PHSP decayer follow the same trend as PYTHIA, but not the others such as $K^*(892)$ and $\bar{K}_2^*(1432)$ channels. So, for this Fast-Simulation decayer we choose evtGen PHSP channel for this Hijing validation. But for our real data analysis, we use evtGen but use DALITZ decay channels which include all the resonance and non-resonance decays.

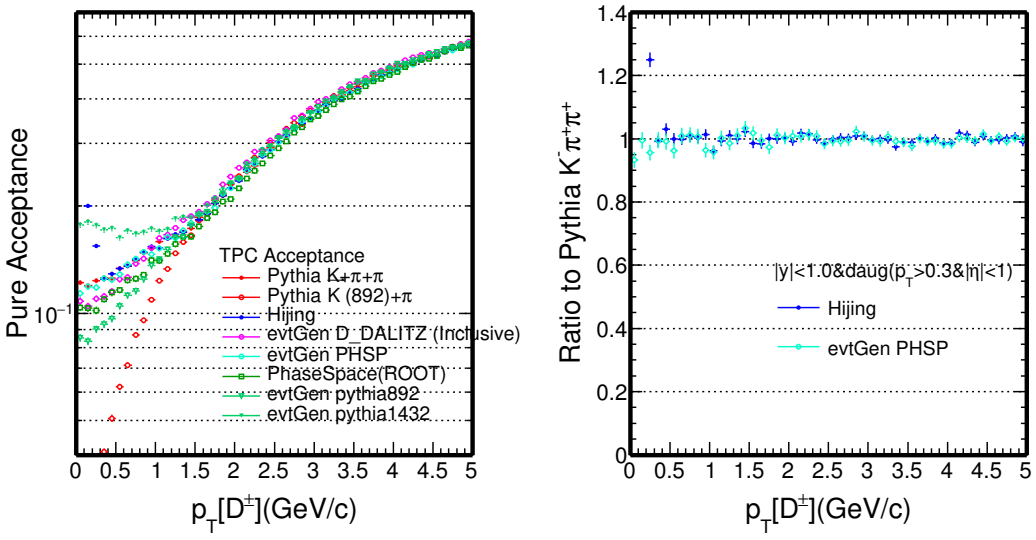

Figure 5.14: $D^{\pm}$ pure acceptance from different MC decayer, such as PYTHIA, Hijing, evtGen and PhaseSpace class. (right) Double ratio of the acceptance to PYTHIA PHSP.

Similar as Λ_c, the next steps will be step by step to check the kinematic with the reconstructed TPC tracking information shown in Fig. 5.15. Left panel shows this efficiency $\times$ Acceptance comparison between Hijing + GEANT (red) and Fast-Simulation with Hijing input (black), the right panel shows the double ratio to Hijing.

The next step is fold in the HFT matching efficiency and consider the HFT acceptance effect shown in Fig. 5.16. Left panel shows this efficiency $\times$ Acceptance comparison after TPC and HFT matching between Hijing + GEANT (red) and Fast-Simulation (black), the right panel shows the double ratio to Hijing.

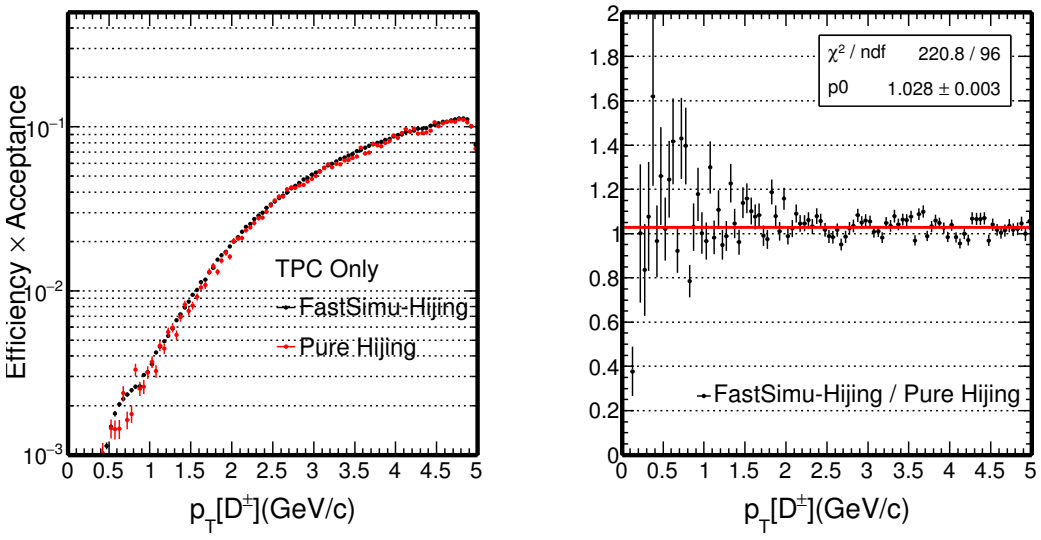

Figure 5.15: The comparison of $D^{\pm}$ TPC acceptance $\times$ efficiency between Hijing + GEANT (red) and Fast-Simulation with Hijing input (black). (right) Double ratio of these acceptance to Hijing.

The last step is folding in the topological cuts and then compare between the Hijing and Fast-Simulation shown in Fig. 5.17. left panel shows this efficiency $\times$ Acceptance comparison after TPC, HFT matching and topological cuts between Hijing + GEANT (red) and Fast-Simulation (black), the right panel shows the double ratio to Hijing. Still the red line is the fit function and the fit results around $\sim$0.9, which means the fast-simulation package still have some room for improvement. This could be due to the longer $D^{\pm}$ decay length compare to D^0 and Λ_c. With longer decay length, the input 2D Dca distributions need more wider range to capture the full geometry information. But limited with the computing source, current we still use the same input as D^0 and Λ_c.

From Hijing + GEANT simulation, we know exactly whether the HFT matched track is real match or mismatch, so we can determine the HFT real matched efficiency $\times$ acceptance for $D^{\pm}$ reconstruction from Hijing sample. As shown on Fig. 5.19 is the real HFT matched efficiency $\times$ acceptance comparison between Hijng + GEANT and our previously Fast-Simulation. The right panel shows the double ratio of these

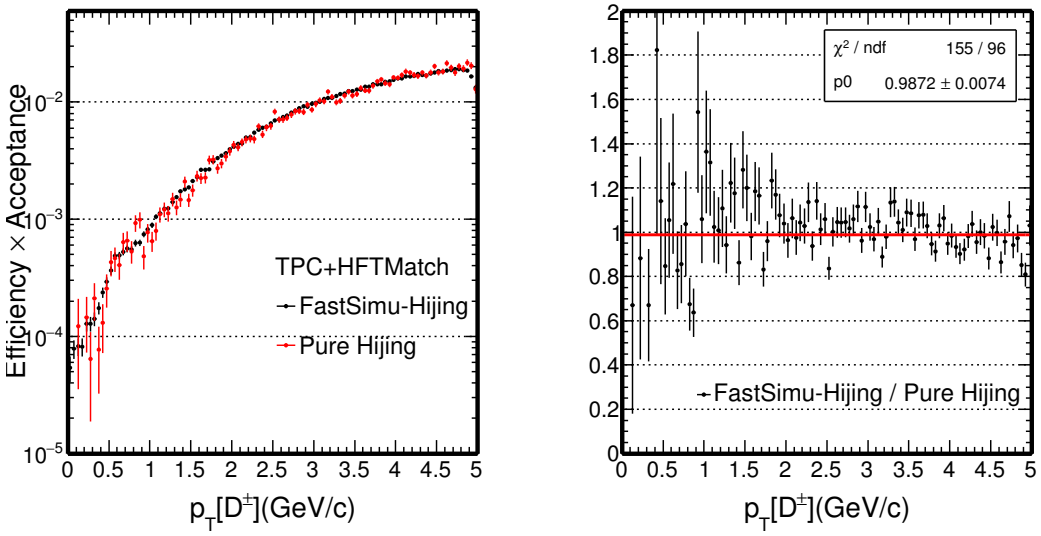

Figure 5.16: The comparison of $D^{\pm}$ TPC + HFT match acceptance × efficiency between Hijing + GEANT (red) and Fast-Simulation with Hijing input (black). (right) Double ratio of these acceptance to Hijing.

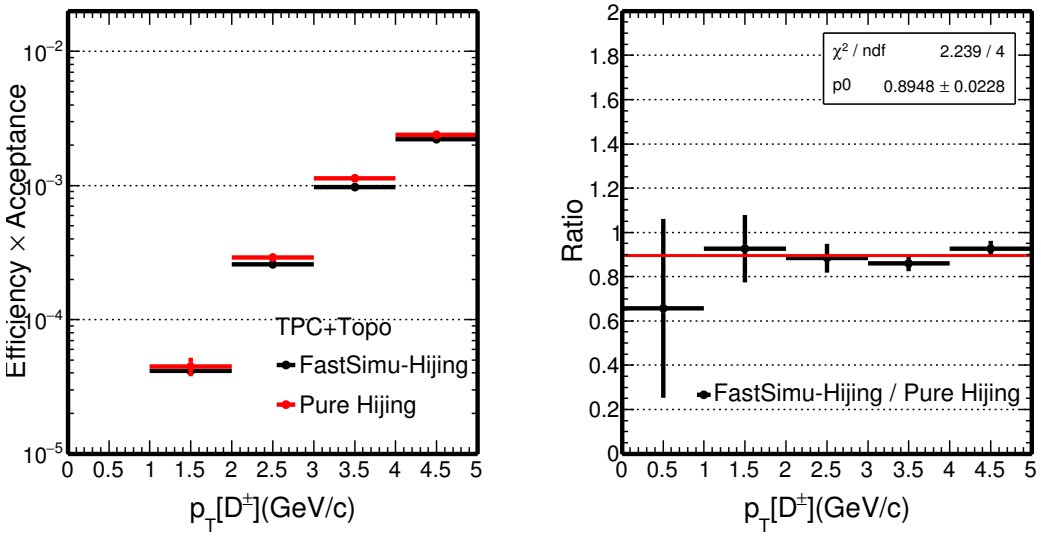

Figure 5.17: The comparison of $D^{\pm}$ TPC + HFT match + Topological acceptance × efficiency between Hijing + GEANT (red) and Fast-Simulation with Hijing input (black). (right) Double ratio of these acceptance to Hijing.

efficiency and fitted with a line, the parameters shows ∼0.966.

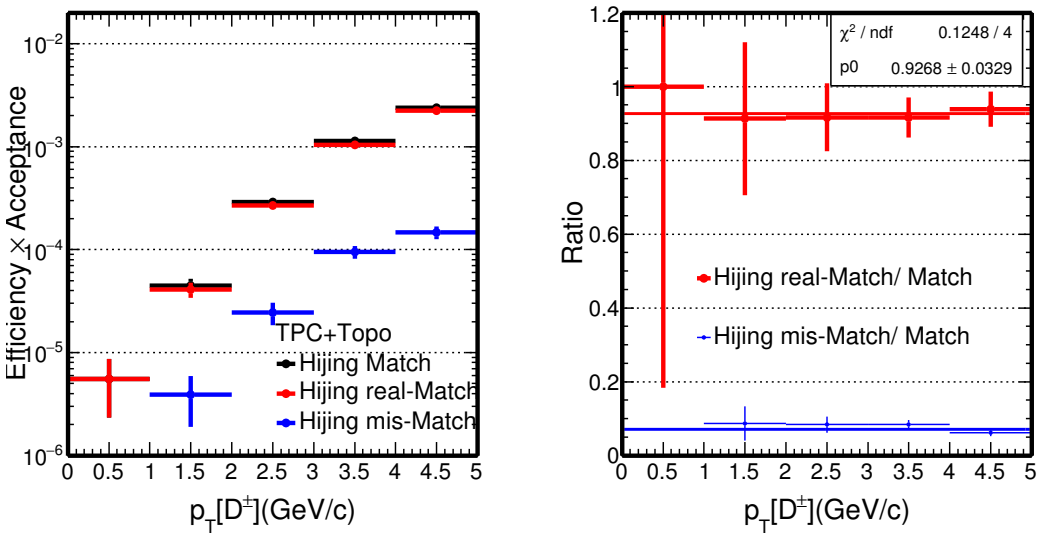

Figure 5.18: The comparison of $D^{\pm}$ TPC + HFT (real/mis) match + Topological acceptance × efficiency for Hijing + GEANT. (right) Double ratio of the components form Hijing.

If we compare with the previous Hijing HFT matched efficiency (not necessary to be real matched), it also indicate that most of the Mis-matched daughter tracks are removed by topological cuts as we said in the assumptions. Fig. 5.18 shows the different components contributions directly from Hijing, the black one is HFT matched, red one requires all the daughter tracks are real matched and the blue one shows at least one of the daughter tracks are mis-matched. Right panel shows the relative fraction of the real match and mis-mismatch contribution.

As see, most of the mis-matched tracks are removed, but still there are ∼8% contribution from this study. Compare to D^0 this relative contributions from mis-matched tracks are slightly big, as we discussed before, this is reasonable since we have 3 daughter tracks here.

Above all the discussions in the section 5.4.1.1, we know that the Fast-Simulation method can reproduce the acceptance and efficiency for this $D^{\pm}$ study. But definitely there are some room for the further improvement. Similar comparison of topological variables for $D^{\pm}$ will be described in the following section.

5.4.1.2 Validation Topological Distributions

We can extract the topological variables from both Hijing + GEANT and Fast-Simulation relay on those Hijing input. Similar as we did for D^0 in Sec. 3.6.2.2, we can compare the topological distributions from these two procedures for $D^{\pm}$. This

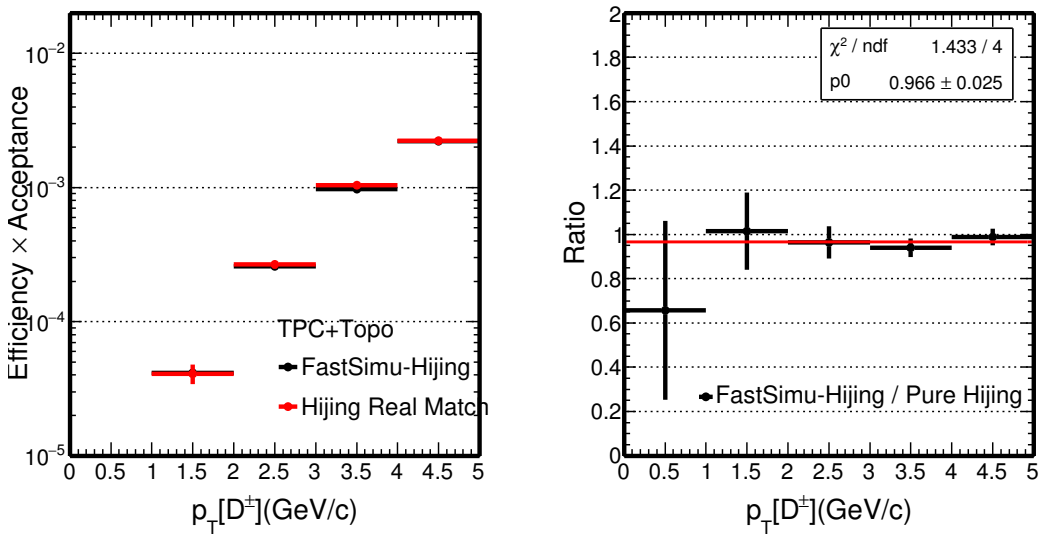

Figure 5.19: The comparison of $D^{\pm}$ TPC + HFT Real match + Topological acceptance × efficiency between Hijing + GEANT (red) and Fast-Simulation with Hijing input (black). (right) Double ratio of these acceptance to Hijing.

will be another evidence that the Fast-Simulation can reproduce the crucial topological variables for $D^{\pm}$ too.

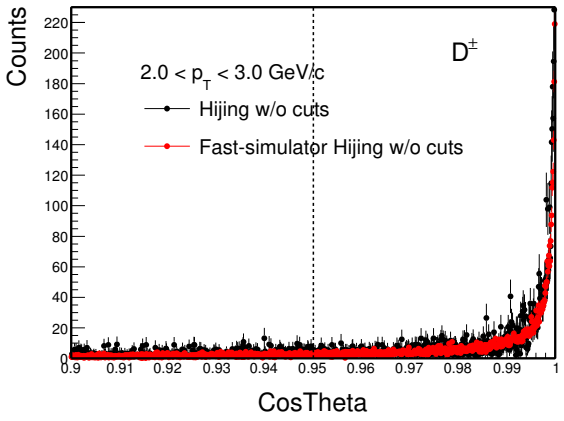

Figure 5.20: $D^{\pm}$ cosTheta distribution in most central 0-10% between Hijing and Fast-Simulation.

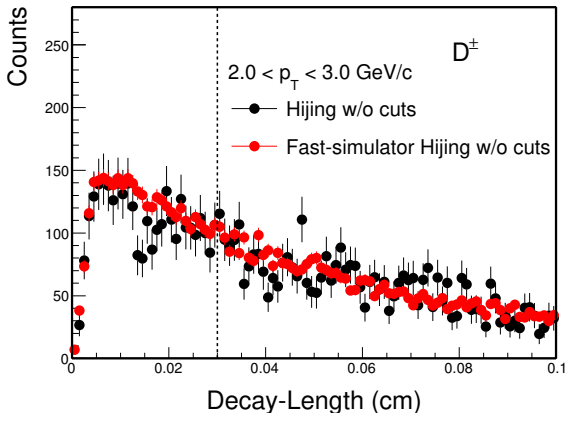

Figure 5.21: $D^{\pm}$ decay length distribution in most central 0-10% between Hijing and Fast-Simulation.

From Fig. 5.20 to Fig. 5.25, these are the 6 topological variables used for the $D^{\pm}$ reconstruction. The topological distributions can be extracted both directly from Hijng + GEANT and from Fast-Simulation relay on Hijing input. The Fast-Simulation part was the modified version similar as we used for the D^0 efficiency study.

As seen, all the comparison of topological variables from Hijing have a very good agreement for $D^{\pm}$, which means again Fast-Simulation method can well reproduce the topological variables in Hijing sample. In another word, the topological efficiency es-

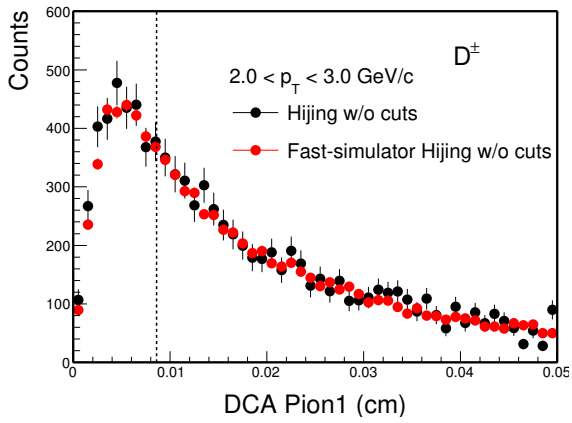

Figure 5.22: $D^{\pm}$ pions1 Dca distribution in most central 0-10% between Hijing and Fast-Simulation.

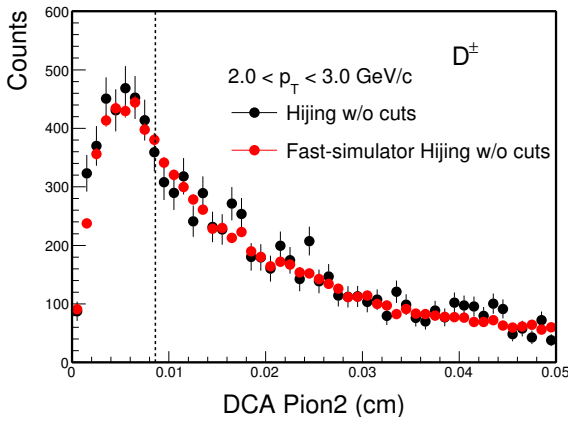

Figure 5.23: $D^{\pm}$ pions2 Dca distribution in most central 0-10% between Hijing and Fast-Simulation.

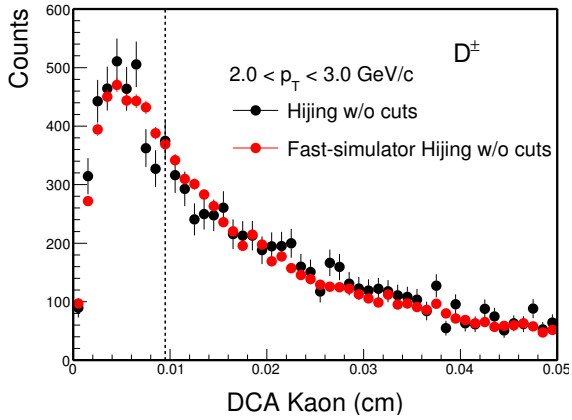

Figure 5.24: $D^{\pm}$ kaons Dca distribution in most central 0-10% between Hijing and Fast-Simulation.

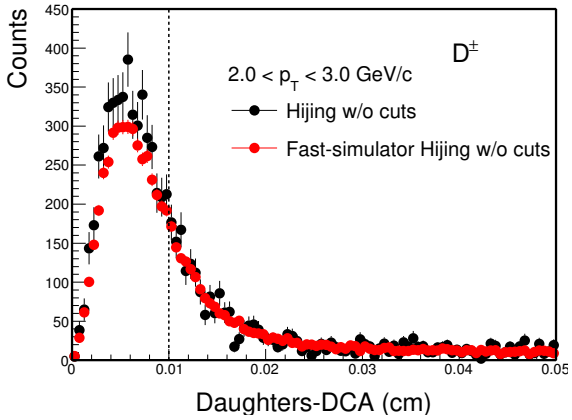

Figure 5.25: $D^{\pm}$ dcaDaughters distribution in most central 0-10% between Hijing and Fast-Simulation.

timation for $D^{\pm}$ from this Hijing-Data-Driven Fast-Simulation is reliable.

5.5 Systematic Uncertainties

The approach for the $D^{\pm}$ systematic uncertainties are similar as D^{0}. Several sources are contributed to the uncertainties. Such as the raw yield extraction, the TPC embedding uncertainties, the fast-simulation package, the vertex resolution contribution, the bin shift correction, and the charm fragmentation uncertainties for $D^{\pm}$ for the comparison with D^{0}. More detailed studies are needed in the future as we discussed before.

Table 5.2 shows an example of the $D^{\pm}$ spectrum uncertainties sources contribution in the most central 0-10% centrality.

Table 5.2: Systematic uncertainties from different sources

p_T range	Yield extra	Embedding	fast-simu	bin shift	charm frag	total
1.0 - 1.5	0.851731	0.09	0.05	0.0416632	0.065	0.861398
1.5 - 2.0	0.269764	0.09	0.05	0.0179911	0.065	0.296515
2.0 - 2.5	0.243506	0.09	0.05	0.00416767	0.065	0.272282
2.5 - 3.0	0.0212626	0.09	0.05	0.00261387	0.065	0.123628
3.0 - 3.5	0.0611226	0.09	0.05	0.00551249	0.065	0.13635
3.5 - 4.0	0.142051	0.09	0.05	0.00646695	0.065	0.187204
4.0 - 5.0	0.120523	0.09	0.05	0.0312138	0.065	0.174141
5.0 - 6.0	0.185863	0.09	0.05	0.0261331	0.065	0.223725

5.6 Other Systematics for the Fast-Simulation

In the previous Fast-Simulation section 3.8, we have two potential concerns for D^0. Here the same as $D^{\pm}$.

Beyond the secondary track and vertex resolutions contributions for this $D^{\pm}$ efficiency correction need to be consider, we still need to improve the precision for the fast-simulation package for $D^{\pm}$ as we saw that $\sim$10% difference.

Chapter 6 Experimental Results and Discussions

The following sections will summarize the results obtained from the processed dataset obtained during Run 14 together with a brief introduction to model comparisons and discussion related to the physics impact of the measurements on our understanding of the QGP.

6.1 The Total D^0 Spectra

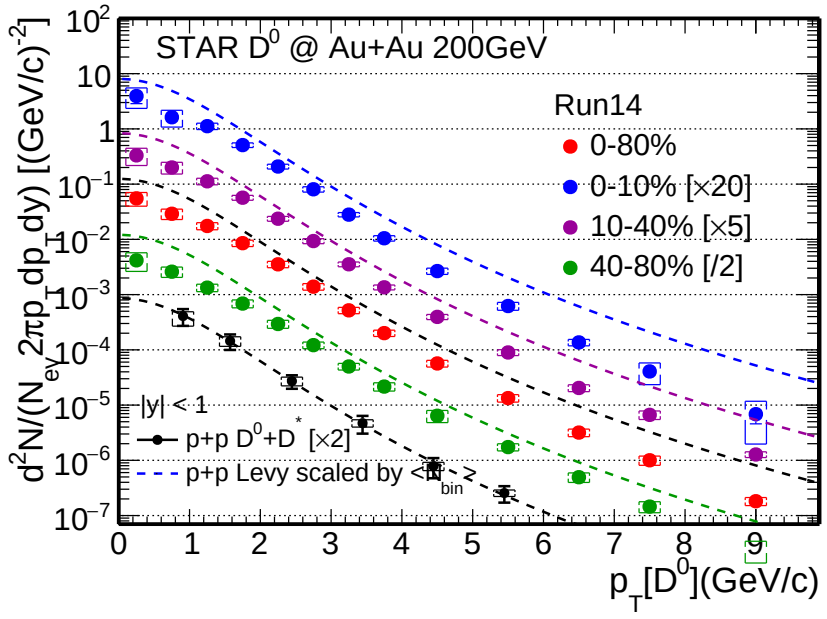

Figure 6.1: D^0 corrected spectra in Au+Au collisions from several centralities.

Fig. 6.1 shows the centrality dependence of the D^0 corrected spectra in Au+Au collisions including 0-10%, 10-40%, 40-80% and 0-80% centrality compared with p+p result. The plotted spectra was after scale for each centrality as shown on the plots. The black circle represent the published D-meson p_T spectrum in p+p collisions at 200 GeV. The dashed line was the fitted p+p levy function after the N_{bin} scaling. The new D_0 results from run14 are consistent with the published result from run10/11 at the high p_T range with much improved precision, but there are some difference at the low p_T range < 2 GeV/c. The re-analysis for the published run10/11 results are still ongoing, most likely there are some issue for the efficiency correction part in the published result, and this is still under investigation. Comparing the Au+Au data with the p+p levy functions, we can clearly see that in the most central collisions 0-10%, the entire p_T

range was suppressed especially for the high p_T range, also the same trend for the other centralities.

6.2 Blast Wave (BW) Model Fit

As discussed before, Blast Wave model was well used to extract the medium parameters. Next is the standard blast wave function used for the D^0 fitting. From the fitting parameters, the average velocity was calculated by Eq. 6.3.

$$\frac{dN}{p_T dp_T} \propto m_T \int_0^R r dr I_0(\alpha_T) K_1(\beta_T) \tag{6.1}$$

$$\rho = tanh^{-1}((\frac{r}{R})^n \beta_s); \quad \alpha_T = (\frac{p_T}{T}) sinh(\rho); \quad \beta_T = (\frac{m_T}{T}) cosh(\rho) \tag{6.2}$$

$$< \beta_T >= \frac{1}{\pi R^2} \int_0^{2\pi} d\phi \int_0^R \beta_s (\frac{r}{R})^n r dr = \frac{2}{n+2} \beta_s \tag{6.3}$$

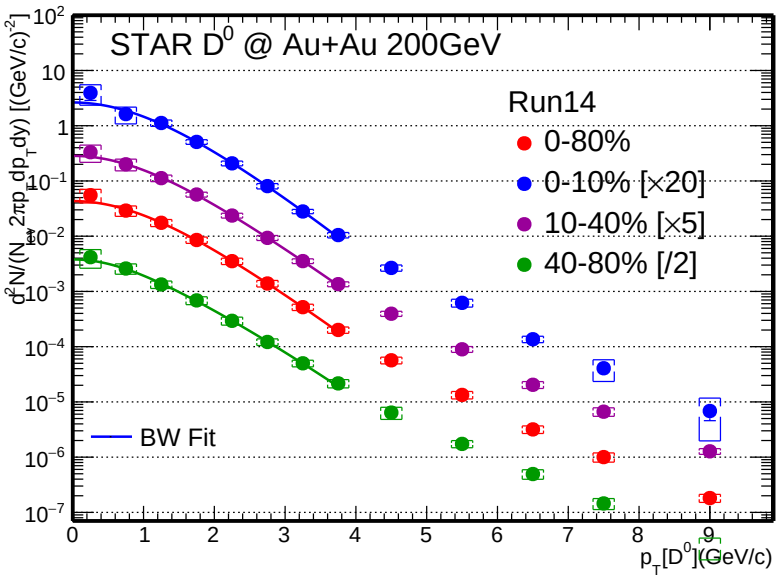

Figure 6.2: D^0 corrected spectra in Au+Au collisions fitting with BW model.

Fig. 6.2 shows the centrality dependence of the D^0 corrected spectra in Au+Au collisions fitting with BW function. The solid line was the fitted function. The fitting range was twice of the D^0 mass and within the uncertainties the fitting results can represent the data points.

The very preliminary fitting results shows that the collective velocity $< \beta_T >$ was much smaller than the previous light hadrons or strangeness hadrons, and the freeze-out

temperatures was higher, which is as expected. For example, from the centrality 10-40%, the fitted $< \beta_T >$ was around $\sim$0.22 while the temperature was around $\sim$0.335. Since this is a first look at the fitting, there are still some unreasonable parameters that getting abnormal terminalization of minimization on the fitting even the fitting looks good. In the near future, we plan to combine several measurements to do some simultaneous fitting to extract the parameters.

6.3 D^0 Nuclear Modification Factor

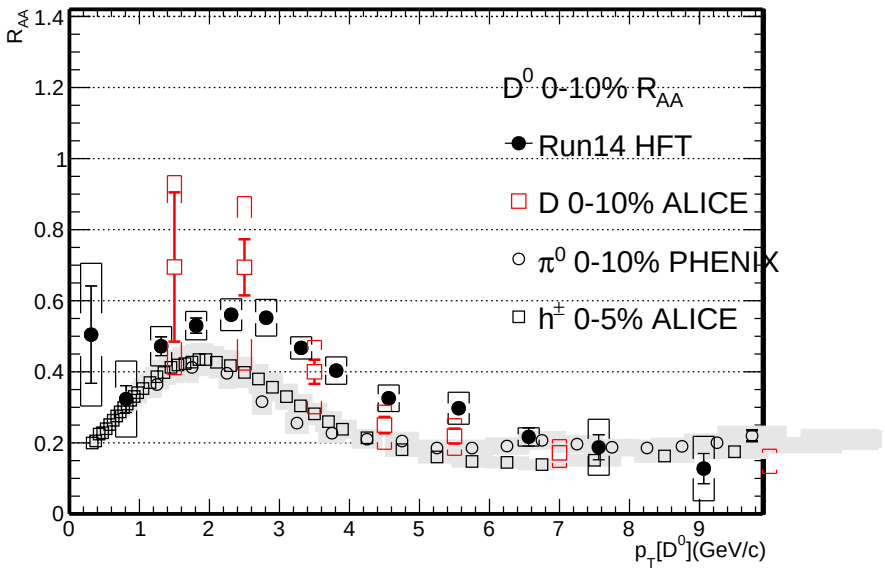

Figure 6.3: D^0 R_{AA} in Au+Au collisions from 0-10% centrality.

In order to see these nuclear modification effect more clearly, we divided the Au+Au data points by the p+p Levy functions. The p+p shape uncertainties are estimate by varying the $pm1\sigma$ of the fit parameters then use the largest deviation from the best fit. The comparison plot was shown in Fig. 6.3, the black data points are the D^0 R_{AA} from the most central 0-10% collisions, the bracket represent the systematically error which will discuss in the following section. As in the plot, the high p_T suppression are obviously seen in the central Au+Au collisions both for D^0. The light hadrons from ALICE at the most central 0-5% collisions, π from PHENIX at the centrality 0-10% and the averaged D meson R_{AA} from ALICE at 0-10% centrality are also plotted here for the comparison. The results show very interesting trends. Firstly, the D^0 result from run14 HFT is quite similar with ALICE averaged D-meson with much better precision while the ALICE result have large uncertainties. Even though the system size and energy is quite different from RHIC to LHC, a factor of $\sim$14 from the energy difference,

but the $D0$ R_{AA} results show the similar suppression structure which may indicating the medium produced in both system could have some similar properties. Secondary, if we compare the D^0 result with light hadrons at ALICE and PHENIX π^0 result, they have quite similar trends and magnitude value. Which means the charmed hadron have strong interaction with the medium as light hadrons. They also have similar energy loss, while maybe both the radiation energy loss and elastic energy loss play an important role. The comparison shows no big difference for both LHC energy and RHIC energy, and also no obvious difference between charmed hadrons and light hadrons.

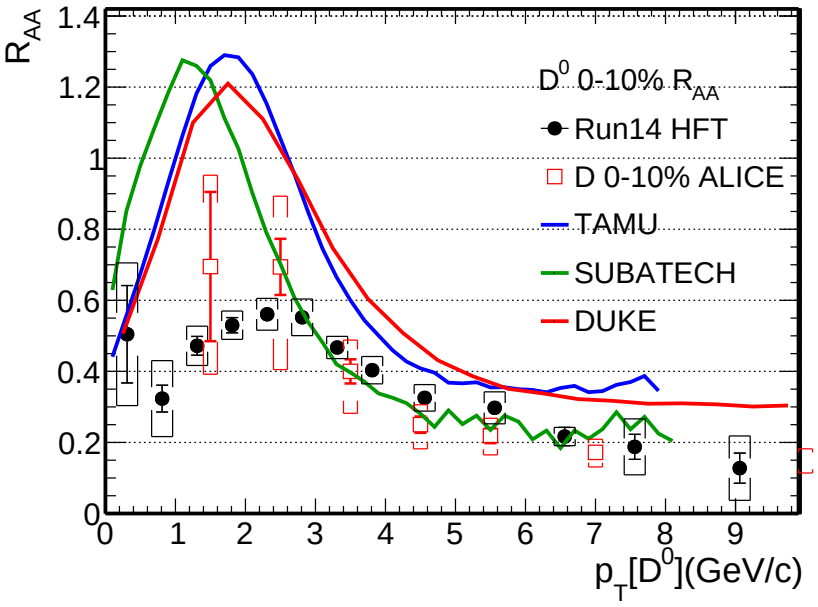

Figure 6.4: D^0 R_{AA} in Au+Au collisions from 0-10% centrality comparison with various models.

Fig. 6.4 shows the D^0 R_{AA} results from the most central 0-10% Au+Au collisions compared with various model calculations. The Duke model uses a Langevin simulation with an input diffusion coefficient parameter- $2\pi TD_S = 7$, where D_S is heavy quark spacial diffusion coefficient and T is medium temperature, which was tuned to the LHC D-meson R_{AA} data [99]. The TAMU calculation uses a non-perturbative approach and the full T-matrix calculation with internal energy potential, which predicts $2\pi TD_S$ to be $\sim$ 2-10. The SUBATECH group uses the pQCD calculation with Hard Thermal Loop technique which indicates the $2\pi TD_S$ $\sim$2-4 [53, 100]. These three models can describe our R_{AA} data points reasonable well at high p_T, but missed the data points at low p_T range, they seem over estimate the magnitude. Currently with the precision of the new data, it will be beneficial to systematically study each ingredient in different model calculations and give us better understandings on the medium properties.

6.4 $D^{\pm}$ Spectra

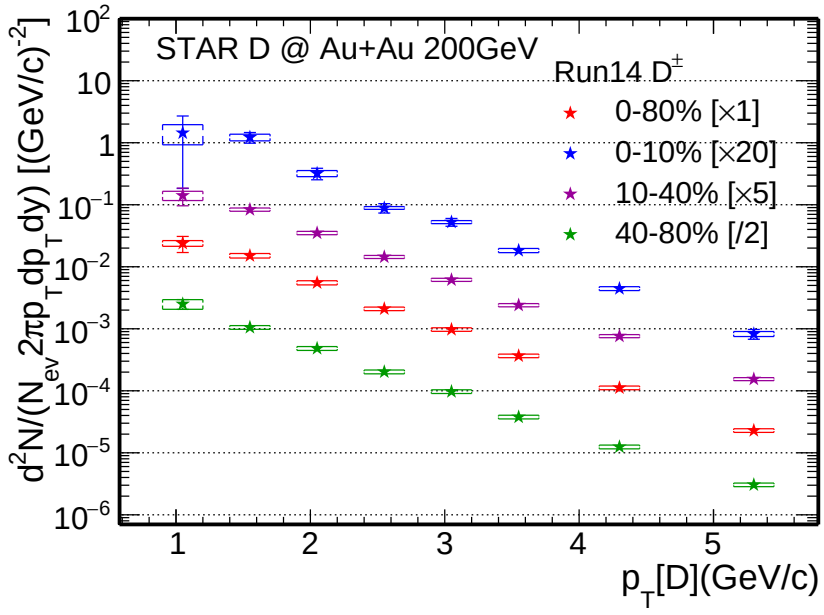

Figure 6.5: $D^{\pm}$ corrected spectra in Au+Au collisions from several centralities.

Fig. 6.5 shows the centrality dependence of the $D^{\pm}$ corrected spectra in Au+Au collisions including 0-10%, 10-40%, 40-80% and 0-80% centrality. The plotted spectra was after scale for each centrality as shown on the plots. The new $D^{\pm}$ results from run14 at the low p_T and high p_T range are missed since the topological cuts are not specifically optimized, the reconstruction acceptance and efficiency are quite small for these kind of three body decay. The analysis with more comprehensive details are still ongoing, most likely we can track the low p_T spectrum down to 0 GeV/c. Fig. 6.6 comparing the $D^{\pm}$ data with the D^0 results, we can see that after the charm fragmentation scale, the $D^{\pm}$ spectrum is consistent with the D^0 results in the measured p_T range within uncertainties, which means the $D^{\pm}$ production mechanism does not change from p+p to Au+Au collisions compare to D^0.

Due to the absence of p+p base line, here we did not plot the R_{AA} for $D^{\pm}$. But as the charm fragmentation does not change from p+p to Au+Au for $D^{\pm}$, the absolute value of nuclear modification effect should be quite similar as D^0 in Fig. 6.3.

6.5 Λ_c/D^0 Ratio and Comparisons to Models

After correcting for the acceptance and efficiency, one can obtain the Λ_c yield and calculate the Λ_c/D^0 ratio. Figure 6.7 shows the first measurement of Λ_c/D^0 ratio for 3

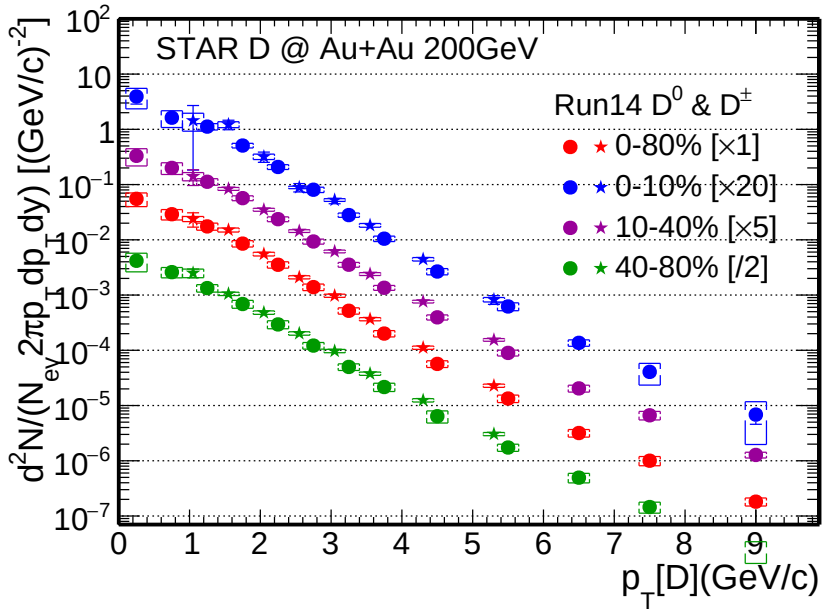

Figure 6.6: $D^{\pm}$ corrected spectra in Au+Au collisions from several centralities comparing with D^0. $D^{\pm}$ is after the charm fragmentation scale to the same level of D^0 for comparison.

$< p_T <$ 6 GeV/c in 10-60% central Au+Au collisions at $\sqrt{s_{\rm NN}}$ = 200 GeV along with model predictions.

The measured Λ_c/D^0 ratio in Au+Au collisions is significantly enhanced compared to the PYTHIA prediction for p+p collisions. The enhancement is also larger than the statistical hadronization model (SHM) predictions. In Ko's model, thermalized charm quarks are used for recombination and the predicted Λ_c/D^0 ratio is comparable to our measurement despite that the calculation is done for the 0-5% centrality bin.

For the coalescence models, there are two different implementations. For the three-quarks implementation, the Λ_c is being treated as a pure three-quark state. In di-quark models, the Λ_c is usually considered as a system consisting of a charm quark and a scalar light [ud] di-quark which could be exist in the strongly coupled quark-gluon plasma (QGP). The predictions for the ratio in low p_T range from these two implementation has some difference, but currently our data does not have the precision to distinguish. One needs measurements at low p_T to further differentiate between three-quark and di-quark recombination scenarios.

In Greco's model, charm quarks diffuse in the QGP medium and then recombine with light quarks to form charm hadrons. The calculated ratio is w.r.t the total charm meson yield including $D^{\pm}$ and $D_s^{\pm}$. One may expect a factor of 1.5 (p+p baseline) or larger (if D_s is enhanced) increase to be compared to our Λ_c/D^0 ratio.

Drawing the baryon-to-meson ratios plots in the same panel as shown in Fig. 6.8,

the interesting results show that, the observed Λ_c/D^0 ratio is quite comparable with the baryon-to-meson ratios for light hadrons and strangeness hadrons.

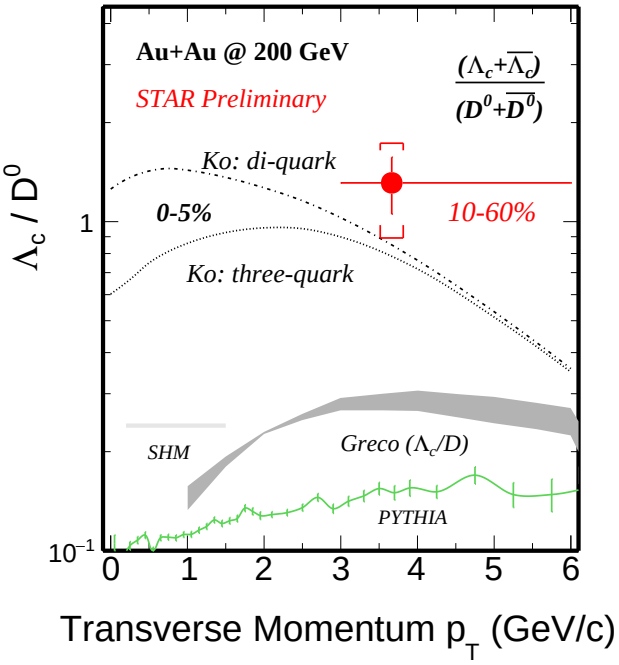

Figure 6.7: Measured Λ_c/D^0 ratio for $3 < p_T < 6$ GeV/c in 10-60% central Au+Au collisions at $\sqrt{s_{\rm NN}}$ = 200 GeV compared to model predictions from PYTHIA, statistical hadronization model (SHM) and coalescence models from Ko and Greco.

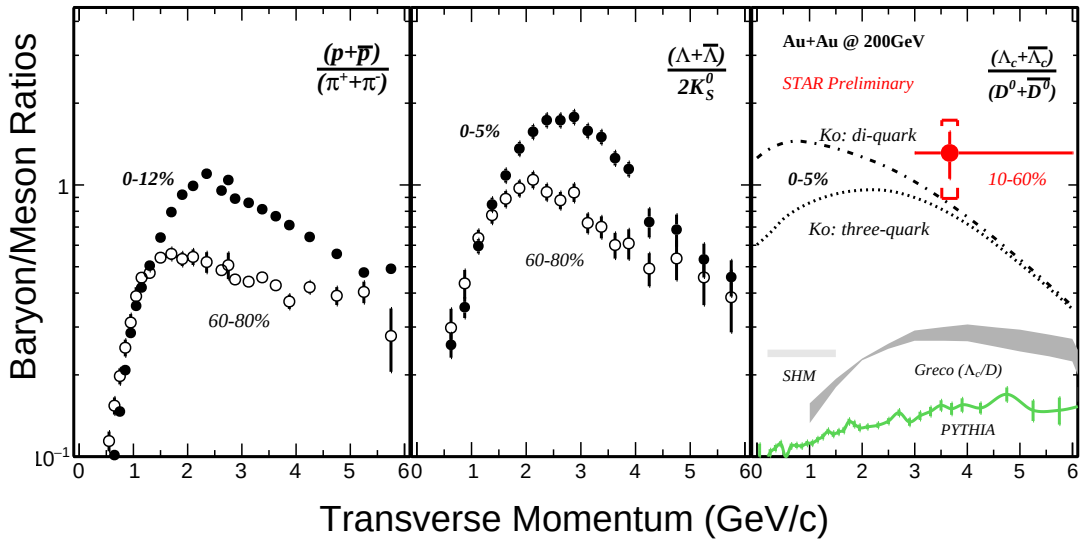

Figure 6.8: Baryon-to-meson ratio for p/π (left panel), Λ/K_s (middle panel) and Λ_c/D^0 (right panel) measured in Au+Au collisions by the STAR experiment. Several model predictions also shown for Λ_c/D^0.

6.6 Some Other's HFT Results (D^0 v_2)

As discussed in the previous section 2.5.2, regarding on the HFT related physics, these dissertation mainly force on the spectra analysis. But also we have some other's results shown recently. An important one is the charm meson flow (v_2) result.

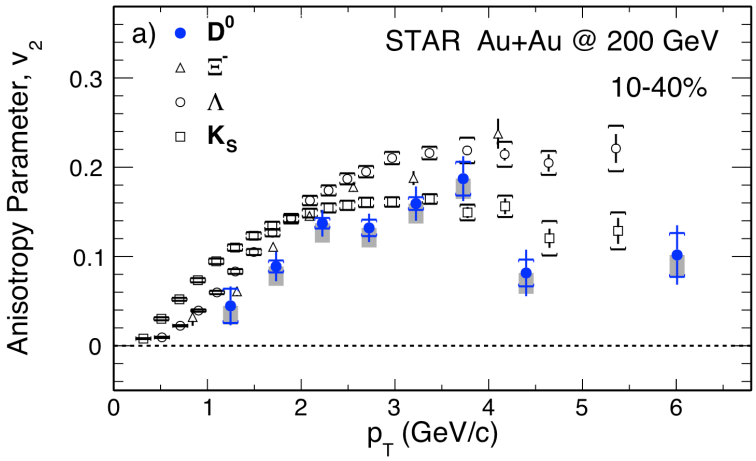

Figure 6.9: v_2 as a function of p_T for D^0 in 10−40% centrality Au+Au collisions compared with K^0_S, Λ, and Ξ^-.

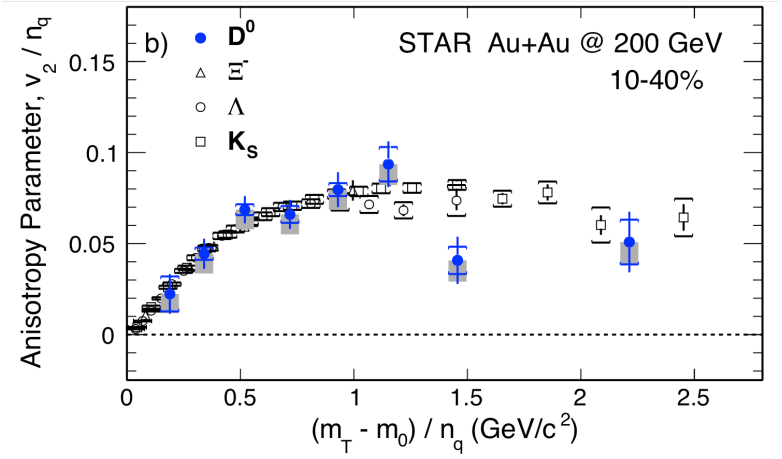

Figure 6.10: v_2/n_q as a function of $(m_T - m_0)/n_q$ for D^0 in 10–40% centrality Au+Au collisions compared with K^0_S, Λ, and Ξ^-.

Fig. 6.9 shows the v_2 as a function of p_T for D^0 in 10 – 40% centrality Au+Au collisions compared with K^0_S, Λ, and Ξ^-. An immediate observation that can be made is the fact that the D^0 elliptic flow is finite. And clearly see the mass ordering for p_T < 2 GeV/c, the D^0 v_2 is smaller than those light and strangeness hadrons. For $p_T > 2$ GeV/c, the D^0 just follows other light mesons.

Furthermore, in order to account for the different particle masses and Number of Constituent Quarks (NCQ), the comparison is done by plotting the v_2/n_q as a function

of $(m_T - m_0)/n_q$ for D^0 where $m_T = \sqrt{m_0^2 + p_T^2}$. After the scaling, all of the particle species, including D^0, follow the same trend. While the 3D viscous hydro model calculations describe the D^0 v_2 well at $p_T <$ 3-4 GeV/c. This is a strong indication that charm quarks are flowing with a thermalized medium where the partons are the relevant degrees of freedom.

Chapter 7 Summary and Outlook

7.1 Summary

In this dissertation analysis, We have shown several of the first measurements of open heavy flavor (D^0, $D^{\pm}$ and Λ_c) through direct topological reconstruction in the hadronic decay channels using the capabilities provided by the HFT at STAR. A dramatic reduction in the combinatorial background is achieved with the HFT. For example, we observe an improvement of over an order of magnitude in the D^0 significance per billion events when compared to previously published results from STAR, permitting the measurement of charm observables with unprecedented precision.

Above all the results shown before from HFT (together with some other's result, D^0 v_2), let's try to summarize them together.

- $\mathbf{R_{AA}(D)} \sim \mathbf{R_{AA}(h)}$ - charm quarks lose significant energy like light quarks
- $\mathbf{v_2(D)} \sim \mathbf{v_2(h)}$ **vs.** $\mathbf{m_T}$ - charm quarks flow like light quarks
- Λ_c /$\mathbf{D^0}$ **enhancement** - coalescence hadronization, observed similar value as light and strangeness hadrons

For D^0, we shown the first measurement of corrected spectra and R_{AA} from HFT with much better precision compared to previous published one. The new results shows significant suppression at high p_T which means the strong interaction between charm quark and the medium and loose energy. And also the D^0 R_{AA} shows quite similar trend as light hadrons.

For $D^{\pm}$, the efficiency corrected spectra was presented. After taken into the charm fragmentation, the $D^{\pm}$ and D^0 spectra have similar/same shape, which means the production mechanism are similar for them.

For Λ_c, we have shown the first measurement of Λ_c in heavy-ion collisions. The enhancement of Λ_c/D^0 ratio was compared to several different models. The coalescence model with thermalized charm quarks are consistent with our data.

From all the observed measurements from this dissertation together with D^0 v_2, charm quarks strongly coupled with the QGP and significantly loss energy. Evidence of charm quark flowing and possibly thermalized in the QGP. Which make charm quarks no big difference compare with light and strangeness quarks. Then a native question will be does charm quark heavy enough as a clean probe to determinate the QGP properties.

7.2 Outlook

The HFT result shown here was from run 2014, HFT has accumulated a significant data set (a factor of 2) for Au+Au minimum bias collisions from 2016 datasets. Furthermore, in 2016 the inner layer of the PiXeL detector have been replaced with aluminum cables to reduce the material budget and improve the HFT's performance at low p_T. Also during the run 2016, PXL have stable and proficient operation, which results to more active sensors as shown in Fig. 7.1 and Fig. 7.2. The average active inner sensors was enhancement to 95% in run 2016 compared to 82% in 2014, while the outer layer was slightly improves from 95% to 97%. On the other hand, the run 2016 experimental environment has much busier occupancy, which will reduce the HFT matched efficiency. This will, in essence complete with each other, but still we expect a factor of 2-3 improvement in the measured significance for measured D^0 and others, hence, the statistical uncertainties presented in these analysis.

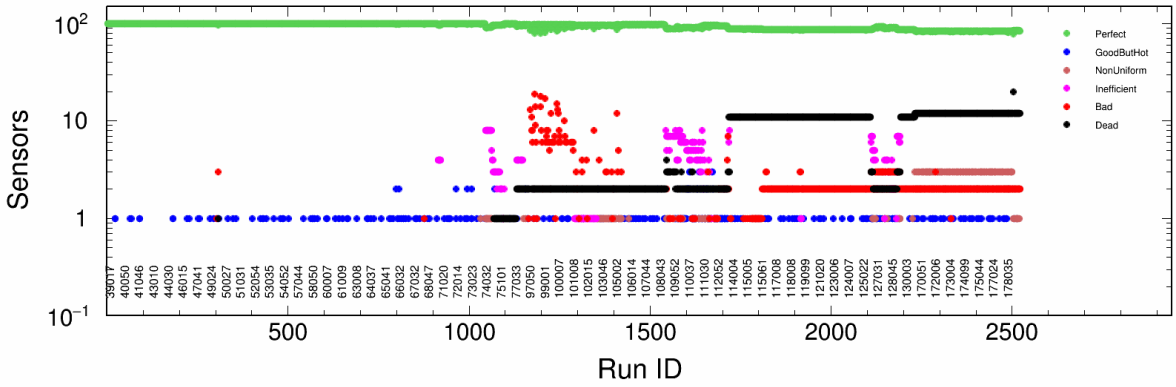

Figure 7.1: PXL inner sensor status vs. all runs in 2016.

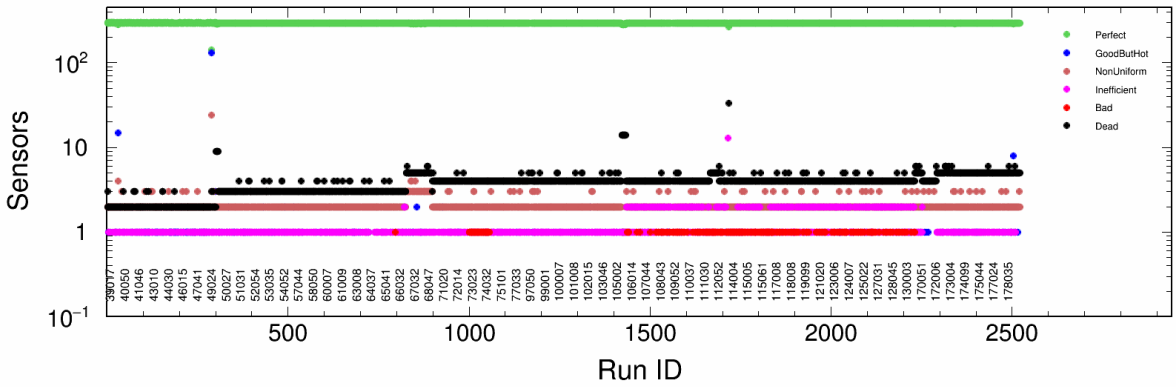

Figure 7.2: PXL outer sensor status vs. all runs in 2016.

Precision measurements with the combined HFT data sets will have an important role in deepening our understanding of the dynamics at play by placing strong con-

straints on the available model calculations as well as opening the doors for many other heavy flavor measurements that will help to complete the picture that is already beginning to form. For instance, the observation of fully thermalized charm quarks at RHIC top energy now brings into question the degree to which bottom quarks, with a mass roughly 4 times that of charm quarks, are interacting with the QGP. Although bottom production is much lower at RHIC, the large datasets with the HFT could provide sufficient to obtain such measurements, and indeed from STAR, we already have some prompt preliminary results for the bottom measurements using the impact parameters method to separate charm and bottom decayed electrons, D^0 and J/Ψ shown in Fig. 7.3.

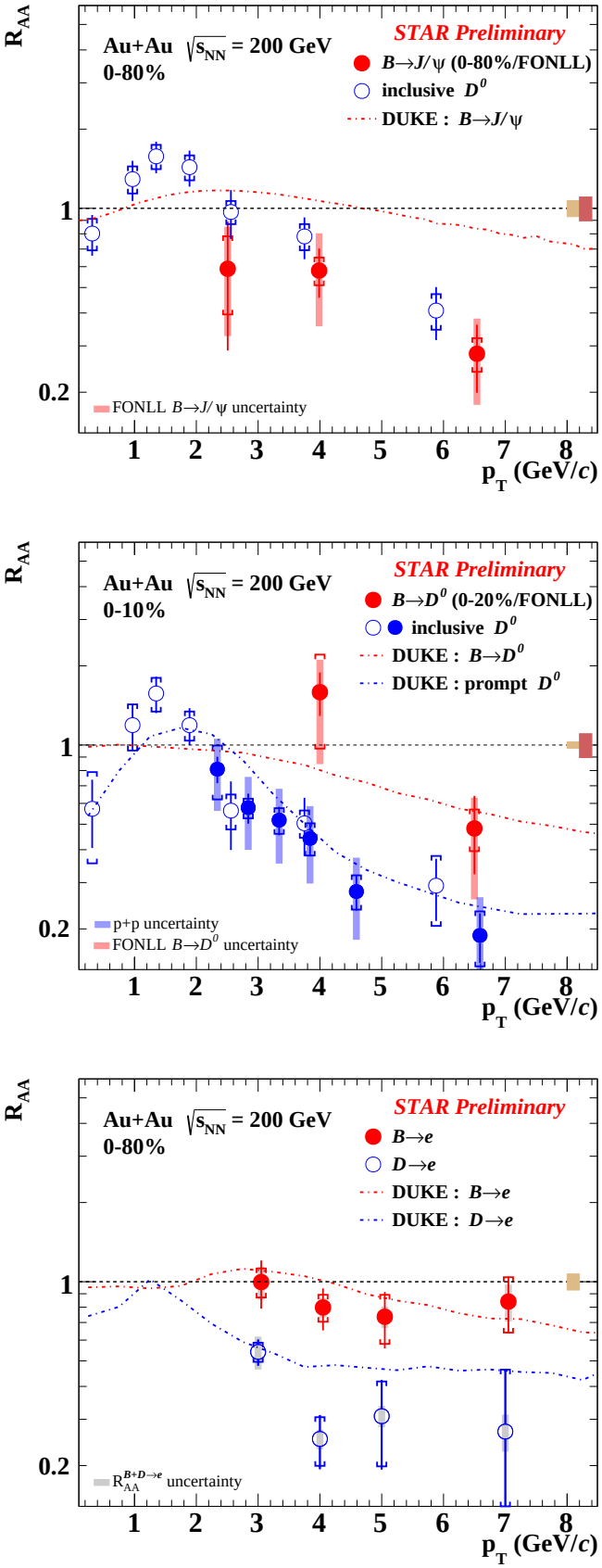

Figure 7.3: The R_{AA} of J/Ψ (top panel), D^0 (middle panel) and electron (bottom panel) from B (filled circles) and D (open circles) hadron decays as a function of p_T in Au+Au collisions at $\sqrt{s_{NN}}$ = 200 GeV.

References

[1] R. Oerter, "The Theory of Almost Everything: The Standard Model, the Unsung Triumph of Modern Physics." *Plume (2006)*.

[2] A. Cho, "Higgs boson makes its debut after decades-long search." *Science. 337 (6091): 141–143 (2012)*.

[3] H. Fritzsch and M. Gell-Mann, "Current algebra: Quarks and what else?" *Proceedings of the XVI International Conference on High Energy Physics. C720906V2, 135 (1972)*.

[4] S. Bethke, "World Summary of α_S" *Nuclear Physics B - Proceedings Supplements. Volume 234, Pages 229-234 (2013)*.

[5] R. Vogt, "Systematics of Heavy Quark Production at RHIC" *arxiv:hep-ph/0203151v1*.

[6] A. Pich, "Quantum Chromodynamics" *arXiv:hep-ph/9505231*.

[7] X. Zhu *et al.*, "D$\bar{\text{D}}$ correlations as a sensitive probe for thermalization in high energy nuclear collisions" *Physics Letters B 647 366–370 (2007)*.

[8] C. Patrignani *et al.*, "Particle Data Group" *Chin. Phys. C, 40, 100001 (2016)*.

[9] K. G. Wilson, "Confinement of quarks" *Phys. Rev. D 10, 2445 (1974)*.

[10] Z. Fodor and S.D. Katz, "Critical point of QCD at finite T and μ, lattice results for physical quark masses." JHEP 0404, 050 (2004).

[11] B. I. Abelev *et al.* (STAR Collaboration), "Experimental Study of the QCD Phase Diagram & Search for the Critical Point: Selected Arguments for the Run-10 Beam Energy Scan." *STAR Internal Note: SN0493 (2009)*.

[12] M. Strickland, "Anisotropic Hydrodynamics: Three lectures." *Acta Physica Polonica B 45, 2355 (2014)*.

[13] S. S. Adler *et al.*, "Systematic studies of the centrality and $\sqrt{s_{NN}}$ dependence of the $dE_T/d\eta$ and $dN_{ch}/d\eta$ in heavy ion collisions at midrapidity." *Phys. Rev. C 71, 034908 (2005)*.

[14] F. Karsch, "Lattice results on QCD thermodynamic." *Nuclear Physics A Volume 698, Issues 1–4, Pages 199-208 (2012)*.

[15] J. Adams *et al.* "Identified Particle Distributions in p+p and Au+Au Collisions at $\sqrt{s_{NN}}$ = 200 GeV" *Phys. Rev. Lett. 92, 112301, (2004)*.

[16] J. Adams *et al.* "Particle-Type Dependence of Azimuthal Anisotropy and Nuclear Modification of Particle Production in Au+Au Collisions at $\sqrt{s_{NN}}$ = 200 GeV" *Phys. Rev. Lett. 92, 052302, (2004)*.

[17] J. Adams *et al.* "ϕ meson production in Au+Au and p+p collisions at $\sqrt{s_{NN}}$ = 200 GeV" *arxiv:nucl-ex/0406003*.

[18] J. Castilllo *et al.* "Elliptic flow of multistrange baryons Ξ and Ω in Au+Au collisions at $\sqrt{s_{NN}}$ = 200 GeV" *J. Phys. G, 30:S1207 (2004)*.

[19] Y. Zhang, "Measurement of charm production cross-section and leptons from its semileptonic decay at RHIC " *Yifei Zhang Theis.*.

[20] E. Schnedermann, J. Sollfrank, U. Heinz "Thermal phenomenology of hadrons from 200A GeV S+S collisions" *Phys. Rev. C 48, 2462 (1993)*.

[21] B. Mohanty and N. Xu "Probe the QCD phase diagram with ϕ-mesons in high energy nuclear collisions" *J. Phys .G, 36:064022 (2009)*.

[22] J. Adams *et al.* "Phi meson production in Au+Au and p+p collisions at $\sqrt{s_{NN}}$=200 GeV" *Phys. Lett. B 612, 181-189 (2005)*.

[23] B. I. Abelev *et al.* "Partonic Flow and ϕ-Meson Production in Au+Au Collisions at $\sqrt{s_{NN}}$=200 GeV" *Phys. Rev. Lett. 99, 112301 (2007)*.

[24] B. I. Abelev *et al.* "Measurements of ϕ meson production in relativistic heavy-ion collisions at RHIC" *Phys. Rev. C 79, 064903 (2009)*.

[25] B. I. Abelev *et al.* "Energy and system size dependence of ϕ meson production in Cu+Cu and Au+Au collisions" *Phys. Lett. B 673, 183-191 (2009)*.

[26] S. S. Adler *et al.* "Production of ϕ mesons at midrapidity in $\sqrt{s_{NN}}$ = 200 GeV Au+Au collisions at relativistic energies" *Phys. Rev. C 72, 014903 (2005)*.

[27] S. Afanasiev *et al.* "Elliptic Flow for ϕ Mesons and (Anti)deuterons in Au+Au Collisions at $\sqrt{s_{NN}}$ = 200 GeV" *Phys. Rev. Lett. 99, 052301 (2007)*.

[28] P. F. Kolb, Ulrich Heinz. "Hydrodynamic description of ultrarelativistic heavy-ion collisions" *arXiv:nucl-th/0305084*.

[29] J. Adams *et al.* "Experimental and Theoretical Challenges in the Search for the Quark Gluon Plasma: The STAR Collaboration's Critical Assessment of the Evidence from RHIC Collisions" *Nucl. Phys. A 757, 102-183 (2005)*.
[30] Z. Lin and C. M. Ko "Flavor Ordering of Elliptic Flows at High Transverse Momentum" *Phys. Rev. Lett. 89, 202302 (2002)*.
[31] D. Molnár and S. A. Voloshin "Elliptic Flow at Large Transverse Momenta from Quark Coalescence" *Phys. Rev. Lett. 91, 092301 (2003)*.
[32] C. Adler *et al.* "Centrality Dependence of High-p_T Hadron Suppression in Au+Au Collisions at $\sqrt{s_{NN}}$ = 130 GeV" *Phys. Rev. Lett. 89, 202301 (2002)*.
[33] C.-Y. Wong "Introduction to High-Energy Heavy-Ion Collisions." *World Scientific Publishing Co. Pte. Ltd., (1994)*.
[34] J. Adams *et al.* "Evidence from d+Au Measurements for Final-State Suppression of High-p_T Hadrons in Au+Au Collisions at RHIC" *Phys. Rev. Lett. 91, 072304 (2003)*.
[35] K.J. Eskola, V.J. Kolhinen, C.A. Salgado "The scale dependent nuclear effects in parton distributions for practical applications" *Eur. Phys. J. C 9, 61-68 (1999)*.
[36] D. de Florian and R. Sassot "Nuclear parton distributions at next to leading order" *Phys. Rev. D 69, 074028 (2004)*.
[37] F. Wang "Measurement of jet modification at RHIC" *J. Phys. G: Nucl. Part. Phys. 30 S1299–S1303 (2004)*.
[38] Yu.L. Dokshitzer, D.E. Kharzeev "Heavy quark colorimetry of QCD matte" *Phys. Lett. B 519, 199-206 (2001)*.
[39] M. Djordjevic, M. Gyulassy, and S. Wicks "Open Charm and Beauty at Ultrarelativistic Heavy Ion Colliders" *Phys. Rev. Lett. 94, 112301 (2005)*.
[40] N. Armesto *et al.* "Testing the color charge and mass dependence of parton energy loss with heavy-to-light ratios at BNL RHIC and CERN LHC" *Phys. Rev. D 71, 054027 (2005)*.
[41] A. Buzzatti and M. Gyulassy "Jet Flavor Tomography of Quark Gluon Plasmas at RHIC and LHC" *Phys. Rev. Lett. 108, 022301 (2012)*.
[42] T. C. Petersen and J. Randrup "Dynamical simulation of DCC formation in Bjorken rods" *Phys. Rev. C 61, 024906 (2000)*.
[43] L. Adamczyk *et al.* "Measurements of D^0 and D^* in p+p collisions at $\sqrt{s}$= 200 GeV" *Phys. Rev. D 86, 072013 (2012)*.
[44] Z. Ye "Open charm hadron production in p+p, Au+Au and U+U collisions at STAR" *Nuclear Physics A Volume 931, Pages 520–524 (2014)*.
[45] D. Acosta *et al.* "Measurement of Prompt Charm Meson Production Cross Sections in p anti-p Collisions at $\sqrt{s}$ = 1.96 TeV" *Phys. Rev. Lett. 91, 241804 (2003)*.
[46] B. Abelev *et al.* "Measurement of charm production at central rapidity in proton-proton collisions at $\sqrt{s}$ = 7 TeV" *J. High Energ. Phys. 2012, 128. (2012)*.
[47] M. Cacciari, P. Nason and R. Vogt "QCD Predictions for Charm and Bottom Production at RHIC" *Phys. Rev. Lett. 95, 122001 (2005)*.
[48] L. Adamczyk *et al.* "Observation of D^0 meson nuclear modifications in Au+Au collisions at $\sqrt{s_{NN}}$ = 200 GeV" *Phys. Rev. Lett. 113, 142301 (2014)*.
[49] L. Adamczyk *et al.* "Open charm yields in d+Au collisions at $\sqrt{s_{NN}}$ = 200 GeV" *Phys. Rev. Lett. 94, 062301 (2005)*.
[50] R. Vogt "The total charm cross section" *Eur. Phys. J. Spec. Top. (2008)*.
[51] B. Abelev *et al.* "Azimuthal anisotropy of D-charm production in Pb-Pb collisions at $\sqrt{s_{NN}}$ = 2.76 TeV" *Phys. Rev. C 90, 034904 (2014)*.
[52] B. Abelev *et al.* "Anisotropic flow of charged hadrons, pions and (anti-)protons measured at high transverse momentum in Pb–Pb collisions at $\sqrt{s_{NN}}$ = 2.76 TeV" *Phys. Lett. B Volume 719, Issues 1–3, Pages 18–28 (2013)*.
[53] L. Adamczyk *et al.* "Measurement of D^0 azimuthal anisotropy at mid-rapidity in Au+Au collisions at $\sqrt{s_{NN}}$ = 200 GeV" *arXiv:1701.06060v3*.
[54] B. I. Abelev *et al.* "Centrality dependence of charged hadron and strange hadron elliptic flow from $\sqrt{s_{NN}}$ = 200 GeV Au+Au collision" *Phys. Rev. C 77, 054901 (2008)*.
[55] B. I. Abelev *et al.* "Identified baryon and meson distributions at large transverse momenta from Au+Au collisions at $\sqrt{s_{NN}}$ = 200 GeV" *Phys. Rev. Lett. 97, 152301 (2006)*.
[56] B. I. Abelev *et al.* "Measurements of identified particles at intermediate transverse momentum in the STAR experiment from Au+Au collisions at $\sqrt{s_{NN}}$ = 200 GeV" *arXiv:nucl-ex/0601042*.
[57] B. I. Abelev *et al.* "Systematic Measurements of Identified Particle Spectra in pp, d+Au and Au+Au Collisions from STAR" *Phys. Rev. C 79, 034909 (2009)*.

[58] P. Sorensen and X. Dong "Suppression of nonphotonic electrons from enhancement of charm baryons in heavy ion collisions" *Phys. Rev. C 74, 024902 (2006)*.

[59] V. Greco, C. M. Ko, and P. Levai "Partonic coalescence in relativistic heavy ion collisions" *Phys. Rev. C 68, 034904 (2003)*.

[60] V. Greco, C. M. Ko, and P. Levai "Parton coalescence and antiproton/pion anomaly at RHIC" *Phys. Rev. Lett. 90, 202302 (2003)* .

[61] I. Kuznetsova, J. Rafelski "Heavy Flavor Hadrons in Statistical Hadronization of Strangeness-rich QGP" *Eur. Phys. J. C 51, 113-133 (2007)* .

[62] S. H. Lee *et al.* "Λ_c Enhancement from Strongly Coupled Quark-Gluon Plasma" *Phys. Rev. Lett. 100, 222301 (2008)* .

[63] A. Andronic, P. Braun-Munzinger, K. Redlich, J. Stachel "Charmonium and open charm production in nuclear collisions at SPS/FAIR energies and the possible influence of a hot hadronic medium" *Phys. Lett. B 659, 149-155 (2008)*.

[64] Y. Oh *et al.* "Ratios of heavy baryons to heavy mesons in relativistic nucleus-nucleus collisions" *Phys. Rev. C 79, 044905 (2009)* .

[65] Y. Oh *et al.* "Diffusion of Λ_c in hot hadronic medium and its impact on Λ_c/D ratio Ratios of heavy baryons to heavy mesons in relativistic nucleus-nucleus collisions" *Phys. Rev. D 90, 054018 (2014)* .

[66] E.C. Aschenauer *et al.*, "The RHIC Spin Program: Achievements and Future Opportunities." *arXiv:1304.0079*.

[67] K.H. Ackermann *et al.* "STAR detector overview." *Nucl. Instr. Meth. A 499, 624 (2003)*.

[68] C. A. Whitten Jr. *et al.* "The Beam□Beam Counter: A Local Polarimeter at STAR." *AIP Conference Proceedings 980, 390 (2008)*.

[69] W.J Llope *et al.* "The STAR Vertex Position Detector." *Nucl. Instr. Meth. A 759, 23 (2014)*.

[70] C. Adler *et al.* "The RHIC zero degree calorimeters." *Nucl. Instr. Meth. A 470, 488 (2001)*.

[71] M. Anderson *et al.* "The Star time projection chamber: A Unique tool for studying high multiplicity events at RHIC." *Nucl. Instrum. Meth. A 499, 659-678, (2003)*.

[72] STAR "The Star Images." *https://drupal.star.bnl.gov/STAR/book/export/html/7278*.

[73] J. Abele *et al.*, "The laser system for the STAR time projection chamber." *Nucl. Instr. Meth. A 499, 692 (2003)*.

[74] H. Bichsel, "A method to improve tracking and particle identification in TPCs and silicon detectors." *Nucl. Instr. Meth. A 562, 154 (2006)*.

[75] M. Shao *et al.*, "Beam test results of two kinds of multi-gap resistive plate chambers." *Nucl. Instr. Meth. A 492, 344 (2002)*.

[76] B. Bonner *et al.*, "A single Time-of-Flight tray based on multigap resistive plate chambers for the STAR experiment at RHIC." *Nucl. Instr. Meth. A 508, 181 (2003)*.

[77] E. Cerron Zeballos *et al.*, "A new type of resistive plate chamber: The multigap RPC." *Nucl. Instr. Meth. A 374, 132 (1996)*.

[78] H. Qiu "STAR heavy flavor tracker" *Nuclear Physics A Volume 931, Pages 1141–1146 (2014)*.

[79] G. Contin (for the STAR Collaboration), "The STAR Heavy Flavor Tracker and Upgrade Plan." *Nuclear Physics A Volume 956, Pages 858-861 (2016)*.

[80] D. Beavis *et al.* "The STAR Heavy Flavor Tracker - Conceptual Design Report" *https://drupal.star.bnl.gov/STAR/starnotes/public/sn0600*.

[81] L. Arnold *et al.* "The STAR silicon strip detector (SSD)" *Nucl. Inst. and Meth. in Phys. Res. Sect. A, Volume 499, Issues 2–3, Pages 692–702 (2003)*.

[82] J. Schambach *et al.* "A MAPS Based Micro-Vertex Detector for the STAR Experiment" *Physics Procedia Volume 66, Pages 514-519, (2015)*.

[83] M. R. Lomnitz "PXL Detector Masking procedures" *STAR internal note https://drupal.star.bnl.gov/STAR/system/files/MaskingDoc.pdf*.

[84] G. Xie "Nuclear Modification Factor of D^0 Meson in Au + Au Collisions at $\sqrt{s_{NN}}$ = 200GeV" *Nuclear Physics A, Volume 956, Pages 473–476 (2016)*.

[85] G. Xie "Measurement of D^0 Meson Production and Azimuthal Anisotropy in Au+Au Collisions at $\sqrt{s_{NN}}$ = 200GeV" *https://arxiv.org/abs/1701.01878*.

[86] G. Xie " Λ_c Production in Au+Au Collisions at $\sqrt{s_{NN}}$ = 200 GeV measured by the STAR experiment" *https://arxiv.org/abs/1704.04353*.

[87] STAR "PicoDst" *http://rnc.lbl.gov/ xdong/SoftHadron/picoDst.html*.

[88] G. Xie *et al.*, "Centrality definitation webpage." *http://www.star.bnl.gov/protected/heavy/xgn1992/Centrality/Run2014/VPDMB5/index.html*.

[89] G. Contin *et al.*, "HFT firmware documents." *https://drupal.star.bnl.gov/STAR/system/files/STAR_PXL_Firmware_Issue_Solved_Final_Report_Oct3_v2.pdf*.
[90] TMVA "TMVA." *http://tmva.sourceforge.net*.
[91] STAR "Embedding p+p run12 ." *https://drupal.star.bnl.gov/STAR/starsimrequests/2013/nov/07/vpdmb-d0d0bar-pp-200-gev-run12*.
[92] F. Karsch and E. Laermann "Thermodynamics and in-medium hadron properties from lattice QCD." *arxiv:hep-lat/0305025*.
[93] P. Crochet, P. B. Munzinger "Investigation of background subtraction techniques for high mass dilepton physics" *Nucl. Instrum. Meth. A 484, 564-572 (2002)*.
[94] M. Cai "Improved Event-mixing for Resonance Measurements" *http://lup.lub.lu.se/luur/download?func=downloadFile&recordOId=8889631&fileOId=8889632*.
[95] STAR "STAR embedding documentation" *https://drupal.star.bnl.gov/STAR/comp/embedding/embedding-procedures/embedding-documentation*.
[96] STAR "STAR analysis note" *https://drupal.star.bnl.gov/STAR/starnotes/private/psn0594*.
[97] STAR "STAR Hijing documentation" *https://drupal.star.bnl.gov/STAR/blog/xlchen/hft-simulation-hijing-hf-simulation*.
[98] S. S. Adler *et al.* "Identified charged particle spectra and yields in Au+Au collisions at $\sqrt{s_{NN}}$ = 200GeV" *Phys. Rev. C 69, 034909 (2004)*.
[99] S. Cao, G. Qin and S. Bass "Energy loss, hadronization, and hadronic interactions of heavy flavors in relativistic heavy-ion collisions" *Phys. Rev. C 92, 024907 (2015)*.
[100] A. Andronic *et al.* "Heavy-flavour and quarkonium production in the LHC era: from proton–proton to heavy-ion collisions" *Eur. Phys. J. C 76: 107 (2016)*.

Appendix A Appendix

ACKNOWLEDGMENTS

This thesis could never come out without the support and help from lots of people. I would like to express my gratitude to these listed in the following and many others I might not mention.

First of all, I would thank Prof. Cheng Li, who has been my adviser for the last five years. He introduced me to this field and provided the opportunity to participate the STAR MTD programs and the MRPC manufacture at USTC. I appreciate his continuous supervision and support in the last five years. My gratitude also goes to Prof. Xin Dong who is the co-advisor of my PhD research at Berkeley Lab. He guided me all the analysis details throughout the thesis, i am impressive by his numerous ideas and enthusiasm on the research and benefited so much from the day-to-day discussion with him in the last three years. He also helped me a lot on my staying at LBNL. I would like to thank Prof. Nu Xu, my another co-advisor at LBNL, for offering me the great opportunity to study at Berkeley, the most wonderful place for relativistic heavy-ion physics research where collected lots of smart people worked together. I would also express my gratitude to Prof. Zebo Tang, who is also my advisor, during the first two years of my PhD he introduced me to the heavy-ion physics field and guided me the whole analysis work at that time. He introduced me and gave me this great opportunity to worked with Xin Dong at Berkeley. I have learned a lot from the tons of fruitful discussions with them.

My special thanks goes to Prof. Yifei Zhang, who introduced me a lot in the HFT ralated analysis in the very first beginning, he also helped me a lot when i first come to Berkeley. My special thanks also goes to Dr. Hao Qiu who taught me a lot in my analysis, HFT related software and hardware works. Many thanks to him since he also helped me a lot during my staying at Berkeley. My special thanks also goes to Dr. Mustafa Mustafa, he has lots of good ideas during our discussion on the analysis and he followd almost all the details, i really learned lots of technical skills and impressived by his productive and enjoyed the great discussions and friendship with him.

I would like to thank Dr. Michael Lomnitz, Dr. Giacomo Contin, my colleagues at Berkeley and we share the same office. I would like to express my thanks for the friendship and memories together. I would also like to thank Prof. Peter Jacobs, Prof. Grazyna Odyniec, Prof. Xiaofeng Luo, and Prof. Shusu Shi, Dr. Alexander Schmah, Dr. Jinlong Zhang, Dr. Sanshiro Mizuno, Dr. Xu Sun, Dr. Yi Guo and Dr. Sooraj Radhakrishnan, Mr. Long Ma, Mr. Ji Xu, Mr. Xiaolong Chen, Mr. Kunsu Oh, Miss. Huijun Ge and Miss Kathryn Meehan. All these smart people from Berkeley lab, i really enjoyed the discussions and appreciate your assistances for my analysis and living at

Berkely.

I would like to thank the HFT group, heavy flavor physics working group in STAR Collaboration, especially Prof. Zhenyu Ye and Dr. Rongrong Ma.

I appreciate many assistances from the High Energy Physics Group at USTC, especially Prof. Ming Shao, Prof. Yongjie Sun and Prof. Yi Zhou. I would also thanks all my colleagues and frineds from USTC, Dr. Tianxiang Chen, Dr. Chi Yang, Dr. Shuai Yang, Dr. Wangmei Zha, Dr. Kun Jiang, Dr. Xiaozhuang Wang, Mr. Hui Zhang, Mr. Qian Yang, Mr. Long Zhou, Mr. Rongxing Yang, Mr. Wenhao You, Mr. Xiaokun Zhao, Miss. Shenghui Zhang, Miss. Zhen Liu, Mr. Dongdong Hu, Mr. Yankun Sun, Mr. Pengfei Wang and Miss. Yuanjing Ji. I appreciate all your helps in the last few years, we lived at USTC like a big family and life is full of happiness every day.

Finally, I express my deep gratitude to my dear family. I would like to thank my parents for their selfless dedication and unconditional support. I would like to thank my sister for the continuous support and understanding. I can not reach where i am today without them.

Presentations and Publication List

Presentations:

1. J/Ψ Production at STAR (talk)

   2014 年中国物理学会高能物理学术年会, Apri.18 - 22, 2014. Wuhan, Chian.

2. High p_T J/Ψ production in U+U collisions at STAR (poster)

   XXIV International Conference on Ultrarelativistic Nucleus-Nucleus Collisions (Quark Matter 2014), May.19 - 24, 2014. Darmstadt, Germany.

3. Nuclear Modification Factor of D^0 Meson in Au + Au Collisions at $\sqrt{s_{NN}}$ = 200GeV (talk)

   XXV International Conference on Ultrarelativistic Nucleus-Nucleus Collisions (Quark Matter 2015), Sep.27 - Oct.3 2015, Kobe, Japan.

4. Measurement of D^0 Meson Production and Azimuthal Anisotropy in Au+Au Collisions at $\sqrt{s_{NN}}$ = 200GeV (talk)

   The 8th International Conference on Hard and Electromagnetic Probes of High-energy Nuclear Collisions (Hard Probes 2016), Sept.23 - 27, 2016. Wuhan, China.

5. Λ_c Production in Au+Au Collisions at $\sqrt{s_{\rm NN}}$ = 200 GeV measured by the STAR experiment (poster + talk)

   XXVI International Conference on Ultrarelativistic Nucleus-Nucleus Collisions (Quark Matter 2017), Feb.6 - 11 2017, Chicago, USA.

Publication List:

1. *Nuclear Modification Factor of D^0 Meson in Au + Au Collisions at $\sqrt{s_{NN}}$ = 200GeV*

   G. Xie (for the STAR Collaboration), Nuclear Physics A, Volume 956, December 2016, Pages 473–476

2. *Measurement of D^0 Meson Production and Azimuthal Anisotropy in Au+Au Collisions at $\sqrt{s_{NN}}$ = 200GeV*

   G. Xie (for the STAR Collaboration), (Submitted to Nuclear and Particle Physics Proceedings)

   https://arxiv.org/abs/1701.01878

3. Λ_c *Production in* Au+Au *Collisions at* $\sqrt{s_{NN}}$ *= 200 GeV measured by the STAR experiment*

   G. Xie (for the STAR Collaboration), (Submitted to Nuclear Physics A)

   https://arxiv.org/abs/1704.04353

STAR Publications as active Author：

1. Measurement of D^0 azimuthal anisotropy at mid-rapidity in Au+Au collisions at $\sqrt{s_{NN}} = 200$ GeV

   L. Adamczyk *et al.* (STAR Collaboration), Phys. Rev. Lett. xxx, xx (2017) (Accepted)

   https://arxiv.org/abs/1701.06060